Optimizing vanadium dispersion in mesoporous silicas using different anchoring metal ions for C-C catalytic bond cleavage in lignin degradation

Xinnan Lu

▶ **To cite this version:**

Xinnan Lu. Optimizing vanadium dispersion in mesoporous silicas using different anchoring metal ions for C-C catalytic bond cleavage in lignin degradation. Catalysis. Université de Lyon; East China normal university (Shanghai), 2017. English. NNT : 2017LYSEN070 . tel-02425998

HAL Id: tel-02425998

https://theses.hal.science/tel-02425998

Submitted on 1 Jan 2020

HAL is a multi-disciplinary open access archive for the deposit and dissemination of scientific research documents, whether they are published or not. The documents may come from teaching and research institutions in France or abroad, or from public or private research centers.

L'archive ouverte pluridisciplinaire **HAL**, est destinée au dépôt et à la diffusion de documents scientifiques de niveau recherche, publiés ou non, émanant des établissements d'enseignement et de recherche français ou étrangers, des laboratoires publics ou privés.

Numéro National de Thèse: 2017LYSEN070

THESE DE DOCTORAT DE L'UNIVERSITE DE LYON

opérée par
l'Ecole Normale Supérieure de Lyon
en co-tutelle avec
l' East China Normal University

Ecole Doctorale N°206
Ecole Doctorale de Chimie (Chimie, Procédés, Environnement)

Discipline : Chimie

Soutenue publiquement le 21 Octobre 2017 par
Mlle LU Xinnan

Optimizing vanadium dispersion in mesoporous silicas using different anchoring metal ions for C-C catalytic bond cleavage in lignin degradation

Optimisation de la dispersion du vanadium dans les silices mésoporeuses par effet d'angrage chimique: dégradation catalytique de la lignine

---

Devant le jury composé de :

M. ORDOMSKY Vitaly, Chargé de recherche au CNRS, E2P2L-CNRS-Solvay,	Rapporteur
M. ZHANG Dengsong, Professeur, Université de Shanghai,	Rapporteur
M. GUO Yun, Professeur, East China University of Science and Technology,	Examinatrice
Mme. PINEL Catherine, Directrice de l'institut, IRCE Lyon,	Examinatrice
M. BONNEVIOT Laurent, Professeur, ENS Lyon,	Directeur de thèse
M. LU Yong, Professeur, Ecole Normale Supérieure de l'Est de la Chine,	Co-directeur de thèse

National Thesis Number: 2017LYSEN070

THESIS OF DOCTORATE OF THE UNIVERSITY OF LYON
Operated by
Ecole Normale Supérieure de Lyon
cotutelle with
East China Normal University

Doctoral School Nº206
Doctoral School of Chemistry

Discipline: Chemistry

Public Defense on 21st October 2017 by

Miss LU Xinnan

Optimizing vanadium dispersion in mesoporous silicas using different anchoring metal ions for C-C catalytic bond cleavage in lignin degradation

---

The jury composed of:

Mr ORDOMSKY Vitaly, Director of research in CNRS, E2P2L-CNRS-Solvay,	Reporter
Mr ZHANG Dengsong, Professor, Shanghai University,	Reporter
Mr GUO Yun, Professor, East China University of Science and Technology,	Examiner
Ms PINEL Catherine, Director of the Institute, IRCE Lyon,	Examiner
Mr BONNEVIOT Laurent, Professor, ENS Lyon,	Supervisor of the thesis
Mr LU Yong, Professor, East China Normal University,	Co-supervisor of the thesis

Abstract

The search for practical large-scale, fast, clean and energy saving chemical processes are highly regarded in the frame of a sustainable development, particularly for the most problematic oxidation reactions. Apart from chemical engineering solutions, improving the process using heterogeneous catalysis is one of the most adapted solution. Vanadium being considered the best metal for such kind of reactions, one had to tackle the problem of its high dispersion on a support to minimize its high propensity for leaching and to optimize its stability for practicable, safe and clean uses. In the present thesis, vanadium is supported inside the nanopores of a mesoporous silica of MCM-41 type where the high dispersion is assisted by the presence of anchoring ions such as Al(III), Ti(IV), Zr(IV) and Ce(IV) ions. A large set of V-(Al/Ti/Zr/Ce)-MCM-41 catalysts was prepared according to three different methods of preparation: i) ultra-fast one-pot synthesis protocol using the assistance of microwave, ii) post-synthesis modification using molecular stencil patterning (MSP) technique and iii) partial thermal treatment (PTT) of the organo-silylated support. The catalysts were characterized thoroughly using a panel of physical techniques and, particularly, the blue shift of the optical gap measured from the vanadium charge transfer band known to correlated with the dispersion of the metal. In complement, the stability was tested from metal leaching using methanol as a corrosive solvent while their catalytic reactivity was estimated in the aerobic oxidation of 1,2-diphenyl-2-methoxyethanol. This is a model reaction that simulates the oxidative C-C bond cleavage in lignin, the most difficult and crucial step in the degradation of this biopolymer, then producing in a clean way valuable methoxylated phenoxy propanol units useful for biomass fuels or bio-sourced precursors for fine chemistry. A high throughput screening approach was applied to test this aerobic oxidation reaction running over 96 reactors in parallel at the same temperature and sorting out the best catalysts with the most suitable anchoring ions and metal loading for the highest catalytic efficiency.

Résumé

Dans le cadre du développement durable, les procédés rapides, propres et peu énergivores sont très recherchés particulièrement en chimie pour les réactions d'oxydation. A part les solutions de génie des procédés, la catalyse est l'un des meilleurs atouts pour améliorer le processus. Le vanadium étant l'un des meilleurs métaux catalytiques pour de tels réactions, nous avions à nous attaquer son problème de relargage dans le milieu réactionnel en vue d'applications acceptables pour l'environnement. Nous proposons donc dans cette thèse des catalyseurs au vanadium fixé à l'intérieur des nano pores de silices mésoporeuses hexagonales de type MCM-41. La grande dispersion et la rétention du vanadium sont promues grâce à la présence d'ion d'ancrage : Al(III), Ti(IV), Zr(IV) and Ce(IV). Une grande variété de catalyseurs de type V-(Al/Ti/Zr/Ce)-MCM-41 ont été préparés à partir de trois méthodes de synthèse: l'une, ultra-rapide en une étape assistée par micro-onde, la seconde à étapes séquentielles multiples mettant en œuvre une technique de pochoir moléculaire et la troisième à nombre d'étapes réduites utilisant un traitement thermique partiel d'une surface préalablement organosilylée avant le greffage des métaux. Un large panel de techniques physicochimiques fut appliqué à la caractérisation de ces solides avec une attention particulière portée à l'analyse de la bande de transfert de charge ligand-métal du vanadium au degré d'oxydation +5 dont le décalage vers le bleu est corrélé à la taille des clusters d'oxyde de ces ions. La rétention du vanadium dans le méthanol a été corrélée à la dispersion du vanadium comme la dégradation à l'air du 1,2-diphényle-2-méthoxyéthanol. Ce substrat fut choisi comme modèle pour étudier la dégradation de la lignine par clivage C-C ou C-O. Notons que ce bio-polymère produit du phénoxypropanol methylé bio-sourcé utilisé dans les bio-carburants et comme précurseur en chimie fine. Dans le cas présent, un balayage à haut débit de la dégradation de cette molécule mettant en œuvre 96 mini-réacteurs en parallèle a permis de sélectionner le solvant, le métal d'ancrage et la teneure des deux métaux donnant la plus haute conversion. Contrairement aux catalyseurs homogènes, nos catalyseurs présentent une très haute sélectivité en clivage C-C.

摘要

在可持续发展的背景下，对于清洁高效节能可行的大规模化工过程尤其是存在诸多问题的氧化反应过程的探索倍受瞩目。除化学工程解决方案之外，通过多相催化来改进反应过程也是最可行的途径之一。钒被认为是最适合于催化此类反应的金属之一，其亟待解决的问题是实现钒在载体上的高度分散，并最大限度地降低其浸出倾向，改善其稳定性，从而实现对其安全清洁有效的利用。本文提出将钒负载于 MCM-41 型六方介孔二氧化硅的纳米孔道中，通过锚定离子如 Al(III)、Ti(IV)、Zr(IV)、Ce(IV)离子的存在促进钒的高度分散和固载。采用三种不同的方法制备了一系列 V-(Al/Ti/Zr/Ce)-MCM-41 催化剂：1、超快微波一步合成法，2、使用分子复刻版技术改性的后嫁接法，3、对有机硅烷化载体进行部分热处理改性的后嫁接法。通过一系列物理化学技术对合成的催化剂进行了充分表征，特别是对与金属分散度相关的钒的电荷跃迁带的测量和与其对应的光谱带隙蓝移进行了分析。随后，以甲醇作为腐蚀溶剂对合成的钒催化剂进行了金属析出的稳定性测试。通过一种木质素模型化合物 1,2-diphenyl-2-methoxyethanol 的需氧氧化反应测试了所合成负载型钒催化剂的催化活性。在相同温度及反应条件下，用 96 通道高通量微反应器技术评价了所制催化剂对该反应的催化性能，筛选出具有最高催化效率的负载型钒催化剂及其最适合的锚定离子。该反应中的碳-碳键裂解反应是木质素降解的最关键也是最困难的步骤之一，可通过这类生物聚合物的降解以清洁的方式生产有用的生物质燃料或生物来源高附加值精细化学品前驱体。

Contents

Chapter 1. Introduction

1.1 General introduction

Mesoporous silicate material is one of the most important types of porous materials. The report of M41S by the Mobil company in 1992 opened a new gate for the mesoporous materials.[1, 2] Mesoporous silica is a very good candidate for the preparation of supported heterogeneous catalysts own to its high surface area, relatively large pores diameter, narrow pores size distribution, various possibility for the modification of surface, controllable hydrophilicity and hydrophobicity, *etc*.[3]

There are many different strategies to do the modification and to incorporate new functions on mesoporous silica, depending on the different methods used for the functionalization, the position and local environment of functional groups or active sites are different.[4]

One-pot synthesis is a very efficient method to accomplish the formation of mesoporous silica support and to introduce the active metal species into the support structure simultaneously. The dispersal of incorporated active sites can be loaded both in the wall of silica and on the surface of mesoporous.[5, 6] The uniform dispersion of functions and convenient preparation process make the one-pot synthesis a potential method with strong operability for the mass production of the supported catalyst in the industry. As the metal species are introduced into the precursor mixture before the structure formation of support, one-pot incorporation lack of fine control of the active site location, and a high loading of the hetero metal sites in silica walls can lead to the loss of ordered arrangement of the mesoporous silica framework.

Post-synthesis is the grafting or modification steps after the synthesis of the mesoporous framework. To modify the surface properties or introduce active sites without entering into the silica skeleton matrix, the functional groups (such as organic functional groups, oxidic species, transition metal, and noble metal species) were incorporated on the mesoporous silica surface. To obtain the post-functionalized mesoporous materials, different strategies can be applied, such as impregnation,[7, 8] ion-exchange,[9] and covalent grafting.[10-12] With these methods, the initial silica phase

can be retained very well and the functional groups are accessible as they were all loaded on the surface of silica matrix, but the dispersion of functional groups may not be perfectly homogeneous.[3, 13] For the post-functionalization, there are several factors that need to be considered: the dispersion and the isolation of the functional groups, the environment of the functional groups, and the relative location of the different functional groups. The fine control at a molecular level should be not only at short distance but also at long distance.

The strategy of surface molecular engineering can be applied for the fine control of incorporated functional groups on mesoporous silica to obtain well-defined active sites with an appropriate environment and a better isolated state.[14] The molecular stencil patterning (MSP) technique[15, 16] is a post-functionalization approach that can be applied for the surface modification of mesoporous silica.[17-19] The main idea of MSP technique is the use of a partial coverage of the silanol groups. The template, such as cetyltrimethylammonium (CTA^+), present in the as-made material during the functionalization, can be used to create a molecular coverage, regularly distributed due to the electrostatic self-repulsion between the cationic heads of the template. To proceed further, the surface silanol groups not masked by the CTA^+ cationic head are capped using organosilanes, such as hexamethyldisilazane (HMDSA) or 2,2,5,5-tetramethyl-2,5-disila-1-azacyclopentane (TMDSACP). The former will produce the covalently linked trimethylsilyl (TMS) and the latter ethyl-1,2-bis(dimethylsilyl) (EBDMS). The role of TMS or EBDMS is to fix the image drawn by the molecular stencil template. The latter pattern acting as a "latent image" to be fixed. After that, the active sites (such as metal ions or complexes) can be grafted on the available surface released by the removing of masking agents. The metal ions are grafted in between the capped silanol groups. Therefore, the MSP technique is a promising approach for developing highly dispersed supported metallic catalysts.[20-25]

Among the supported translation metal heterogeneous catalysts, vanadium is a good candidate as the active species, which is wildly used in the oxidation of alkanes and alkylaromatics, epoxidation reactions, oxidation of alcohols, oxidative

bromination reactions, oxidative strecker reactions, sulfoxidation, *etc*.[26, 27] Vanadium active sites can be incorporated onto the surface of mesoporous silica to prepare heterogeneous vanadium catalysts, the high dispersion and low leaching effect of vanadium active sites are critical qualities for an efficiently supported vanadium catalyst.

Though the supports were normally considered as inert matrices, there is an interaction known as the metal oxide-support effect that contributes to the improvement of the catalysts performance.[28] The fine control of surface active sites dispersion by the modification of the support surface properties would be a potential strategy to develop high performance supported vanadium catalysts.[29-31] In this study, we propose to introduce Al(III), Ti(IV), Zr(IV), and Ce(IV) ions on the surface of mesoporous silica. Indeed, these hetero ions were expected to act as anchors to improve the surface interaction between the vanadium active sites and the support.

In chapter 1, a brief introduction of this thesis is summarized followed by a structure tracks of each chapter. In chapter 2, the development of mesoporous silica supported vanadium catalysts and their applications are reviewed based on the literature survey. Chapter 3 lists the chemicals and characterization methods employed in this research. In chapter 4, vanadium ions as well as the anchoring aluminum, titanium, zirconium, or cerium ion salts are incorporated into the mesoporous silica structure by microwave assisted one-pot synthesis. In chapter 5, the vanadium active species and the aluminum, titanium, zirconium, or cerium anchors are incorporated on the surface of mesoporous silica by MSP technique with the EBDMS functions. In chapter 6, a simpler silanol technique of silanol isolation called partial thermal treatment technique are developed. It is based on the partial silanol recovery by controlled calcination after a full silanol capping followed by grafting the vanadium sites with or without anchoring ions. Several different characterizations are carried out in chapter 4 to 6 for the understanding of the structure features of these catalysts and the effect of the different anchors loadings. In chapter 7, all the above supported vanadium catalysts are tested in the lignin model degradations via a high throughput screen technique, the oxidative carbon-carbon bond cleavage of

1,2-diphenyl-2-methoxyethanol is catalyzed by these vanadium catalysts with different efficiency, which is discussed in details. Finally, chapter 8 summarizes the results in this thesis and presents a conclusion and the perspectives. More data and figures related to this research are collected in the appendix.

1.2 References

1. Kresge, C.; Leonowicz, M.; Roth, W.; Vartuli, J.; Beck, J. *nature* **1992,** 359, (6397), 710-712.
2. Beck, J.; Vartuli, J.; Roth, W. J.; Leonowicz, M.; Kresge, C.; Schmitt, K.; Chu, C.; Olson, D. H.; Sheppard, E.; McCullen, S. *J. Am. Chem. Soc.* **1992,** 114, (27), 10834-10843.
3. Hoffmann, F.; Cornelius, M.; Morell, J.; Fröba, M. *Angew. Chem. Int. Ed.* **2006,** 45, (20), 3216-3251.
4. Taguchi, A.; Schüth, F. *Microporous Mesoporous Mater.* **2005,** 77, (1), 1-45.
5. Dufaud, V.; Beauchesne, F.; Bonneviot, L. *Angew. Chem. Int. Ed.* **2005,** 44, (22), 3475-3477.
6. Zhang, M.; Zhu, W.; Li, H.; Xun, S.; Ding, W.; Liu, J.; Zhao, Z.; Wang, Q. *Chem. Eng. J.* **2014,** 243, 386-393.
7. Shin, E. W.; Han, J. S.; Jang, M.; Min, S.-H.; Park, J. K.; Rowell, R. M. *Environ. Sci. Technol.* **2004,** 38, (3), 912-917.
8. Heydari-Gorji, A.; Belmabkhout, Y.; Sayari, A. *Langmuir* **2011,** 27, (20), 12411-12416.
9. Zhang, Z.; Dai, S.; Fan, X.; Blom, D. A.; Pennycook, S. J.; Wei, Y. *J. Phys. Chem. B* **2001,** 105, (29), 6755-6758.
10. Maschmeyer, T.; Rey, F.; Sankar, G.; Thomas, J. M. *Nature* **1995,** 378, (6553), 159-162.
11. Mercier, L.; Pinnavaia, T. J. *Environ. Sci. Technol.* **1998,** 32, (18), 2749-2754.
12. Mal, N. K.; Fujiwara, M.; Tanaka, Y. *Nature* **2003,** 421, (6921), 350-353.
13. Lim, M. H.; Stein, A. *Chem. Mater.* **1999,** 11, (11), 3285-3295.
14. Albela, B.; Bonneviot, L. *New J. Chem.* **2016,** 40, (5), 4115-4131.
15. Abry, S.; Albela, B.; Bonneviot, L. *C. R. Chim.* **2005,** 8, (3), 741-752.
16. Badiei, A.; Bonneviot, L.; Crowther, N.; Ziarani, G. M. *J. Organomet. Chem.* **2006,** 691, (26), 5911-5919.
17. Abry, S.; Lux, F.; Albela, B.; Artigas-Miquel, A.; Nicolas, S.; Jarry, B.; Perriat, P.; Lemercier, G.; Bonneviot, L. *Chem. Mater.* **2009,** 21, (12), 2349-2359.
18. Calmettes, S.; Albela, B.; Hamelin, O.; Menage, S.; Miomandre, F.; Bonneviot, L. *New J. Chem.* **2008,** 32, (4), 727-737.
19. Abry, S.; Thibon, A.; Albela, B.; Delichère, P.; Banse, F.; Bonneviot, L. *New J. Chem.* **2009,** 33, (3), 484-496.
20. Zhang, K.; Albela, B.; He, M.-Y.; Wang, Y.; Bonneviot, L. *PCCP* **2009,** 11, (16), 2912-2921.
21. Zhang, K.; Lam, K. F.; Albela, B.; Xue, T.; Khrouz, L.; Hou, Q. W.; Yuan, E. H.; He, M. Y.; Bonneviot, L. *Chem. Eur. J.* **2011,** 17, (50), 14258-14266.
22. Zhang, K.; Zhang, Y.; Hou, Q.-W.; Yuan, E.-H.; Jiang, J.-G.; Albela, B.; He, M.-Y.; Bonneviot, L. *Microporous Mesoporous Mater.* **2011,** 143, (2), 401-405.
23. Jollet, V.; Albela, B.; Sénéchal-David, K.; Jégou, P.; Kolodziej, E.; Sainton, J.; Bonneviot, L.; Banse, F. *Dalton Trans.* **2013,** 42, (32), 11607-11613.
24. Chaignon, J.; Stiriba, S.-E.; Lloret, F.; Yuste, C.; Pilet, G.; Bonneviot, L.; Albela, B.; Castro, I. *Dalton Trans.* **2014,** 43, (25), 9704-9713.
25. Zribi, S.; Albela, B.; Bonneviot, L.; Zina, M. S. *Appl. Catal., A* **2015,** 502, 195-203.
26. Ligtenbarg, A. G.; Hage, R.; Feringa, B. L. *Coord. Chem. Rev.* **2003,** 237, (1), 89-101.
27. Sutradhar, M.; Martins, L. M.; da Silva, M. F. C. G.; Pombeiro, A. J. *Coord. Chem. Rev.* **2015,** 301, 200-239.
28. Weckhuysen, B. M.; Keller, D. E. *Catal. Today* **2003,** 78, (1), 25-46.

29. Roozeboom, F.; Mittelmeijer-Hazeleger, M.; Moulijn, J.; Medema, J.; De Beer, V.; Gellings, P. *J. Phys. Chem.* **1980,** 84, (21), 2783-2791.

30. Muylaert, I.; Van Der Voort, P. *PCCP* **2009,** 11, (16), 2826-2832.

31. Beck, B.; Harth, M.; Hamilton, N. G.; Carrero, C.; Uhlrich, J. J.; Trunschke, A.; Shaikhutdinov, S.; Schubert, H.; Freund, H.-J.; Schlögl, R. *J. Catal.* **2012,** 296, 120-131.

Chapter 2. Literature Survey

2.1 Porous minerals

2.1.1 History

Since the discovery of the stilbites, the first zeolite mineral (*zeo* and *lithos* are from two Greek words which mean "to boil" and "a stone") in 1756 by the Swedish mineralogist Cronstedt,[1] people have tried for more than 260 years to develop porous materials, not only natural minerals, but also synthetic minerals, for their structures and their industrial applications (Table 1). Due to their controllable skeleton constitution and porosity structure, porous minerals exhibit a series of properties such as adsorption, desorption, shape selectivity, *etc*. Therefore, they were widely used in the field of catalysis, separation, medicine, energy storage, sensors, *etc*.[2]

Table 1. Early History of Zeolite.[3]

Year	Reporter	Discovery
1756	Cronstedt	First zeolite mineral: stilbite[1]
1862	St. Claire Deville	First hydrothermal synthesis of zeolite: levynite[4]
1896	Friedel	Dehydrated zeolites consisting of open spongy frameworks[5, 6]
1909	Grandjean	Dehydrated chabazite adsorption[7]
1925	Weigel & Steinhoff	First molecular sieve effect[8]
1927	Leonard	The first use of XRD identification in mineral synthesis[9]
1930	Taylor & Pauling	First single crystal structures zeolite mineral[10-12]
1932	McBain	Established the term of "molecular sieve"[13]
1945	Richard M. Barrer	The first classification of zeolites by molecular size[14]
1948	Richard M. Barrer	First definitive synthesis of zeolites[15]
1954	Union Carbide	Commercialized synthetic zeolites

2.1.2 Definition and classification

According to the definition given by the IUPAC (the International Union of Pure and Applied Chemistry), porous materials were classified into three categories according to their porous sizes:[16]

(i) macropores with the pore diameter exceeding about 0.05 μm or 50 nm (500 Å);

(ii) micropores with the pore diameter not exceeding about 2.0 nm (20 Å);

(iii) mesopores with the intermediate size pores (2.0 nm ~ 50 nm).

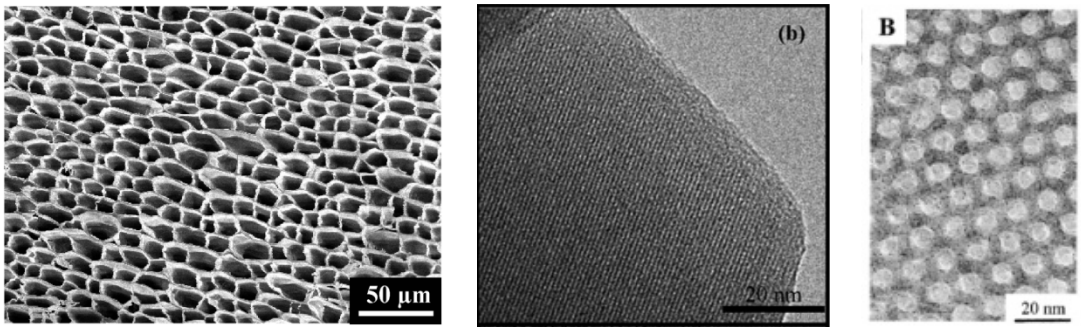

Figure 1. SEM and TEM images of (a) macroporous,[17] (b) microporous,[18] and (c) mesoporous[19] minerals.

2.2 Mesoporous materials

2.2.1 History

Since the intensive discovery of new structures of zeolites from 1980s, hundreds of zeolites with different compositions and pore size have been developed.[20] But their catalytic applications were limited due to the microporous pore size, which can only be available for some small molecules. Therefore, pore enlargement was needed for the catalytic application of larger molecules. In 1992, the Mobil company reported a major advance in molecular sieves; their researchers designed a new family of mesoporous materials M41S,[21, 22] which opened a new gate for an active research field.

2.2.2 Types and structures

Mesoporous silicate materials are one of the most quickly developed systems. They have a flexible structure that can be precisely controlled, and a stable framework with a modifiable surface. According to their unique structures ordering, several typical examples are summarized in Table 2. The three members of the M41S family that are most widely known are MCM-41, MCM-48, and MCM-50 (Figure 2).

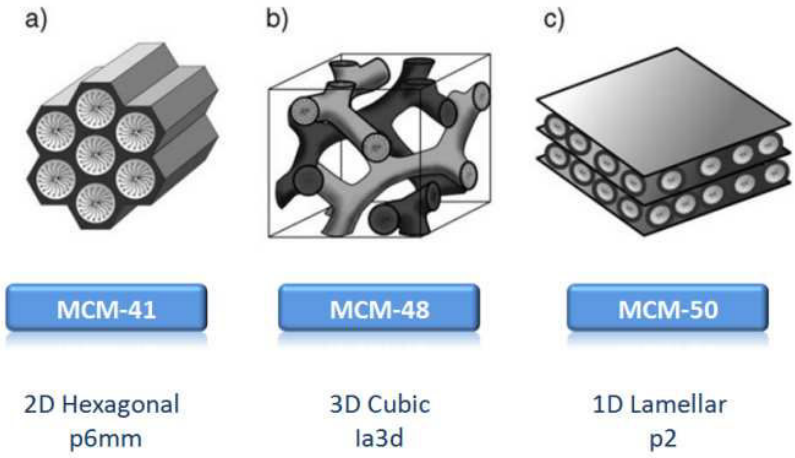

Figure 2. Structures of mesoporous M41S materials: a) MCM-41, b) MCM-48, and c) MCM-50.[23]

2.2.3 Synthesis of mesoporous silica

2.2.3.1 Chemical source

Chemicals used for the synthesis of mesoporous silica include a variety of the silica sources: sodium silicate (Na_2SiO_3), amorphous silica (SiO_2), colloidal silica (LUDOX), tetramethyl orthosilicate (TMOS), tetraethyl orthosilicate (TEOS), tetrapropyl orthosilicate (TPOS), tetrabutyl orthosilicate (TBOS). The most important ingredient is the surfactant template to create the porosity, such as: cetyltrimethylammonium (CTMA), hexadecyltrimethylammonium bromide (CTAB), cetyltrimethylammonium chloride (CTAC), cetyltriethylammonium (CTEA), nonionic surfactants, block copolymers, *etc*. Some typical sources for the synthesis of mesoporous silica are summarized in Table 3.

Table 2. Typical mesoporous materials with different structures.[24]

Framework	Syngony	Space group	Example
Low ordering			MSU-n
			HMS
			KIT-1
One dimensional	Lamellar	p2	MCM-50
Two dimensional	Hexagonal	p6mm (17)	MCM-41
			SBA-3
			SBA-15
			FSM-16
			TMS-1
	Tetragonal	c2mm (9)	SBA-8
			KSW-2
Three dimensional	Cubic	Pm3n (223)	SBA-1
			SBA-6
		Im3m (229)	SBA-16
		Fd3m (227)	FDU-2
		Fm3m (225)	FDU-12
		Pm3m (221)	SBA-11
		Ia3d (230)	MCM-48
			FDU-5
		Pn3m (224)	HOM-7
	Tetragonal	$I4_1/a$ (88)	CMK-1
			HUM-1

Table 3. Examples of some mesoporous silica with their synthesis source.[24]

Mesoporous silica	Source of silica	Template	pH	Porous diameter
MCM-41[21, 25]	Na_2SiO_3, TEOS, SiO_2	C_nTMA	Alkaline	2~10 nm
MCM-48[22, 26-28]	TEOS, SiO_2	C_nTMA	Alkaline	2~4 nm
SBA-1[25]	TEOS	C_nTEA	Acidic	2~3 nm
SBA-3[25]	TEOS	C_nTMA	Acidic	2~3 nm
SBA-15[18, 29]	Na_2SiO_3, TEOS	Block copolymer	Acidic	5~30 nm
SBA-16[18, 29]	TEOS	Block copolymer	Acidic	5~30 nm

In addition to the synthesis based on surfactant or block co-polymers (soft templates), there are also some synthesis methods based on hard templates, for example, carbon, resin, *etc*.[30-36] Here, we mainly focusing on the soft template synthesis.

2.2.3.2 Synthesis methods

There are different methods for the synthesis of mesoporous materials:[24] (1) room temperature synthesis,[37, 38] (2) hydro-thermal synthesis,[39] (3) microwave-assisted synthesis,[40, 41] (4) wet gel calcination,[42] (5) phase transition,[43, 44] (6) solvent evaporation method,[45-48] (7) non-aqueous system synthesis, [49, 50] *etc*.

The typical synthesis process consists of mixing the silica source (or other precursors) with the template (as structure-directing agent), followed by the aging or heating step, and the removal of the template by calcination or extraction (Figure 3).

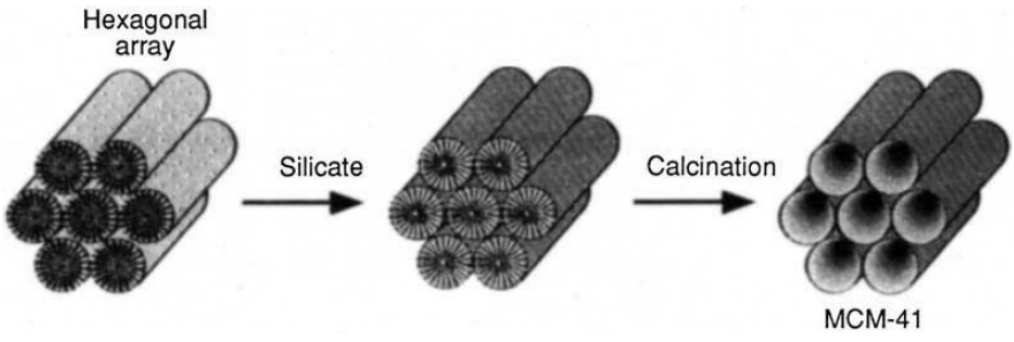

Figure 3. Typical synthesis process of MCM-41.[21]

There are several important factors that can influence the pore size. The most obvious factor is the type of template,[18, 29] and even using the same type of template, the pore size can be adjusted by the surfactant chain length (e.g. long-chain alkyltrimethylammonium halides).[22, 51, 52] The synthesis temperature, time, pressure, pH, concentration, solvent, and additives can also control the morphology and structure of mesoporous materials.[22, 29, 53, 54] The surface modification or thermal treatment with solvent after synthesis can improve the pores size control or the hydrothermal stability.[55-57]

2.2.4 Mechanism

2.2.4.1 The interaction between silica and template

In most of the synthesis approaches, the formation of mesoporous silica relies on the matching of charge at the silica-template interface.[58] Different interactions (Figure 4) are possible: (a) the interaction between the silica anions (SiO^-) and quaternary ammonium cations in basic environment; (b) the interaction between positive charged silica and cationic surfactant with the additional mediating halide ion X^- in acidic environment; (c) the interaction between negatively charged silica and anionic surfactant with the additional mediating M^+ cations in basic environment; (d) the interaction between positively charged silica and anionic surfactant in acidic environment; (e) the interaction between uncharged silica and nonionic surfactant via hydrogen bonds; (f) the interaction between silica ion pairs and nonionic surfactant via hydrogen bonds.[25, 52]

Since the discovery of MCM-41, people have proposed several different mechanisms for the formation of the mesoporous structure, even though there is not a full understanding of its true essence of the mechanism until now. Here we introduce some of the most representative theories.

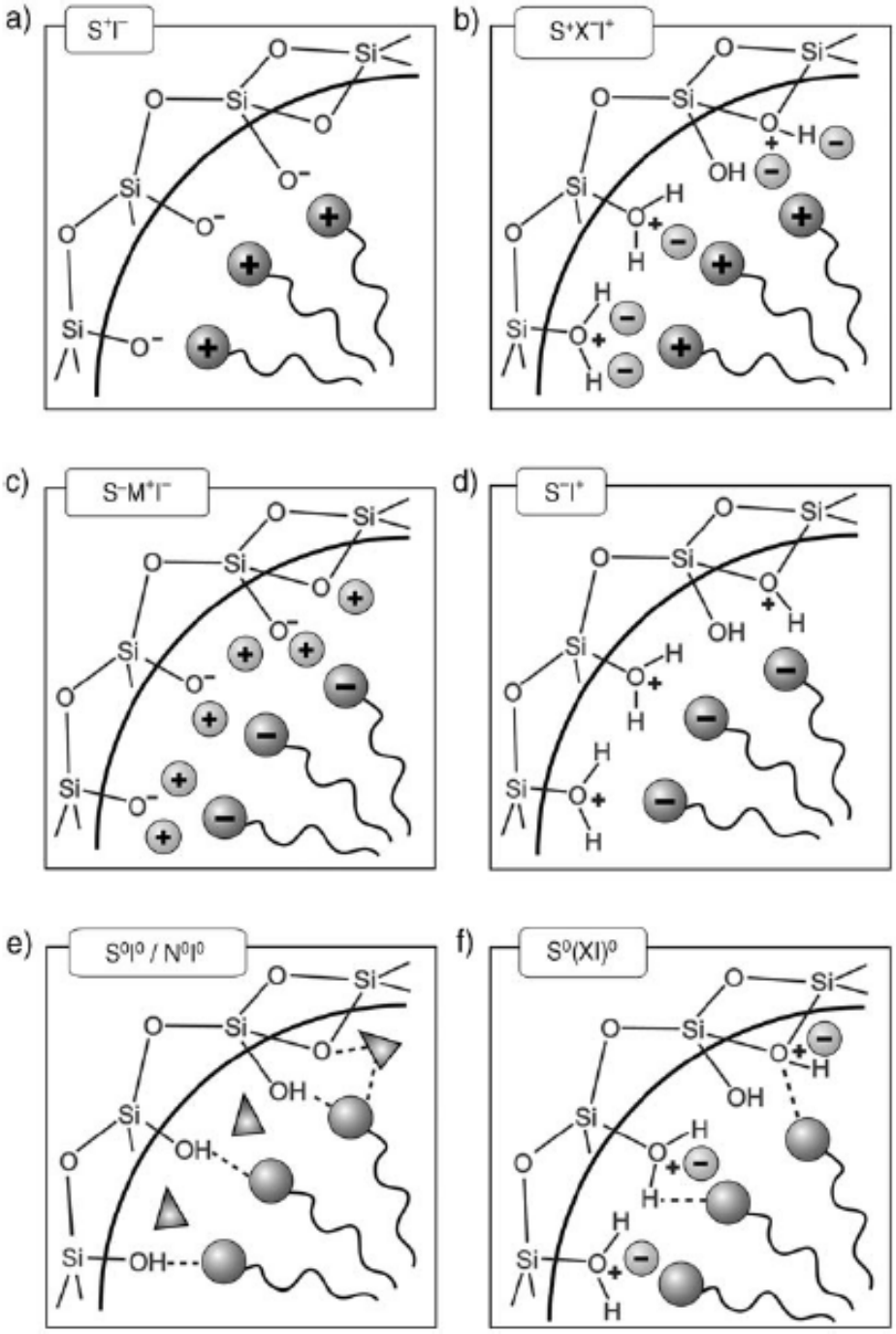

Figure 4. Interactions between the inorganic species and the head group of the surfactant with consideration of the possible synthetic pathway in acidic, basic, or neutral media (S: surfactant; I: inorganic species).[23, 59]

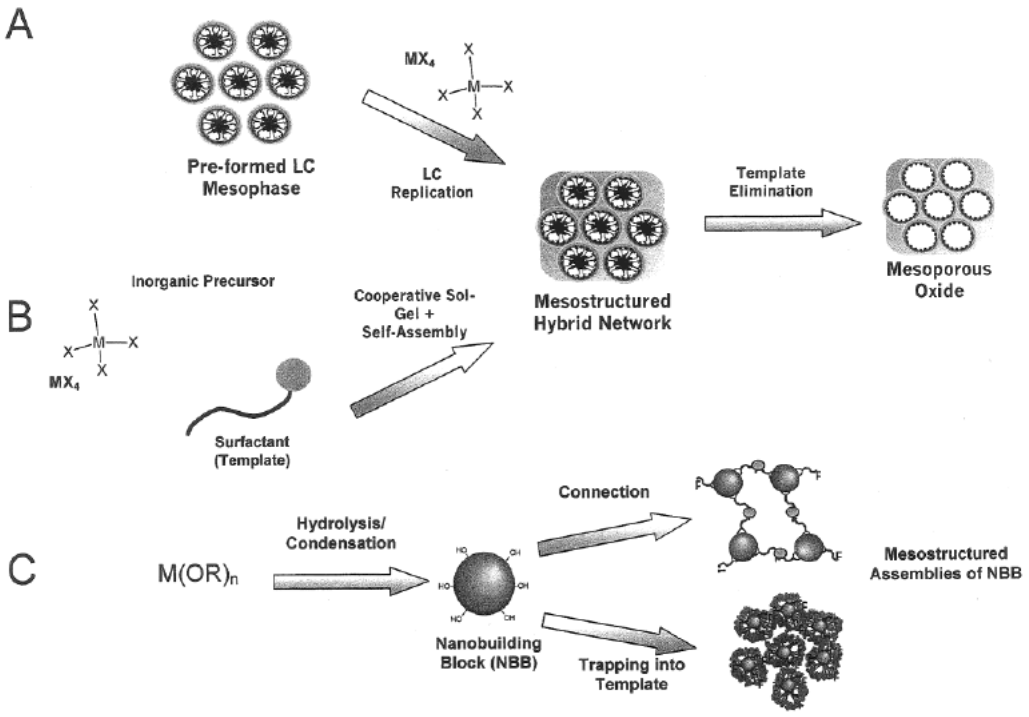

Figure 5. Main synthetic routes for the preparation of mesostructured materials.[60]

2.2.4.2 Liquid crystal templating

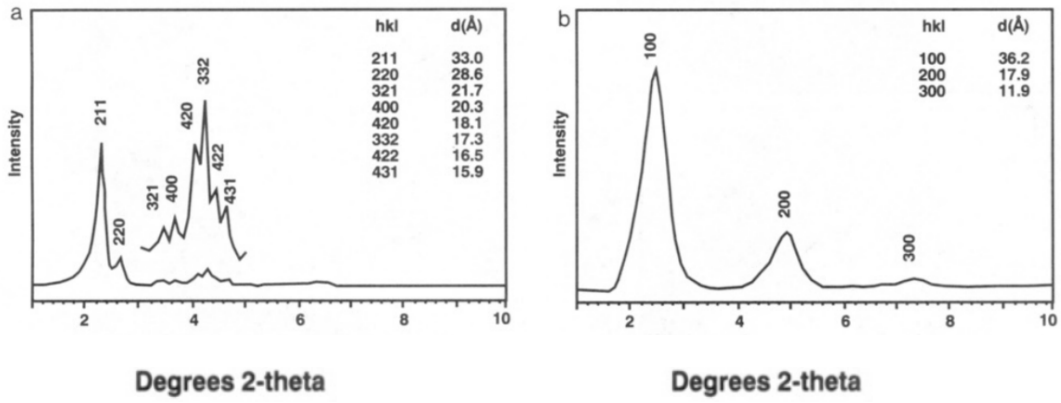

Figure 6. Powder X-ray diffraction patterns of (a) calcined cubic material and (b) the as-synthesized unstable lamellar material.[22]

In 1992, Beck *et al.*[22] proposed the liquid crystal templating (LCT) mechanism. During the synthesis and characterization of MCM-41, they found that the structure characterized either by microscopy or by X-ray diffraction were remarkably similar to that of liquid crystals or micellar phases formed in surfactant/ water systems (Figure

6). They proposed that the surfactant molecules self-assembled into liquid crystals were acting as templating agent, inside which the silicate precursors were penetrating and condensing forming the inorganic walls (Figure 5. A). They proposed also alternative pathways where the condensation of the silicate walls could possible occurs at different stages of the liquid crystal formation (Figure 7). The surfactant carbon chain length is a decisive factor to the size of the micelle as well as the size of the pores. The ^{13}C-NMR spectrum of the as-synthesized MCM-41 also indicated the presence of quite similar phases between the surfactant in the pores and the liquid crystal, which means that the surfactant molecules arrange in a micellar array in the as-made MCM-41.

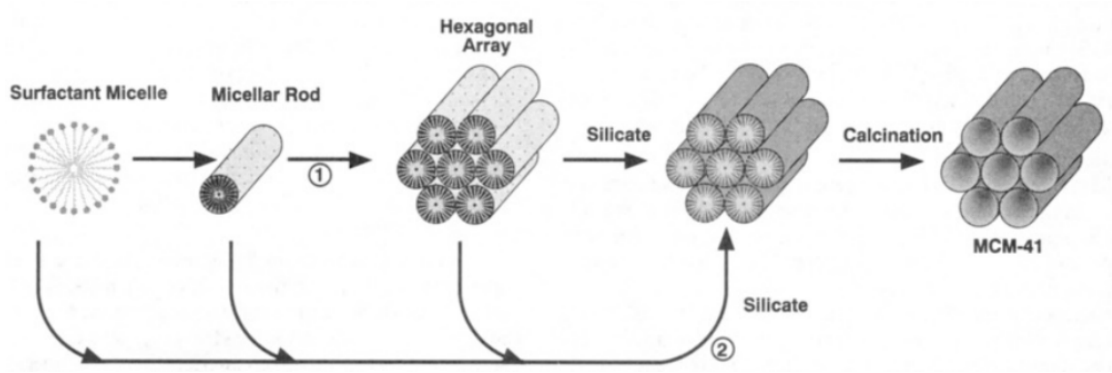

Figure 7. Possible mechanistic pathways for the formation of MCM-41: (1) liquid crystal phase initiated and (2) silicate anion initiated.[22]

2.2.4.3 Self-assembly and cooperative self-assembly

The cooperative mechanism (Figure 5. B) considers that the formation of mesophase is the interaction between the acceleration of inorganic species condensation (caused by the existence of micelles) and the promotion of liquid crystal ordered arrangement (caused by the inorganic species condensation). These complicated interactions may contain, for example, electrostatic attractions, hydrogen bonds, and coordination bonds.

Figure 8 shows the model proposed by Davis.[39, 61] The initial step is the formation of randomly ordered rod-like organic micelles; the second step yields tubes of silica surrounded micelles (two or three monolayers of tubular silica encapsulation), which occurs during the synthesis mixture when micelles interact with silicate species;

the third step is the spontaneous packing of randomly ordered composite species into hexagonal arrangement that produces the long-range in MCM-41; the fourth step is the further condensation of silicate species with heating. However, there is no complete condensation of silicate species because of the charge compensation between SiO^- species and alkylammonium ions.

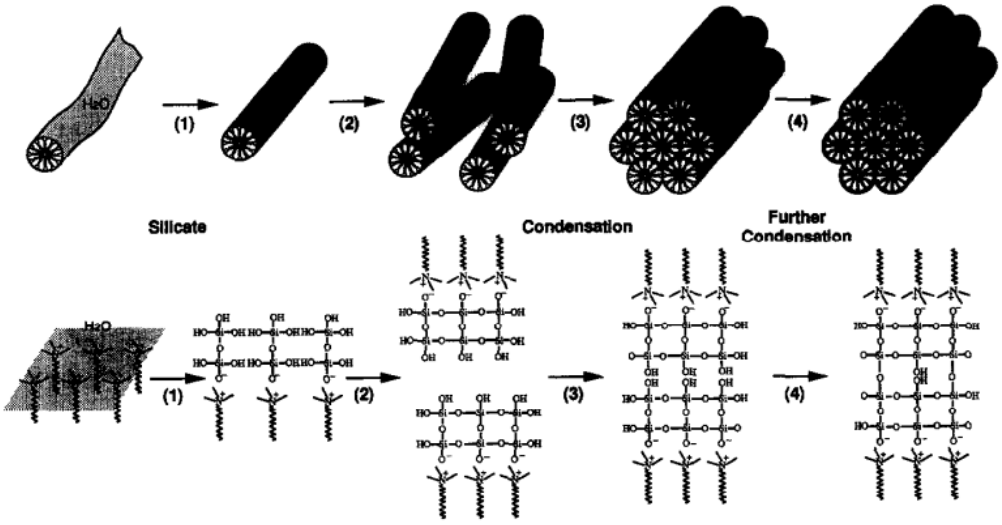

Figure 8. The mechanism proposed here for the formation of MCM-41.[39]

Figure 9 shows the model of Stucky.[52, 62] The initial step is the formation of organic and inorganic precursor solutions, the micelles can have different shapes (spherical, cylindrical or ellipsoidal) depending on the concentration of surfactant. After the mixing of organic and inorganic precursors, inorganic-organic aggregates appear with the ion exchange between silicate oligomers and Br^-, OH^- anions; the screening of electrostatic double-layer repulsion can induce self-assembly of silica tropic liquid crystalline mesophases. This model can explain the different phases obtained through variations of synthesis parameters (for example mixture composition and temperature), and the dynamic interplay among ion-pair inorganic and organic species was regarded as the decisive factor.

Based on the cooperative interaction mechanism, Stucky *et al.*[25] developed the generalized liquid crystal templating mechanism, which can be adapted to the synthesis of non-silicon-based ordered mesoporous materials as well. The cooperative charge matched templating, ligand-assisted templating, and neutral templating are the

three main models involved in this mechanism.

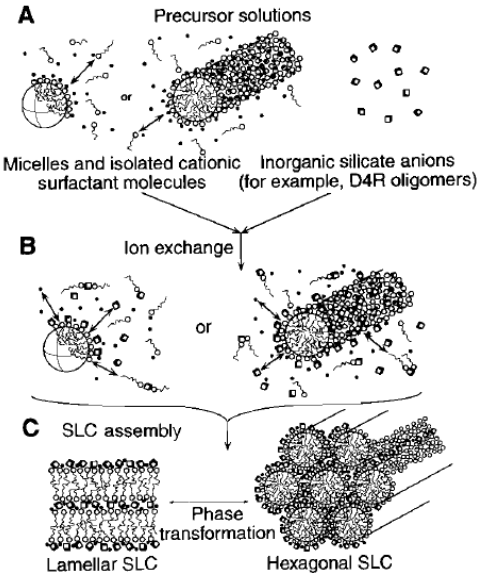

Figure 9. Schematic diagram of the cooperative organization of silicate-surfactant mesophases.[62]

2.2.4.4 Nanometric building blocks

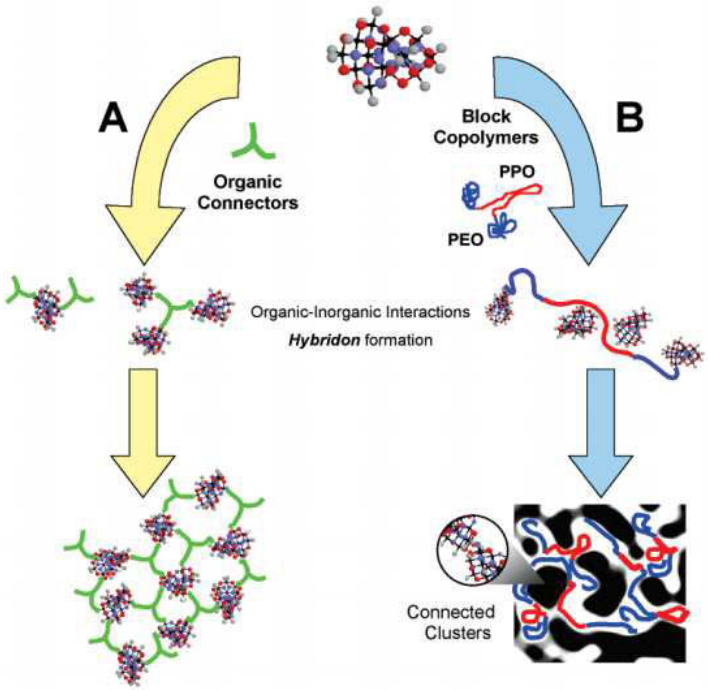

Figure 10. Different nanometric building blocks approaches involving clusters and different connectors.[63]

In solutions, micelle interiors, emulsions, or vesicles, the nanometric inorganic

building blocks are formed by inorganic polymerization or precipitation reactions. By controlling these dynamic processes, the blocks can be assembled and linked to each other. The organic functions dangling on the particle surface or other organic connectors serve as linkages (Figure 5. C) .[60]

There are two main synthetic routes of nanometric building blocks approaches (Figure 10). One strategy is the Lego-like mesotextured hybrid materials built by the cross-linking hybrid moieties;[64] the other strategy is the simultaneous process including hydrolysis-condensation and transalcoholysis reactions.[65]

2.2.4.5 Micellar structures

There are several different shapes of surfactant micelles, such as spheres, cylinders, planar bilayers, reverse micelles, bicontinuous phases, liposomes, *etc*. (Figure 11),[60, 66] which corresponds to a variation of the interfacial curvature.

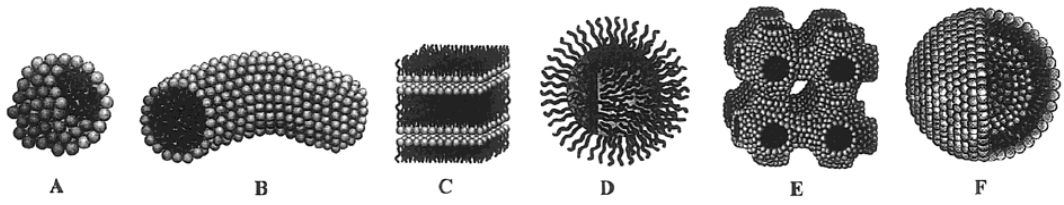

Figure 11. Different shapes of micellar structures.[60, 66]

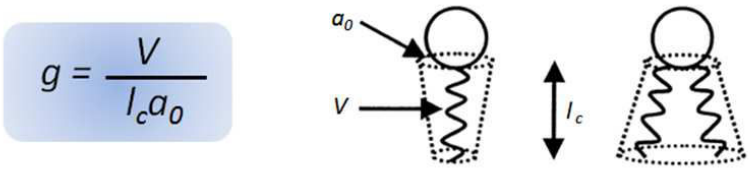

Figure 12. Formula of packing parameter *g* and schematic representation of amphiphilic molecules.[60]

Israelachvili *et al.*[67, 68] proposed a simple model for micellar structures, which can predict the mesophase with a packing parameter *g* (Figure 12). In this model, the surfactant is composed of a hydrophilic spherical head and a hydrophobic chain tail. In the packing parameter formula, "V" is the total volume (surfactant chains with

co-solvent/organic additive), "l_c" is the fully extended surfactant tail length, and "a_0" is the effective head group area at the "micelles" surface.

With different *g* factors, different shapes of micellar structures can be obtained. (Table 4 and Figure 13)

Table 4. Packing parameter *g* of different micellar structures.[60, 67, 68]

$g = v/l_c a_0$	Structures	Examples
g < 0.33	spherical micelles	single chain lipids with a large polar head (soaps or ionic detergents)
g = 0.33~0.5	cylindrical micelles	single chain lipids with a small polar head (soaps or ionic detergents in concentrated electrolyte solutions)
g = 0.5~1	bilayer (vesicles)	double-chain lipids
g = 1~2	bilayer (membranes)	
g = 2~3	inverse cylindrical micelles	double-chain lipids and a small polar head
g > 3	inverse spherical micelles	

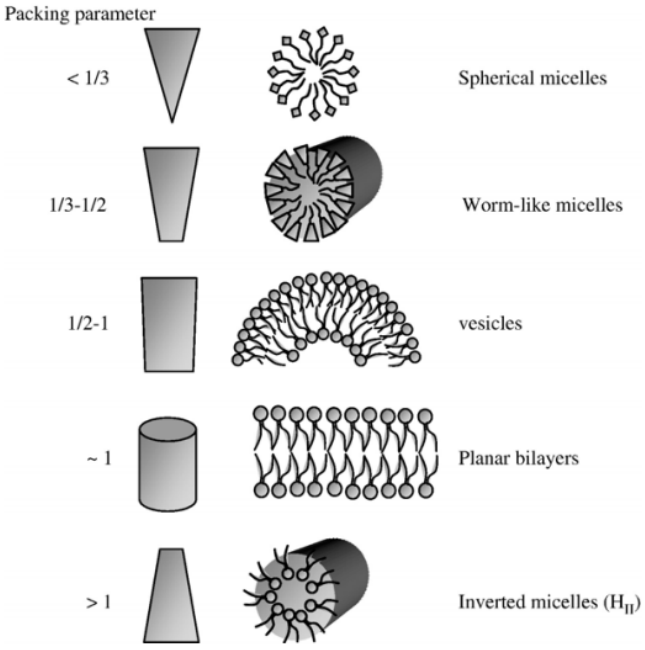

Figure 13. Schematic representation of different *g* factors and the determined micellar structures.[69]

Though some mechanisms and models are idealized and simplified, with the

understanding of synthesis mechanism and parameter control, we can do the design and the synthesis of mesoporous materials more purposeful and make the structures more predictable.

2.3 Modification and functionalization of mesoporous materials

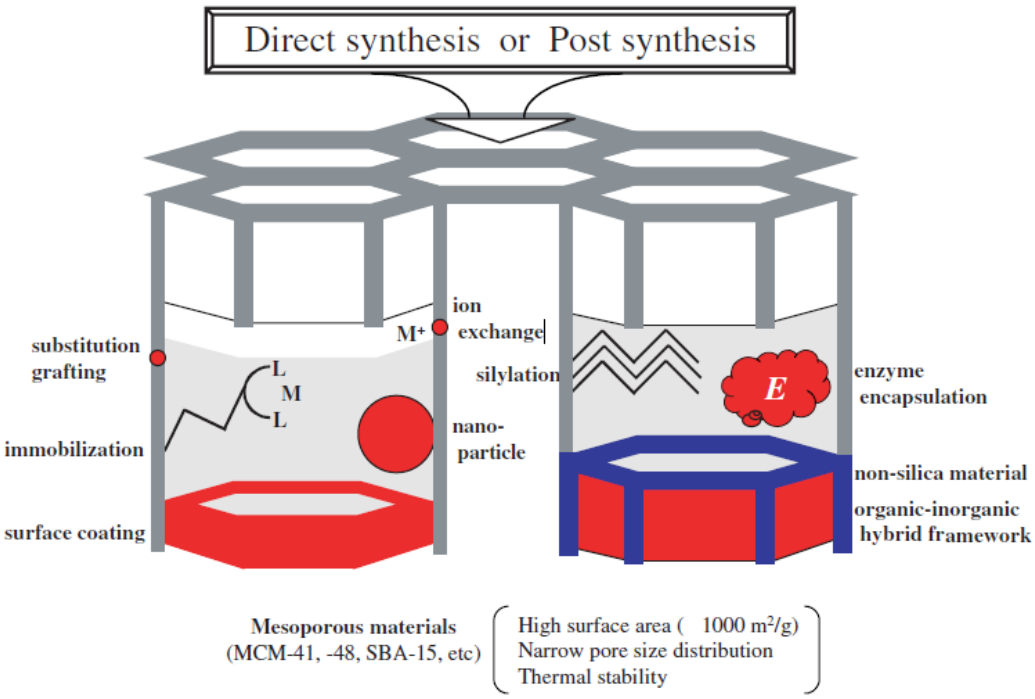

Figure 14. Design of functionalized mesoporous materials for various catalyzed reactions.[70]

There are many different strategies to do the modification and incorporate new functions in mesoporous materials. Depending on the different methods used for the functionalization, the position and local environment of functional groups or active sites are different (Figure 14). By direct synthesis, the functional groups can be inserted into the framework of the mesoporous structure; while by post synthesis, the functional groups can be grafted or coated on the surface of mesoporous materials. Due to the relatively large pore size and the high surface area, mesoporous materials have a great potential for the design and the exploitation of new catalysts. Figure 15 shows some examples of reactions catalyzed by functionalized mesoporous silica.[71]

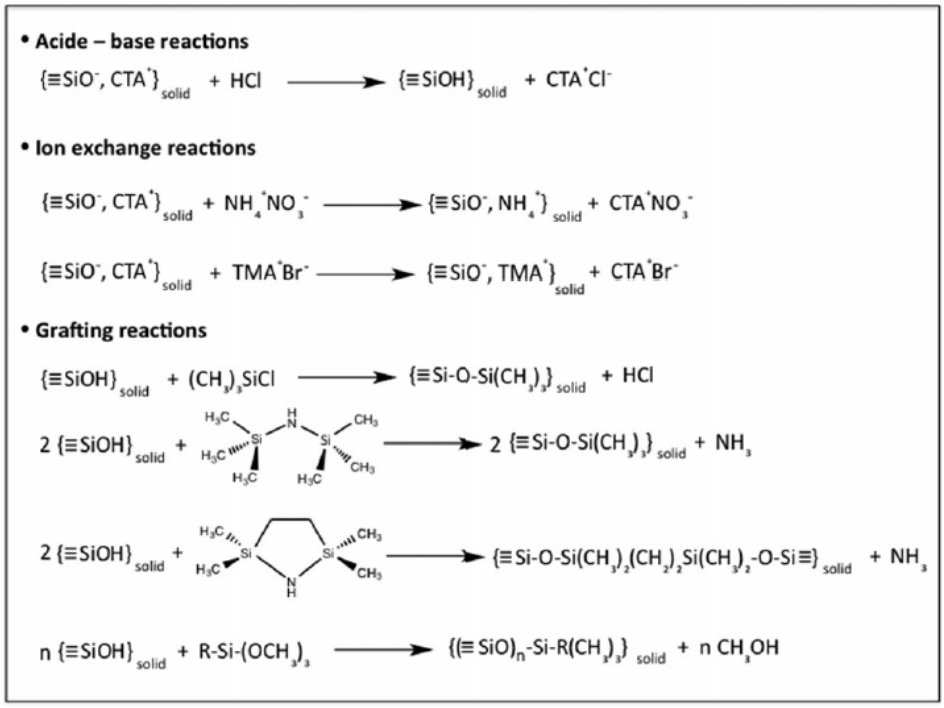

Figure 15. Examples of reactions involved in the functionalization of mesoporous silica.[71]

2.3.1 Strategies

2.3.1.1 Direct synthesis

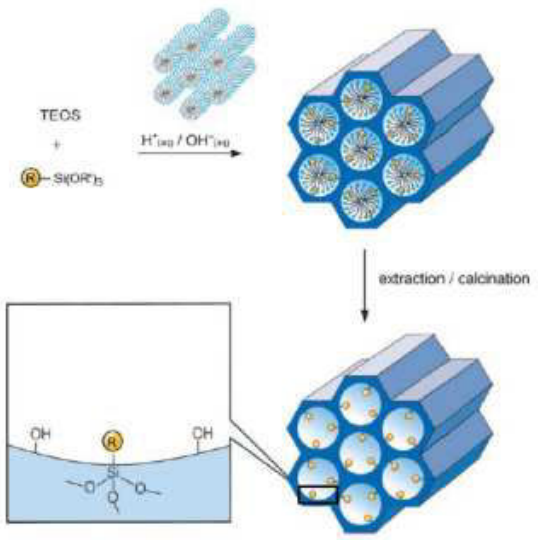

Figure 16. Insertion of organic function by direct synthesis using co-condensation of organosilanes (R represents the organic functional group).[23]

Direct synthesis of functionalized mesoporous silica is also called one-pot synthesis.[72-75] For example, by con-condensation of $(RO)_4Si$, $(R'O)_3SiR$, and surfactant template, the organic functional groups can be anchored to the pore walls of mesoporous silica (Figure 16). The one-pot synthesis is very simple and in principle efficient. With this method, the functional groups are supposed to be homogeneously dispersed within the silica matrix, and there is no pore blocking. But the surfactant must be carefully removed without destroying the functional groups, and not all the active sites are accessible because some of the functional groups are dispersed into the framework of silica. Nonetheless, the inclusion of heterofunctions affects the structure of the silica matrix.

2.3.1.2 Post synthesis

The post-synthesis consists to modify chemically the already-made mesoporous framework. The functional groups are incorporated on the surface of the mesoporous materials maintaining the ordered matrix skeleton. For example, the grafting of organosilanes $(R'O)_3SiR$ on the surface of the pores of a mesostructured silica (Figure 17). This method may lead to the decrease of pores diameter and to a non-homogeneous dispersion of the functional groups. However, the initial silica phase can be retained very well and the functional groups are more accessible as they are all loaded on the surface of the matrix.[76]

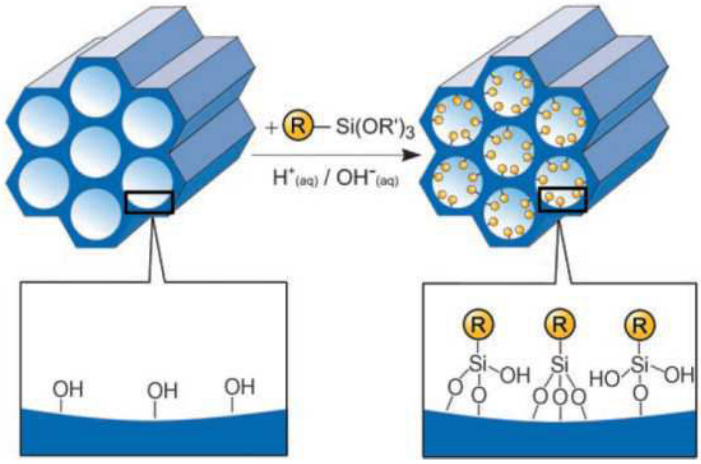

Figure 17. Post-synthesis by grafting organosilanes on the pore surface of mesoporous silica (R represent the organic functional group).[23]

In order to obtain the post-functionalized mesoporous materials, three main strategies can be applied: impregnation,[77, 78] ion-exchange,[79] and covalent grafting.[80-82] Within these methods, the functional groups have different interactions with the matrix, and the location of the functional groups will be different as well.

2.3.1.3 Comparison of different methods

By using these different synthesis methods, the functional groups can be immobilized with different location, for example: anchored, surfacing and embedded. The requirement and preference for the location of the functional group should be guided by the application, then, implying the appropriate strategy. Several aspects should be considered, for example, the structural flexibility and choice of the sites, the accessibility to the sites, the sites distribution homogeneity, the porous volume, and the structural defaults. Figure 18 shows the comparison of the advantages and disadvantages of each type of functional groups.[71]

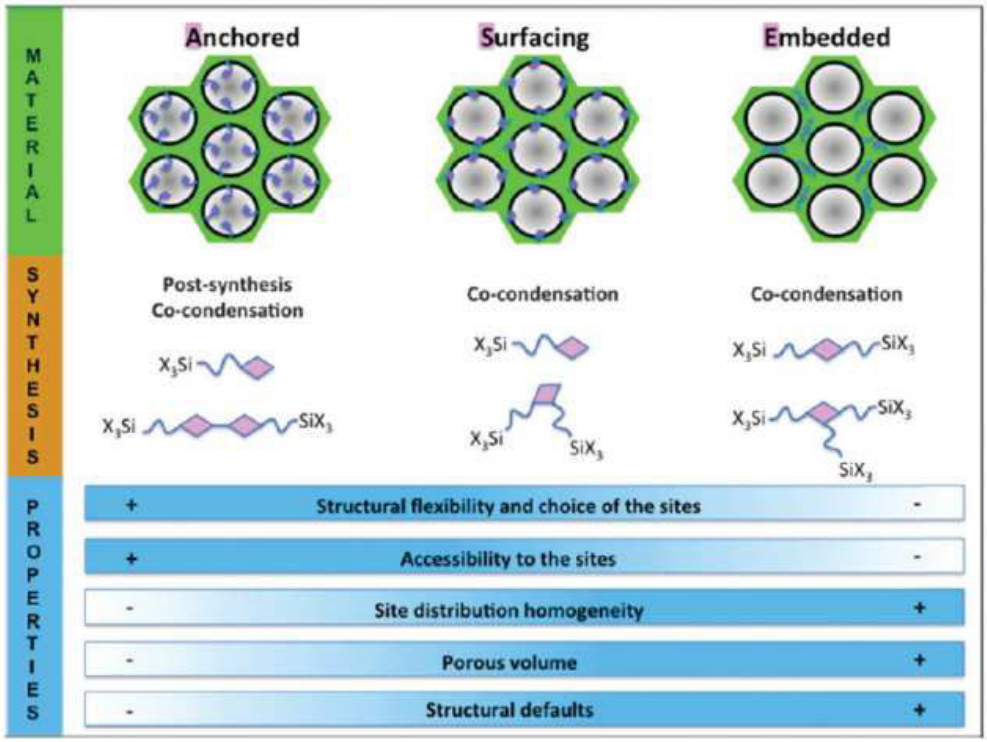

Figure 18. Comparison of different locations of the functional groups in the mesoporous silica.[71]

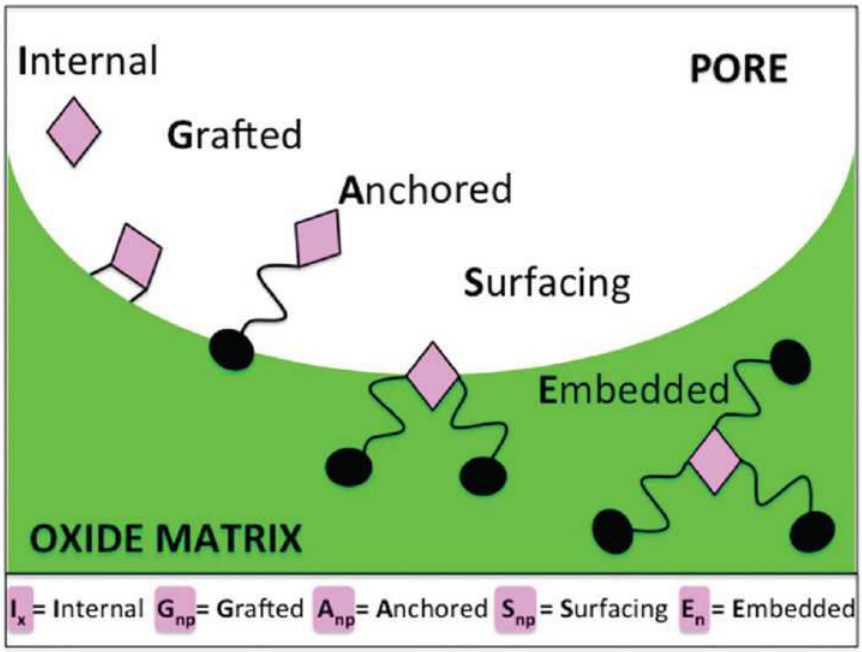

Figure 19. InGASE nomenclature for the location of a function in a porous solid.[71]

To describe the different location of immobilized functional groups, a new nomenclature (InGASE) was proposed,[71] which indicates the information of the function location at the solid-fluid (gas or liquid) interface and the binding mode to the solid. Figure 19 shows the five types of possible function locations.

2.3.2 Functional groups category

Several different kinds of functional groups can be introduced on the mesoporous silica surface, for example, organic functional groups, transition metal ions and oxide species, noble metal species, *etc*. They are incorporated as active sites to modify the solid properties.

2.3.2.1 Organic functional groups

When organic functional groups are introduced, the chemical properties of mesoporous silica are modified, including the stability, hydrophilicity, hydrophobicity, pore size, surface silicon hydroxyl density, *etc*. Table 5 shows some examples of the organic functional groups commonly used in literature.

Table 5. Summary of common organic groups and their functions.

Organic groups	Function
amino or aminopropyl	better accessibility for binding heavy metal species[83, 84]
	enhanced absorptivity to acetaldehyde[85]
	selective adsorption of dye pollutants[86]
	selective binding of acidic gases[87]
diamino or triamino	adsorb chromate and arsenat[88]
	CO_2 capture[89]
ethylenediamine	CO_2 adsorption[90]
malonamide	heterogeneous extraction of radionuclide[91]
carboxy	protein immobilization[92]
thiol	removing heavy metal ions from waste water[81, 84]
1-allyl	mercury removal[93]
1-benzoyl-3-propylthiourea	mercury removal[94, 95]
dithiocarbamate	mercury removal[96]
imidazole	selective adsorption of precious metal ions[97, 98]
saccharides	boron removal[99]

2.3.2.2 Transition metals and oxide species

The transition metals and oxide species can be introduced on the surface of mesoporous silica and work as catalytic active sites. There are a lot of reports about transition metallic catalysts supported on mesoporous silica (Table 6).

2.3.2.3 Noble metal species

By ion exchange, deposition-precipitation, impregnation, and some technique such as vacuum evaporation, chemical vapor deposition, and super critical CO_2 methods, the noble metal species can be incorporated onto mesoporous silica and they were widely used as catalysts in many reactions (Table 7).[70]

Table 6. Examples of transition metals and oxide species supported on mesoporous silica.

Metal	Catalysis
Ti	selective oxidation reactions, epoxidation reactions, *etc.*[100-103]
V	oxidation reactions, oxidative dehydrogenation reactions, *etc.*[104-106]
Cu	oxidation, epoxidation, hydroxylation reactions, *etc.* [107-110]
Fe	oxidation, epoxidation, hydroxylation reactions, *etc.*[111-113]
Mn	oxidation reactions, epoxidation reactions, *etc.*[114-116]
Co	oxidation reactions, photocatalysis, *etc.*[117-119]
Ni	methanol reforming, hydrogenation reactions, *etc.*[120-122]
Al	acidity, cracking reactions, *etc.*[123-125]

Table 7. Examples of noble metal catalysts and the method of preparation.[126-142]

Metal	Preparation method	Catalysis
Pt	Inclusion in synthetic gel	CO oxidation
	Vacuum evaporation	
	Super critical CO_2	
	Ion exchange to positively charged trimethylalkyl ammonium functionalized surface and reduction	
	Ship-in-the-Bottle	Water-gas shift reaction alkene hydrogenation
Ph (Rh-Pt)	Super critical CO_2	Butane hydrogenolysis to ethane
Au	Ion exchange to trimethylalkyl ammonium functional group and reduction	CO oxidation
	Chemical vapor deposition	
Ru, Ru-Sn, Ru-Pt, Cu-Ru	Impregnation of carbonyl cluster together with organic counter cations	Hydrogenation
Pd	Vapor phase diffusion-deposition	Heck reaction
	Deposition-precipitation	Phenol hydrogenation
Pd, Au	Inclusion in synthetic gel/ incipient wetness	CO oxidation

2.3.3 Fine control of functional groups

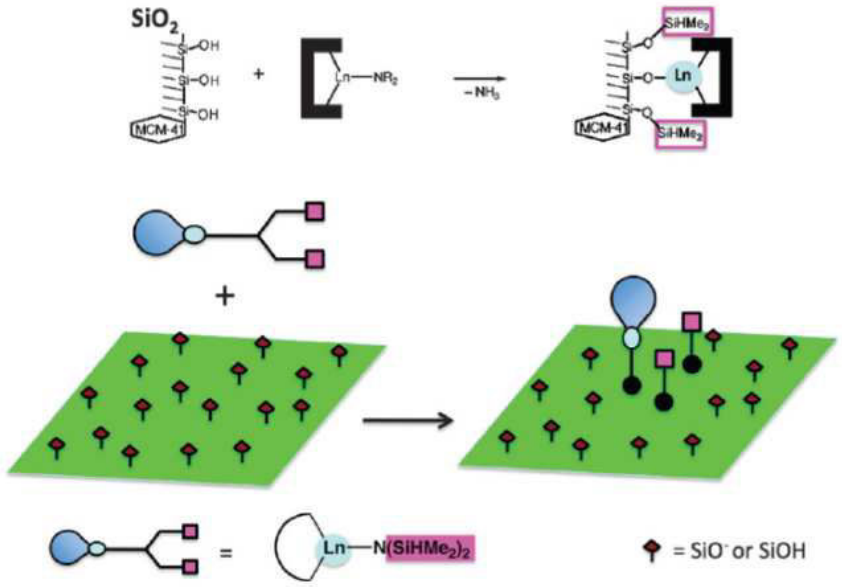

Figure 20. Controlled degradation of precursor for functional sites isolation.[71, 143]

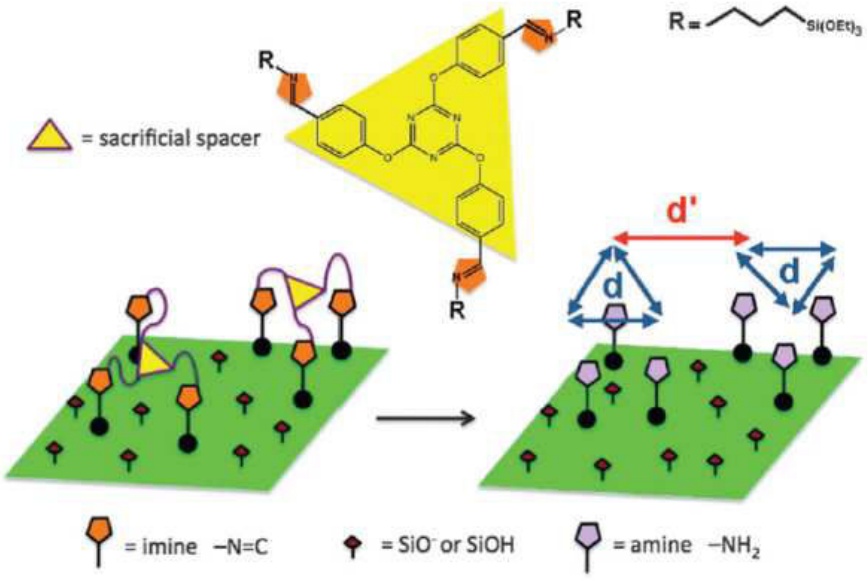

Figure 21. Dismountable molecular assistant control of grafting.[71, 144-146]

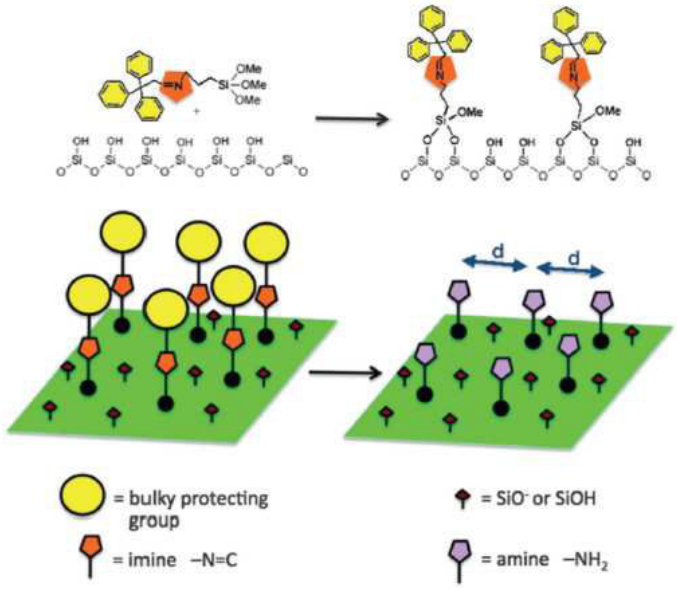

Figure 22. Protection-deprotection method with bulky protecting groups.[71, 147]

The strategy of surface molecular engineering can be applied for the fine control of the incorporation of functional groups on mesoporous silica to obtain well-defined active sites, with an appropriate environment and a better isolated state. There are several factors that we need to consider: the dispersion and the isolation of functional groups, the environment of functional groups, and the relative location of different functional groups, *etc.* The fine control at molecular level should not only be at short distance but also at long distance. Figures 20~22 show some examples of the approaches with different strategies.[71]

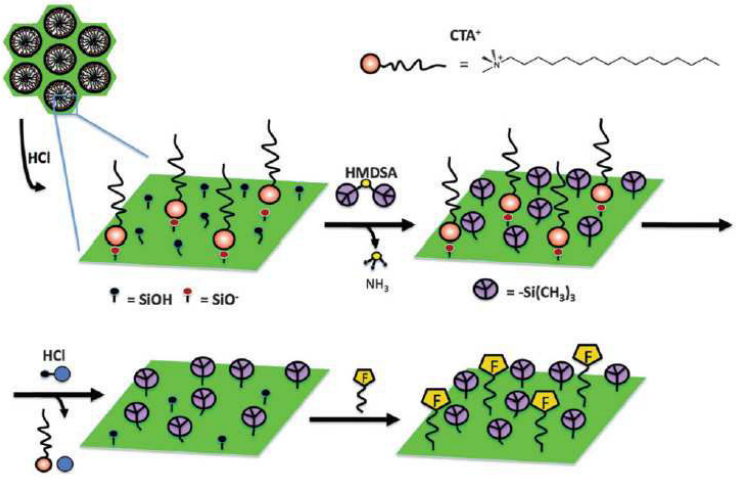

Figure 23. Schematic of molecular stencil pattering technique.[71]

Surface organometallic chemistry (SOMC) approaches are widely used to control the grafting of organometallic complexes.[148-152] Molecular stencil pattering (MSP) technique can be applied to the synthesis of multifunctional materials.[153-155] The main idea of the MSP technique is the partial coverage of functional groups. Figure 23 shows an example of this procedure: cetyltrimethylammonium (CTA^+) or trimethyl ammonium (TMA^+) can be used as molecular stencil because their cationic heads have electrostatic self-repulsion which make them regularly patterned on the surface of silica. The as made MCM-41 is washed with diluted HCl-ethanol solution to remove part of the surfactant so that the remained surface is available for the grafting of the first functional groups hexamethyldisilazane (HMDSA). Then, the residual surfactant is removed to make space for the following grafting of the second functional groups or active species. The role of HMDSA is to prepare isolated sites, thereby the second functional groups can be better dispersed. Besides HMDSA, several other organosilanes can be used as isolation sites to reduce the density of the site which is available for grafting, and they can also provide the hydrophobic surface of the silica, such as chlorotrimethylsilane (CTMS), 2,2,5,5-tetramethyl-2,5-disila-1-azacyclopentane, *etc*. Figure 24 shows the structure of some organosilanes that can be grafted on silica.

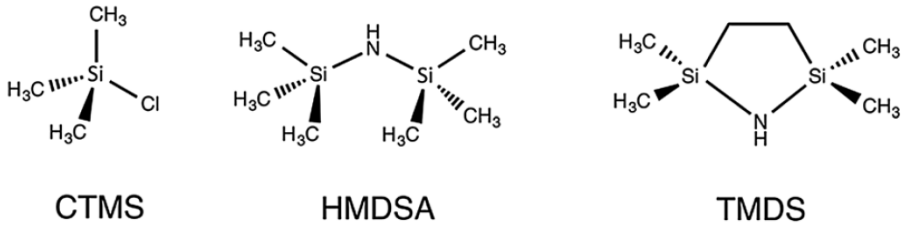

Figure 24. Examples of organosilanes that can be grafted on silica.[71]

2.3.4 Applications

2.3.3.1 Catalysis

Mesoporous silica is a very good candidate for the preparation of supported heterogeneous catalysts own to its high surface area, relatively large pores diameter, narrow pores size distribution, various possibility for the modification of surface,

controllable hydrophilicity and hydrophobicity, *etc*. Inspired by biology science, the biomimetic catalysts are also a potential route for the design of mesoporous silicate catalysts. The catalysis applications of mesoporous materials include redox reactions, polymerization reactions, hydrogenation reactions, acid catalysis, base catalysis, halogenation reactions, photocatalysis, *etc*.[156-158] We have summarized some examples of mesoporous silica supported metal catalysts in Table 6 and Table 7.

2.3.3.2 Adsorption and desorption

Table 8. Extraction of metal ions by different functionalized mesoporous materials.[159]

Mesoporous materials	Functional groups	Metal ion	Adsorption capacity	Detection limit	Detection methods
Mesoporous silica	Tetraacetamide derivative of cyclam	Pb^{2+}		2.7×10^{-9} M	Electroanalysis
Mesoporous silica	3-Aminopropyl	Cr^{5+}	4.35 mmol g^{-1}	1.2 pg mL^{-1}	AAS
Mesoporous TiO_2		V, Cr, Cu		1.1~6.3 pg mL^{-1}	ETV-ICP-MS
MCM-41	2,4-Dihydroxybenzaldehyde	Be^{2+}	34 mg g^{-1}	0.3 pg mL^{-1}	ICP-OES
Mesoporous Al_2O_3		As^{3+},Cr^{3+},$As5^{+}$,Cr^{5+}		0.7~74 pg mL^{-1}	ICP-MS
MCM-41	Thiophene-2-carbaldehyde	Pd^{2+}	5.0 mg g^{-1}	0.2 ng mL^{-1}	ICP-AES
SBA-15	5-Mercapto-1-methyltetrazole	Zn^{2+}	0.96±0.01 mmol g^{-1}	8.0×10^{-9} M	FAAS
SBA-15	2-Mercaptopyrimidine	Cd^{2+}	0.99±0.03 mmol g^{-1}		FAAS
Mesoporous silica	Chitosan	V, Cu, Pb, Cd, Hg	12.2~22.9 mg g^{-1}	0.05~0.96 ng mL^{-1}	ICP-OES
MCM-41	5-Nitro-2-furaldehyde	U^{5+}, Th^{4+}	47~49 mg g^{-1}	0.3 ng mL^{-1}	ICP-OES
Mesoporous TiO_2	Dimercaptosuccinic acid	As^{3+},Sb^{3+},As^{5+},Sb^{5+}		0.10~0.15 ng mL^{-1}	ICP-OES
Mesoporous silica	3-(2-Aminoethylami-no) propyl	As^{3+}, AS^{5+}	10.3 mg g^{-1}	0.05 ng mL^{-1}	ICP-OES
SBA-15	Ethylenediamine	Cd^{2+}, Pb^{2+}	360±1.41±0.6 mgg^{-1}		AAS

Ordered mesoporous materials are an ideal choice as adsorbents for polluted water treatment. They present a high adsorption capacity, tunable surface functionalization, simple operation and recyclability. Table 8 gathers some examples of functionalized mesoporous materials and their corresponding adsorbable metal ions.[160-172]

Carbon dioxide capture and conversion is an important research topic as the greenhouse effect and global warming arise more and more attention in the world. Mesoporous silica with organic amine functional groups is promising solid adsorbent of CO_2 favorable for the rapid gas diffusion and easy regeneration. Several different amine groups can be incorporated into mesoporous silica to improve the efficiency of

CO_2 adsoption.[173-176]

Mesoporous silica modified with nickel, aluminium, or other functional groups can have a good hydrogen storage capacity,[177-179] and are potentially suitable porous materials for energy storage as well.

2.3.3.3 Sensors

Mesoporous silica is a promising material for developing electrochemical sensors, gas sensors, and biosensors, which can be applied to the environment monitoring, optical detection, and food security control. Their high surface area, large porous volumes, and unique electronic properties are favorable for mass diffusion and sensible response to very low concentration target molecules. Figure 25 shows the advantages of porous silica materials for developing sensors. More information about mesoporous silica sensors can be found in several reviews.[180-184]

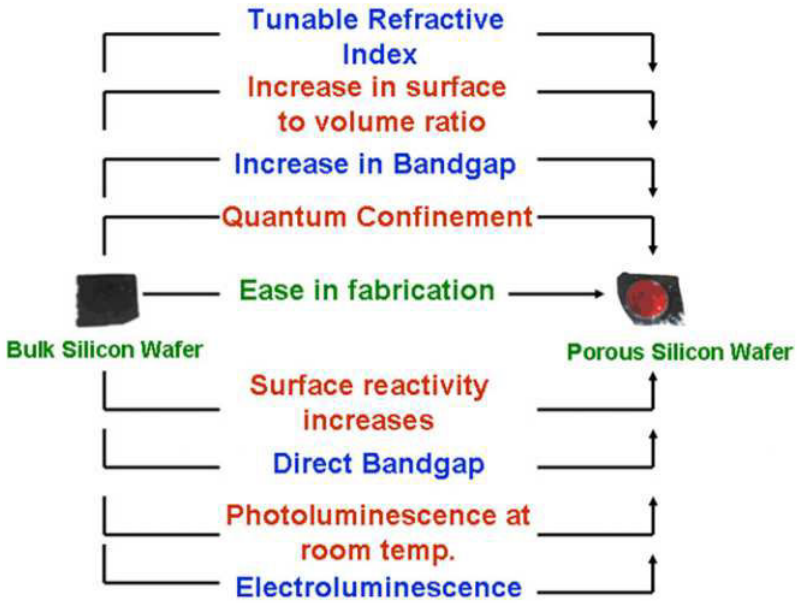

Figure 25. Advantages of porous silica materials for developing sensors.[183]

2.3.3.4 Biological and medical fields

Mesoporous silica nanoparticles (MSNs) are wildly used in the field of drug carriers, protein and gene delivery, cancer therapy, *etc*. MSNs present a lot of advantages in medical applications as they have tunable size, shape, surface, and good

biocompatibility. The drug loading can be very high own to the high surface area (600~1000 m^2/g) and pore volume (0.6~1.0 mL/g) of MSNs, and the targeted delivery and release can be controlled by the surface functionalization of the silica. There are several factors that need to be considered for the design of MSNs for medical application, not only the characteristics of MSN, but also their behavior and interaction in the biological environment (cells, tissues, and circulation systems, *etc*), the toxicity, safety, and curative effects are very important. Figure 26 shows the considerations highlighted for the design mesoporous silica nanoparticles for biological and medical applications. Several groups have reviewed the progress of MSNs applications in biological and medical fields.[185-189] The development of new drugs based on mesoporous materials has great potential and it may open a door for the clinical therapy of some serious diseases.

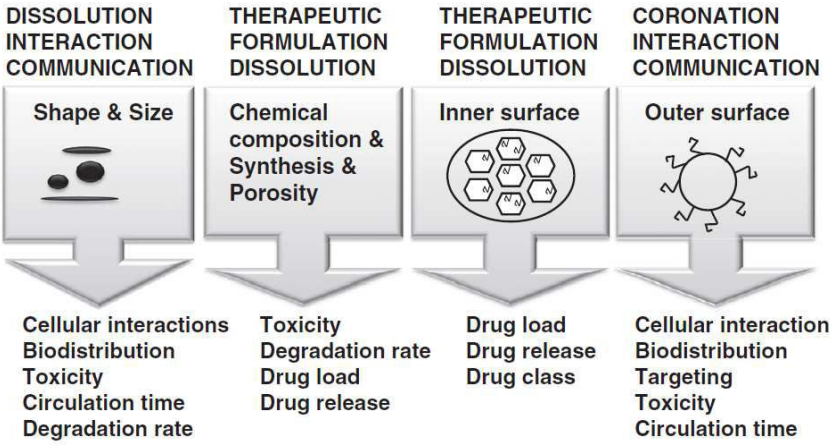

Figure 26. The considerations highlighted for the design of mesoporous silica nanoparticles for biological and medical applications.[185]

2.4 Heterogeneous supported vanadium catalyst

2.4.1 Introduction

Vanadium (Z=23) is the twenty-second most abundant element in the earth crust (0.013 % w/w).[190] As very important strategic resources, it was wildly used in mechanical manufacturing, aerospace industry, steel and oil industry, architecture and transportation, chemistry and electrochemistry industry, nuclear fusion reactor, *etc*.[191]

Back to the 1870s, vanadium was used as the oxidation catalyst for the formation of aniline black from aniline. In 1895, vanadium oxide (V_2O_5) was used as the catalyst for the oxidation of toluene and benzaldehyde.[190] Nowadays, vanadium and vanadium oxide compounds have become one of the most important oxidation catalysts in lots of industrial processes. Table 9 summarizes some industrial catalytic processes using vanadium oxides.[192] Catalysts based on vanadium complexes, both homogeneous and heterogeneous, are wildly used in the oxidation of alkanes and alkylaromatics, epoxidation reactions, oxidation of alcohols, oxidative bromination reactions, oxidative strecker reactions, sulfoxidation, *etc*. Manas Sutradhar *et al*. have reviewed several oxidation reactions catalyzed by vanadium complexes in recent years.[193, 194]

Table 9. Industrial catalytic processes using vanadium oxides.[195-201]

Industrial process	**Catalyst material**
Oxidation of SO_2 to SO_3 in the production of sulfuric acid	V_2O_5
Oxidation of benzene to maleic anhydride	V_2O_5
Oxidation of naphthalene to phthalic anhydride	V, Mo oxides
Oxidation of butene to phthalic anhydride	V, P oxides
Oxidation of *o*-xylene to phthalic anhydride	V, Ti oxides
Selective reduction of NO_x with NH_3	V_2O_5/ WO_3/ TiO_2

2.4.2 Vanadium incorporation in different supports

To improve the activity, selectivity, and mechanical strength of vanadium catalysts, vanadium oxide can be deposited on the surface of inorganic supports such as SiO_2, TiO_2, Al_2O_3, ZrO_2, *etc*. Though the supports is normally considered as inert substance, there is an unclear interaction known as the metal oxide-support effect that contributes to the improvement of the catalyst performance. Table 10 summarizes some examples of vanadium oxide catalysts on different supports.[192]

Table 10. Different supports with different synthesis methods for the maximum vanadium oxide loading without formation of V_2O_5 crystals.[192]

Support Oxide	Preparation method	Surface area of support (m^2g^{-1})	Maximum loading of vanadium (V atoms per nm^2 of support)	Detection method
SiO_2	Impregnation with NH_4VO_3	150	0.7	NMR
	Impregnation with NH_4VO_3	200	1.0	RS
	Impregnation with NH_4VO_3	200	1.0	NMR
	Impregnation with NH_4VO_3	300	0.6	RS
	Impregnation with NH_4VO_3	530	0.2	RS
	Impregnation with NH_4VO_3	350	0.4	XRD
	Impregnation with ammonium vanadyl oxalate	530	0.4	RS
	Impregnation with ammonium vanadyl oxalate	90	1.0	RS
	Impregnation with ammonium vanadyl oxalate	203	1.0	XRD
	Impregnation with ammonium vanadyl oxalate	90	1.0	RS
	Grafting with VCl_3	160	0.5	EXAFS
	Chemical vapor deposition with $VO(OC_2H_5)_3$	203	3.9	XRD
Al_2O_3	Impregnation with NH_4VO_3	205	8.0	NMR
	Impregnation with NH_4VO_3	262	2.2	XRD
	Impregnation with NH_4VO_3	78	5.6	RS
	Impregnation with NH_4VO_3	187	5.0	XRD
	Impregnation with NH_4VO_3	145	6.5	NMR
	Impregnation with NH_4VO_3	101	3.1	XRD
	Impregnation with NH_4VO_3	100	4.4	RS
	Impregnation with NH_4VO_3	188	2.3	XRD
	Grafting with VCl_3	80	9.4	EXAFS
	Chemical vapor deposition with $VO(OC_2H_5)_3$	93	18.0	XRD
	Grafting with $VO(OC_2H_5)_3$	180	1.8	NMR
TiO_2	Impregnation with NH_4VO_3	45	8.3	RS
	Impregnation with NH_4VO_3	35	7.1	XRD
	Impregnation with NH_4VO_3	50	13.0	XRD
	Impregnation with ammonium vanadyl oxalate	50	7.8	RS
	Impregnation with ammonium vanadyl oxalate	52	1.7	RS
	Impregnation with ammonium vanadyl oxalate	50	5.6	RS
	Impregnation with ammonium vanadyl oxalate	59	7.2	XRD
	Impregnation with ammonium vanadyl oxalate	98	6.6	RS
	Grafting with VCl_3	120	8.0	EXAFS
ZrO_2	Impregnation with NH_4VO_3	71	3.5	XRD
	Impregnation with NH_4VO_3	49	3.5	XRD
	Impregnation with ammonium vanadyl oxalate	63	0.8	RS
	Impregnation with ammonium vanadyl oxalate	330	7.5	RS
	Impregnation with ammonium vanadyl oxalate	140	7.0	RS

2.4.3 Preparation methods

There are several different methods to prepare the heterogeneous supported vanadium catalysts, such as co-precipitation, impregnation,[202-210] grafting,[211-215] chemical vapor deposition (CVD),[216-219] atomic layer deposition (ALD),[220] thermal spreading,[221, 222] *etc*. We have discussed the influence of the different strategies of synthesis in chapter 2.3.1. For the incorporation of vanadium oxide active sites, it is important to have a good dispersion of the active sites and avoid the formation of V_2O_5 crystals. Table 10 summarizes some examples of different vanadium loading limits on different supports with different synthesis methods. As we have discussed in chapter 2.3.3, with the assistance of organic functional groups, the fine control of the surface active sites dispersion would be a potential strategy to develop high performance supported vanadium catalysts.

2.4.4 Vanadium species and structures

Vanadium was named vanadin by Sefström, this is from the name of Nordic goddess Vanadis, who symbolises beauty and fertility,[190] which are also the features of vanadium chemistry. Vanadium compounds have different beautiful colors depending on the oxidation states of vanadium. The electron configuration of vanadium is $[Ar]3d^3 4s^2$, taking the reduction of NH_4VO_3 as an example, V^{5+} (d^0) species show a yellow color, V^{4+} (d^1) species show a blue color, V^{3+} (d^2) species show a green color, while V^{2+} (d^3) species show a violet color.[223] The easily interconvertible vanadium oxidation states and their high affinity to oxygen encourage the application of vanadium catalysts for oxidation reactions.

V^{5+} and V^{4+} are the most common and stable states. There are three main coordination states of V^{5+}: tetrahedral (VO_4), pentahedral (VO_5) and octahedral (VO_6). In the solid state, V_2O_5 is an acidic oxide with the orange-red color, each vanadium oxide unit has an octahedrally coordinated VO_6. By mild reduction of V_2O_5, a dark blue amphoteric oxide VO_2 can be obtained. However, in aqueous it is more complicated, depending on the vanadium concentration and the solution pH, different vanadium oxide species can be observed. Figure 27 shows the different stable

vanadium species that can exist in aqueous solutions with different pH and vanadium oxide concentrations.[192]

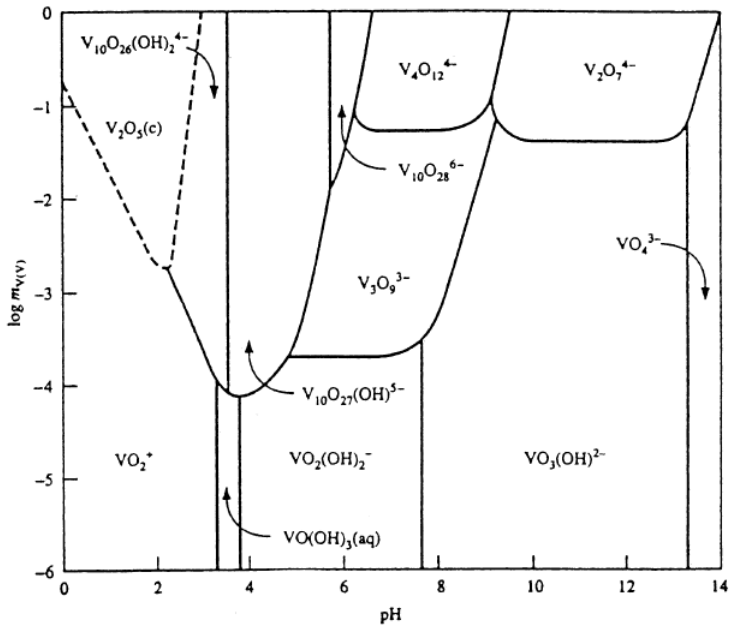

Figure 27. Pourbaix diagram of vanadium (temperature: 25 ◦C, ionic strength: 1M).[192]

The supported vanadium oxides are quite different from the unsupported ones on their chemical and electronic properties. Taking the impregnation of NH_4VO_3 as an example, after the drying and calcination steps, the vanadium oxide compound can be chemically anchored onto the surface of the support (Figure 28).[192]

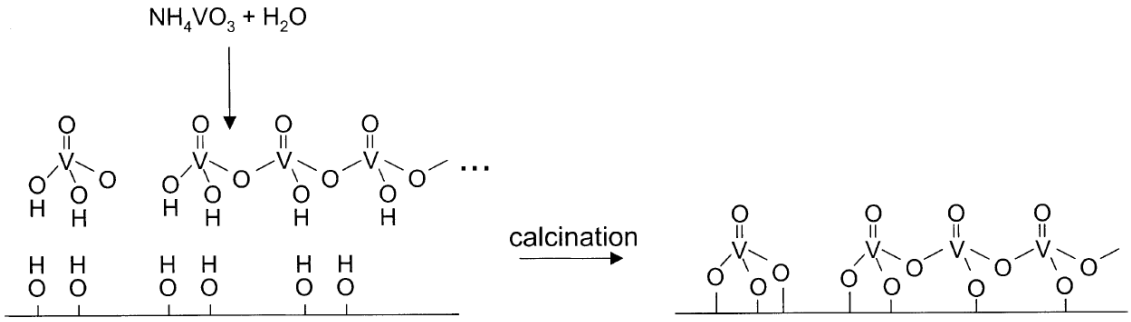

Figure 28. Synthesis of a supported vanadium oxide catalyst by impregnation of a NH_4VO_3 solution followed by calcination in the presence of oxygen.[192]

Even by different synthesis methods, or on different oxide supports, after calcination, the supported vanadium oxide catalysts are found to have the same vanadium oxide configurations.[195, 197, 224, 225] During the heating procedure, the adsorbed water molecules are removed, and by the esterification reaction, the oxidized V^{5+} compound can be anchored through the hydroxyl groups on the support. The resulting species possesses essentially the same local coordination environment as supported vanadium oxides. The isolated VO_4 units (symmetry C_{3v}) with one terminal mono-oxo V=O bond (~1.62 Å) and three bridging V-O-Support bonds (~1.81 Å) are formed at low loading of vanadium (Figure 29 a).[192, 226] For high loading of vanadium, dimeric and polymeric chains of VO_4 units can be formed (with one V-O-Support bond, two bridging V-O-V bonds, and a terminal V=O bond) (Figure 29 b).

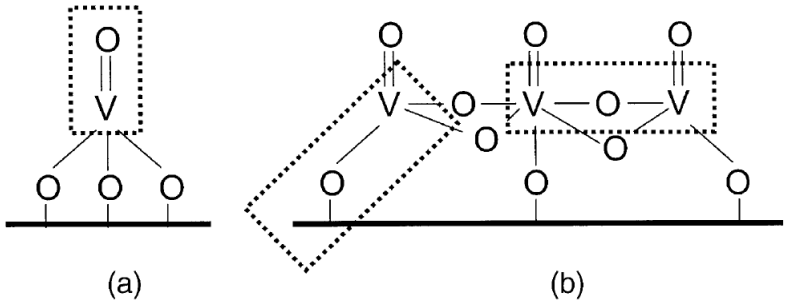

Figure 29. Three types of V-O bonds in monomeric and polymeric VO_4 species.[192]

The different dispersion states of vanadium oxides on the supports may include several molecular configurations: isolated vanadium ions (Figure 30 a), dimeric species (Figure 30 b), polymeric species, two-dimensional over-layer built up by chains of vanadium ions (Figure 30 c), three-dimensional vanadium oxides, V_2O_5 crystals (Figure 30 d) and mixed metal oxide phases with the support. The available surface area and surface hydroxyl groups are two important factors for the formation of different aggregation states of surface vanadium species. High surface area usually means more hydroxyl groups, which are favorable for a better dispersion of isolated vanadium oxide species.[192]

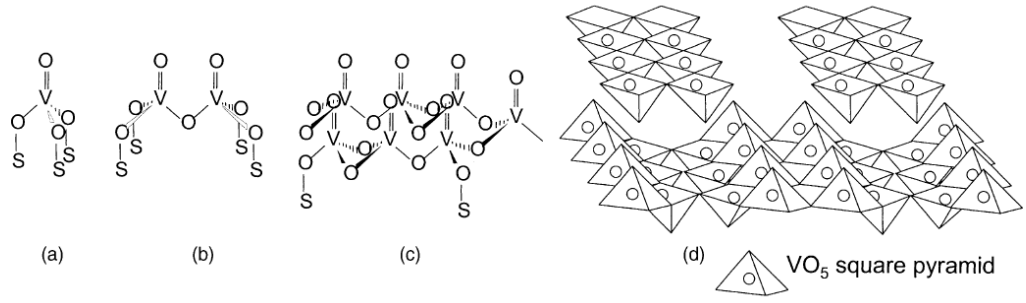

Figure 30. Possible molecular configurations for supported vanadium oxides (with S the support cation).[192]

Figure 29 shows three types of V-O bonds: terminal V=O, bridging V-O-V, and V-O-support bonds. It is important to point out the unique V=O bond, which acts as the oxidation active site in supported vanadium oxide catalysts.[227-229] Several researches on the selective oxidation of methanol to formaldehyde over supported vanadium oxide catalysts have indicated that the terminal V=O bond and the bridging V-O-V bond do not contain the critical oxygen that participates in this reaction, while the oxygen in V-O-Support bond is critical for the oxidation of methanol to formaldehyde. Therefore, to optimize the supported vanadium oxide catalysts, the careful choice and modification of the support oxide will be decisive.[192, 195, 225, 230, 231]

2.4.5 Applications

Supported vanadium catalysts are wildly used in a lot of reactions, especially for some important selective oxidation processes. Between 1967 and 2000, about 28 % papers among supported transition metals oxide catalysis researches in open literature were based on supported vanadium oxide catalysts (Figure 31).[192, 232] Bert M. *et al.* have summarized the reactions catalyzed by supported vanadium oxides in the literature.[192]

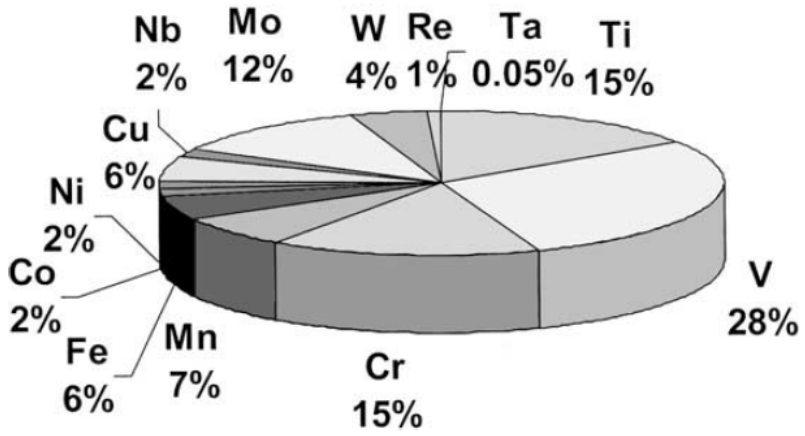

Figure 31. Percentage of papers based on different supported transition metals oxide catalysis in open literature between 1967 and 2000.[192]

2.5 Characterization of mesoporous silica supported vanadium catalyst

For the characterization of mesoporous silica supported vanadium catalysts, several different characterization techniques are required. Each technique can provide some information about the structure and feature of the catalyst. In order to have a deep understanding of the catalyst, the analysis needs to be based on the comparison of multiple characterization techniques.

2.5.1 X ray diffraction (XRD)

X ray diffraction (XRD) is one of the most important methods to study the structure of crystals and solid materials. Through some mathematical processing, the results from XRD can be applied for the analysis of phase structures, phase content, crystalline grain size, composition, *etc*. For mesoporous silica, the corresponding angular positions of the 2Θ diffraction peaks are at low angles, between 1^{o} and 10^{o}. Figure 32 shows the typical XRD pattern of the MCM-41, which has a pore array of hexagonal symmetry. The four typical diffraction peaks observed belong to the unit cells of d_{100}, d_{110}, d_{200} and d_{210} respectively, and there are no peaks at high angles, as the wall of the MCM-41 consists of amorphous silica.

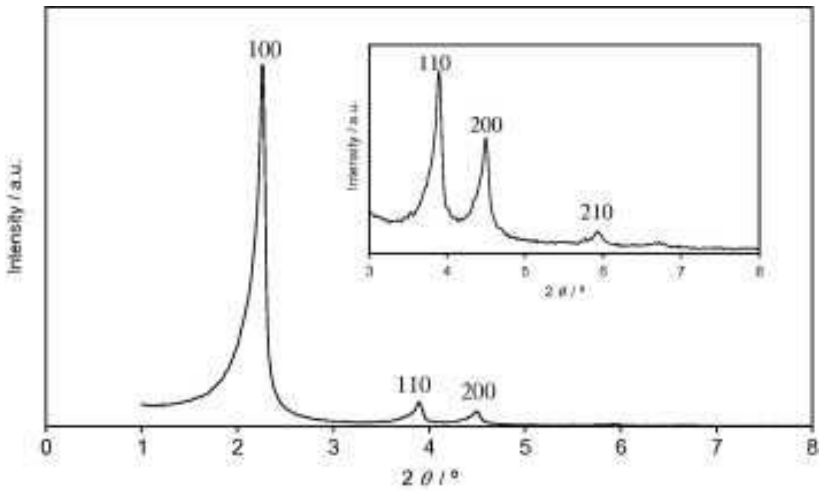

Figure 32. Typical XRD pattern of MCM-41.[233]

By comparison of XRD patterns of mesoporous silica catalysts before and after functionalization, after loading active metals, or after running reactions, the peaks modifications can indicate the loss of order and structure changes of the material. Normally, the peaks can broaden and their intensity is decreased, which means a slight disorder of the mesoporous silica or a reduction of the X ray scattering contrast after the modification.[234-238] Since the loading of vanadium is usually low and no V_2O_5 crystals exist, there are no vanadium oxide crystal peaks at the high angle range are observed.

2.5.2 N_2 adsorption-desorption isotherms

N_2 adsorption-desorption isotherms are very useful for the characterization of the mesoporous supported catalysts. By the measurement of the adsorption and desorption of N_2 as a function of its partial pressure, the isotherm can provide a lot of information about the surface area, pore volume, average pore diameter, and pore size distribution, which are related to the diffusion properties of the mesoporous catalysts. The most wildly used models to treat the experimental data are the BET[239] and BJH[240] methods for mesoporous materials.

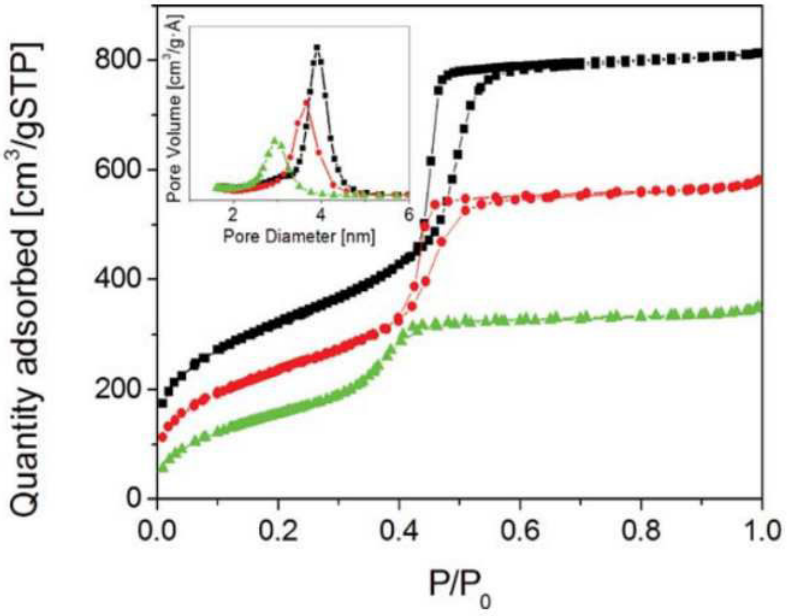

Figure 33. Example of N_2 adsorption-desorption isotherms and the BJH pore size distribution of MCM-41 before (black line) and after (red and green lines) functionalization.[241]

The N_2 adsorption-desorption isotherm of MCM-41 exhibits a typical type-IV isotherm according to the IUPAC classification (Figure 33).[242] The adsorption at low relative pressure corresponds to the monolayer adsorption of N_2 on the mesoporous walls. At the higher relative pressures, the multilayer adsorption takes place until the condensation gives rise to a sharp adsorption volume increase at a pressure determined by Kelvin-type rules.[243] After various functionalizations and the introduction of vanadium or other metal active sites, there are always some shifts of the isotherm that indicates the decrease of the surface area and the pore size as the pores are filled by some ligand groups on the walls.[238, 244-246]

2.5.3 Thermogravimetric analysis (TGA)

The thermogravimetric analysis is based on the weight loss of the material according to a programmed temperature increase in the O_2 or N_2 atmosphere, which is helpful to understand the nature of the functional groups incorporated into the support. The surfactant amount in the mesoporous silica can be estimated through the final

residual weight. The thermogravimetric (TG) curve shows the weight loss with the increase of temperature, while the derivative thermogravimetric (DTG) curve shows the mass change rate with the increase of temperature, indicating more clearly the desorption or decomposition of different species. Figure 34 shows an example of DTG and TGA curves for an as-synthesized MCM-41 sample. The weight loss peak below 400 K is usually attributed to the loss of condensed and physically adsorbed H_2O, and the second peak at about 473 K is assigned to the decomposition of the surfactant template. The third peak at about 563 K is related to the combustion of the remaining carbon species, while the fourth peak at about 753 K is due to the condensation of silanol groups. When there are other organic functional groups or ligands, the peaks of the combustion of the encapsulated or grafted organic molecules will also show in the DTG curves and may overlap with the template combustion peak.

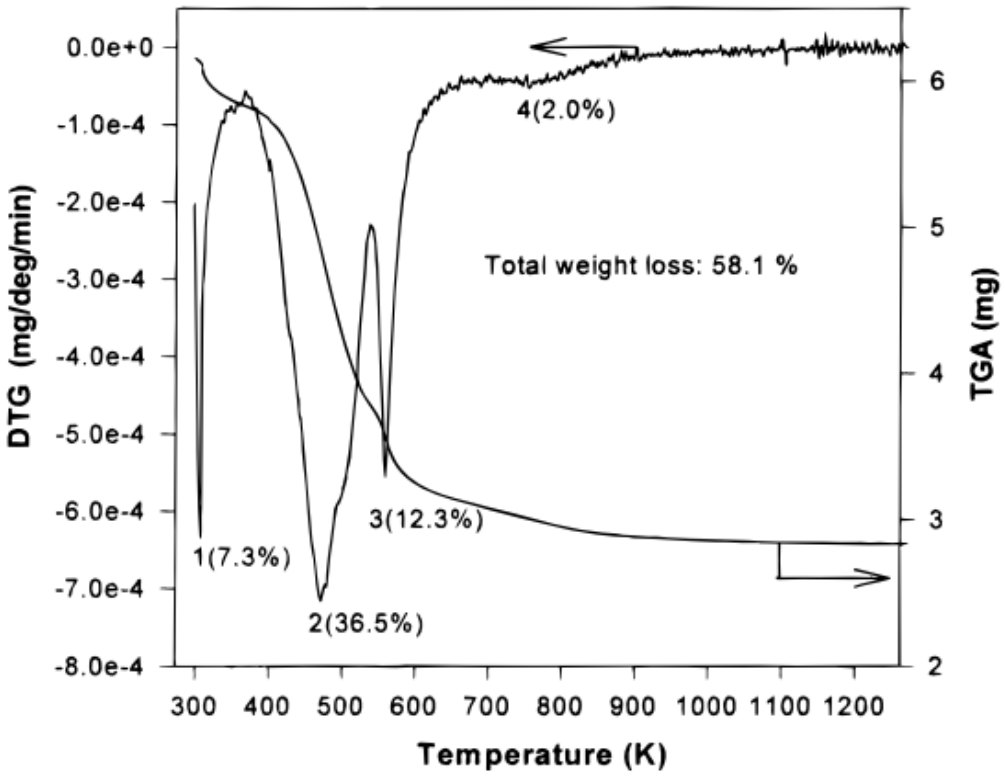

Figure 34. DTG and TGA curves for the as-synthesized MCM-41 sample.[247]

2.5.4 Scanning electron microscopy (SEM)

Scanning electron microscopy is a useful technique to investigate the morphology of heterogeneous catalysts and materials at the nano-scale level. For the mesoporous silica supported catalyst, SEM can be used to check the morphology before and after running the reactions to control the stability of the porous solid. With the development of different synthesis processes and recipes, new types of mesoporous silica with different shapes and morphologies have been obtained, such as spherical particles, rodlike and discoid, hollow spheres, thin films, *etc*.[42, 248-258] Figure 35 shows some examples of the different morphologies of MCM-41.

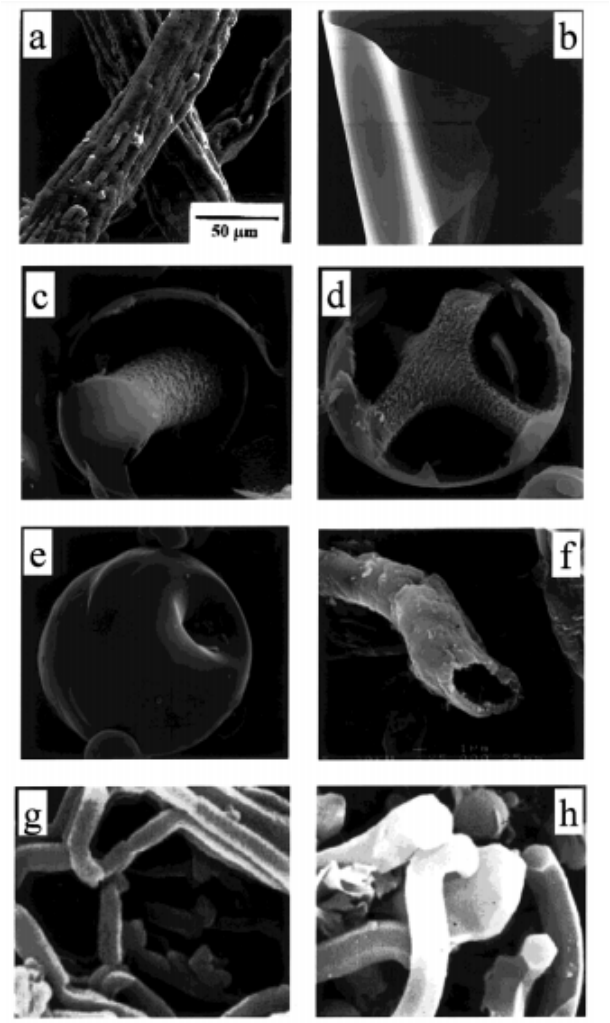

Figure 35. Scanning electron micrographs of MCM-41 samples with different morphologies.[259]

2.5.5 Transmission electron microscopy (TEM)

Transmission electron microscopy is a very powerful technique for the researching of mesoporous structures. Indeed, it can reveal the detail of regular hexagonal arrays and uniform channels in mesoporous silica as well as the dispersion of some metals inside the silica matrix. In addition, for a selected area electron diffraction patterns can provide information about the structure periodicity.[260] Figure 36 shows a representative TEM image of MCM-41. In Figure 37, the different structure details of stellate, raspberry, and worm-like mesoporous silica nanoparticles are clearly revealed by the HR TEM images.[261]

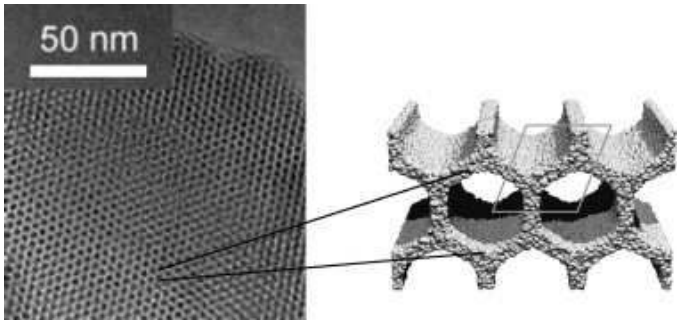

Figure 36. Transmission electron micrograph of MCM-41 and a schematic of its honeycomb structure.[233]

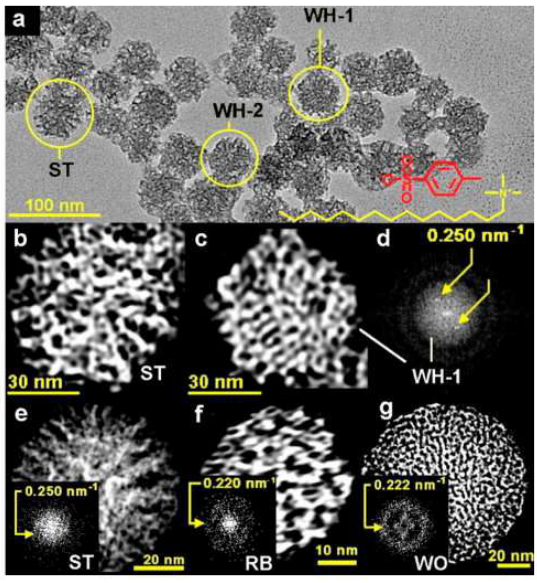

Figure 37. HR TEM images of three types of mesoporous silica nanoparticles.[261]

2.5.6 Solid state nuclear magnetic resonance spectroscopy (NMR)

Solid state nuclear magnetic resonance spectroscopy is a bulk technique which provides information about the oxygen coordination state of vanadium as well as the support oxide phase. For example, from the solid state ^{51}V NMR, ^{29}Si NMR, ^{27}Al NMR, ^{13}C NMR, the distribution of different oxide phases can be revealed by quantitative analysis.[233, 262-266]

Figure 38 shows an example of solid NMR quantitative analysis of ^{29}Si in MCM-41. The pure silica MCM-41 has a single Q^4 (-110 ppm) peak which corresponds to the silicon coordinated with four oxygen atoms (Figure 38 a). After the controlled hydration modification, three species of silicon coordination state appeared (Figure 38 b), Q^4, Q^3 (-101 ppm, each silicon atom coordinated with three oxygen atoms and one hydroxy), and Q^2 (-92 ppm, each silicon atom coordinated with two oxygen atoms and two hydroxy); after the hydrolysis and incorporation of zirconium isopropoxide, the disappearance of Q^2 and Q^3 species indicate the consumption of hydroxyls (Figure 38 c).[267] When there are organic functional groups grafted on the silica, the appearance of T^3 (-55 ppm, C-Si$(OSi)_3$), T^2 (-57 ppm, C-Si$(OSi)_2OR$), T^1 (-48 ppm, C-Si$(OSi)(OR)_2$); D^2 (-16 ppm, C_2-Si$(OSi)_2$), D^1 (-10 ppm, C_2-Si(OSi)OR); and M^1 (13 ppm, C_3-Si(OSi)), M^0 (18 ppm, C_3-Si(OR)) species will provide more information about the status of linkage between the organic groups and silicon.[268, 269]

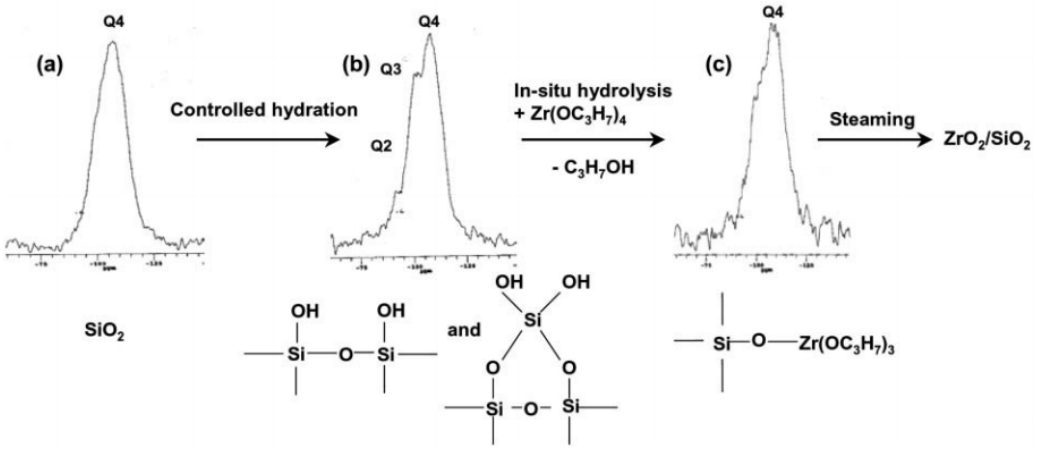

Figure 38. ^{29}Si NMR of MCM-41 before and after hydration and incorporation of zirconium isopropoxide.[267]

The ^{13}C NMR spectrum can show the peaks of different C atom bonded to Si atom which is useful to affirm the incorporation of organic functional groups on mesoporous silica.[238] In ^{27}Al NMR spectrum, the ratio of tetrahedral Al (~53 ppm) and hexacoordinated Al (~7 ppm) can be calculated by the quantitative analysis,[270] and ^{51}V NMR spectrum can show different vanadium oxide species bonded to the support.[271, 272]

2.5.7 Fourier transform infrared spectroscopy (FTIR)

Fourier transform infrared spectroscopy can be used for obtaining the adsorption signals from the support oxides, it can also be applied under *in suit* conditions for probing reactant molecules which adsorb on the surface of catalysts.[273-282]

FTIR spectra is wildly used to monitor the assembly of functional groups inside the mesoporous silica, the characteristic bands such as C-O (1280 cm^{-1}-1290 cm^{-1}), C=O (1550 cm^{-1}-1610 cm^{-1} and 1350 cm^{-1}-1420 cm^{-1}), aromatic CH- (1500 cm^{-1}-1550 cm^{-1}), aromatic C=C (1450 cm^{-1}-1560 cm^{-1}), C=N (1620 cm^{-1}-1690 cm^{-1}), *etc*, are important indicators for confirming the anchoring of ligands on support.[236, 245, 266] Figure 39 shows the FTIR spectra of MCM-41 functionalized with TEPSA and pentane-1,2-dicarboxylic acid. The structure features of MCM-41 silica framework include the Si-OH bending vibration (820 cm^{-1} and 750 cm^{-1}), Si-OH bond stretching vibration of silanol groups (966 cm^{-1}), Si-O-Si asymmetric stretching vibration (1250 cm^{-1} and 1084 cm^{-1}); the peak in 1630 cm^{-1} come from the -OH bending vibration of adsorbed water, and there is the O-H stretching vibration (3200 cm^{-1}-3700 cm^{-1}) from hydrogen bonded surface silanol, hydroxyl groups of carboxylic acid groups and absorbed water. The existence of -C=O stretch of carboxylic acid (1750 cm^{-1} -1680cm^{-1}), anhydride species (1868 cm^{-1}-1779 cm^{-1}), in plane deformation of carboxylic acid (1250 cm^{-1} and 1084 cm^{-1}), and aliphatic -C-H stretching vibration (2800 cm^{-1}-3000 cm^{-1}) indicated the incorporation of organic functional groups.[283]

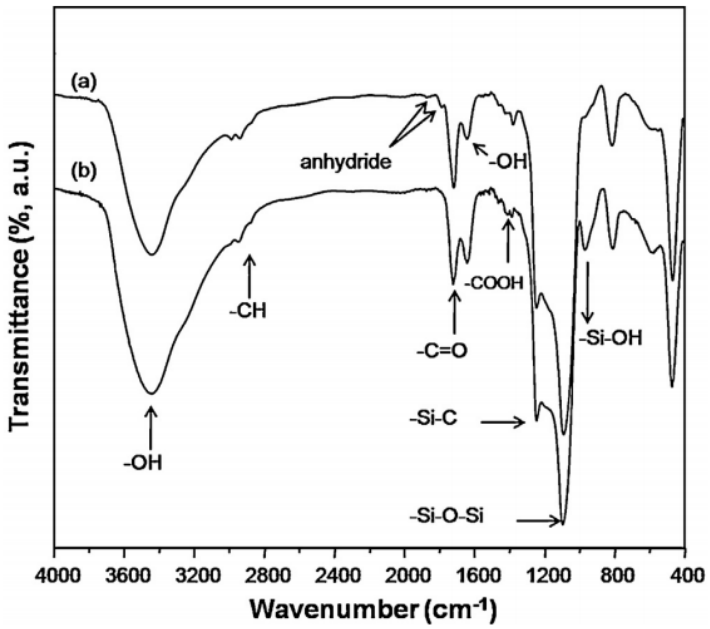

Figure 39. MCM-41 functionalized with TEPSA (a) and pentane-1,2-dicarboxylic acid (b).[283]

2.5.8 Ultraviolet visible (UV-vis) diffuse reflectance spectroscopy (DRS)

Ultraviolet and visible diffuse reflectance spectroscopy can be applied to the analysis of different electronic transitions of vanadium as well as the other metal ions in support oxide.[284-286] It can probe the charge transfer transitions of vanadium ions. The UV-vis DRS can monitor the ligand to metal charge transfer (LMCT) transition of V^{5+} and the d-d transition of V^{4+}.[192] The signal can be influenced by several parameters such as the local and overall symmetry, the condensation degree, the polarization effect, the size of counteraction, the dispersion of loading metals, *etc*.[287, 288]

The UV-vis DRS can show different electronic transitions for isolated and polymeric vanadia structures. Comparing to monomeric surface vanadia species, the polymeric vanadia species has a greater electron delocalization which leads to the shifting of V^{5+} LMCT transition to lower energy. Based on these differences, the UV-vis edge energy (E_g) can be used as the quantitative analysis parameter for the vanadia polymerization degree. The structure with more V-O-V bridging bonds will have a lower E_g value. As the spectra should follow the rule in Kubelka-Munk

function, the samples need to be diluted until getting the results within the limit of $F(R_\infty) < 1$, then, by plotting the $[F(R_\infty)h\nu]^2$ against $h\nu$ (incident photon energy) through mathematical transition (Figure 40), the E_g can be indicated by the intercept of low energy slope.[289-300]

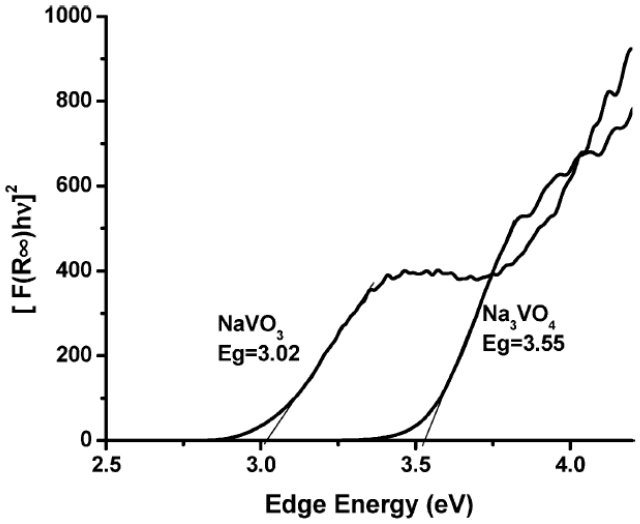

Figure 40. UV-vis DRS spectra and E_g values of Na_3VO_4 and $NaVO_3$.[300]

2.5.9 Raman spectroscopy (RS)

To discriminate the different vanadium oxide structures with different coordinations and bond lengths, Raman spectroscopy is an ideal approach,[301-309] it can provide the information about the surface vanadium oxide species and can be applied to the *in situ* conditions to observe the structural changes of these species. But the Raman spectroscopy also has a limitation when there is an overlap of the vibration from the support oxide with the vibration from surface vanadium oxide phase.[197] For silica and alumina supports, there are very weak Raman adsorption bands in 1100-100 cm^{-1}, while for titania and zirconia oxides, there are strong Raman bands below 700 cm^{-1}.[192]

Compared to the visible Raman spectroscopy (line radiation at 488 nm), the UV Raman spectroscopy (line radiation at 244 nm) is more sensitive as it can increase the intensity of Raman signal and decrease the intensity of fluorescence background (Figure 41).[310, 311] For V-MCM-41 and MCM-41, in the visible Raman spectra, the band of 490 cm^{-1} belong to the 3 Si siloxane rings, while the band of 610 cm^{-1} belong

to the 4 Si siloxane rings, the band at 810 cm^{-1} attributed to the siloxane bridges, and the band at 910 cm^{-1} come from the surface silanol groups. In the UV Raman spectra for MCM-41, the band at 970 cm^{-1} attributed to the surface silanol stretching vibrations, and the weak bands between 1100-1200 cm^{-1} assigned to the asymmetric stretching modes of Si-O-Si bridges; while for V-MCM-41, the band at 930 cm^{-1} assigned to the V=O symmetric stretching mode of polymerized vanadium oxides, the band at 1030 cm^{-1} attributed to the V=O stretching vibration of monomeric vanadyl species bond directly to the support, and due to the strong structural tension of tetrahedral coordinated vanadium species, the higher position at 1070 cm^{-1} corresponds to the shortest V=O bond distance.[312-314]

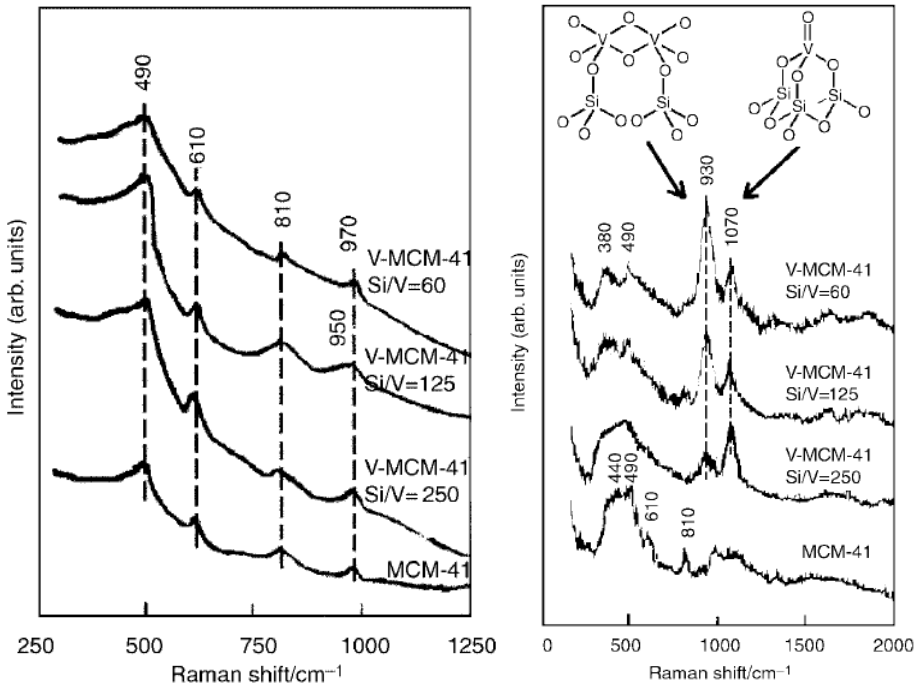

Figure 41. Raman spectra of V-MCM-41 and MCM-41 (line radiation: 488 nm (left) and 244 nm (right)).[314]

2.5.10 Electron paramagnetic resonance spectroscopy (EPR)

The electron paramagnetic resonance spectroscopy can be used to determine the paramagnetic vanadium (IV) oxide species in diamagnetic matrices as the interaction between unpaired electron of V^{4+} ion and ^{51}V nucleus can arise the hyperfine splitting signals.[315, 316]

Figure 42 shows the typical EPR spectra of V-MCM-41 at 77 K. The spectra of the as-synthesized samples displays an eight-line hyperfine patterns corresponding to the well dispersed vanadyl ions $(V^{IV}=O)^{2+}$ in the axially symmetric crystal field; while the sample after calcination has no axially symmetric signal which indicated that all the $(V^{IV}=O)^{2+}$ ions have been oxidized to $(V^{V}=O)^{3+}$; by the reduction of this sample in H_2, the spectra recovered to the original hyperfine structure except the intensity was lower than the as-synthesized sample.[312]

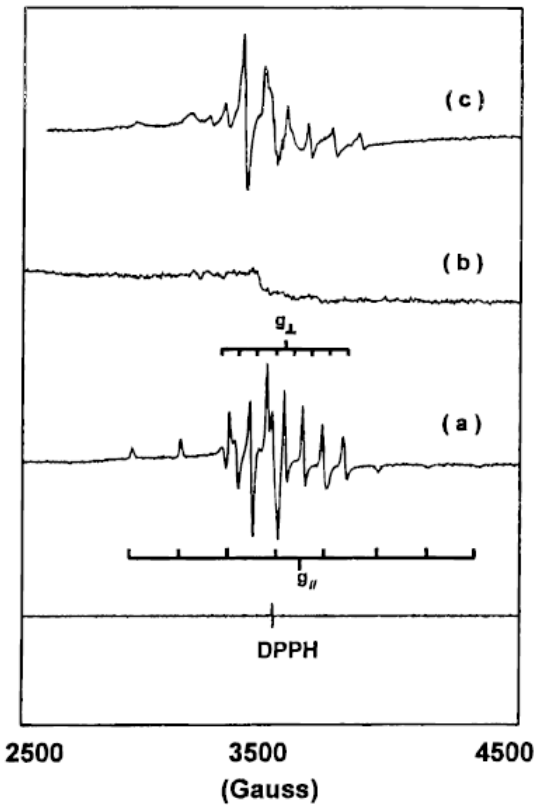

Figure 42. EPR spectra of (a) as-synthesized, (b) calcined, (c) H_2 reduced V-MCM-41 samples at 77 K.[312]

2.5.11 Additional characterization techniques

More characterization technique may be involved to describe and understand better the reactivity of mesoporous silica supported vanadium catalysts. For example, by elemental analysis (atomic absorption spectroscopy (AAS) or inductively coupled plasma spectrometer (ICP)), the ratio of different metal loading or leaching compare

to silica can be calculated; X-ray absorption spectroscopy (XAS) can indicate the oxidation state, local coordination environment and symmetry of vanadium species; dispersive X-ray analysis (EDX), auger electron spectroscopy (AES), and X-ray photoelectron spectroscopy (XPS) can also provide the elemental analysis information of catalyst; and chemical adsorption-desorption can be applied to test the redox property of active sites, *etc*. With the development of new technology, there will be more methods which could bring interesting answers on the coordination state, the oxidation state and the nuclearity of the supported vanadium species.[192, 266, 317] Of course, a reasonable choice is a compromise with the availability, the cost and the information provided.

2.6 Oxidation of lignin model compound

2.6.1 Environment and biomass

In the 21st century, the climate change and environment problems attract broad attention, and the energy crisis is another concern of the greatest importance today. Different countries around the world have invested a lot of resources in research concerning global warming and carbon cycle.[318, 319] Our industry rely mostly on the fossil fuels including coal, petroleum, and natural gas, which are non-renewable energy formed millions of years ago that correspond to a limited reserve of resources. The continuing development of industry offering an accessibility to legitime modern life and comfort for a larger fraction of the population prompt us to move urgently towards renewable and sustainable sources of energy.

Biomass is one of the renewable energy sources, which comes from the organic matter produced by plants. Plants can convert the CO_2 from the atmosphere into biopolymers, sugars, and lipids by photosynthesis, which is a very important link for the carbon cycle. Therefore, biomass resource is one of the ideal alternative energy sources of traditional fossil fuels with great potential in the future.[320]

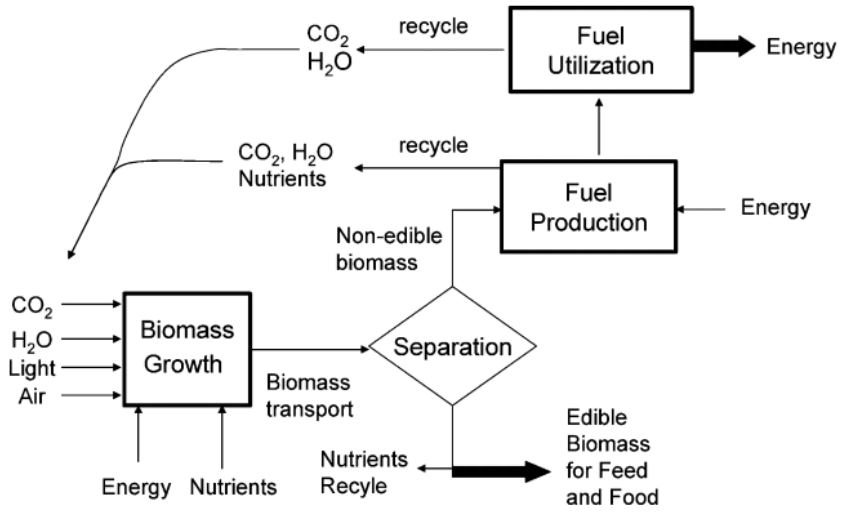

Figure 43. Sustainable production of transportation fuels from biomass in an integrated biomass production-conversion system.[320]

Lignin, cellulose, and hemicellulose are the main constituents of plant cytoskeleton. By chemical degradation of these natural polymers, high value small molecular weight chemicals can be obtained. Figure 44 shows the basic structural unit of cellulose, hemicellulose, and lignin.[321]

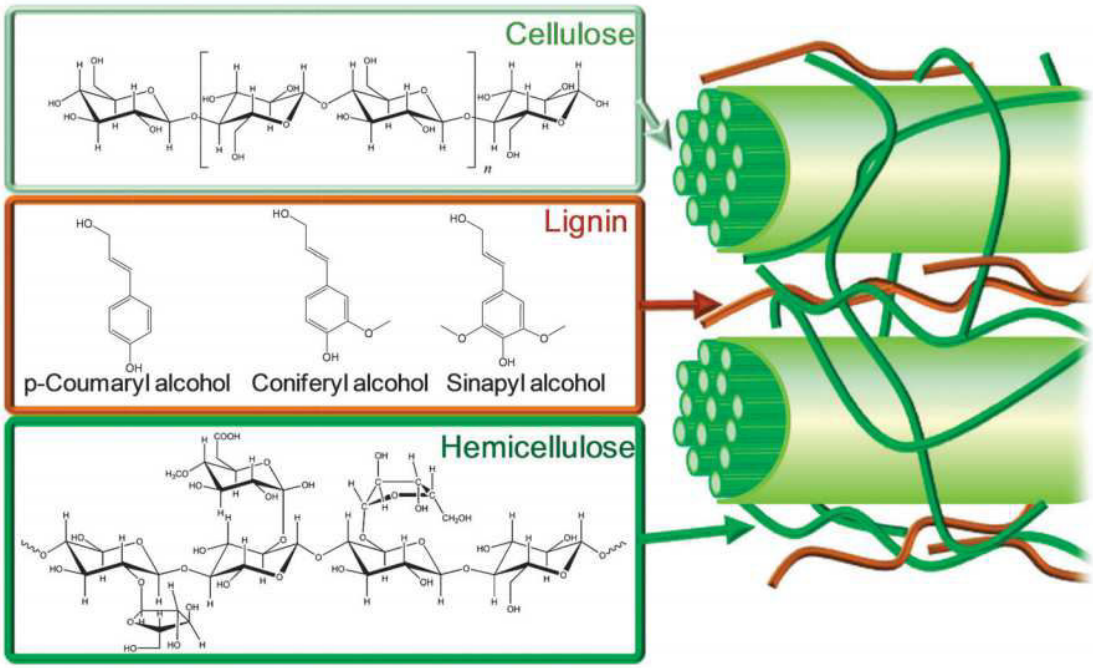

Figure 44. The structure of lignocellulosic biomass with cellulose, hemicellulose and lignin (with building blocks) represented.[321]

2.6.2 Lignin structure and lignin model compounds

For the combination of lignocellulosic biomass, lignin makes up 15-30 wt%. The three primary monomers in lignin are p-coumaryl alcohol, coniferyl alcohol, sinapyl alcohol (Figure 44). The different composition of these building blocks constitutes the different lignin structure which depending on the species of plants and their growing conditions (Figure 45). Among the complicated structure linkages in lignin, the most important and abundant one is the β-O-4 linkage (Figure 46). To break the complicated linkages and process lignin polymer into small blocks and convert them into value-added chemicals and fuels is a worthwhile project.[322]

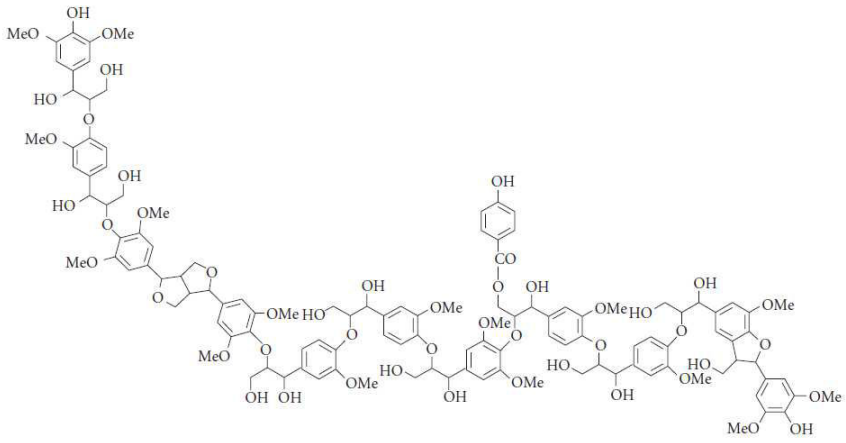

Figure 45. Lignin polymer model for lignins from poplar.[322]

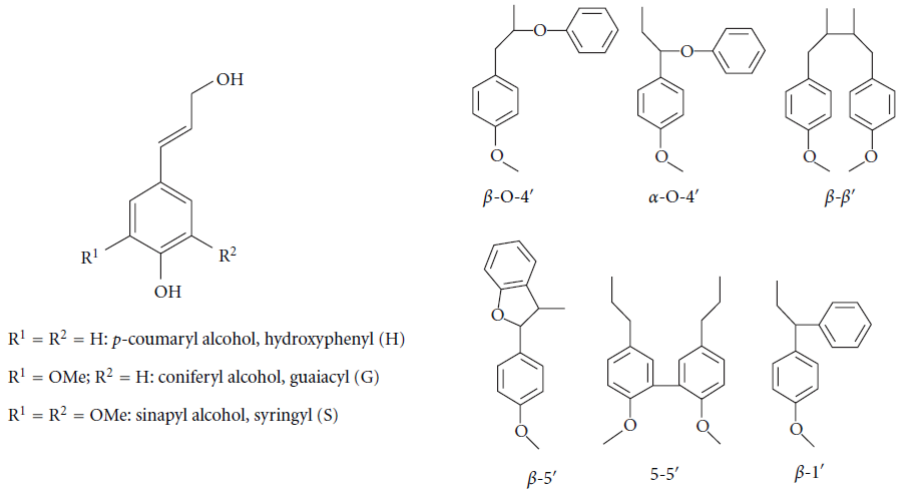

Figure 46. Building blocks of lignin and common linkages between phenyl propane units.[322]

To simplify the investigation of lignin degradation, scientists found convenient molecules mimicking typical fragments of lignin. For example, one counts among them the pinacol monomethyl ether, 2-phenoxyethanol, 1,2-diphenyl-2-methoxyethanol, 1-phenyl-2-phenoxy-ethanol.[323] Some larger model chemicals were also considered, such as 1-(3,5-dimethoxyphenyl)-2-(2-ethoxyphenoxy)-propane-1,3-diol, 1-(4-hydroxy-3,5-dimethoxyphenyl)-2-(2-methoxyphenoxy)-propane-1,3-diol, *etc*.[324-326]

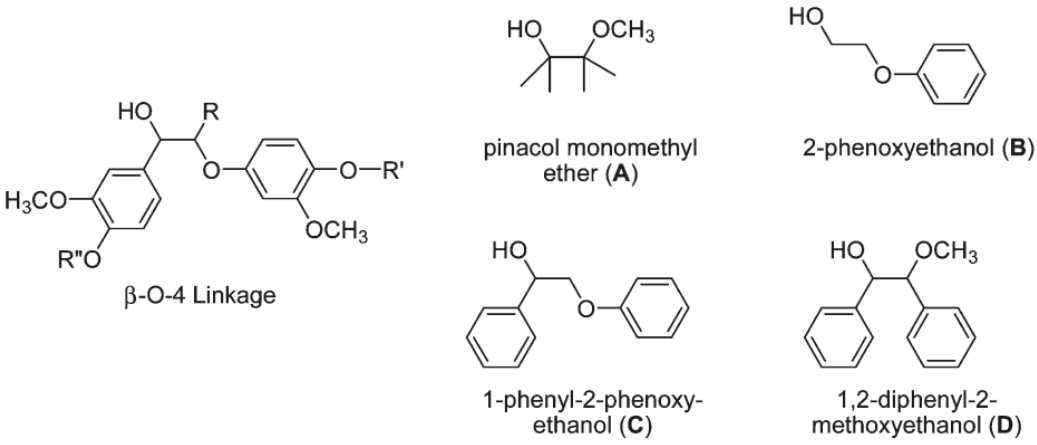

Figure 47. Examples of some simple molecules mimicking typical lignin fragments.[323]

2.6.3 Catalysts for lignin valorization

Developing catalysts for depolymerization of lignin is a promising pathway to obtain the high-value chemicals from biomass. Homogeneous and heterogeneous catalysts have been exploited with different metal active species. The principal fragmentation reactions for catalytic lignin valorization are lignin cracking, lignin hydrolysis, lignin reduction, and lignin oxidation.[327]

Here we focus on the lignin oxidation reactions, which tend to form aromatic compounds with useful functionality for fine chemistry. There are several advantages of the oxidative cleavage of lignin, such as the moderate reaction conditions (low pressure and temperature requirement), cheap and available oxidants (peroxide or air). A wide variety of catalysts for lignin oxidation are based on the transition metal (Cu,

Fe, Co, V, Mn, Ru, *etc*.) compounds. Baker *et al*. developed the Cu(I)/TEMPO catalyst for the selective C-C bond cleavage of lignin models (Figure 48).[325, 328] Andrioletti *et al*. reported the Fe(TAML)Li catalyst to the oxidative cleavage of lignin model molecules.[329] Sedai *et al*. investigated the six-coordinate vanadium complex $(HQ)_2V^V(O)(O^iPr)$ (HQ = 8-oxyquinolinate) catalyst aerobic oxidation of the nonphenolic β-1 lignin model compound.[325] Mottweiler *et al*. compared several transition-metal-containing hydrotalcites with different loading of Cu, Fe, Zn, V, Co, *etc*. as catalysts and multimetal catalysts for the degradation of different lignin sources to get high activity and good selectivity.[330] Photocatalytic oxidation catalysts involve TiO_2 were also developed for the degradation of lignin.[331-333] More catalyst systems for the valorization of lignin can be found in the review of Zakzeski *et al*.[327]

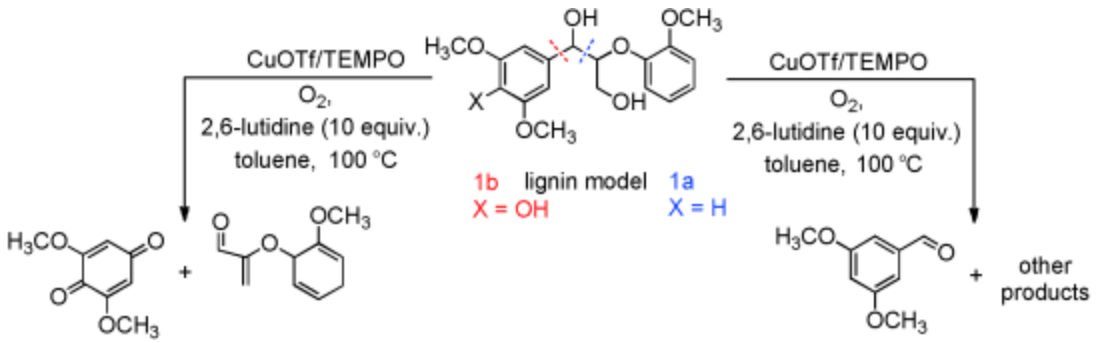

Figure 48. CuOTf/TEMPO catalyst towards the selective C-C bond cleavage of acylglycerol β-aryl ether lignin model compounds.[328]

2.6.4 Oxidation of lignin model compound by vanadium catalysts

Inspired by the vanadium-containing enzymes, bionic vanadium complexes were designed as catalysts for many kinds of oxidation reactions.[194] Vanadium catalysts are effective for various oxidative carbon-carbon bond cleavage. Figure 49 shows some examples of different types of C-C bond cleavage reactions promoted by vanadium catalysts, the substrates including 1,2-diols, 1,2-hydroxy ethers, and lignin models, *etc*.[334]

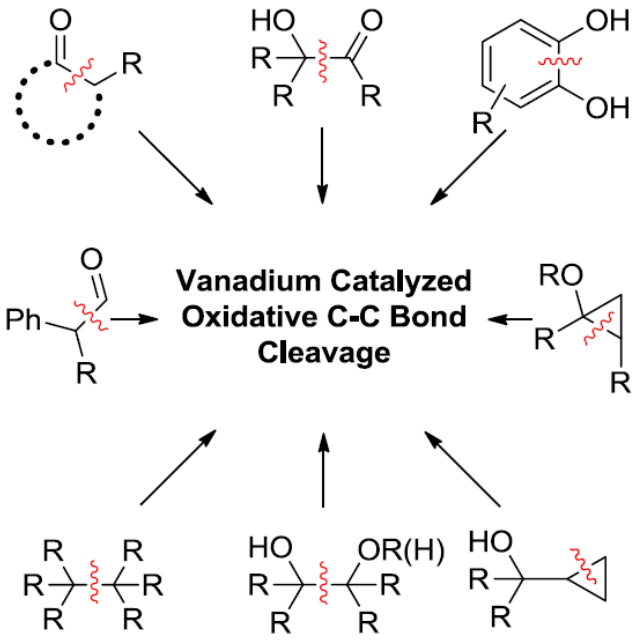

Figure 49. Vanadium-catalyzed oxidative C-C bond cleavage substrates.[334]

Hanson *et al.*[323, 335] tested the aerobic oxidation of pinacol monomethyl ether, 2-phenoxyethanol, 1-phenyl-2-phenoxyethanol, and 1,2-diphenyl-2-methoxyethanol catalyzed by dipicolinate vanadium(V) complexes, the effective breaking of carbon-carbon bonds of substrates indicated the potential of dipicolinate vanadium(V) complexes for the selective oxidative disassembly of lignin. Sedai *et al.*[324, 325] compared the reactivity of copper and vanadium complexes catalysts for the aerobic oxidation of lignin models, different products were observed which indicated the different selectivity and pathway of these reactions. Díaz-Urrutia *et al.*[336] made comparative studies of catalyzed oxidative lignin depolymerization using homogeneous oxovanadium, copper and cobalt complexes, they found the oxovanadium(V) complexes demonstrated the highest degree of organosol lignin depolymerization. To control the selectivity (involving C-H vs. C-O vs. C-C bond cleavage) of products is a challenge due to the coexistence of multiple different linkages and functional groups in the complicated lignin structures.

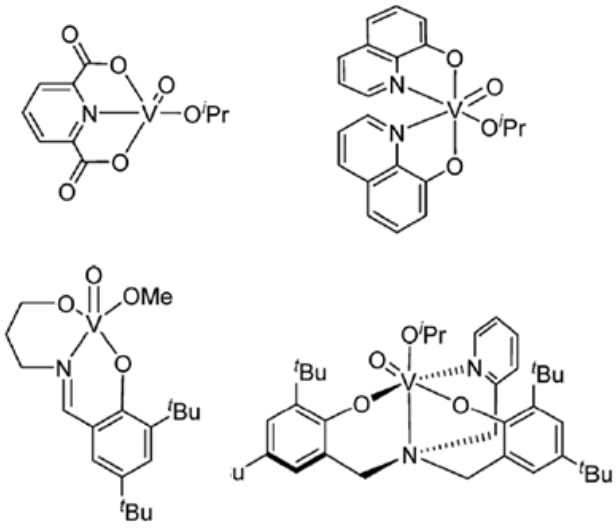

Figure 50. Examples of the oxovanadium(V) complexes catalysts.[336]

2.6.5 Applications and prospects

Nowadays, most of the lignin was burned as a waste from paper and pulp industry, the effective utilization of lignin as a renewable source to produce high-value aromatic compound is a challenge for sustainable chemical industry and environmental protection (Figure 51).[327]

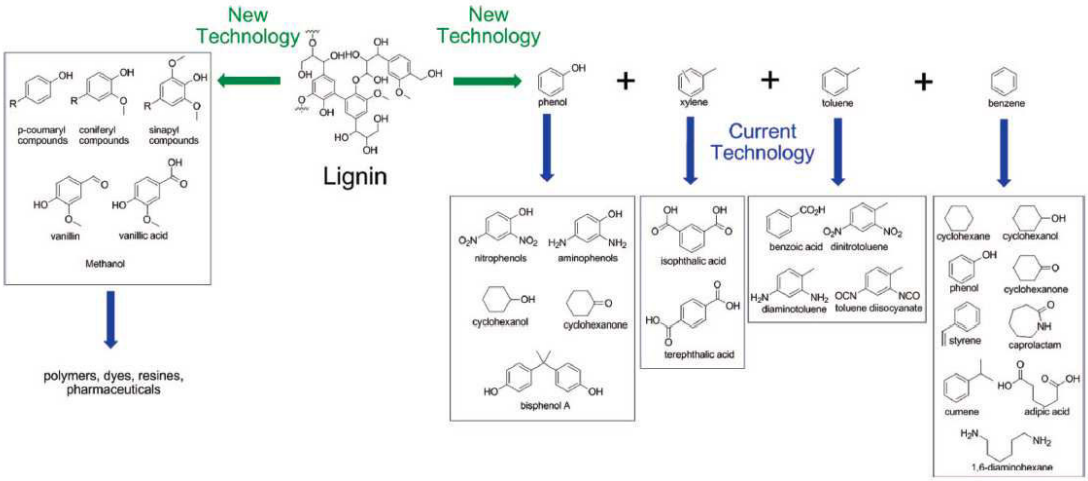

Figure 51. High-value chemicals potentially obtained from lignin.[327]

Though considerable effort has been devoted to develop new catalysts for the valorization of lignin, there are still a lot of limitations of the current processes, such as the long reaction time, poor selectivity and low yield of the high-value target products, difficult separation of products, *etc*, therefore it is still a long way to meet the requirement in industrial application. Besides the investigation of new catalysts, to take advantages of electrochemistry, photochemistry, ionic liquids, supercritical fluids, *etc*. may arise new strategies for the transformation of lignin.[337]

2.7 References

1. Cronstedt, A. F., *Rön och beskrifning om en obekant bärg art, som kallas Zeolites*. **1756**.
2. Flanigen, E. M. *Stud. Surf. Sci. Catal.* **2001**, 137, 11-35.
3. Flanigen, E. M.; Broach, R. W.; Wilson, S. T. *Zeolites in Industrial Separation and Catalysis* **2010**, 1-26.
4. Deville, H. d. S. C.; Debray, H. *Sci* **1862**, 54, 324.
5. Friedel, G. *Bull. Soc. Fr. Minéral. Cristallogr* **1896**, 19, 363-390.
6. Friedel, G. *CR Acad. Sci* **1896**, 122, 948-951.
7. Grandjean, F. *CR Acad. Sci* **1910**, 149, 866-868.
8. Weigel, O.; Steinhoff, E. *Z. Kristallogr* **1925**, 61, 125-154.
9. Leonard, R. J. *Econ. Geol* **1927**, 22, (1), 18-43.
10. Taylor, W. *Z. Kristallogr. Cryst. Mater.* **1930**, 74, (1-6), 1-19.
11. Pauling, L. *Proc. Natl. Acad. Sci.* **1930**, 16, (7), 453-459.
12. Pauling, L. *Z. Kristallogr. Cryst. Mater.* **1930**, 74, (1-6), 213-225.
13. McBain, J. W., *J. Phys. Chem.* **1933**, 37 (1), 149–150.
14. Barrer, R., *Sci. and Chem.* Ind: **1945**.
15. Barrer, R. M. *J. Chem. Soc.* **1948**, 2158-2163.
16. Everett, D. *Pure Appl. Chem.* **1972**, 31, (4), 577-638.
17. Nishihara, H.; Mukai, S. R.; Yamashita, D.; Tamon, H. *Chem. Mater.* **2005**, 17, (3), 683-689.
18. Zhao, D.; Feng, J.; Huo, Q.; Melosh, N.; Fredrickson, G. H.; Chmelka, B. F.; Stucky, G. D. *Science* **1998**, 279, (5350), 548-552.
19. Serrano, D.; Sanz, R.; Pizarro, P.; Moreno, I. *Chem. Commun.* **2009**, (11), 1407-1409.
20. Baerlocher, C.; McCusker, L. B.; Olson, D. H., *Atlas of zeolite framework types*. Elsevier: **2007**.
21. Kresge, C.; Leonowicz, M.; Roth, W.; Vartuli, J.; Beck, J. *Nature* **1992**, 359, (6397), 710-712.
22. Beck, J.; Vartuli, J.; Roth, W. J.; Leonowicz, M.; Kresge, C.; Schmitt, K.; Chu, C.; Olson, D. H.; Sheppard, E.; McCullen, S. *J. Am. Chem. Soc.* **1992**, 114, (27), 10834-10843.
23. Hoffmann, F.; Cornelius, M.; Morell, J.; Fröba, M. *Angew. Chem. Int. Ed.* **2006**, 45, (20), 3216-3251.
24. 徐如人; 庞文琴; 于吉红, *分子筛与多孔材料化学*. 北京: 科学出版社: **2004**.
25. Hou, Q.; Margolese, D.; Cielsa, U.; Feng, P.; Gier, T.; Sieger, P.; Leon, R.; Petroff, P.; Schiith, F.; Stucky, G. *Nature* **1994**, 368, 317-321.
26. Monnier, A.; Schüth, F.; Huo, Q.; Kumar, D.; Margolese, D.; Maxwell, R.; Stucky, G.; Krishnamurty, M.; Petroff, P.; Firouzi, A. *Science* **1993**, 261, (5126), 1299-1303.
27. Huo, Q.; Margolese, D. I.; Stucky, G. D. *Chem. Mater.* **1996**, 8, (5), 1147-1160.
28. Collart, O.; Van Der Voort, P.; Vansant, E.; Desplantier, D.; Galarneau, A.; Di Renzo, F.; Fajula, F. *J. Phys. Chem. B* **2001**, 105, (51), 12771-12777.
29. Zhao, D.; Huo, Q.; Feng, J.; Chmelka, B. F.; Stucky, G. D. *J. Am. Chem. Soc.* **1998**, 120, (24), 6024-6036.
30. Lu, A. H.; Schüth, F. *Adv. Mater.* **2006**, 18, (14), 1793-1805.
31. Sun, X.; Shi, Y.; Zhang, P.; Zheng, C.; Zheng, X.; Zhang, F.; Zhang, Y.; Guan, N.; Zhao, D.; Stucky, G. D. *J. Am. Chem. Soc.* **2011**, 133, (37), 14542-14545.
32. Thomas, A.; Goettmann, F.; Antonietti, M. *Chem. Mater.* **2008**, 20, (3), 738-755.

33. Tiemann, M. *Chem. Mater.* **2007**, 20, (3), 961-971.

34. Wan, Y.; Shi, Y.; Zhao, D. *Chem. Mater.* **2007**, 20, (3), 932-945.

35. Schüth, F. *Angew. Chem. Int. Ed.* **2003**, 42, (31), 3604-3622.

36. Lebeau, B.; Parmentier, J.; Soulard, M.; Fowler, C.; Zana, R.; Vix-Guterl, C.; Patarin, J. *C. R. Chim.* **2005**, 8, (3), 597-607.

37. Edler, K. J.; White, J. W. *J. Chem. Soc., Chem. Commun.* **1995**, (2), 155-156.

38. Chatterjee, M.; Iwasaki, T.; Hayashi, H.; Onodera, Y.; Ebina, T.; Nagase, T. *Catal. Lett.* **1998**, 52, (1-2), 21-23.

39. Chen, C.-Y.; Burkett, S. L.; Li, H.-X.; Davis, M. E. *Microporous Mater.* **1993**, 2, (1), 27-34.

40. Wu, C.-G.; Bein, T. *Chem. Commun.* **1996**, (8), 925-926.

41. Newalkar, B. L.; Komarneni, S.; Katsuki, H. *Chem. Commun.* **2000**, (23), 2389-2390.

42. Lin, W.; Chen, J.; Sun, Y.; Pang, W. *J. Chem. Soc., Chem. Commun.* **1995**, (23), 2367-2368.

43. Fyfe, C. A.; Fu, G. *J. Am. Chem. Soc.* **1995**, 117, (38), 9709-9714.

44. Gallis, K. W.; Landry, C. C. *Chem. Mater.* **1997**, 9, (10), 2035-2038.

45. Zhao, D.; Yang, P.; Melosh, N.; Feng, J.; Chmelka, B. F.; Stucky, G. D. *Adv. Mater.* **1998**, 10, (16), 1380-1385.

46. Brinker, C. J.; Lu, Y.; Sellinger, A.; Fan, H. *Adv. Mater.* **1999**, 11, (7), 579-585.

47. Melosh, N.; Lipic, P.; Bates, F.; Wudl, F.; Stucky, G.; Fredrickson, G.; Chmelka, B. *Macromolecules* **1999**, 32, (13), 4332-4342.

48. Melosh, N.; Davidson, P.; Chmelka, B. *J. Am. Chem. Soc.* **2000**, 122, (5), 823-829.

49. MacLachlan, M. J.; Coombs, N.; Ozin, G. A. *Nature* **1999**, 397, (6721), 681-684.

50. Yang, P.; Zhao, D.; Margolese, D. I.; Chmelka, B. F.; Stucky, G. D. *Nature* **1998**, 396, (6707), 152-155.

51. Tanev, P. T.; Pinnavaia, T. J. *Science* **1995**, 267, (5199), 865.

52. Huo, Q.; Margolese, D. I.; Ciesla, U.; Demuth, D. G.; Feng, P.; Gier, T. E.; Sieger, P.; Firouzi, A.; Chmelka, B. F. *Chem. Mater.* **1994**, 6, (8), 1176-1191.

53. Vinu, A.; Murugesan, V.; Hartmann, M. *Chem. Mater.* **2003**, 15, (6), 1385-1393.

54. Wang, A.; Kabe, T. *Chem. Commun.* **1999**, (20), 2067-2068.

55. Sayari, A.; Yang, Y.; Kruk, M.; Jaroniec, M. *J. Phys. Chem. B* **1999**, 103, (18), 3651-3658.

56. Sun, J. H.; Moulijn, J.; Jansen, J.; Maschmeyer, T.; Coppens, M. O. *Adv. Mater.* **2001**, 13, (5), 327-331.

57. áSong Zhao, X. *Chem. Commun.* **1999**, (15), 1391-1392.

58. Clark, J.; Macquarrie, D. *Chem. Commun.* **1998**, (8), 853-860.

59. Attard, G. S.; Glyde, J. C.; GOltner, C. G. *Nature* **1995**, 378, (6555), 366-368.

60. Soler-Illia, G. J. d. A.; Sanchez, C.; Lebeau, B.; Patarin, J. *Chem. Rev.* **2002**, 102, (11), 4093-4138.

61. Chen, C.-Y.; Li, H.-X.; Davis, M. E. *Microporous Mater.* **1993**, 2, (1), 17-26.

62. Firouzi, A.; Kumar, D.; Bull, L.; Besier, T.; Sieger, P.; Huo, Q.; Walker, S.; Zasadzinski, J.; Glinka, C.; Nicol, J. *Science* **1995**, 267, (5201), 1138-1143.

63. Sanchez, C.; Soler-Illia, G. d. A.; Ribot, F.; Lalot, T.; Mayer, C.; Cabuil, V. *Chem. Mater.* **2001**, 13, (10), 3061-3083.

64. Soler-Illia, G. J.; Rozes, L.; Boggiano, M. K.; Sanchez, C.; Turrin, C. O.; Caminade, A. M.; Majoral, J. P. *Angew. Chem. Int. Ed.* **2000**, 39, (23), 4249-4254.

65. de AA Soler–Illia, G. J.; Sanchez, C. *New J. Chem.* **2000**, 24, (7), 493-499.

66. Evans, D. F.; Wennerstrom, H., *The colloid domain, where physics, chemistry and biology meet*. Wiley-VCH, New York: **1994**.

67. Israelachvili, J. N.; Mitchell, D. J.; Ninham, B. W. *J. Chem. Soc. Faraday Trans.* **1976**, 72, 1525-1568.

68. Israelachvili J. *Intermolecular and surface forces*. Academic Press; New York: **1992**.

69. Stuart, M. C.; Boekema, E. J. *Biochim. Biophys. Acta* **2007**, 1768, (11), 2681-2689.

70. Taguchi, A.; Schüth, F. *Microporous Mesoporous Mater.* **2005**, 77, (1), 1-45.

71. Albela, B.; Bonneviot, L. *New J. Chem.* **2016**, 40, (5), 4115-4131.

72. Lim, M. H.; Blanford, C. F.; Stein, A. *J. Am. Chem. Soc.* **1997**, 119, (17), 4090-4091.

73. Yokoi, T.; Yoshitake, H.; Tatsumi, T. *J. Mater. Chem.* **2004**, 14, (6), 951-957.

74. Burkett, S. L.; Sims, S. D.; Mann, S. *Chem. Commun.* **1996**, (11), 1367-1368.

75. Huh, S.; Wiench, J. W.; Yoo, J.-C.; Pruski, M.; Lin, V. S.-Y. *Chem. Mater.* **2003**, 15, (22), 4247-4256.

76. Lim, M. H.; Stein, A. *Chem. Mater.* **1999**, 11, (11), 3285-3295.

77. Shin, E. W.; Han, J. S.; Jang, M.; Min, S.-H.; Park, J. K.; Rowell, R. M. *Environ. Sci. Technol.* **2004**, 38, (3), 912-917.

78. Heydari-Gorji, A.; Belmabkhout, Y.; Sayari, A. *Langmuir* **2011**, 27, (20), 12411-12416.

79. Zhang, Z.; Dai, S.; Fan, X.; Blom, D. A.; Pennycook, S. J.; Wei, Y. *J. Phys. Chem. B* **2001**, 105, (29), 6755-6758.

80. Maschmeyer, T.; Rey, F.; Sankar, G.; Thomas, J. M. *Nature* **1995**, 378, (6553), 159-162.

81. Mercier, L.; Pinnavaia, T. J. *Environ. Sci. Technol.* **1998**, 32, (18), 2749-2754.

82. Mal, N. K.; Fujiwara, M.; Tanaka, Y. *Nature* **2003**, 421, (6921), 350-353.

83. Walcarius, A.; Etienne, M.; Lebeau, B. *Chem. Mater.* **2003**, 15, (11), 2161-2173.

84. Liu, A.; Hidajat, K.; Kawi, S.; Zhao, D. *Chem Commun.* **2000**, (13), 1145-1146.

85. Matsumoto, A.; Tsutsumi, K.; Schumacher, K.; Unger, K. K. *Langmuir* **2002**, 18, (10), 4014-4019.

86. Ho, K. Y.; McKay, G.; Yeung, K. L. *Langmuir* **2003**, 19, (7), 3019-3024.

87. Huang, H. Y.; Yang, R. T.; Chinn, D.; Munson, C. L. *Ind. Eng. Chem. Res.* **2003**, 42, (12), 2427-2433.

88. Yoshitake, H.; Yokoi, T.; Tatsumi, T. *Chem. Mater.* **2002**, 14, (11), 4603-4610.

89. Khatri, R. A.; Chuang, S. S.; Soong, Y.; Gray, M. *Ind. Eng. Chem. Res.* **2005**, 44, (10), 3702-3708.

90. Zheng, F.; Tran, D. N.; Busche, B. J.; Fryxell, G. E.; Addleman, R. S.; Zemanian, T. S.; Aardahl, C. L. *Ind. Eng. Chem. Res.* **2005**, 44, (9), 3099-3105.

91. Trens, P.; Russell, M. L.; Spjuth, L.; Hudson, M. J.; Liljenzin, J.-O. *Ind. Eng. Chem. Res.* **2002**, 41, (21), 5220-5225.

92. Lei, C.; Shin, Y.; Liu, J.; Ackerman, E. J. *J. Am. Chem. Soc.* **2002**, 124, (38), 11242-11243.

93. Antochshuk, V.; Jaroniec, M. *Chem. Commun.* **2002**, (3), 258-259.

94. Antochshuk, V.; Olkhovyk, O.; Jaroniec, M.; Park, I.-S.; Ryoo, R. *Langmuir* **2003**, 19, (7), 3031-3034.

95. Olkhovyk, O.; Antochshuk, V.; Jaroniec, M. *Colloids Surf., A* **2004**, 236, (1), 69-72.

96. Venkatesan, K.; Srinivasan, T.; Rao, P. V. *J. Radioanal. Nucl. Chem.* **2003**, 256, (2), 213-218.

97. Kang, T.; Park, Y.; Choi, K.; Lee, J. S.; Yi, J. *J. Mater. Chem.* **2004**, 14, (6), 1043-1049.

98. Kang, T.; Park, Y.; Yi, J. *Ind. Eng. Chem. Res.* **2004**, 43, (6), 1478-1484.

99. Rodríguez-López, G.; Marcos, M. D.; Martínez-Máñez, R.; Sancenón, F.; Soto, J.; Villaescusa, L. A.; Beltrán, D.; Amorós, P. *Chem. Commun.* **2004**, (19), 2198-2199.

100. Blasco, T.; Corma, A.; Navarro, M.; Pariente, J. P. *J. Catal.* **1995**, 156, (1), 65-74.

101. Bhaumik, A.; Tatsumi, T. *J. Catal.* **2000**, 189, (1), 31-39.

102. Koyano, K.; Tatsumi, T. *Microporous Mater.* **1997**, 10, (4), 259-271.
103. Corma, A.; Navarro, M.; Pariente, J. P. *J. Chem. Soc., Chem. Commun.* **1994**, (2), 147-148.
104. Solsona, B.; Blasco, T.; Nieto, J. L.; Pena, M.; Rey, F.; Vidal-Moya, A. *J. Catal.* **2001**, 203, (2), 443-452.
105. Shylesh, S.; Singh, A. *J. Catal.* **2004**, 228, (2), 333-346.
106. Wu, K.; Li, B.; Han, C.; Liu, J. *Appl. Catal., A* **2014**, 479, 70-75.
107. Gomes, H.; Selvam, P.; Dapurkar, S.; Figueiredo, J.; Faria, J. *Microporous Mesoporous Mater.* **2005**, 86, (1), 287-294.
108. Jana, S.; Dutta, B.; Bera, R.; Koner, S. *Langmuir* **2007**, 23, (5), 2492-2496.
109. Norena-Franco, L.; Hernandez-Perez, I.; Aguilar-Pliego, J.; Maubert-Franco, A. *Catal. Today* **2002**, 75, (1), 189-195.
110. Hadjiivanov, K.; Tsoncheva, T.; Dimitrov, M.; Minchev, C.; Knözinger, H. *Appl. Catal., A* **2003**, 241, (1), 331-340.
111. Carvalho, W. A.; Wallau, M.; Schuchardt, U. *J. Mol. Catal. A: Chem.* **1999**, 144, (1), 91-99.
112. Choi, J.-S.; Yoon, S.-S.; Jang, S.-H.; Ahn, W.-S. *Catal. Today* **2006**, 111, (3), 280-287.
113. Wang, Y.; Zhang, Q.; Shishido, T.; Takehira, K. *J. Catal.* **2002**, 209, (1), 186-196.
114. Zhao, D.; Goldfarb, D. *J. Chem. Soc., Chem. Commun.* **1995**, (8), 875-876.
115. Xiang, S.; Zhang, Y.; Xin, Q.; Li, C. *Chem. Commun.* **2002**, (22), 2696-2697.
116. Kureshy, R. I.; Ahmad, I.; Noor-ul, H. K.; Abdi, S. H.; Pathak, K.; Jasra, R. V. *J. Catal.* **2006**, 238, (1), 134-141.
117. Diaz, J. F.; Balkus, K. J.; Bedioui, F.; Kurshev, V.; Kevan, L. *Chem. Mater.* **1997**, 9, (1), 61-67.
118. Khodakov, A. Y.; Zholobenko, V. L.; Bechara, R.; Durand, D. *Microporous Mesoporous Mater.* **2005**, 79, (1), 29-39.
119. Bhoware, S. S.; Singh, A. *J. Mol. Catal. A: Chem.* **2007**, 266, (1), 118-130.
120. Liu, D.; Lau, R.; Borgna, A.; Yang, Y. *Appl. Catal., A* **2009**, 358, (2), 110-118.
121. Liu, D.; Quek, X. Y.; Cheo, W. N. E.; Lau, R.; Borgna, A.; Yang, Y. *J. Catal.* **2009**, 266, (2), 380-390.
122. Yang, Y.; Lim, S.; Du, G.; Chen, Y.; Ciuparu, D.; Haller, G. L. *J. Phys. Chem. B* **2005**, 109, (27), 13237-13246.
123. Antonakou, E.; Lappas, A.; Nilsen, M. H.; Bouzga, A.; Stöcker, M. *Fuel* **2006**, 85, (14), 2202-2212.
124. Kosslick, H.; Lischke, G.; Parlitz, B.; Storek, W.; Fricke, R. *Appl. Catal., A* **1999**, 184, (1), 49-60.
125. Mokaya, R. *Chem. Commun.* **1997**, (22), 2185-2186.
126. Junges, U.; Jacobs, W.; Voigt-Martin, I.; Krutzsch, B.; Schüth, F. *J. Chem. Soc., Chem. Commun.* **1995**, (22), 2283-2284.
127. Aramendía, M. Á.; Borau, V.; Jiménez, C.; Marinas, J. M.; Romero, F. J. *Chem. Commun.* **1999**, (10), 873-874.
128. Yao, N.; Pinckney, C.; Lim, S.; Pak, C.; Haller, G. L. *Microporous Mesoporous Mater.* **2001**, 44, 377-384.
129. Wakayama, H.; Setoyama, N.; Fukushima, Y. *Adv. Mater.* **2003**, 15, (9), 742-745.
130. Dhepe, P. L.; Fukuoka, A.; Ichikawa, M. *Chem. Commun.* **2003**, (5), 590-591.
131. Yang, C.-m.; Liu, P.-h.; Ho, Y.-f.; Chiu, C.-y.; Chao, K.-j. *Chem. Mater.* **2003**, 15, (1), 275-280.
132. Yang, C.-m.; Kalwei, M.; Schüth, F.; Chao, K.-j. *Appl. Catal., A* **2003**, 254, (2), 289-296.
133. Yamamoto, T.; Shido, T.; Inagaki, S.; Fukushima, Y.; Ichikawa, M. *J. Am. Chem. Soc.* **1996**, 118, (24), 5810-5811.
134. Yamamoto, T.; Shido, T.; Inagaki, S.; Fukushima, Y.; Ichikawa, M. *J. Phys. Chem. B* **1998**, 102, (20),

3866-3875.
135. Zhou, W.; Thomas, J. M.; Shephard, D. S.; Johnson, B. F.; Ozkaya, D.; Maschmeyer, T.; Bell, R. G.; Ge, Q. *Science* **1998**, 280, (5364), 705-708.
136. Shephard, D. S.; Maschmeyer, T.; Sankar, G.; Thomas, J. M.; Ozkaya, D.; Johnson, B. F.; Raja, R.; Oldroyd, R. D.; Bell, R. G. *Chem. Eur. J.***1998**, 4, (7), 1214-1224.
137. Raja, R.; Khimyak, T.; Thomas, J. M.; Hermans, S.; Johnson, B. F. *Angew. Chem. Int. Ed.* **2001**, 40, (24), 4638-4642.
138. Mehnert, C. P. *Chem. Commun.* **1997**, (22), 2215-2216.
139. Mehnert, C. P.; Weaver, D. W.; Ying, J. Y. *J. Am. Chem. Soc.* **1998**, 120, (47), 12289-12296.
140. Okumura, M.; Tsubota, S.; Iwamoto, M.; Haruta, M. *Chem. Lett.* **1998**, (4), 315-316.
141. Junges, U.; Schüth, F.; Schmid, G.; Uchida, Y.; Schlögl, R. *Ber. Bunsen-Ges. Phys. Chem.* **1997**, 101, (11), 1631-1634.
142. Velu, S.; Kapoor, M.; Inagaki, S.; Suzuki, K. *Appl. Catal., A* **2003**, 245, (2), 317-331.
143. Anwander, R. *Chem. Mater.* **2001**, 13, (12), 4419-4438.
144. Tahmassebi, D. C.; Sasaki, T. *J. Org. Chem* **1994**, 59, (3), 679-681.
145. Hwang, K.-O.; Yakura, Y.; Ohuchi, F. S.; Sasaki, T. *Mater. Sci. Eng. C* **1995**, 3, (2), 137-141.
146. Shin, Y.; Liu, J.; Wang, L. Q.; Nie, Z.; Samuels, W. D.; Fryxell, G. E.; Exarhos, G. J. *Angew. Chem.* **2000**, 112, (15), 2814-2819.
147. Hicks, J. C.; Dabestani, R.; Buchanan, A.; Jones, C. W. *Inorg. Chim. Acta* **2008**, 361, (11), 3024-3032.
148. Basset, J.-M.; Psaro, R.; Roberto, D.; Ugo, R., *Modern surface organometallic chemistry*. John Wiley & Sons: **2009**.
149. Basset, J.; Candy, J.; Choplin, A.; Nedez, C.; Quignard, F.; Santini, C.; Theolier, A. *Mater. Chem. Phys.* **1991**, 29, (1), 5-32.
150. Basset, J.-M.; Lefebvre, F.; Santini, C. *Coord. Chem. Rev.* **1998**, 178, 1703-1723.
151. Copéret, C.; Chabanas, M.; Petroff Saint-Arroman, R.; Basset, J. M. *Angew. Chem. Int. Ed.* **2003**, 42, (2), 156-181.
152. Ryndin, Y. A.; Yermakov, Y. I.; Basset, J., *Surface organometallic chemistry molecular approaches to surface catalysis*. Kluwer, Edition: **1988**.
153. Abry, S.; Lux, F.; Albela, B.; Artigas-Miquel, A.; Nicolas, S.; Jarry, B.; Perriat, P.; Lemercier, G.; Bonneviot, L. *Chem. Mater.* **2009**, 21, (12), 2349-2359.
154. Abry, S.; Albela, B.; Bonneviot, L. *C. R. Chim.* **2005**, 8, (3), 741-752.
155. Calmettes, S.; Albela, B.; Hamelin, O.; Menage, S.; Miomandre, F.; Bonneviot, L. *New J. Chem.* **2008**, 32, (4), 727-737.
156. Zhao, X. S.; Lu, G.; Millar, G. J. *Ind. Eng. Chem. Res.* **1996**, 35, (7), 2075-2090.
157. Giraldo, L.; López, B.; Pérez, L.; Urrego, S.; Sierra, L.; Mesa, M. *Mesoporous silica applications*, Macromolecular symposia, **2007**; Wiley Online Library: pp 129-141.
158. Perego, C.; Millini, R. *Chem. Soc. Rev.* 2013, 42, (9), 3956-3976.
159. Zhao, L.; Qin, H.; Wu, R. a.; Zou, H. *J. Chromatogr. A* **2012**, 1228, 193-204.
160. Goubert-Renaudin, S.; Moreau, M.; Despas, C.; Meyer, M.; Denat, F.; Lebeau, B.; Walcarius, A. *Electroanalysis* **2009**, 21, (15), 1731-1742.
161. Kim, M.; Stripeikis, J.; Tudino, M. *Spectrochim. Acta B* **2009**, 64, (6), 500-505.

162. Wu, Y.; Zhu, X.; Du, Z., *New Trends in Fluid Mechanics Research*, Springer: **2007**; pp 467-470.
163. Yousefi, S. R.; Shemirani, F.; Jamali, M. R.; Salavati-Niasari, M. *Microchimica Acta* **2010**, 169, (3-4), 241-248.
164. Hu, W.; Zheng, F.; Hu, B. *J. Hazard. Mater.* **2008**, 151, (1), 58-64.
165. Jamali, M. R.; Assadi, Y.; Shemirani, F.; Salavati-Niasari, M. *Talanta* **2007**, 71, (4), 1524-1529.
166. Pérez-Quintanilla, D.; Sánchez, A.; del Hierro, I.; Fajardo, M.; Sierra, I. *J. Hazard. Mater.* **2009**, 166, (2), 1449-1458.
167. Pérez-Quintanilla, D.; del Hierro, I.; Fajardo, M.; Sierra, I. *J. Mater. Chem.* **2006**, 16, (18), 1757-1764.
168. Chen, D.; Hu, B.; Huang, C. *Talanta* **2009**, 78, (2), 491-497.
169. Yousefi, S. R.; Ahmadi, S. J.; Shemirani, F.; Jamali, M. R.; Salavati-Niasari, M. *Talanta* **2009**, 80, (1), 212-217.
170. Huang, C.; Hu, B.; Jiang, Z. *Spectrochim. Acta B* **2007**, 62, (5), 454-460.
171. Chen, D.; Huang, C.; He, M.; Hu, B. *J. Hazard. Mater.* **2009**, 164, (2), 1146-1151.
172. Hajiaghababaei, L.; Badiei, A.; Ganjali, M. R.; Heydari, S.; Khaniani, Y.; Ziarani, G. M. *Desalination* **2011**, 266, (1), 182-187.
173. Kamarudin, K. S. N.; Alias, N. *Fuel Process. Technol.* **2013**, 106, 332-337.
174. Knöfel, C.; Descarpentries, J.; Benzaouia, A.; Zeleňák, V.; Mornet, S.; Llewellyn, P.; Hornebecq, V. *Microporous Mesoporous Mater.* **2007**, 99, (1), 79-85.
175. LIU, Z.-l.; Yang, T.; ZHANG, K.; Yan, C.; PAN, W.-p. *J. Fuel Chem. Tech.* **2013**, 41, (4), 469-475.
176. Xu, X.; Song, C.; Andresen, J. M.; Miller, B. G.; Scaroni, A. W. *Energy & Fuels* **2002**, 16, (6), 1463-1469.
177. Park, S.-J.; Lee, S.-Y. *J. Colloid Interface Sci.* **2010**, 346, (1), 194-198.
178. Ramachandran, S.; Ha, J.-H.; Kim, D. K. *Catal. Commun.* **2007**, 8, (12), 1934-1938.
179. Zheng, S.; Fang, F.; Zhou, G.; Chen, G.; Ouyang, L.; Zhu, M.; Sun, D. *Chem. Mater.* **2008**, 20, (12), 3954-3958.
180. Wagner, T.; Haffer, S.; Weinberger, C.; Klaus, D.; Tiemann, M. *Chem. Soc. Rev.* **2013**, 42, (9), 4036-4053.
181. Asefa, T.; Duncan, C. T.; Sharma, K. K. *Analyst* **2009**, 134, (10), 1980-1990.
182. Martínez-Máñez, R.; Sancenón, F.; Hecht, M.; Biyikal, M.; Rurack, K. *Anal. Bioanal. Chem* **2011**, 399, (1), 55-74.
183. Dhanekar, S.; Jain, S. *Biosens. Bioelectron.* **2013**, 41, 54-64.
184. Hasanzadeh, M.; Shadjou, N.; Eskandani, M.; de la Guardia, M. *TrAC, Trends Anal. Chem.* **2012**, 40, 106-118.
185. Mamaeva, V.; Sahlgren, C.; Lindén, M. *Adv. Drug Deliv. Rev.* **2013**, 65, (5), 689-702.
186. Tang, F.; Li, L.; Chen, D. *Adv. Mater.* **2012**, 24, (12), 1504-1534.
187. Argyo, C.; Weiss, V.; Bräuchle, C.; Bein, T. *Chem. Mater.* **2013**, 26, (1), 435-451.
188. Zhou, Z.; Hartmann, M. *Chem. Soc. Rev.* **2013**, 42, (9), 3894-3912.
189. Slowing, I. I.; Trewyn, B. G.; Giri, S.; Lin, V. Y. *Adv. Funct. Mater.* **2007**, 17, (8), 1225-1236.
190. Rehder, D., *Bioinorganic vanadium chemistry*. John Wiley & Sons: **2008**; Vol. 30.
191. Moskalyk, R.; Alfantazi, A. *Miner. Eng.* **2003**, 16, (9), 793-805.
192. Weckhuysen, B. M.; Keller, D. E. *Catal. Today* **2003**, 78, (1), 25-46.
193. Sutradhar, M.; Martins, L. M.; da Silva, M. F. C. G.; Pombeiro, A. J. *Coord. Chem. Rev.* **2015**, 301, 200-239.

194. Ligtenbarg, A. G.; Hage, R.; Feringa, B. L. *Coord. Chem. Rev.* **2003**, 237, (1), 89-101.
195. Wachs, I. E.; Weckhuysen, B. M. *Appl. Catal., A* **1997**, 157, (1), 67-90.
196. Bond, G. C.; Tahir, S. F. *Appl. Catal.* **1991**, 71, (1), 1-31.
197. Haber, J. *Crit. Rev. Surf. Chem.***1994**, 4, (3/4), 141-187.
198. Ertl, G.; Knozinger, H.; Weitkamp, J., *Handbook of heterogeneous catalysis*. VCH: **1997**.
199. Muhler, M. *Ber. Bunsen-Ges. Phys. Chem* **1997**, 101, (10), 1560-1560.
200. Hagen, J. *Industrial Catalysis: A Practical Approach* **1999**, 99-210.
201. Rase, H. F., *Handbook of commercial catalysts: heterogeneous catalysts*. CRC press: **2000**.
202. Silbernagel, B. *J. Catal.* **1979**, 56, (3), 315-320.
203. Busca, G.; Cavani, F.; Trifirò, F. *J. Catal.* **1987**, 106, (2), 471-482.
204. Zhu, J.; Andersson, S. L. T. *J. Chem. Soc. Faraday Trans.* **1989**, 85, (11), 3629-3644.
205. Zhu, J.; Rebenstorf, B.; Andersson, S. L. T. *J. Chem. Soc. Faraday Trans.* **1989**, 85, (11), 3645-3662.
206. Spencer, N. D.; Pereira, C. J. *J. Catal.* **1989**, 116, (2), 399-406.
207. Nakamura, M.; Kawai, K.; Fujiwara, Y. *J. Catal.* **1974**, 34, (3), 345-355.
208. Murakami, Y.; Niwa, M.; Hattori, T.; Osawa, S.-i.; Igushi, I.; Ando, H. *J. Catal.* **1977**, 49, (1), 83-91.
209. Agarwal, D.; Nigam, P.; Srivastava, R. *J. Catal.* **1978**, 55, (1), 1-9.
210. Mori, K.; Miyamoto, A.; Murakami, Y. *J. Catal.* **1985**, 95, (2), 482-491.
211. Wokaun, A.; Schraml, M.; Baiker, A. *J. Catal.* **1989**, 116, (2), 595-599.
212. Amiridis, M. D.; Wachs, I. E.; Deo, G.; Jehng, J.-M. *J. Catal.* **1996**, 161, (1), 247-253.
213. Michalakos, P.; Birkeland, K.; Kung, H. H. *J. Catal.* **1996**, 158, (1), 349-353.
214. Vuurman, M. A.; Stufkens, D. J.; Oskam, A.; Deo, G.; Wachs, I. E. *J. Chem. Soc., Faraday Trans.* **1996**, 92, (17), 3259-3265.
215. Jehng, J.-M.; Deo, G.; Weckhuysen, B. M.; Wachs, I. E. *J. Mol. Catal. A: Chem.* **1996**, 110, (1), 41-54.
216. Marshneva, V.; Slavinskaya, E.; Kalinkina, O.; Odegova, G.; Moroz, E.; Lavrova, G.; Salanov, A. *J. Catal.* **1995**, 155, (2), 171-183.
217. Inumaru, K.; Okuhara, T.; Misono, M. *J. Phys. Chem.* **1991**, 95, (12), 4826-4832.
218. Inumaru, K.; Misono, M.; Okuhara, T. *Appl. Catal., A* **1997**, 149, (1), 133-149.
219. Centi, G.; Pinelli, D.; Trifiro, F.; Ghoussoub, D.; Guelton, M.; Gengembre, L. *J. Catal.* **1991**, 130, (1), 238-256.
220. Keränen, J.; Auroux, A.; Ek, S.; Niinistö, L. *Appl. Catal., A* **2002**, 228, (1), 213-225.
221. Centi, G.; Giamello, E.; Pinelli, D.; Trifiro, F. *J. Catal.* **1991**, 130, (1), 220-237.
222. Bulushev, D.; Kiwi-Minsker, L.; Renken, A. *Catal. Today* **2000**, 57, (3), 231-239.
223. Haber, J. *Catal. Today* **2009**, 142, (3), 100-113.
224. Machej, T.; Haber, J.; Turek, A. M.; Wachs, I. E. *Appl. Catal.* **1991**, 70, (1), 115-128.
225. Nalwa, H. S., *Handbook of Surfaces and Interfaces of Materials: Surface and interface phenomena*. Academic Press: **200**1; Vol. 1.
226. Weckhuysen, B. M.; Jehng, J.-M.; Wachs, I. E. *J. Phys. Chem. B* **2000**, 104, (31), 7382-7387.
227. Weckhuysen, B.; Wachs, I.; Deo, G.; Andreini, A.; Vuurman, M. A.; Boer, M. d.; Amiridis, M. D. J. *Catal.* **1996**, 161, 211-221.
228. Wachs, I. E.; Jehng, J.-M.; Deo, G.; Weckhuysen, B. M.; Guliants, V. V.; Benziger, J. B. *Catal. Today* **1996**, 32, (1), 47-55.
229. Wachs, I. E.; Jehng, J.-M.; Deo, G.; Weckhuysen, B. M.; Guliants, V.; Benziger, J.; Sundaresan, S. *J. Catal.* **1997**, 170, (1), 75-88.

230. Wachs, I. E.; Deo, G.; Juskelis, M. V.; Weckhuysen, B. M. *Stud. Surf. Sci. Catal.* **1997**, 109, 305-314.
231. Deo, G.; Wachs, I. E. *J. Catal.* **1994**, 146, (2), 323-334.
232. Weckhuysen, B. M., *Spectroscopy of transition metal ions on surfaces*. Leuven University Press: **2000**.
233. Meynen, V.; Cool, P.; Vansant, E. *Microporous Mesoporous Mater.* **2009**, 125, (3), 170-223.
234. Balkus, K. J.; Khanmamedova, A. K.; Dixon, K. M.; Bedioui, F. *Appl. Catal., A* **1996**, 143, (1), 159-173.
235. Kozlov, A.; Asakura, K.; Iwasawa, Y. *Microporous Mesoporous Mater.* **1998**, 21, (4), 571-579.
236. Joseph, T.; Srinivas, D.; Gopinath, C.; Halligudi, S. *Catal. Lett.* **2002**, 83, (3-4), 209-214.
237. de Azevedo Marques, A. P.; Dockal, E. R.; Skrobot, F. C.; Rosa, I. L. V. *Inorg. Chem. Commun.* **2007**, 10, (3), 255-261.
238. Parida, K.; Singha, S.; Sahoo, P. *J. Mol. Catal. A: Chem.* **2010**, 325, (1), 40-47.
239. Brunauer, S.; Emmett, P. H.; Teller, E. *J. Am. Chem. Soc.* **1938**, 60, (2), 309-319.
240. Barrett, E. P.; Joyner, L. G.; Halenda, P. P. *J. Am. Chem. Soc.* **1951**, 73, (1), 373-380.
241. Deschner, T.; Lønstad, B.-T.; Widenmeyer, M.; Anwander, R. *J. Mater. Chem.* **2011**, 21, (15), 5620-5628.
242. Gregg, S. J.; Sing, K. S. W.; Salzberg, H. *J. Electrochem. Soc.* **1967**, 114, (11), 279C-279C.
243. Leofanti, G.; Padovan, M.; Tozzola, G.; Venturelli, B. *Catal. Today* **1998**, 41, (1), 207-219.
244. Fernandes, T. A.; Nunes, C. D.; Vaz, P. D.; Calhorda, M. J.; Brandao, P.; Rocha, J.; Gonçalves, I. S.; Valente, A. A.; Ferreira, L. P.; Godinho, M. *Microporous Mesoporous Mater.* **2008**, 112, (1), 14-25.
245. Joseph, T.; Hartmann, M.; Ernst, S.; Halligudi, S. *J. Mol. Catal. A: Chem.* **2004**, 207, (2), 131-137.
246. Parvulescu, V.; Anastasescu, C.; Su, B. *J. Mol. Catal. A: Chem.* **2003**, 198, (1), 249-261.
247. Zhao, X.; Lu, G.; Whittaker, A.; Millar, G.; Zhu, H. *J. Phys. Chem. B* **1997**, 101, (33), 6525-6531.
248. Ishikawa, H.; Kikuchi, T. *J. Mater. Chem.* **1998**, 8, (8), 1783-1786.
249. Wang, L.-z.; Shi, J.-l.; Tang, F.-q.; Yu, J.; Ruan, M.-L.; Yan, D.-s. *J. Mater. Chem.* **1999**, 9, (3), 643-645.
250. Shio, S.; Kimura, A.; Yamaguchi, M.; Yoshida, K.; Kuroda, K. *Chem. Commun.* **1998**, (22), 2461-2462.
251. Singh, P. S.; Kosuge, K. *Chem. Lett.* **1998**, (1), 101-102.
252. Huo, Q.; Feng, J.; Schüth, F.; Stucky, G. D. *Chem. Mater.* **1997**, 9, (1), 14-17.
253. Qi, L.; Ma, J.; Cheng, H.; Zhao, Z. *Chem. Mater.* **1998**, 10, (6), 1623-1626.
254. Ogawa, M. *J. Am. Chem. Soc.* **1994**, 116, (17), 7941-7942.
255. Yang, H.; Kuperman, A.; Coombs, N.; Mamiche-Afara, S.; Ozin, G. A. *Nature* **1996**, 379, (6567), 703-705.
256. Lin, H.-P.; Cheng, Y.-R.; Mou, C.-Y. *Chem. Mater.* **1998**, 10, (12), 3772-3776.
257. Lin, H.-P.; Cheng, S.; Mou, C.-Y. *Chem. Mater.* **1998**, 10, (2), 581-589.
258. Lin, H.-P.; Liu, S.-B.; Mou, C.-Y.; Tang, C.-Y. *Chem. Commun.* **1999**, (7), 583-584.
259. Selvam, P.; Bhatia, S. K.; Sonwane, C. G. *Ind. Eng. Chem. Res.* **2001**, 40, (15), 3237-3261.
260. Williams, D. B.; Carter, C. B., *Transmission electron microscopy*, Springer: **1996**; pp 3-17.
261. Zhang, K.; Xu, L.-L.; Jiang, J.-G.; Calin, N.; Lam, K.-F.; Zhang, S.-J.; Wu, H.-H.; Wu, G.-D.; Albela, B. l.; Bonneviot, L. *J. Am. Chem. Soc.* **2013**, 135, (7), 2427-2430.
262. Eckert, H.; Wachs, I. E. *The Journal of Physical Chemistry* **1989**, 93, (18), 6796-6805.
263. Lapina, O.; Mastikhin, V.; Shubin, A.; Krasilnikov, V.; Zamaraev, K. *Prog. Nucl. Magn. Reson. Spectrosc.* **1992**, 24, (6), 457-525.

264. Lapina, O.; Mastikhin, V.; Simonova, L.; Bulgakova, Y. O. *J. Mol. Catal.* **1991**, 69, (1), 61-73.
265. Sobalik, Z.; Markvart, M.; Stopka, P.; Lapina, O.; Mastikhin, V. *J. Mol. Catal.* **1992**, 71, (1), 69-79.
266. Maurya, M. R.; Kumar, A.; Pessoa, J. C. *Coord. Chem. Rev.* **2011**, 255, (19), 2315-2344.
267. Wang, Y.; Lee, K.-Y.; Choi, S.; Liu, J.; Wang, L.-Q.; Peden, C. H. *Green Chem.* **2007**, 9, (6), 540-544.
268. Bobadilla, L. F.; Blasco, T.; Odriozola, J. A. *PCCP* **2013**, 15, (39), 16927-16934.
269. Shimojima, A.; Umeda, N.; Kuroda, K. *Chem. Mater.* **2001**, 13, (10), 3610-3616.
270. Luan, Z.; Cheng, C.-F.; Zhou, W.; Klinowski, J. *J. Phys. Chem.* **1995**, 99, (3), 1018-1024.
271. Lewandowska, A.; Banares, M.; Khabibulin, D.; Lapina, O. *J. Phys. Chem. C* **2009**, 113, (48), 20648-20656.
272. MadhusudanáReddy, K. *J. Chem. Soc., Chem. Commun.* **1994**, (9), 1059-1060.
273. Busca, G.; Elmi, A. S.; Forzatti, P. *J. Phys. Chem.* **1987**, 91, (20), 5263-5269.
274. Busca, G. *J. Mol. Catal.* **1989**, 50, (2), 241-249.
275. Elmi, A. S.; Tronconi, E.; Cristiani, C.; Gomez Martin, J. P.; Forzatti, P.; Busca, G. *Ind. Eng. Chem. Res.* **1989**, 28, (4), 387-393.
276. Sanchez Escribano, V.; Busca, G.; Lorenzelli, V. *J. Phys. Chem.* **1990**, 94, (26), 8939-8945.
277. Sanchez Escribano, V.; Busca, G.; Lorenzelli, V. *J. Phys. Chem.* **1990**, 94, (26), 8945-8950.
278. Sanchez Escribano, V.; Busca, G.; Lorenzelli, V. *J. Phys. Chem.* **1991**, 95, (14), 5541-5545.
279. BUSCA, G. *Preprints- American Chemical Society. Division of Petroleum Chemistry* **1992**, 37, (4), 1054-1061.
280. Miyata, H.; Nakagawa, Y.; Ono, T.; Kubokawa, Y. *Chem. Lett.* **1983**, 12, (8), 1141-1144.
281. Miyata, H.; Fujii, K.; Ono, T. *J. Chem. Soc. Faraday Trans.* **1988**, 84, (9), 3121-3128.
282. Turek, A. M.; Wachs, I. E.; DeCanio, E. *J. Phys. Chem.* **1992**, 96, (12), 5000-5007.
283. Parambadath, S.; Mathew, A.; Park, S. S.; Ha, C.-S. *J. Environ. Chem. Eng.* **2015**, 3, (3), 1918-1927.
284. Anpo, M.; Sunamoto, M.; Che, M. *J. Phys. Chem.* **1989**, 93, (4), 1187-1189.
285. Iwamoto, M.; Furukawa, H.; Matsukami, K.; Takenaka, T.; Kagawa, S. *J. Am. Chem. Soc.* **1983**, 105, (11), 3719-3720.
286. Hazenkamp, M.; Blasse, G. *J. Phys. Chem.* **1992**, 96, (8), 3442-3446.
287. Fournier, M.; Louis, C.; Che, M.; Chaquin, P.; Masure, D. *J. Catal.* **1989**, 119, (2), 400-414.
288. Masure, D.; Chaquin, P.; Louis, C.; Che, M.; Fournier, M. *J. Catal.* **1989**, 119, (2), 415-425.
289. Gao, X.; Bare, S. R.; Weckhuysen, B. M.; Wachs, I. E. *J. Phys. Chem. B* **1998**, 102, (52), 10842-10852.
290. Gao, X.; Bañares, M. A.; Wachs, I. E. *J. Catal.* **1999**, 188, (2), 325-331.
291. Gao, X.; Wachs, I. E. *J. Phys. Chem. B* **2000**, 104, (6), 1261-1268.
292. Gao, X.; Jehng, J.-M.; Wachs, I. E. *J. Catal.* **2002**, 209, (1), 43-50.
293. Schraml-Marth, M.; Wokaun, A.; Pohl, M.; Krauss, H.-L. *J. Chem. Soc., Faraday Trans.* **1991**, 87, (16), 2635-2646.
294. Catana, G.; Rao, R. R.; Weckhuysen, B. M.; Van Der Voort, P.; Vansant, E.; Schoonheydt, R. A. *J. Phys. Chem. B* **1998**, 102, (41), 8005-8012.
295. Baltes, M.; Collart, O.; Van Der Voort, P.; Vansant, E. *Langmuir* **1999**, 15, (18), 5841-5845.
296. Baltes, M.; Van Der Voort, P.; Weckhuysen, B. M.; Rao, R. R.; Catana, G.; Schoonheydt, R. A.; Vansant, E. F. *PCCP* **2000**, 2, (11), 2673-2680.
297. Argyle, M. D.; Chen, K.; Resini, C.; Krebs, C.; Bell, A. T.; Iglesia, E. *J. Phys. Chem. B* **2004**, 108, (7), 2345-2353.
298. Chen, K.; Bell, A. T.; Iglesia, E. *J. Phys. Chem. B* **2000**, 104, (6), 1292-1299.

299. Olthof, B.; Khodakov, A.; Bell, A. T.; Iglesia, E. *J. Phys. Chem. B* **2000**, 104, (7), 1516-1528.
300. Tian, H.; Ross, E. I.; Wachs, I. E. *J. Phys. Chem. B* **2006**, 110, (19), 9593-9600.
301. Griffith, W.; Wickins, T. *J. Chem. Soc. A* **1966**, 1087-1090.
302. Griffith, W. *J. Chem. Soc. A* **1967**, 905-908.
303. Griffith, W.; Lesniak, P. *J. Chem. Soc. A* **1969**, 1066-1071.
304. Brown, R.; Ross, S. *Spectrochim. Acta Mol. Biomol. Spectrosc.* **1972**, 28, (7), 1263-1274.
305. Botto, I. L.; Baran, E. J.; Pedregosa, J. C.; Aymonino, P. J. *Monatsh. Chem.* **1979**, 110, (4), 895-898.
306. Onodera, S.; Ikegami, Y. *Inorg. Chem.* **1980**, 19, (3), 615-618.
307. Deo, G.; Hardcastle, F.; Richards, M.; Hirt, A.; Wachs, I. E. *Novel materials in heterogeneous catalysis* **1990**, 437, 317.
308. Deo, G.; Hardcastle, F.; Richards, M.; Wachs, I. *Prepr. - Am. Chem. Soc., Div. Pet. Chem.* **1989**, 34, (3), 529-534.
309. Hardcastle, F. D.; Wachs, I. E. *J. Phys. Chem.* **1991**, 95, (13), 5031-5041.
310. Stair, P. C.; Li, C. *J. Vac. Sci. Technol.* **1997**, 15, (3), 1679-1684.
311. Xiong, G.; Li, C.; Feng, Z.; Ying, P.; Xin, Q.; Liu, J. *J. Catal.* **1999**, 186, (1), 234-237.
312. Chao, K.; Wu, C.; Chang, H.; Lee, L.; Hu, S.-f. *J. Phys. Chem.B* **1997**, 101, (33), 6341-6349.
313. Luan, Z.; Meloni, P. A.; Czernuszewicz, R. S.; Kevan, L. *J. Phys. Chem. B* **1997**, 101, (44), 9046-9051.
314. Xiong, G.; Li, C.; Li, H.; Xin, Q.; Feng, Z. *Chem. Commun.* **2000**, (8), 677-678.
315. Busca, G.; Giamello, E. *Mater. Chem. Phys.* **1990**, 25, (5), 475-485.
316. Busca, G.; Centi, G.; Marchetti, L.; Trifiro, F. *Langmuir* **1986**, 2, (5), 568-577.
317. Che, M.; Védrine, J. C., *Characterization of solid materials and heterogeneous catalysts: From structure to surface reactivity*. John Wiley & Sons: **2012**.
318. Falkner, R.; Stephan, H.; Vogler, J. *Global Policy* **2010**, 1, (3), 252-262.
319. Parry, M.; Lowe, J.; Hanson, C. *Nature* **2009**, 458, (7242), 1102-1103.
320. Huber, G. W.; Iborra, S.; Corma, A. *Chem. Rev.* **2006**, 106, (9), 4044-4098.
321. Alonso, D. M.; Wettstein, S. G.; Dumesic, J. A. *Chem. Soc. Rev.* **2012**, 41, (24), 8075-8098.
322. Brosse, N.; Mohamad Ibrahim, M. N.; Abdul Rahim, A. *ISRN Materials Science* **2011**, 2011.
323. Hanson, S. K.; Baker, R. T.; Gordon, J. C.; Scott, B. L.; Thorn, D. L. *Inorg. Chem.* **2010**, 49, (12), 5611-5618.
324. Sedai, B.; Díaz-Urrutia, C.; Baker, R. T.; Wu, R.; Silks, L. P.; Hanson, S. K. *ACS Catal.* **2011**, 1, (7), 794-804.
325. Sedai, B.; Díaz-Urrutia, C.; Baker, R. T.; Wu, R.; Silks, L. P.; Hanson, S. K. *ACS Catal.* **2013**, 3, (12), 3111-3122.
326. Díaz-Urrutia, C.; Hurisso, B. B.; Gauthier, P. M.; Sedai, B.; Singer, R. D.; Baker, R. T. *J. Mol. Catal. A: Chem.* **2016**, 423, 414-422.
327. Zakzeski, J.; Bruijnincx, P. C.; Jongerius, A. L.; Weckhuysen, B. M. *Chem. Rev.* **2010**, 110, (6), 3552-3599.
328. Sedai, B.; Baker, R. T. *Adv. Synth. Catal.* **2014**, 356, (17), 3563-3574.
329. Napoly, F.; Jean-Gérard, L.; Goux-Henry, C.; Draye, M.; Andrioletti, B. *Eur. J. Org. Chem.* 2014, **2014**, (4), 781-787.
330. Mottweiler, J.; Puche, M.; Räuber, C.; Schmidt, T.; Concepción, P.; Corma, A.; Bolm, C. *ChemSusChem* **2015**, 8, (12), 2106-2113.
331. Portjanskaja, E.; Stepanova, K.; Klauson, D.; Preis, S. *Catal. Today* **2009**, 144, (1), 26-30.

332. Ma, Y.-S.; Chang, C.-N.; Chiang, Y.-P.; Sung, H.-F.; Chao, A. C. *Chemosphere* **2008**, 71, (5), 998-1004.
333. Portjanskaja, E.; Preis, S. *J. Photoenergy* **2007**.
334. Amadio, E.; Di Lorenzo, R.; Zonta, C.; Licini, G. *Coord. Chem. Rev.* **2015**, 301, 147-162.
335. Hanson, S. K.; Baker, R. T.; Gordon, J. C.; Scott, B. L.; Sutton, A. D.; Thorn, D. L. *J. Am. Chem. Soc.* **2008**, 131, (2), 428-429.
336. Díaz-Urrutia, C.; Chen, W.-C.; Crites, C.-O.; Daccache, J.; Korobkov, I.; Baker, R. T. *RSC Adv.* **2015**, 5, (86), 70502-70511.
337. Behling, R.; Valange, S.; Chatel, G. *Green Chem.* 2016, 18, (7), 1839-1854.

Chapter 3. Chemicals and characterization methods

3.1 Commercial products

3.1.1 Solvents

Table 1. Solvents utilized in this study

Solvent	**Purity**	**Provider**	**CAS**
Ethanol	96 % v/v	Sigma-Aldrich	64-17-5
Ethanol	> 99.8 %	Sigma-Aldrich	64-17-5
Acetone	99.5 %	Sigma-Aldrich	67-64-1
Cyclohexane	99.5 %	Sigma-Aldrich	110-82-7
Acetonitrile	99.8 %	Sigma-Aldrich	75-05-8
Chloroform	> 99 %	Sigma-Aldrich	67-66-3
Benzene	99.8 %	Sigma-Aldrich	71-43-2
Ethyl acetate	99.8 %	Sigma-Aldrich	141-78-6
Toluene	99.8 %	Sigma-Aldrich	108-88-3
CH_2Cl_2	99.8 %	Sigma-Aldrich	75-09-2
Dioxane	99.8 %	Sigma-Aldrich	123-91-1
Tetrahydrofuran	99.9 %	Sigma-Aldrich	109-99-9
Dimethyl sulfoxide	99.5%	Sigma	67-68-5
Pyridine	99.8 %	Sigma-Aldrich	110-86-1
Methanol	99.8 %	Sigma-Aldrich	67-56-1
Diethyl ether	> 99.7 %	Sigma-Aldrich	60-29-7
Deionized water	-	-	7732-18-5

3.1.2 Gases

Table 2. Gases utilized in this study

Gas	**Quality**	**Provider**	**Utilization**
Argon	α	Air Liquid	Protection gas for synthesis[a]
Nitrogen	U	Air Liquid	Working gas for equipment
Air	Industrial	Air Liquid	Working gas for equipment
Hydrogen	U	Air Liquid	Working gas for equipment

[a] Cartidge filtration multifunction: dehydration, deoxygenation, dehydrocarbon.

3.1.3 Reagents

Table 3. Reagents utilized in this study

Reagents	**Purity**	**Provider**	**CAS**
Ludox® HS-40 colloidal silica	40 wt % in H_2O	Sigma-Aldrich	7631-86-9
Sodium hydroxide	98 %	Acros	1310-73-2
Hexadecyltrimethylammonium p-toluenesulfonate (CTATos)	> 99 %	Sigma-Aldrich	138-32-9
Tetramethylammonium hydroxide (TMAOH)	25 wt % in H_2O	Alfa Aesar	75-59-2
Tetraethyl orthosilicate (TEOS)	98 %	Sigma-Aldrich	78-10-4
Tetramethylammonium bromide (TMABr)	98 %	Alfa Aesar	64-20-0
Hydrochloric acid in water (HCl)	1 N	Acros	7647-01-1
Titanium (IV) n-butoxide (TBOT)	> 99 %	Alfa Aesar	5593-70-4
Titanium(IV) isopropoxide	> 98 %	Acros Organics	546-68-9
Vanadium (IV) sulfate oxide hydrate	99.9 %	Alfa Aesar	123334-20-3
Vanadium (V) triisopropoxide	96 %	Alfa Aesar	5588-84-1
Zirconium n-butoxide	80 % w/w in 1-butanol	Alfa Aesar	1071-76-7
Zirconium(IV) oxynitrate hydrate	99.9 %	Alfa Aesar	14985-18-3

Cerium(III) acetylacetonate hydrate	> 99 %	Sigma-Aldrich	206996-61-4
Ammonium cerium(IV) nitrate	> 99.99 %	Alfa Aesar	16774-21-3
Aluminum sulfate hydrate	98 %	Sigma-Aldrich	17927-65-0
Red-Al® sodium bis(2-methoxyethoxy)aluminum hydride solution	(~60 wt% in toluene	Sigma-Aldrich	22722-98-1
2,2,5,5-tetramethyl-2,5-disila-1-azacyclopentane (TMDSACP)	97 %	ABCR	7418-19-1
Hexamethyldisilazane (HMDSA)	> 99 %	Sigma-Aldrich	999-97-3
Benzyl Alcohol	99 %	Alfa Aesar	100-51-6
Methyl benzoate	99 %	Alfa Aesar	93-58-3
Benzoin methyl ether	97 %	Alfa Aesar	3524-62-7
Pinacol	99 %	Alfa Aesar	76-09-5
Meso-hydrobenzoin	99 %	Sigma-Aldrich	579-43-1
2,2,6,6-Tetramethyl-1-piperidinyloxy (TEMPO)	98 %	Sigma-Aldrich	2564-83-2
Triethylamine (TEA)	> 99 %	Sigma-Aldrich	121-44-8
N-Ethyldiisopropylamine (EDPA)	> 98 %	Sigma-Aldrich	7087-68-5
Copper(II) nitrate trihydrate	99 %	Acros Organics	10031-43-3
Iron(III) nitrate nonahydrate	99 %	Acros Organics	7782-61-8
Sodium borohydride	> 96 %	Sigma-Aldrich	16940-66-2
Ammonium chloride	> 99.5 %	Sigma-Aldrich	12125-02-9
Mesitylene	> 99.8 %	Sigma-Aldrich	108-67-8

3.2 Characterization methods

XRD: Low angle X-ray powder diffraction analysis was carried out using a Bruker (Siemens) D5005 diffractometer with Cu Kα monochromatic radiation.

TGA: Thermogravimetric measurements were collected by using a DTA-TG Netzsch STA 409 PC/PG instrument. 5-10 mg sample powder was placed in a 70 μL alumina crucible then heated in air flow (40 mL/min) up to 1000 ^{o}C at a heating rate of 10 ^{o}C/min with N_2 as supporting gas (15 mL/min).

N_2 adsorption-desorption: Nitrogen adsorption-desorption isotherms were carried out at 77 K by a BELSORP max (BEL Japan, INC) instrument. Samples (~50 mg) without organic groups were pretreated at 130 ^{o}C in vacuum overnight for degassing, while samples with organic groups were pretreated at 80 ^{o}C in vacuum overnight for degassing.

FT-IR spectroscopy: Fourier transform infrared spectra were measured by a JASCO FT/IR-4200 spectrometer with ATR PRO470-H accessory.

UV-vis spectroscopy: Solid UV-visible spectra were measured by a JASCO V-670 spectrophotometer with the diffuse reflectance mode.

Raman spectroscopy: Unpolarized Raman spectra were excited by the 514.5 nm argon-ion laser with an objective of 100 times. The power was set at about 35 mW, and the hole was 100 μm. The acquisition time was set as 10 sec*6, and the grating was 600 gr/mm. The signals were recorded by the Horiba Jobin-Yvon Labram HR800 visible spectrometer in backscattering mode at room temperature.

NMR: Solid nuclear magnetic resonance spectra were measured by a Bruker AVANCE III 500 spectrometer at 99.362 MHz. Sample powder was put in a 4 mm

zirconia rotor and the spectra were recorded by magic angle spinning (MAS) at 5 kHz. Chemical shift was externally referred to tetramethylsilane (δ=0 ppm). The spinning rate of the rotor was about 5 kHz and the number of scans was 10000.

EPR: Electron paramagnetic resonance spectra were recorded by a Bruker Elexsys e500 X-band (9.4 GHz) spectrometer with a standard cavity.

TEM: Transmission electron microscopy images were taken by an FEI G2F30 Tecnai™ transmission electron microscope, the accelerating voltage was 300 kV, and the crystallographic image processing on HRTEM images was carried out with the CRISP program.

Elemental analysis: The elemental analysis was carried out by CREALINS laboratory (https://crealins.com/) with the ICP (Inductively Coupled Plasma) techniques on an instrument of ICP AES, ICAP model from Thermofisher Scientific.

GC: Gas chromatography analysis was carried out by Agilent Technologies 6850 Series II Network GC System. Column: Restek RTX-1, 30 m*320 μm*0.25 μm. Inlet: 50:1, 250 ^{o}C, 10.9 psi. Temperature program: 55 ^{o}C for 2 minutes, ramp (35 ^{o}C/min) to 150 ^{o}C and hold for 1 minute, then ramp (35 ^{o}C/min) to 200 ^{o}C and hold 1.25 minutes, finally ramp (35 ^{o}C/min) to 275 ^{o}C and hold for 3.25 minutes.

Chapter 4. One pot synthesis of vanadium containing MCM-41 with the assistance of microwave irradiation

4.1 Introduction

Microwave energy is used as an increasingly popular heating method in chemistry for organic synthesis, polymer synthesis, drug discovery, biochemical processes, material sciences and nanotechnology. Compared to the conductive heating methods, which are slow and inefficient, the microwave heating is fairly rapid and efficient. Though microwave heating is not conceptually straightforward, it can be turned on and off instantaneously, ramp-up to the appointed temperature is very efficiently and fine control over the bulk reaction temperature is feasible.[1]

Since Wu and Bein[2] reported the first microwave-assisted synthesis of mesoporous silica which took 80 minutes at 150 ^{o}C in 1996, more and more mesoporous materials such as SBA-15, FDU-1, PSU-1 have been successfully prepared by microwave hydrothermal methods, and better crystallization as well as higher yields can be now achieved in shorter times.[3]

Chaignon et al.[4] explored the ultra-fast gram scale synthesis of highly ordered MCM-41 with the assistance of microwave irradiation, they use the trimethylcetylammonium (CTA^{+}) template and inexpensive aqueous colloidal silica to synthesis hexagonal mesoporous silica. A fast temperature ramping (~1 min) and final temperatures above 180 ^{o}C were required to obtain high quality mesostructures. The synthesis procedure is time and energy saving, and the tosylate salts of the template can be conveniently recovered and recycled.

Incorporation of catalytic transition metal ions into high surface area porous silica as well as search for fast, clean and energy saving catalyst syntheses are highly desirable for practical large-scale applications in catalysis of oxidation.[5] Mesoporous silica MCM-41 was chosen in this study as a support for vanadium as it allows reactions of large molecules and provides good opportunities for high dispersion particularly with the help of some anchoring ions. Therefore, a large set of V-(Ti/Zr/Ce/Al)-MCM-41 catalysts were prepared according to an ultra-fast one-pot

synthesis protocol with the assistance of microwave. The structure and characterization of these one-pot microwave-assisted synthesized V-(Ti/Zr/Ce/Al)-MCM-41 catalysts will be discussed in this chapter.

4.2 Experiments

4.2.1 Preparation of mesoporous silica MWL[4]

32.0 g sodium hydroxide was dissolved in 800 mL deionized water, then 187 mL Ludox (40 wt%) were added into the above NaOH solution and closely stirred at 40 ^{o}C overnight (until clear) to prepare the Na_2SiO_3 solution. This Na_2SiO_3 solution can be stored in a sealed teflon bottle at room temperature for several weeks as long as it is clear.

3.92 g CTATos were dissolved in 142 mL deionized water and closely stirred (slowly to avoid too many bubbles) at 60 ^{o}C for 1 hour until the surfactant was dissolved completely to form a clear viscous solution. At the same time, 98 mL (105.22 g) above Na_2SiO_3 solution were stirred at 60 ^{o}C for 1 hour. Then added the CTATos solution was dropwise into the Na_2SiO_3 solution. The gel molar composition was: 1 SiO_2/ 0.05 CTATos/ 0.5 NaOH/ 80 H_2O. After 1 hour of vigorous stirring at 60 ^{o}C, this mixture was transferred into 6 teflon autoclaves (as the volume of each autoclave is 100 mL, the appropriate capacity should be 30~60 mL) and heated in the microwave oven. The program of the microwave oven was set as 1 minute to ramp up to 180 ^{o}C and heating at 180 ^{o}C for 9 minutes. After the heating program finished, the autoclaves were taken out and cooled to room temperature for 30 minutes and then in a water bath for half an hour. The solid was filtered on a Büchner funnel and washed with 1.5 L deionized water, then dried at 80 ^{o}C overnight to obtain an average of 5.8 g white powder which was named as-made MWL (Microwave synthesis with Ludox as silica source).

After calcination in a tube furnace with flowing air, the MCM-41 with mesoporous structure was prepared; this white powder was named MWL-cal. The calcination program was set as 2 ^{o}C/min to ramp up from room temperature to 550 ^{o}C, and heating at 550 ^{o}C for 6 hours, then cooled down in air.

Besides calcination, the surfactant can be removed by chemical extraction as well. 1 g of as-made MWL was stirred in 200 mL of technical ethanol (96 % v/v) with the addition of 2 mL HCl (1 M) for 1 hour at room temperature. Then the solid was filtered on a Büchner funnel and washed twice with 50 mL of technical ethanol. After drying at 80 ^{o}C overnight, the white powder was named MWL-R ("R" means "surfactant removed by chemical extraction").

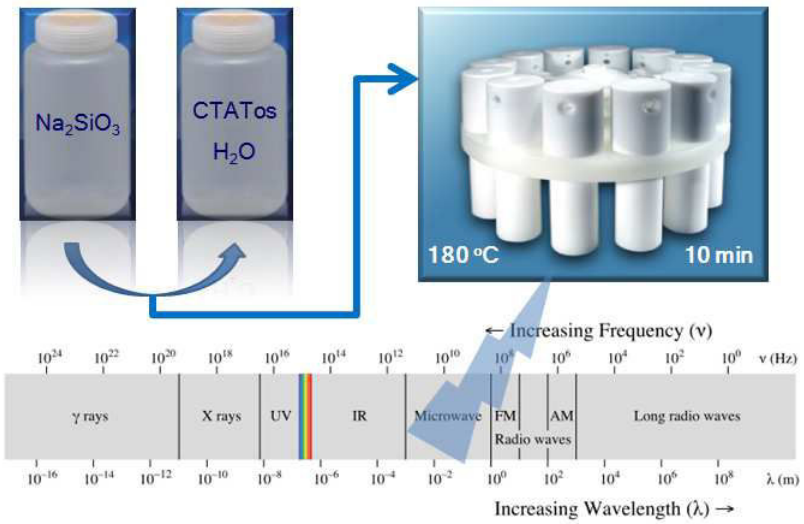

Figure 1. Sketch of synthesis of MCM-41 with microwave assistance.

4.2.2 Preparation of V-MWL

V-MWL was prepared in a similar way as MWL except that vanadyl sulfate was dissolved in the deionized water before the addition of CTATos in the solution. After 1 hour of stirring at 60 ^{o}C, the surfactant solution with $VOSO_4$ appeared as a clear blue viscous solution. When the surfactant solution was mixed with the Na_2SiO_3 solution, the color of this mixture turned from light blue to dark green during the stirring at 60 ^{o}C. The gel molar composition was: 1 SiO_2/ 0.05 CTATos/ 0.5 NaOH/ 80 H_2O/ n $VOSO_4$ (n=0.01/ 0.025/ 0.05). After heating in microwave and filtration, the powder was pale green while the filtrated aqueous solution was light yellow. The as-made pale green powder was named V-MWL. After calcination, the powder was white when taken out from oven and then turned to yellow in air. The yellow powder after calcination was named as V-MWL-cal.

4.2.3 Preparation of VTi-MWT

Solution A: 25.52 g TMAOH (25 wt%) were dissolved in 90 g deionized water, then 41.66 g TEOS were added dropwise in the TMAOH solution with stirring. This mixture was closely stirred at room temperature overnight until it was clear.

Solution B: 0.68 g TBOT were dissolved in 25 mL isopropanol.

Solution C: solution B was added dropwise in solution A with stirring at 0 ^{o}C, the resulting mixture was stirred at 0 ^{o}C until clear and separated into 4 parts averagely, each part was about 44.5 g.

Solution D: four surfactant solutions were prepared in parallel and named D1, D2, D3 and D4. Each one contained 2.05 g CTATos dissolved in 44.8 g of deionized water and was stirred at 60 ^{o}C for 1 hour. Solution D1 was a clear surfactant solution without additional of vanadyl sulfate. 0.106 g, 0.266 g and 0.531 g of vanadyl sulfate were added in solution D2, D3, D4 separately, and stirred for another 1 hour at 60 ^{o}C.

44.5 g solution C was added dropwise in solution D1 and stirred at 60 ^{o}C for 2 hours. After heating in microwave, filtration and drying overnight, which were the same procedures as for the synthesis of MWL, the white powder was named as made 1Ti-MWT (Microwave synthesis with TEOS as silica source); then after calcination to remove the surfactant, the product was named 1Ti-MWT-cal.

The gel molar composition was: 1 SiO_2/ 0.09 CTATos/ 0.35 TMAOH/ 80 H_2O/ xTiO_2 (x=0.01/ 0.025/ 0.05/ 0.10).

Solutions D2, D3 and D4 was mixed with 44.2 g solution C separately and the same procedure was followed to prepare V-Ti-MCM-41 materials. The corresponding solids were named (1-1)VTi-MWT(-cal), (2.5-1)VTi-MWT(-cal) and (5-1)VTi-MWT(-cal), respectively.

4.2.4 Preparation of VZr-MWL and VZr-MWT

Preparation of VZr-MWT followed the similar procedure as preparation of V-Ti-MWT, using zirconium *n*-butoxide (80 % w/w in 1-butanol) was used as Zr source. The gel molar composition was: 1 SiO_2/ 0.09 CTATos/ 0.35 TMAOH/ 80 H_2O/ x ZrO_2 / n $VOSO_4$ (x=0.025/ 0.05, n=0.00/ 0.01/ 0.025/ 0.05). The products were named (n-x)VZr_B-MWT(-cal).

The preparation of VZr-MWL was similar to the synthesis of V-MWL(-cal), using $ZrO(NO_3)_2$ as Zr source. The only difference was that before the addition of vanadyl sulfate, $ZrO(NO_3)_2$ was added in the surfactant solution (2 times the CTATos concentration compared to the ratio for synthesis of V-MWL). After 1 hour of stirring at 60 ^oC, $VOSO_4$ was added and followed another 1 hour of stirring at 60 ^oC. The gel molar composition was: 1 SiO_2/ 0.1 CTATos/ 0.5 NaOH/ 80 H_2O/ x ZrO_2/ n $VOSO_4$ (x=0.025/ 0.05, n=0.00/ 0.01/ 0.025/ 0.05). The products were named (n-x)VZr_N-MWL(-cal).

4.2.5 Preparation of VCe-MWL and VCe-MWT

Preparation of VCe-MWL and VCe-MWT followed the similar procedure as preparation of VZr-MWL and VZr-MWT. Two kinds of Ce sources were used: cerium(III) acetylacetonate hydrate and ammonium cerium(IV) nitrate. When using Ludox as Si source, the gel molar composition was: 1 SiO_2/ 0.1 CTATos/ 0.5 NaOH/ 80 H_2O/ 0.025 CeO_2/n $VOSO_4$ (n=0.00/ 0.01/ 0.025/ 0.05), and the products were named (n-2.5)VCe_A-MWL(-cal) and (n-2.5)VCe_N-MWL(-cal). When using TEOS as Si source, the gel molar composition was: 1 SiO_2/ 0.09 CTATos/ 0.35 TMAOH/ 80 H_2O/ 0.025 CeO_2/ n $VOSO_4$ (n=0.00/ 0.01/ 0.025/ 0.05) and the products were named (n-2.5)VCe_A-MWT(-cal) and (n-2.5)VCe_N-MWT(-cal).

4.2.6 Preparation of VAl-MWL

Aluminum sulfate was chosen as Al source, the preparation procedure was the same as for V-MWL(-cal). The only difference was that before the addition of vanadyl sulfate, aluminum sulfate was added to the surfactant solution (2 times the CTATos concentration compared to the ratio for synthesis of V-MWL), after 1 hour of stirring at 60 ^oC, $VOSO_4$ was added and followed another 1 hour of stirring at 60 ^oC for one hour more. The gel molar composition was: 1 SiO_2/ 0.1 CTATos/ 0.5 NaOH/ 80 H_2O/ x Al_2O_3/ n $VOSO_4$ (x=0.005/ 0.125/ 0.25/ 0.05, n=0.00/ 0.01/ 0.025/ 0.05). The products were named (n-2x)VAl-MWL(-cal).

4.3 Results and discussion

4.3.1 Textural characterization

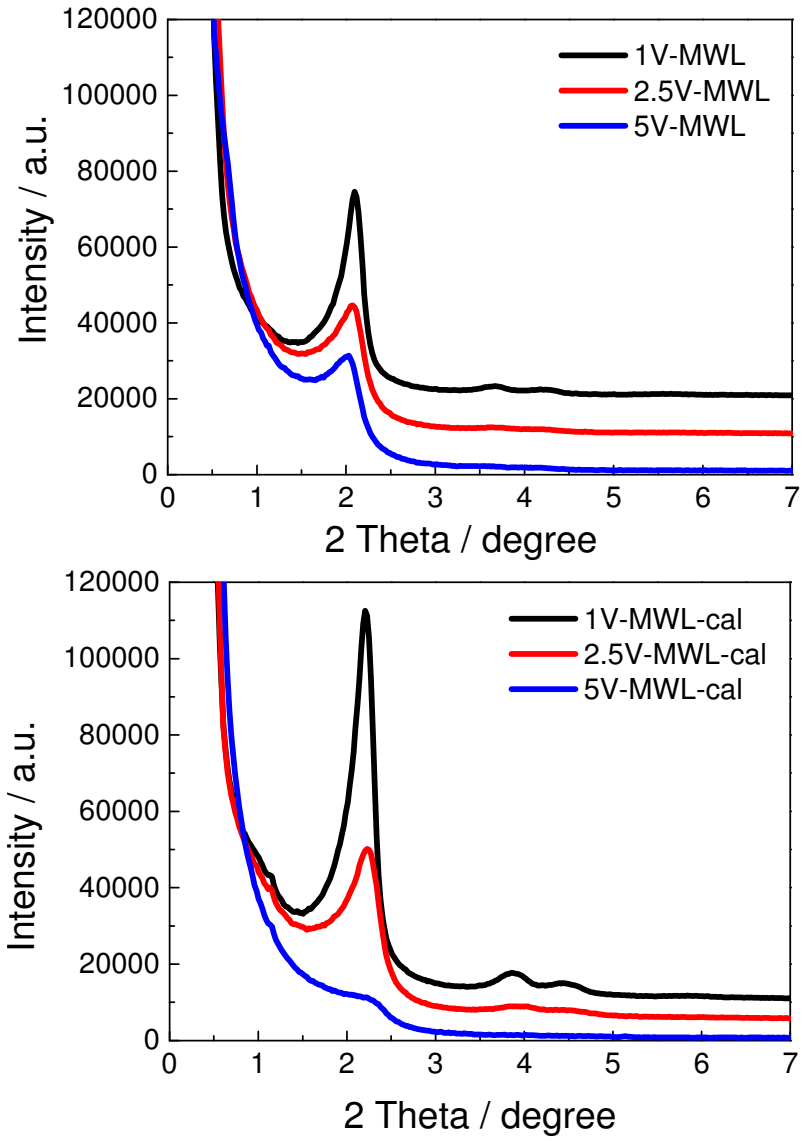

Figure 2. Low-angle XRD patterns of as-made V-MWL and V-MWL-cal.

The low-angle XRD pattern of as-made 1V-MWL displays four characteristic peaks corresponding to the (100), (110), and (200) plane diffractions respectively (Figure 2), typical of the hexagonal structure (p6mm symmetry) of MCM-41.[4] No peaks were observed between 2θ of 7 ^{o} to 70 ^{o}, discarding the formation of crystals of vanadium species. With the increasing loading of vanadium, the intensity of peaks obviously decreased, which indicated that the vanadium species were incorporated

into the skeleton of the mesoporous silica. The diffraction peaks were enhanced after the removal of the surfactant by calcination. However, for the sample of 5V-MWL-cal, the hexagonal structure was almost destroyed, showing that the high loading of vanadium negatively influenced the formation and stability of the mesoporous silica structure negatively.

Figure 3 shows the TEM images of 1V-MWL-cal. The ordered fingerprint 2D hexagonal honeycomb pores were clearly observed. The diameter of pores is about 3 nm and the wall thickness is about 1 nm.

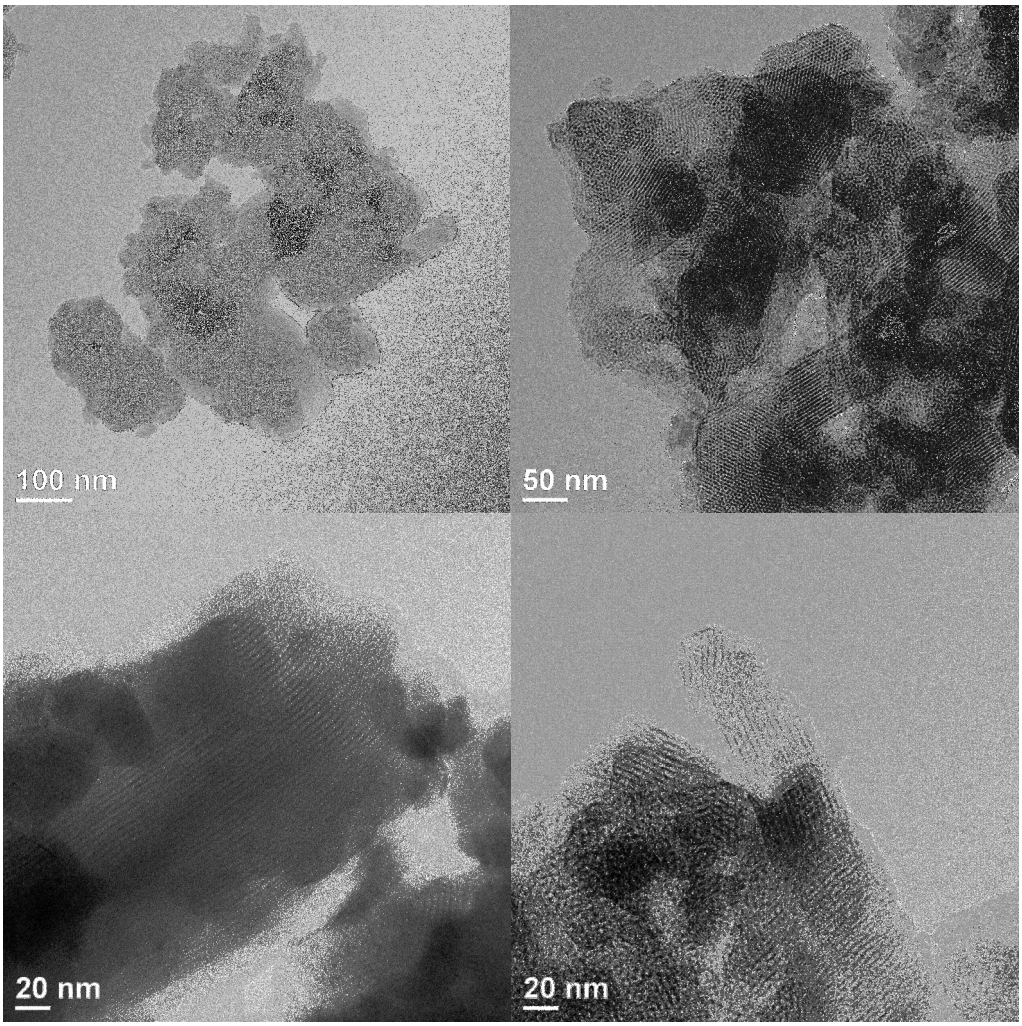

Figure 3. TEM images of 1V-MWL-cal.

XRD patterns of vanadium incorporated MCM-41 with Ti/Al/Zr/Ce anchors were collected in Appendix A1.1. Different ratios of vanadium and anchors were incorporated into the MCM-41 structures by one-pot microwave synthesis. From 1

mol% to 10 mol% of the Ti/Si ratio, the higher loading of Ti anchor ions corresponded to the lower intensity of peaks in XRD patterns, which indicated that less ordered hexagonal structures were obtained. For the same loading of Ti, the intensity of XRD peaks decreased with the increasing loading of vanadium. With different loading of Al anchor ions, the structure of the samples presented the same trends as for the Ti-V series. However, the ordered structures of silica were more difficult to keep when Al was introduced. This phenomenon indicated that both the anchor ions and the vanadium species were incorporated into the skeleton of mesoporous silica, and therefore either a high loading of anchor ions or vanadium ions may lead to less ordered structures or even to a collapse of the hexagonal mesoporous structure. To maintain the mesoporous framework, the tolerance to the Ti and Al hetero metal ions of the support structure was not higher than 5 mol% to Si. The atomic radius of Zr and Ce are larger than Al and Ti; therefore, the larger of the hetero atoms, the more negative effect they will cause to the framework of mesoporous silica support. So for Zr and Ce, we incorporated 5 mol% or 2.5 mol% of anchors to avoid the collapse of the mesoporous structure.

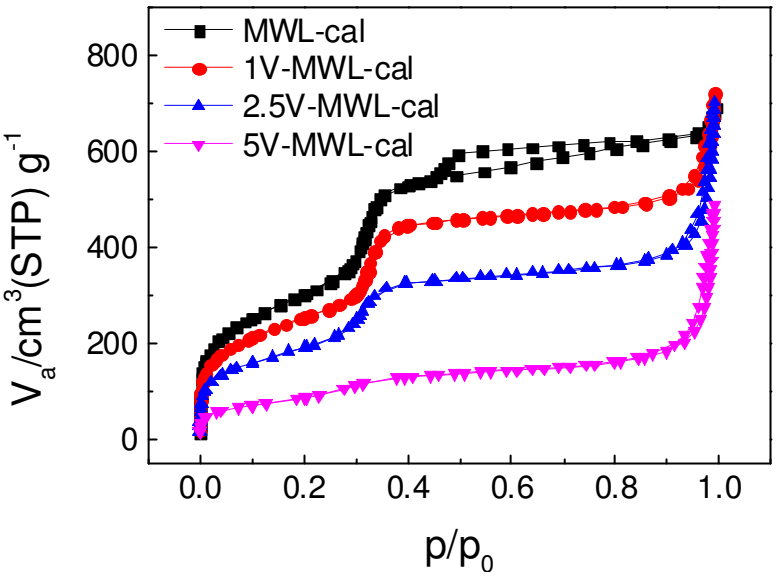

Figure 4. N_2 adsorption-desorption isotherms of V-MWL-cal at 77 K.

The N_2 adsorption-desorption isotherms of V-MWL-cal with 0 %, 1.0 % and 2.5 %

vanadium loading (Figure 4) exhibits the typical type IV isotherm according to the IUPAC classification. There are three different volume rises: the rises at low, medium and high relative pressure, which correspond to the filling of microporous, mesoporous, and inter-grain volumes respectively. 5V-MWL-cal presents a different profile, since its mesoporous structure was almost collapsed. Table 1 shows that with the increasing loading of vanadium, the specific surface area, pores volume, and pores diameter of V-MWL-cal decreased. This was mainly due to the incorporation of vanadium both on the pore surface and in the walls of SiO_2. The N_2 adsorption-desorption isotherms and porosity data of vanadium incorporated MCM-41 with Ti/Al/Zr/Ce anchors are collected in Appendix A2.1. The incorporation of anchor ions also led to the systematic decrease of specific surface area, pores volume, and pores diameter.

Table 1. Porosity data derived from N_2 adsorption-desorption isotherms.

Sample	a_0[a] (nm)	V_{total}[b] ($cm^3 \cdot g^{-1}$)	V_p[c] ($cm^3 \cdot g^{-1}$)	S_{BET}[d] ($m^2 \cdot g^{-1}$)	d_{HK}[e] (nm)	d_{BdB}[f] (nm)	$T_{w\ BdB}$[g] (nm)	C
MWL-cal	4.6	1.05	0.90	1107	3.0	3.5	1.1	83
1V-MWL-cal	4.6	1.10	0.67	929	3.1	3.6	1.0	81
2.5V-MWL-cal	4.6	1.07	0.47	704	2.9	3.5	1.1	76
5V-MWL-cal	4.6	0.74	0.16	323	2.8	3.3	1.3	61

(a) Hexagonal lattice parameter calculated from XRD, $a_0 = 2d_{100}/1.732$, accuracy ± 0.1 nm; (b) V_{total} at $p/p_0 = 0.99$, accuracy ± 0.01 cm^3g^{-1}; (c) V_p at $P/P_0 = 0$ on the adsorption plateau of t-plot, accuracy ± 0.01 cm^3g^{-1}; (d) from BET equation at $0.05 \leq p/p_0 \leq 0.16$, accuracy ± 50 m^2g^{-1}; (e) pore diameter extrapolated from Horvath-Kawazoe method, accuracy ± 0.1 nm; (f) pore diameter extrapolated from Broekhoff and De Boer method, accuracy ± 0.1 nm; (g) pore wall thickness calculated from a_0-d_{BdB}, accuracy ± 0.2 nm.

Figure 5 shows the ^{29}Si quantitative NMR spectra of as-made 2.5V-MWL. The ^{29}Si quantitative NMR spectra of vanadium incorporated MCM-41 with Ti/Al/Zr/Ce anchors are gathered in Appendix A7.1, and the quantitative analysis of NMR peaks is summarized in Table 2. All these samples have three types of silicon coordination states: Q^4 (-110 ppm, silicon coordinated with four oxygen atoms), Q^3 (-101 ppm, each silicon atom coordinated with three oxygen atoms and one hydroxy), and Q^2 (-92 ppm, each silicon atom coordinated with two oxygen atoms and tow hydroxy). The

decreasing of the Q^4 signal after the introduction of anchor ions indicated that the anchor ions were incorporated into the skeleton of SiO_2.

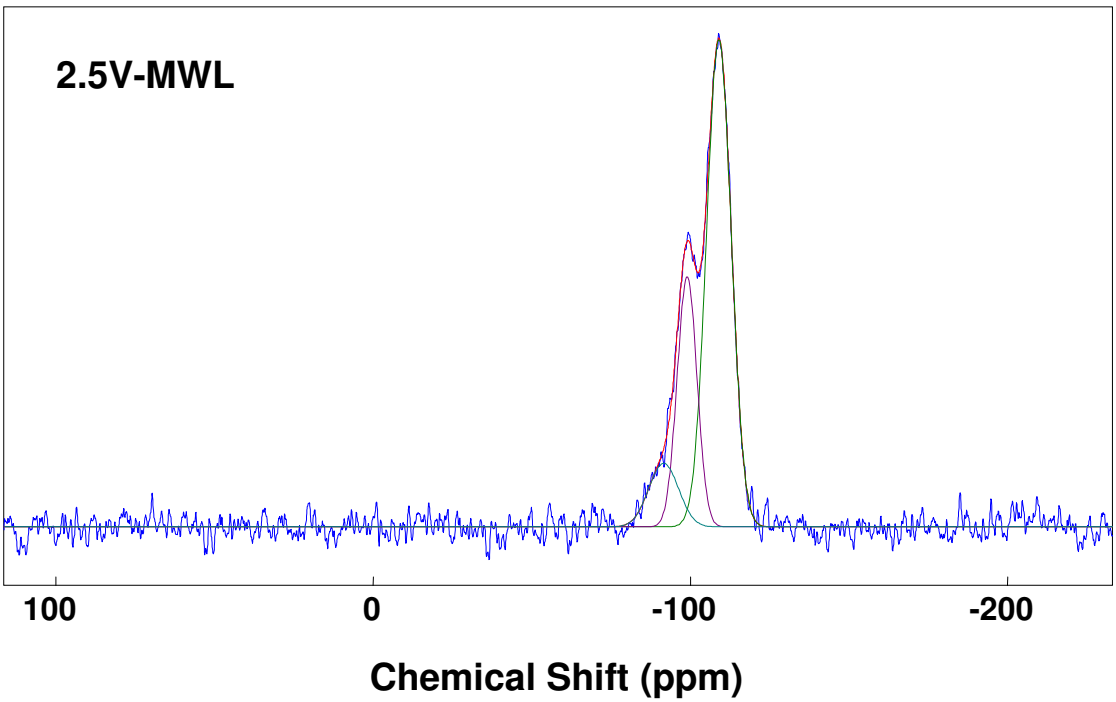

Figure 5. ^{29}Si quantitative NMR spectra of as-made 2.5V-MWL.

Table 2. ^{29}Si quantitative NMR analysis of vanadium incorporated MCM-41 with Ti/Al/Zr/Ce anchors (as-made).

Sample	Q^4	Q^3	Q^2	Si (iorg)
2.5V-MWL	64	26	10	100
2.5Ti-MWT	50	41	9	100
2.5Al-MWL	45	42	13	100
2.5Zr_N-MWL	47	44	9	100
2.5Ce_A-MWT	55	39	6	100
(2.5-2.5)VTi-MWT	50	40	10	100
(2.5-2.5)VAl-MWL	47	47	6	100
(2.5-2.5)VZr_N-MWL	54	25	21	100
(2.5-2.5)VCe_A-MWT	53	39	8	100

Figure 6 shows the ^{27}Al quantitative NMR spectra of as-made 2.5Al-MWL. The ^{27}Al quantitative NMR spectra of as-made Al-MWL and VAl-MWL were collected in

Appendix A7.1, and the quantitative analysis of NMR peaks was summarized in Table 3. All the samples show the incorporated Al existed as tetrahedral Al (~55 ppm), there was no pentahedral (~35 ppm) and octahedral (~5 ppm) Al.

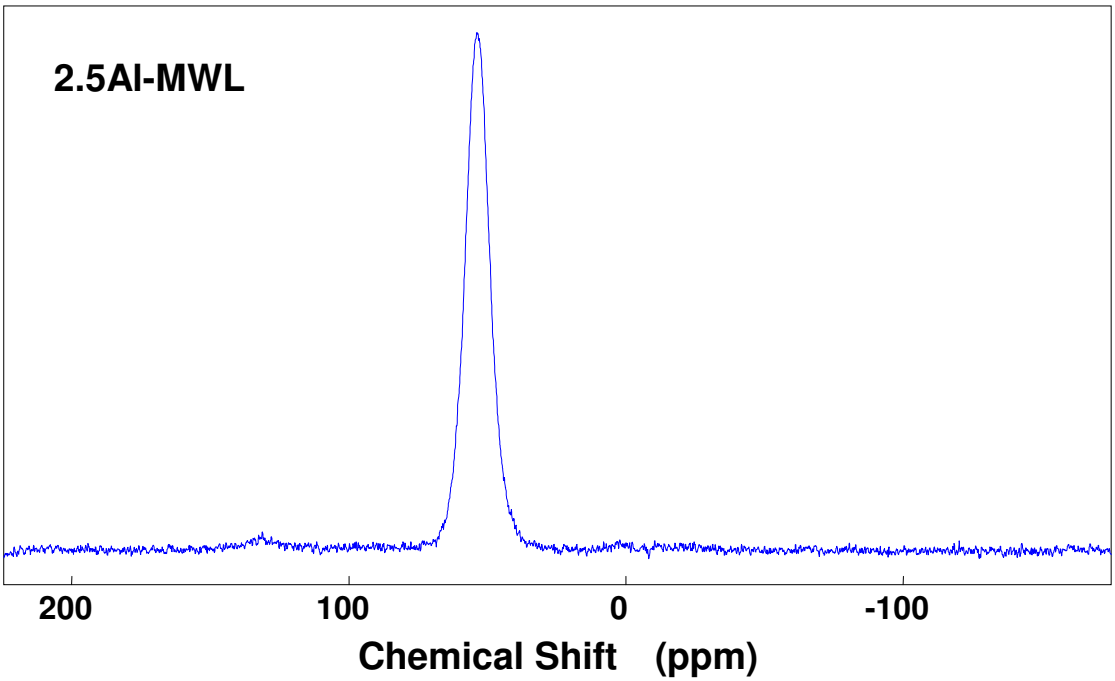

Figure 6 ^{27}Al quantitative NMR spectra of as-made 2.5Al-MWL.

Table 3. ^{27}Al quantitative NMR analysis of as-made Al-MWL and VAl-MWL.

Sample	Al (tet)	Al (oct)	Al (penta)
1Al-MWL	100	0	0
(1-1)VAl-MWL	100	0	0
2.5Al-MWL	100	0	0
(1-2.5)VAl-MWL	100	0	0
5Al-MWL	100	0	0
(1-5)VAl-MWL	100	0	0
10Al-MWL	100	0	0
(1-10)VAl-MWL	100	0	0

4.3.2 Decomposition of organic surfactant template

Figure 7 and Table 4 show the TG and DTG analysis of as-made V-MWL. Sample mass decreased with the increasing of temperature, and there were mainly 4 peaks of mass change. Peak 1 was in the range of room temperature to about 130 ^{o}C,

it corresponded to the desorption of H_2O, which indicated the hydrophilicity of samples; peak 2 was in the range of 130 °C to about 300 °C, it was attributed to the degradation of surfactant CTA^+ linked to the surface silanol; peak 3 was in the range of about 300 °C to 400 °C, it corresponded to the decomposition of trapped surfactant CTATos in channels; peak 4 was in the range of about 400 °C to 800 °C, it was from the silanol condensation. With the increasing loading of vanadium, the residual mass decrease, while peak 2 decrease and peak 3 increase respectively, that means there were fewer CAT^+ linked to the surface silanol and more CTA^+ linked to their counter anion Tos^-, because some of silanol groups were occupied by the linkage with vanadium species. It followed the same trends for the TG and DTG analysis of vanadium incorporated MCM-41 with Ti/Al/Zr/Ce anchors which were collected in Appendix A3.1.

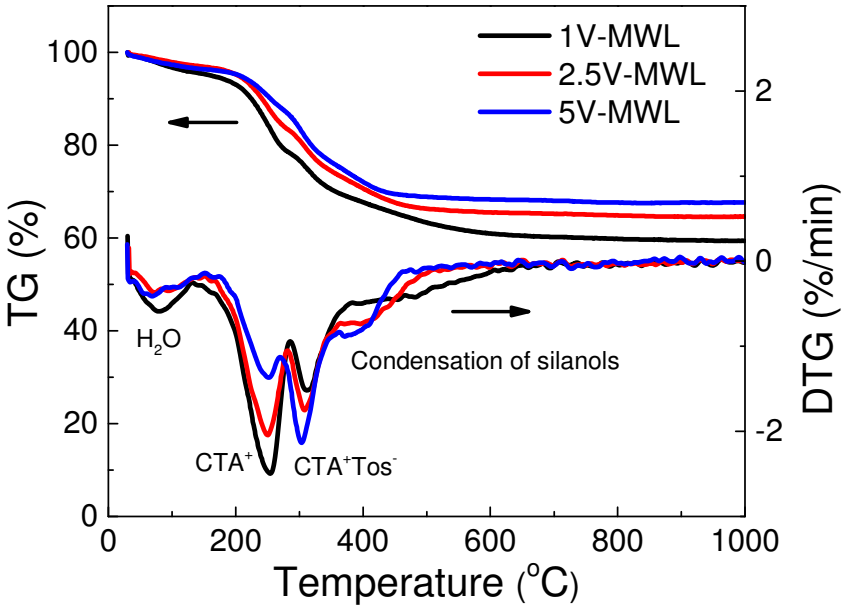

Figure 7. TG and DTG analysis of as-made V-MWL.

Table 4. DTG analysis of as-made V-MWL.

Sample	PEAK 1	PEAK 2	PEAK 3	PEAK 4	Residual Mass
	mass change from DTG (%)				(%)
1V-MWL	4.29	17.43	9.70	8.30	59.22
2.5V-MWL	3.11	13.38	10.24	7.98	64.55
5V-MWL	3.66	8.07	13.01	6.64	67.69

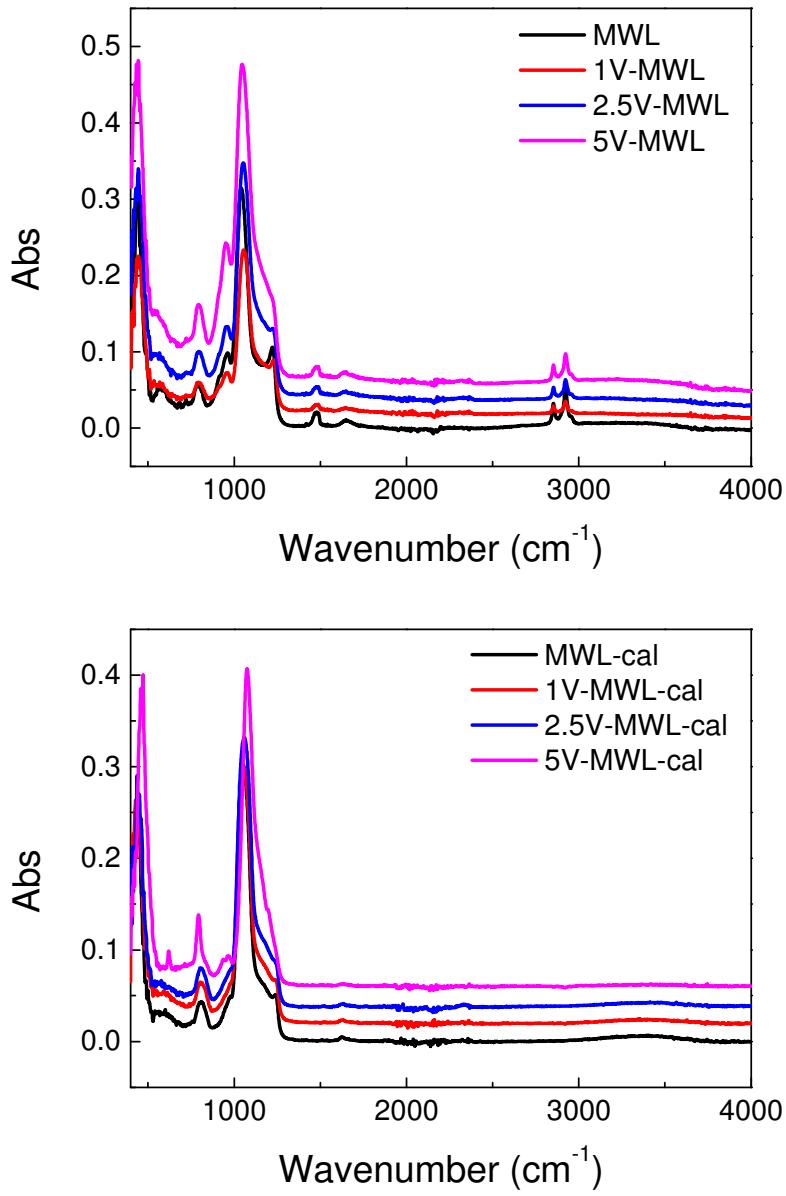

Figure 8. FT-IR spectra of as-made V-MWL and V-MWL-cal.

From the FT-IR spectra of as-made V-MWL (Figure 8), the band at about 1490 cm^{-1} come from the C-H bending (δ_{C-H}) vibrations of surfactant, and the bands in the region of 2800 cm^{-1} to 3000 cm^{-1} were derived from the C-H stretching (ν_{C-H}) vibrations of $-CH_3-$ and $-CH_2-$ in surfactant, after calcination at 550 ^oC for 6 hours, these bands disappeared, which indicated the total removal of organic surfactant template. The band derived from Si-OH bond stretching vibration of the silanol groups at 960 cm^{-1} decreased after calcination, this was due to the condensation of silanol groups inside the pore walls during the calcination. With the increasing

loading of vanadium, the bands in the range between 1000 cm^{-1} and 1200 cm^{-1} were enhanced due to the stretching vibration of V=O,[6, 7] which was overlapped with the Si-O-Si asymmetric stretching vibration.[8] The FT-IR spectra of vanadium incorporated MCM-41 with Ti/Al/Zr/Ce anchors were collected in Appendix A4.1. They all in accordance with the bands of V-MWL and V-MWL-cal.

4.3.3 Vanadium species

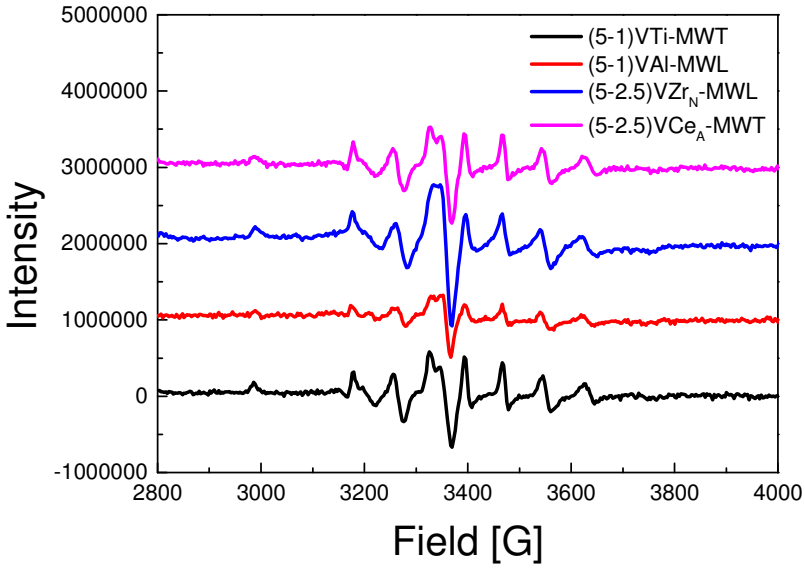

Figure 9. EPR spectra of vanadium incorporated MCM-41 with Ti/Al/Zr/Ce anchors.

Figure 9 shows the EPR spectra of as made samples of vanadium incorporated MCM-41 with Ti/Al/Zr/Ce anchors, the typical hyperfine splitting signal corresponded to the well dispersed vanadyl ions $(V^{IV}=O)^{2+}$, while after calcination, no EPR signal was obtained, which means all the vanadium species were oxidized into $(V^{V}=O)^{3+}$.

For the diffuse reflectance UV-visible spectroscopy of vanadia species (Figure 10), the peaks between 200-500 nm wavelength were attributed to the charge transfer of oxygen to V(V), the wide bands indicated the coexistence of monomeric and polymeric vanadia species, the higher wavelength bands corresponding to the lower transition energy of polymeric vanadia structures, while the lower wavelength bands corresponding to the higher transition energy of monomeric vanadia structures.[9, 10]

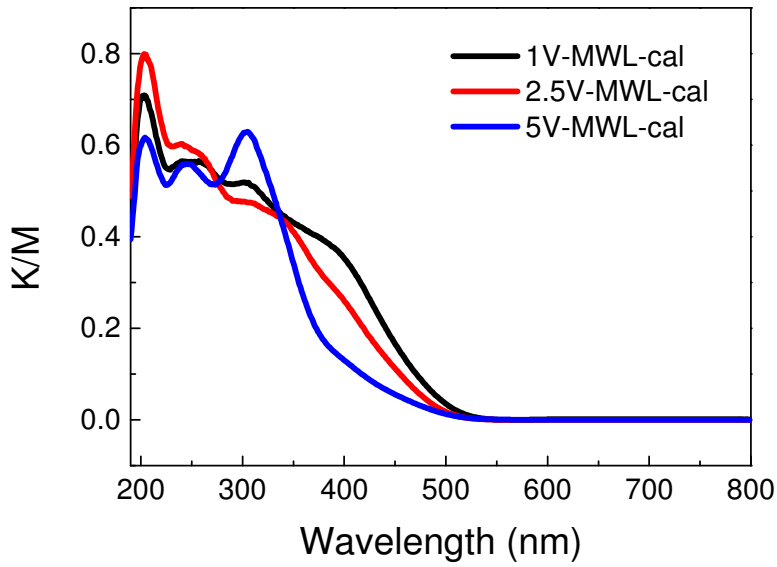

Figure 10. UV-vis spectra of V-MWL-cal. MWL-cal was used as blank, and before measurement, samples were diluted by MWL-cal to keep the spectra intensity in the range of 0.2-0.8 K/M.

When anchors ions were incorporated, here we take VTi-MWL-cal as an example (Figure 11). With the same ratio of Ti loading, the bands of vanadium have more red shift with the increasing loading of V, which corresponding to the less isolated vanadium species, this was caused by the aggregation of vanadium species with the high loading; while with a higher loading of Ti, there were less red shift with the increasing loading of V. This phenomenon indicated that the incorporation of Ti as anchor ions improved the vanadium dispersion and avoided the clusters of vanadia species. UV-vis spectra of vanadium incorporated MCM-41 with Al/Zr/Ce anchors were collected in Appendix A5.1, they also followed the same trend as the UV-vis spectra of VTi-MWL-cal, the increasing incorporation of Al, Zr, Ce anchor ions led to the blue shift of V spectra, which corresponding to the more isolated vanadium species.

To facilitate the comparison of different samples, we use the Tauc's plot to compare the band gap of samples[11, 12]. Based on the data from UV-vis spectra, in Tauc's plot, the X-axis was energy ($E = h\nu = hc/\lambda$) and the Y-axis was $(F(R)h\nu)^2$

where the F(R) was the absorption coefficient as K/M. Then a straight line was drawn as the slope of the plot, and the x-intercept was considered as the edge energy of that sample.[13, 14] The high edge energy corresponding to the better-dispersed monomer vanadium species, while the low edge energy corresponding to the poor dispersion of polymer vanadium species. The Tauc's plot and edge energy table of vanadium incorporated MCM-41 with Ti/Al/Zr/Ce anchors were collected in Appendix A6.1, and Figure 12 was derived from these edge energy data.

Figure 12 shows that the samples with Ti anchor ions have the highest edge energy, which means the vanadium species with Ti anchors ions has a better dispersion on MCM-41.

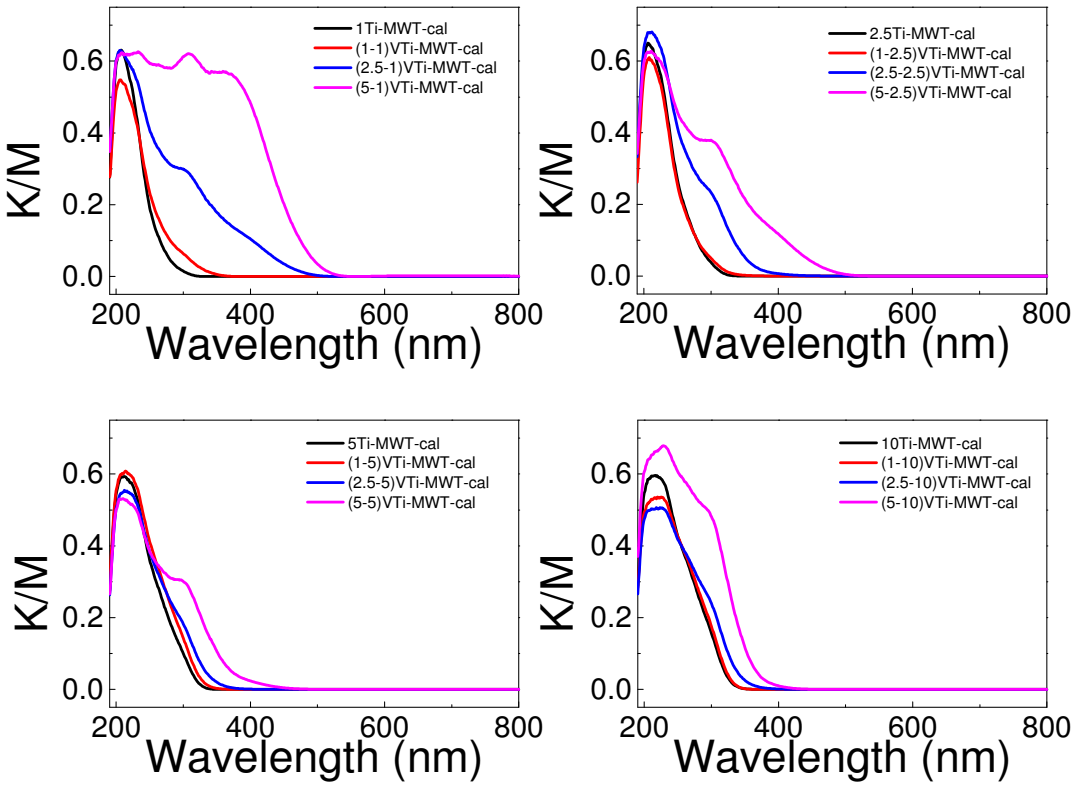

Figure 11. UV-vis spectra of VTi-MWL-cal. MWL-cal was used as blank, and before measurement, samples were diluted by MWL-cal to keep the spectra intensity in the range of 0.2-0.8 K/M.

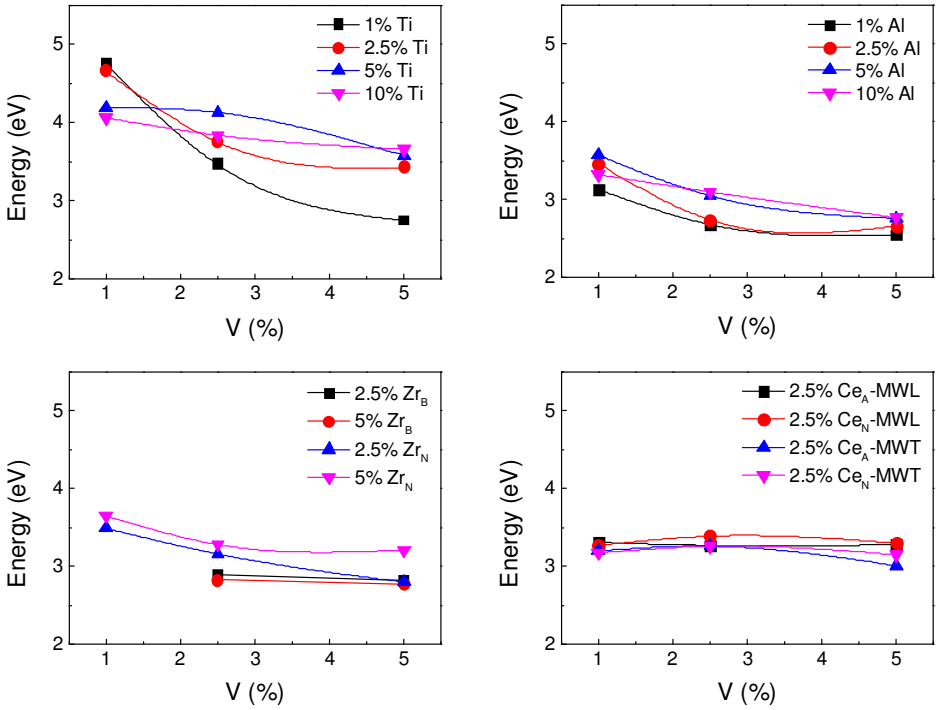

Figure 12. Edge energy of vanadium incorporated MCM-41 with Ti/Al/Zr/Ce anchors. (Sample No. corresponding to the tables in Appendix A6.1)

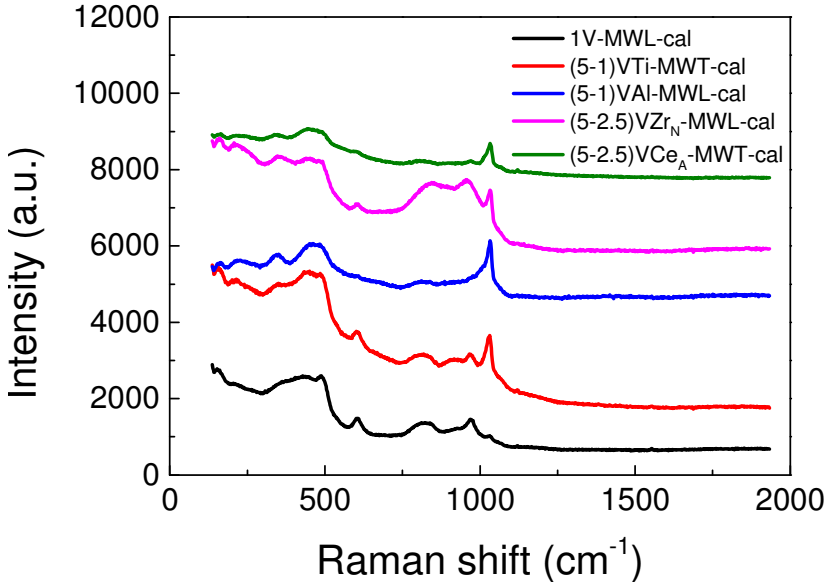

Figure 13. Raman spectra of vanadium incorporated MCM-41 with Ti/Al/Zr/Ce anchors.

The Raman spectra of vanadium incorporated MCM-41 with Ti/Al/Zr/Ce anchors (Figure 13) provided the information about the surface vanadium oxide species. The band at 1030 cm^{-1} attributed to the V=O stretching vibration of monomeric species bond directly to the support. There was no band at 930 cm^{-1} which assigned to the V=O symmetric stretching mode of polymerized vanadium oxides. The band of 490 cm^{-1} belong to the 3 Si siloxane rings, the band of 610 cm^{-1} belong to the 4 Si siloxane rings, the band at 810 cm^{-1} attributed to the siloxane bridges, and the band at 970 cm^{-1} attributed to the surface silanol stretching vibrations.

Table 5. Elemental analysis of vanadium incorporated MCM-41 with Ti/Al/Zr/Ce anchor ions.

Sample	**V (mol%)**	**M (mol%)**
1V-MWL-cal	0.7	0
(2.5-2.5)VTi-MWT-cal	0.69	2.8
(2.5-2.5)VAl-MWL-cal	2.23	4.76
(2.5-2.5)VZr_N-MWL-cal	2.2	4.08
(2.5-2.5)VCe_A-MWT-cal	1.21	2.53

Compared with the samples synthesized with TEOS (MWT), when Ludox was used as Si source (MWL), not all the stoichiometric Si was precipitated, the efficacious utilization of Ludox was about 50 mol%,[4] that is why the samples of MWL have a higher actual loading (almost 2 times than MWT) of anchor ions (Table 5). For all the samples in Table 5, there is the loss of vanadium during the synthesis. The leaching test of these supported vanadium samples will be discussed in chapter 7.

4.4 Conclusion

One pot microwave synthesized vanadium incorporated mesoporous silica with different loading of Ti/Al/Zr/Ce anchor ions were obtained within 10 minutes heating in microwave. The vanadium and anchor ions were incorporated both on the surface and into the framework of SiO_2. With the low loading of vanadium and anchor ions (e.g. 1 mol%, 2.5 mol%), the hexagonal honeycomb structure of silica can be kept very well, while with the high loading of heteroatom (e.g. 5 mol%, 10 mol%), the mesoporous skeleton was collapsed. The specific surface area, pores volume, and pores diameter of samples decreased systematically with the increasing loading of vanadium and anchor ions. After calcination, the organic template was removed and the V^{4+} was oxidized to V^{5+}. When anchor ions were introduced, the UV-vis spectra of vanadium had blue shift which indicated a better dispersion of vanadium species. Raman spectra shows the vanadium exist as monomeric species bond directly to the support. By the comparison of the band gap, samples with Ti anchor ions has the highest edge energy, which means the vanadium species with Ti anchors ions has a better dispersion state on mesoporous silica. The demand of high loading of vanadium active sites, the requirement of better dispersion of active sites, and the imperative to maintain the hexagonal mesoporous structure are the aspects that need to be balanced during the exploitation of the supported vanadium catalyst with high activity. The synthesis procedures were clean and efficient and the synthesized mesoporous silica supported vanadium catalysts are promising for the oxidation reactions.

4.5 References

1. Kappe, C. O.; Dallinger, D.; Murphree, S. S., *Practical microwave synthesis for organic chemists*. John Wiley & Sons: **2008**.
2. Wu, C.-G.; Bein, T. *Chem. Commun.* **1996**, (8), 925-926.
3. Tompsett, G. A.; Conner, W. C.; Yngvesson, K. S. *ChemPhysChem* **2006,** 7, (2), 296-319.
4. Chaignon, J.; Bouizi, Y.; Davin, L.; Calin, N.; Albela, B.; Bonneviot, L. *Green Chem.* **2015,** 17, (5), 3130-3140.
5. Taguchi, A.; Schüth, F. *Microporous Mesoporous Mater.* **2005,** 77, (1), 1-45.
6. Chen, Y.; Yang, G.; Zhang, Z.; Yang, X.; Hou, W.; Zhu, J.-J. *Nanoscale* **2010,** 2, (10), 2131-2138.
7. Sanchez, C.; Livage, J.; Lucazeau, G. *J. Raman Spectrosc.* **1982,** 12, (1), 68-72.
8. Parambadath, S.; Mathew, A.; Park, S. S.; Ha, C.-S. *J. Environ. Chem. Eng.* **2015,** 3, (3), 1918-1927.
9. Dutoit, D.; Schneider, M.; Fabrizioli, P.; Baiker, A. *Chem. Mater.* **1996,** 8, (3), 734-743.
10. Chao, K.; Wu, C.; Chang, H.; Lee, L.; Hu, S.-f. *J. Phys. Chem. B* **1997,** 101, (33), 6341-6349.
11. Tauc, J.; Grigorovici, R.; Vancu, *A. Phys. Status Solidi B* **1966,** 15, (2), 627-637.
12. Swanepoel, R. *J. Phys. E: Sci. Instrum.* **1983,** 16, (12), 1214.
13. Gao, X.; Wachs, I. E. *J. Phys. Chem. B* **2000,** 104, (6), 1261-1268.
14. Bulánek, R.; Čičmanec, P.; Sheng-Yang, H.; Knotek, P.; Čapek, L.; Setnička, M. *Appl. Catal., A* **2012,** 415, 29-39.

Chapter 5. Surface molecular engineering of vanadium containing MCM-41 with molecular stencil patterning (MSP) technique

5.1 Introduction

Molecular stencil patterning (MSP) technique[1, 2] is a post-functionalization approach which can be applied for the surface modification of mesoporous silica. The structure template (such as cetyltrimethylammonium) was used as a molecular stencil and the electrostatic self-repulsion between the cationic heads of structure template can generate a regularly patterned surface. By the controllable coverage of molecular stencil, the trimethylsilyl (TMS) or ethyl-1,2-bis(dimethylsilyl) (EBDMS) functions can be grafted onto the available surface of mesoporous silica without or with a minimal displacement of the masking agents. Once the function groups were grafted, the masking agents can be removed to reveal the "latent image", just like the classical photograph developing. After that, the active sites (such as metal ions or complexes) can be grafted on the available surface released by the removing of masking agents. The active sites were isolated because of the existence of previously grafted function groups. Therefore, MSP technique is a promising approach for developing highly dispersed supported metallic catalysts.[3-11]

Vanadium active sites can be incorporated into the framework or grafted on the surface of mesoporous silica to prepare heterogeneous vanadium catalysts, the high dispersion and low leaching effect of vanadium active sites are critical qualities for an efficiently supported vanadium catalyst. In this chapter, vanadium was grafted on the surface of mesoporous silica MCM-41, in order to get isolated vanadium active sites, EBDMS groups were incorporated on the surface of MCM-41 by MSP technique. To improve the dispersion of vanadium active sites, Ti(IV), Zr(IV), Ce(IV) and Al(III) ions were grafted as anchors for the following loading of vanadium. The structures and characterization of these grafted V-(Ti/Zr/Ce/Al)-MCM-41 catalysts based on MSP technique will be discussed in detail.

5.2 Experiments

5.2.1 Surface molecular engineering of MCM-41 with EBDMS

The preparation of as made MCM-41 with the assistance of microwave following the same procedure as it was described in chapter 4.2.1, the product was named MWL.[12]

1.7 g TMABr was dissolved in 150 mL EtOH (70 % v/v) and stirred at 40 ^{o}C for 10 minutes, then 3.0 g MWL was added to this solution and stirred closely at 40 ^{o}C for 45 minutes, the solid was filtered and washed twice with 50 mL EtOH (70 % v/v) afterwards. This procedure was repeated three times to ensure a total exchange of TMA^{+}. After drying at 80 ^{o}C overnight, the white powder was named MWL-TMA.[6]

1.0 g MWL-TMA was stirred at 130 ^{o}C in vacuum for 2 hours to remove the H_2O and air absorbed on the solid, then cooled down in argon to room temperature, after that, 40 mL cyclohexane was added with stirring in argon, when the solid was dispersed uniformly in the solvent, 2.63 mL (~5eq to SiO_2) TMDSACP was added. The mixture was stirred under argon for 0.5 hours at room temperature, then refluxed at 80 ^{o}C in argon for 16 hours. After filtration, the solid was washed with cyclohexane and acetone, then dried at 80 ^{o}C overnight. The white powder was named MWL-TMA-EBDMS.[6]

1.0 g MWL-TMA-EBDMS was stirred in 200 mL technical ethanol (96 % v/v) with the additional of 2 mL HCl (1 M) for 1 hour at room temperature. Then the solid was filtered on a Büchner funnel and washed twice with 50 mL technical ethanol. After dried at 80 ^{o}C overnight, the white powder was named MWL-TMA-EBDMS-R ("R" means "surfactant removed by chemical extraction") or PS (Partially Silylated MCM-41) for short.[12]

1.0 g MWL-TMA was stirred in 200 mL technical ethanol (96 % v/v) with the additional of 2 mL HCl (1 M) for 1 hour at room temperature. Then the solid was filtered on a Büchner funnel and washed twice with 50 mL technical ethanol. After dried at 80 ^{o}C overnight, the white powder was named MWL-TMA-R ("R" means "surfactant removed by chemical extraction").[12]

1.0 g MWL-TMA-R was stirred at 130 ^{o}C in vacuum for 2 hours to remove the

H_2O and air absorbed on the solid, then cooled down in argon to room temperature, after that, 40 mL cyclohexane was added with stirring in argon, when the solid was dispersed uniformly in the solvent, 2.63 mL (~5eq to SiO_2) TMDSACP was added. The mixture was stirred under argon for 0.5 hours at room temperature, then refluxed at 80 ^oC in argon for 16 hours. After filtration, the solid was washed using cyclohexane and acetone, then dried at 80 ^oC overnight. The white powder was named MWL-TMA-R-EBDMS or FS (Full Silylated MCM-41).[6]

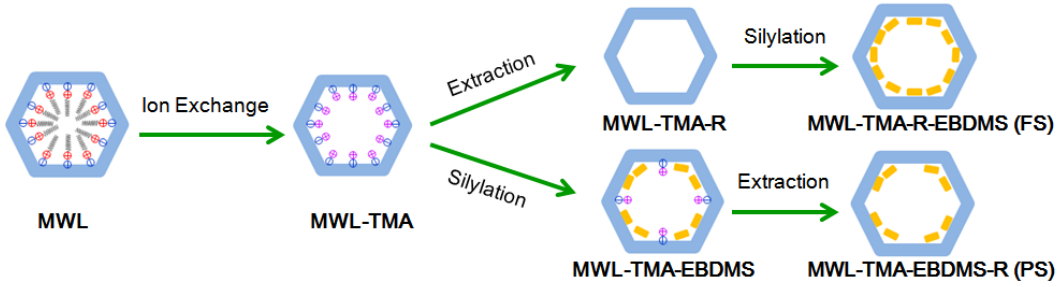

Figure 1. Surface molecular engineering of MCM-41 with EBDMS

5.2.2 Grafting of Ti/Zr/Ce/Al on modified MCM-41

1.0 g PS was stirred at 130 ^oC in vacuum for 2 hours to remove the H_2O and air absorbed on the solid, then cooled down in argon to room temperature, after that, 44.4 µL titanium(IV) isopropoxide was dissolved in 40 mL cyclohexane and added to the solid with stirring under argon. The mixture was stirred under argon for 0.5 hours at room temperature, then refluxed at 80 ^oC in argon for 16 hours. After filtration, the solid was washed with cyclohexane and dried at 80 ^oC overnight. The white powder was named 1Ti-GPS ("1Ti" for 1% Ti/Si mol %, and "GPS" for metal Grafted Partially Silylated MCM-41). With the same procedure, 3Ti-GPS was prepared as well.[13]

1.0 g PS was stirred at 130 ^oC in vacuum for 2 hours to remove the H_2O and air absorbed on the solid, then cooled down in argon to room temperature, after that, 67.2 µL zirconium(IV) butoxide (80 wt% in 1-butanol) was dissolved in 40 mL cyclohexane and added to the solid with stirring under argon. The mixture was stirred under argon for 0.5 hours at room temperature, then refluxed at 80 ^oC in argon for 16

hours. After filtration, the solid was washed with cyclohexane and dried at 80 ^{o}C overnight. The white powder was named 1Zr-GPS (same nomenclature than 1Ti-GPS sample replacing Ti by Zr). With the same procedure, 3Zr-GPS was prepared as well.

1.0 g PS was stirred at 130 ^{o}C in vacuum for 2 hours to remove the H_2O and air absorbed on the solid, then cooled down in argon to room temperature, after that, 0.0656 cerium(III) acetylacetonate hydrate was dissolved in 40 mL acetonitrile and added to the solid with stirring under argon. The mixture was stirred under argon for 0.5 hours at room temperature, then refluxed at 80 ^{o}C in argon for 16 hours. After filtration, the solid was washed with acetonitrile and dried at 80 ^{o}C overnight. The product was named 1Ce-GPS (same nomenclature than 1Ti-GPS sample replacing Ti by Ce). With the same procedure, 3Ce-GPS was prepared as well.

1.0 g PS was stirred at 130 ^{o}C in vacuum for 2 hours to remove the H_2O and air absorbed on the solid, then cooled down in argon to room temperature, after that, 49.0 µL sodium bis(2-methoxyethoxy)aluminum hydride solution (~60 wt% in toluene) was dissolved in 40 mL toluene and added to the solid with stirring under argon. The mixture was stirred under argon for 0.5 hours at room temperature, then refluxed at 80 ^{o}C in argon for 16 hours. After filtration, the solid was washed with toluene and dried at 80 ^{o}C overnight. The white powder was named 1Al-GPS (same nomenclature than 1Ti-GPS sample replacing Ti by Al). With the same procedure, 3Al-GPS was prepared as well.

5.2.3 Grafting of vanadium on Ti/Zr/Ce/Al containing MCM-41

0.5 g 1Ti-GPS was stirred at 130 ^{o}C in vacuum for 2 hours to remove the H_2O and air absorbed on the solid, then cooled down in argon to room temperature, after that, 18.2 µL vanadium(V) triisopropoxide was dissolved in 20 mL cyclohexane and added to the solid with stirring under argon. The mixture was stirred under argon for 0.5 hours at room temperature, then refluxed at 80 ^{o}C in argon for 16 hours. After filtration, the solid was washed with cyclohexane and dried at 80 ^{o}C overnight. The product was named (1-1)VTi-GPS (same nomenclature than 1Ti-GPS sample, and (1-1) for 1 mol% V/Si to 1 mol % Ti/Si). With the same procedure, (1-3)VTi-GPS

((1-3) for 1 mol % V/Si to 3 mol % Ti/Si) and (3-3)VTi-GPS ((3-3) for 3 mol % V/Si to 3 mol % Ti/Si) was prepared as well.[13]

The preparation of VZr/Ce/Al-GPS followed the same method as VTi-GPS.

5.3 Results and discussion

5.3.1 Textural characterization

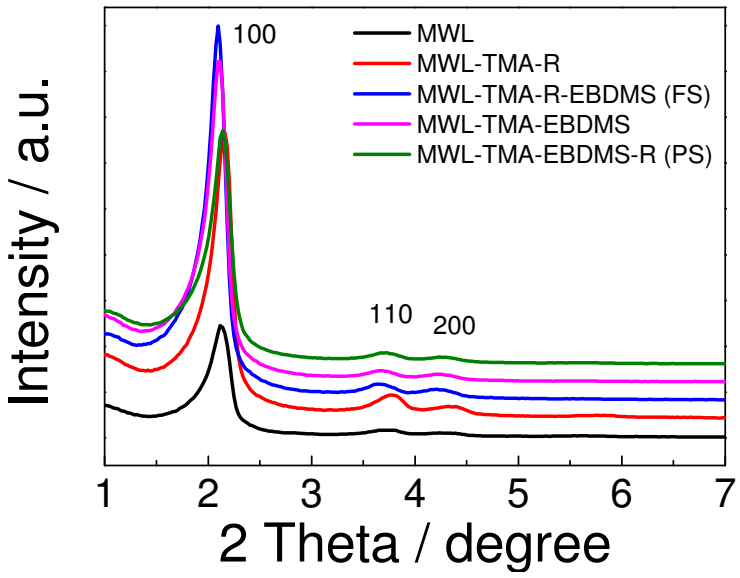

Figure 2. Low angle XRD patterns of MWL, MWL-TMA-R, MWL-TMA-R-EBDMS (FS), MWL-TMA-EBDMS, and MWL-TMA-EBDMS-R (PS).

The characteristic peaks of the (100), (110) and (200) plane diffractions in mesoporous silica are clearly displayed for all the samples before and after the ion exchange and the surface silylation in Figure 2, which corresponding to the typical MCM-41 hexagonal mesoporous framework structure. After the ion exchange of TMA or the extraction of surfactant, the surfactant CTATos were removed and the pores were exposed, so the intensity of XRD peaks of the other four samples in Figure 2 are stronger than the as-made MWL. All the modification with MSP technique were on the surface of the mesoporous structure without the influence of the silica skeleton network, so the honeycomb hexagonal structure of MCM-41 was maintained. The

typical hexagonal mesoporous framework structure did not alter after the grafting of vanadium ions and Ti/Al/Zr/Ce anchors, the peaks intensity and position of VTi/Al/Zr/Ce-GPS XRD patterns were kept as well as the pattern of PS (Appendix A1.2).

5.3.2 Characterization of the EBDMS functional groups

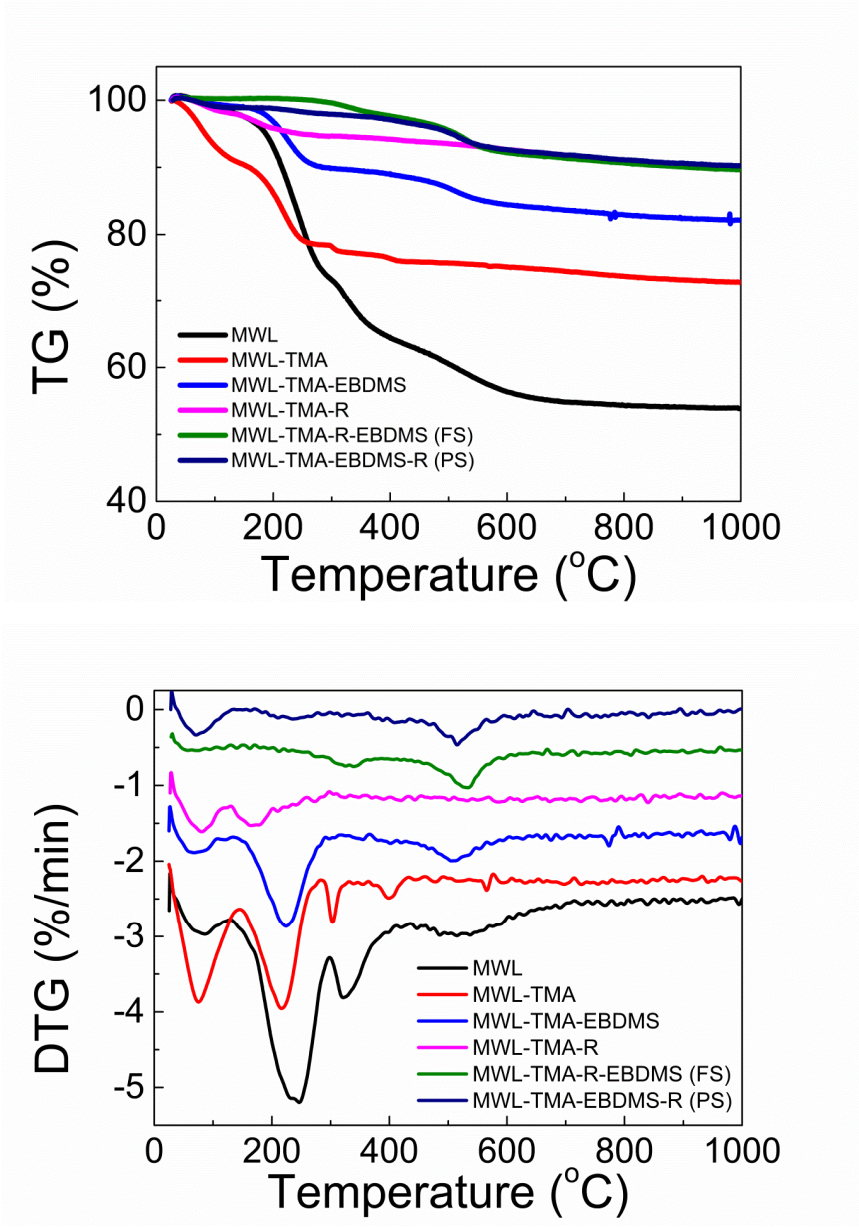

Figure 3. TG and DTG analysis of MWL, MWL-TMA, MWL-TMA-EBDMS, MWL-TMA-R, MWL-TMA-R-EBDMS (FS), and MWL-TMA-EBDMS-R (PS).

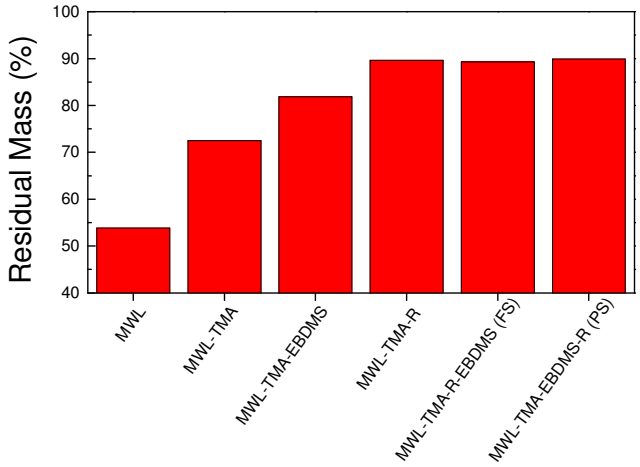

Figure 4. TG analysis of MWL, MWL-TMA, MWL-TMA-EBDMS, MWL-TMA-R, MWL-TMA-R-EBDMS (FS), and MWL-TMA-EBDMS-R (PS).

TGA can illustrate the loss of mass occurring mainly in these modification steps. The DTG representation is preferred for a more precise description. Figure 3 shows DTG analysis of different samples in the surface modification procedures, the desorption peaks of H_2O in the region below 130 ^oC; the peaks between 130 ^oC to 400 ^oC come from the degradation of TMA^+ linked to the surface silanol (for MWL, the two peaks corresponding to the degradation of CTA^+ and CTATos), and the peaks between 400 ^oC to 700 ^oC come from the degradation of EBDMS groups and silanol condensation. There are some differences between the DTG curves of MWL-TMA-EBDMS and MWL-TMA-R-EBDMS. If the TMA^+ was removed before the grafting of EBDMS, there was a full silylation, and no surface silanol left, so the sample of MWL-TMA-R-EBDMS was hydrophobic, there was no H_2O desorption peak in its DTG curve. If the EBDMS functional groups were grafted on MWL-TMA directly, there was still a lot of TMA^+ existed in the sample, so the sample MWL-TMA-EBDMS was not fully silylated. The difference of residual mass (Figure 4) between MWL-TMA and MWL-TMA-EBDMS indicates there was a partial leaching of TMA^+ during the grafting of EBDMS groups. After the removing of TMA^+, there was almost no weight change whether the sample was no silylated (MWL-TMA-R), partial silylated (MWL-TMA-EBDMS-R), or fully silylated (MWL-TMA-R-EBDMS). The DTG curves of partially silylated samples grafted with

vanadium and Ti/Zr/Ce/Al anchor ions can be found in Appendix A3.2, the slight weight loss come from the degradation of EBDMS groups and the anchor precursors. As the EBDMS was acting as islands to isolate the metal sites during the grafting of anchor ions or vanadium species, after the metal sites were already dispersed, the presence or absence of EBDMS groups was not crucial. Before the supported vanadium catalysts were taken to run in the reactions, a short calcination at 550 ^{o}C for 1 hour can make sure all the vanadium sites are activated as V^{5+}.

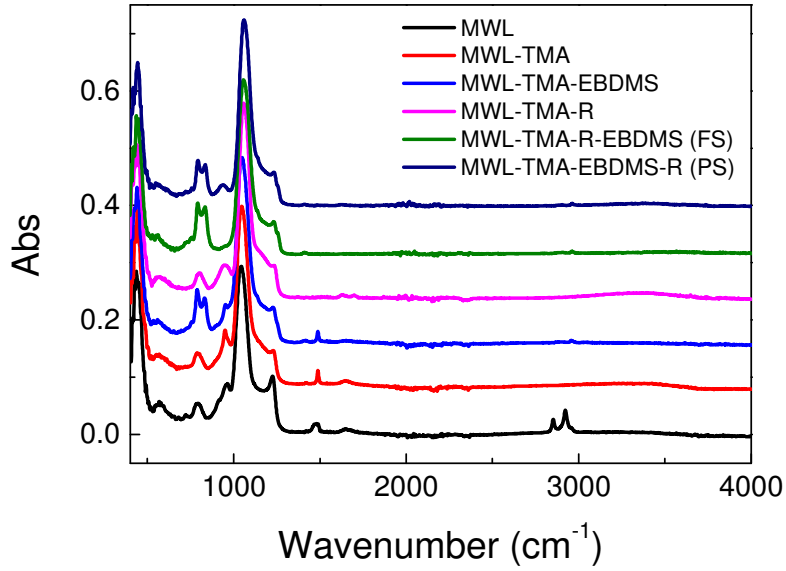

Figure 5. FT-IR spectra of MWL, MWL-TMA, MWL-TMA-EBDMS, MWL-TMA-R, MWL-TMA-R-EBDMS (FS), and MWL-TMA-EBDMS-R (PS).

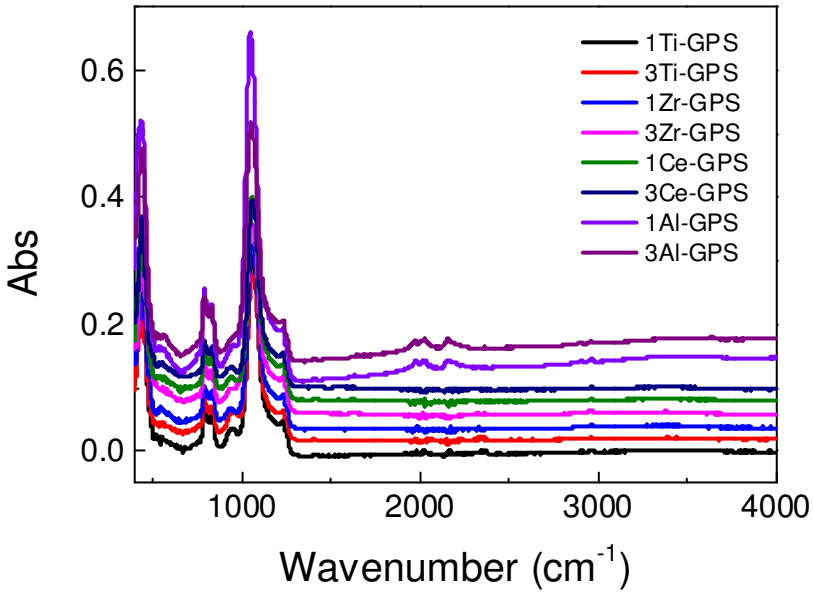

Figure 6. FT-IR spectra of GPS after grafting of Ti/Zr/Ce/Al anchor ions.

In the FT-IR spectra of MWL (Figure 5), the bands in the region of 2800 cm^{-1} to 3000 cm^{-1} were derived from the C-H stretching vibrations of $-CH_3-$ and $-CH_2-$ in surfactant CTATos; after the TMA^+ ion exchange, these bands were nonexistent, and a new peak appeared at 1490 cm^{-1} which assigned to the C-H bending vibration of $-CH_3$ in TMA^+. The peak at 950 cm^{-1} also come from the TMA^+. After the direct grafting of EBDMS on MWL-TMA, two bands appeared at 785 cm^{-1} and 834 cm^{-1}, these bands assigned to the Si-C stretching vibrations of EBDMS functional groups, and the band at 834 cm^{-1} can be considered as a fingerprint of the EBDMS moieties. The coexistence of bands at 831 cm^{-1} and 1490 cm^{-1} indicated the successful grafting of EBDMS and the partial left of TMA^+ in MWL-TMA-EBDMS. After the removing of TMA^+, the bands at 1490 cm^{-1} was nonexistent in MWL-TMA-EBDMS-R (PS). Compared to this partially silylated sample, the fully silylated one MWL-TMA-R-EBDMS (FS) shows the stronger bands at 785 cm^{-1} and 834 cm^{-1}, and there was no band at 938 cm^{-1} as there was no surface Si-OH available after the full coverage of EBDMS groups. The fingerprint peak of EBDMS at 834 cm^{-1} can be used for the quantification analysis to monitor the grafting of EBDMS groups. The weakly coupled valence bond angle vibration ($\delta_{Si\text{-}O\text{-}Si}$) of the siliceous matrix [SiO_4] band at 450 cm^{-1} was used as the reference peak for the normalization. After normalization, the peak intensity at 834 cm^{-1} can be compared with the IR spectra of different samples:

$$\frac{\text{EBDMS (PS)}}{\text{EBDMS (FS)}} = 70\,\% (\pm\ 5\%)$$

If the grafted EBDMS amount on the fully silylated sample (FS) was considered as 100 %, then for the partial silylated sample (PS), the grafted EBDMS amount was about 70 %, and about 30 % of the surface silanol was protected by the TMS^+, so after removing of the protected TMS^+, there was still 30 % silanol sites available for the following grafting of metal ions. After the grafting of Ti/Zr/Ce/Al anchor ions and vanadium sites on the partially silylated samples (PS), the EBDMS bands at 785 cm^{-1}

and 834 cm^{-1} did not change (Figure 6 and Appendix A4.2), so there was no loss of EBDMS after the grafting of metal ions. The bands of Al-GPS at 1900 cm^{-1} to 2300 cm^{-1} come from the C-H stretching vibrations in the aluminum precursor (sodium bis(2-methoxyethoxy) aluminum hydride solution).

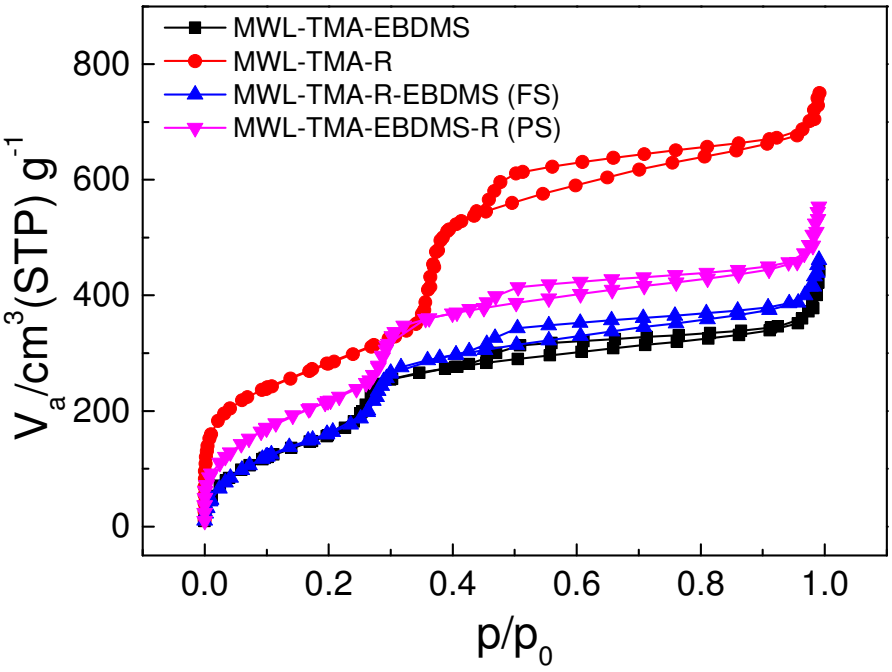

Figure 7. N_2 adsorption-desorption isotherms of MWL-TMA-EBDMS, MWL-TMA-R, MWL-TMA-R-EBDMS (FS), MWL-TMA-EBDMS-R (PS).

Table 1. Porosity data derived from N_2 adsorption-desorption isotherms.

Sample	a_0[a] (nm)	V_{total}[b] ($cm^3 \cdot g^{-1}$)	V_p[c] ($cm^3 \cdot g^{-1}$)	S_{BET}[d] ($m^2 \cdot g^{-1}$)	d_{HK}[e] (nm)	d_{BdB}[f] (nm)	$T_{w\ BdB}$[g] (nm)	C
MWL-TMA-EBDMS	4.8	0.66	0.45	629	2.6	3.1	1.7	26
MWL-TMA-R	4.7	1.14	0.92	1024	3.4	3.9	0.8	105
MWL-TMA-R-EBDMS (FS)	4.9	0.71	0.50	642	2.7	3.3	1.6	25
MWL-TMA-EBDMS-R (PS)	4.8	0.84	0.61	839	2.8	3.3	1.5	36

(a) Hexagonal lattice parameter calculated from XRD, $a_0 = 2d_{100}/1.732$, accuracy ± 0.1 nm; (b) V_{total} at $p/p_0 = 0.99$, accuracy ± 0.01 cm^3g^{-1}; (c) V_p at $P/P_0 = 0$ on the adsorption plateau of t-plot, accuracy ± 0.01 cm^3g^{-1}; (d) from BET equation at $0.05 \leq p/p_0 \leq 0.16$, accuracy ± 50 m^2g^{-1}; (e) pore diameter extrapolated from Horvath-Kawazoe method, accuracy ± 0.1 nm; (f) pore diameter extrapolated from Broekhoff and De Boer method, accuracy ± 0.1 nm; (g) pore wall thickness calculated from a_0-d_{BdB}, accuracy ± 0.2 nm.

As the molecular stencil patterning and grafting were just taking place on the surface of mesoporous silica, no modification was inserted into the silica network, the N_2 adsorption-desorption isotherms of samples before and after silylation all exhibit the typical type IV isotherms of mesoporous silica, there was no structure destruction nor collapse (Figure7 and Table 1). By chemical extraction, the surfactant was removed from the sample MWL-TMA-R, the pure silica mesoporous structure has a very high specific surface area (1024 $m^2 \cdot g^{-1}$) and a very high pore volume (0.92 $cm^3 \cdot g^{-1}$), the C parameter (105) is also higher than the PS sample (36) as all the surface silanols were available. After full silylation (MWL-TMA-R-EBDMS) using EBDMS grafting functions on the surface of mesopores, compared to the pure silica pores, there was less space in the pore after the functionalization, so the pore diameter (2.7~ 3.3 nm), specific surface area (642 $m^2 \cdot g^{-1}$) and pore volume (0.50 $cm^3 \cdot g^{-1}$) were decreased; as all the surface silanol was occupied by the EBDMS groups, the C parameter was very low (25). For the partially silylated sample, when there was the coexistence of EBDMS and TMA^+ (MWL-TMA-EBDMS), the N_2 adsorption-desorption isotherms was quite similar to the fully silylated sample; after the TMA^+ was removed (MWL-TMA-EBDMS-R), the EBDMS was partially covering the pore surface and the silanol sites, which were protected by the released TMA^+, so this sample is characterized by a higher C parameter (36), pore diameter (2.8~ 3.3 nm), specific surface area (839 $m^2 \cdot g^{-1}$) and pore volume (0.64 $cm^3 \cdot g^{-1}$) than the full silylated sample. The porosity data of partially silylated samples grafted with vanadium and Ti/Zr/Ce/Al anchor ions can be found in Appendix A2.2. As the grafting of low ratio metal ions (1~3 mol % to Si) on the mesoporous surface, the porosity data of these metal grafted samples were very similar with the MWL-TMA-EBDMS-R (PS), only very slightly decrease of pore diameter (-0.02~ -0.13 nm of change), specific surface area (-21~ -162 $m^2 \cdot g^{-1}$ of change) and pore volume (0~ -0.2 $cm^3 \cdot g^{-1}$ of change) were observed due to the loading of metal sites. The higher loading of hetero-metal ions leads to a lower surface area and pore volume, this was due to the occupation of limited space in pores by the loaded species. All these surface modifications and their corresponding structure changes were monitored

by the N_2 adsorption-desorption characterization very clearly.

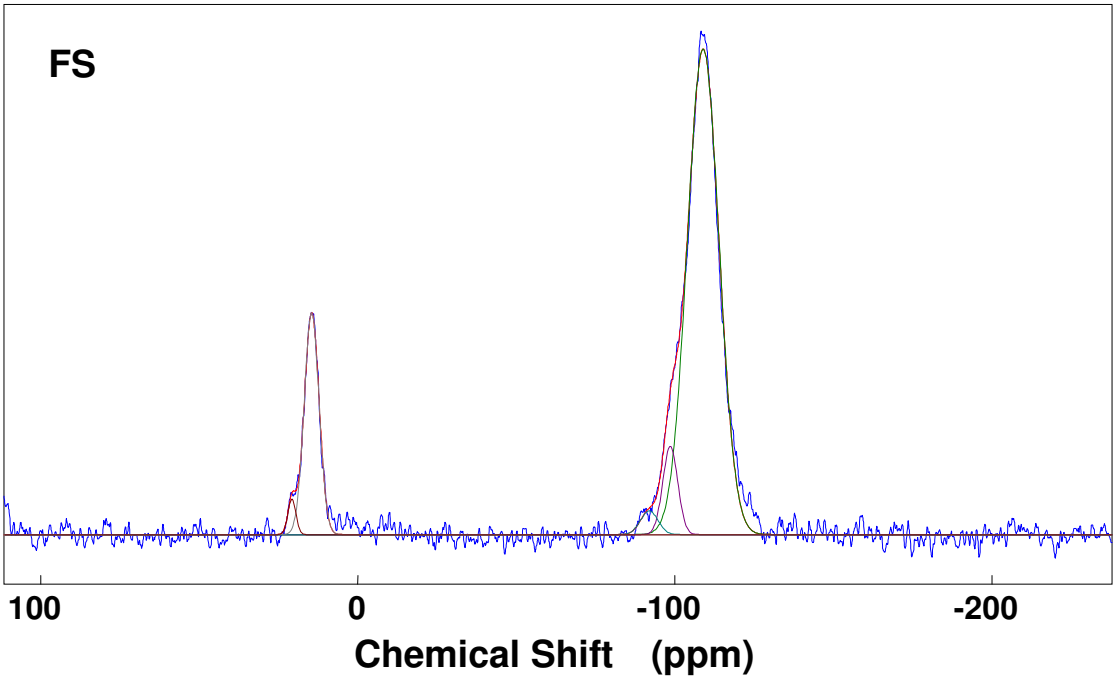

Figure 8. ^{29}Si quantitative NMR spectra of as-made FS.

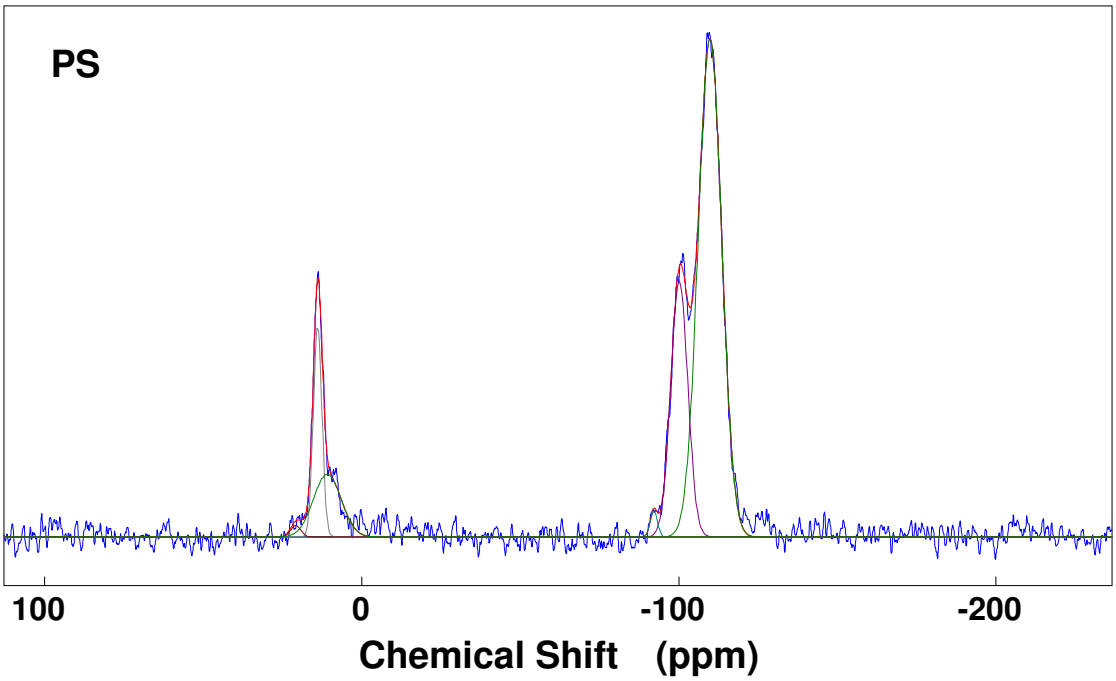

Figure 9. ^{29}Si quantitative NMR spectra of as-made PS.

Figure 8 and Figure 9 show the ^{29}Si quantitative NMR spectra of as-made samples FS and PS. The ^{29}Si quantitative and ^{13}C NMR spectra of as-made

VTi/Al/Zr/Ce-GPS were collected in Appendix A7.2, and the quantitative analysis of NMR peaks was summarized in Table 2.

Table 2. ^{29}Si quantitative NMR analysis of as-made FS, PS, and VTi/Zr/Ce/Al-GPS.

Sample **Peak Position**	**Q^4** **-109**	**Q^3** **-100**	**Q^2** **-92**	**Si** **(iorg)**	**M^1** **14**	**M^0** **20**	**M^1-M^1** **9**	**Si** **(org)**
MWL-TMA-EBDMS	61	16	8	85	13	0	2	15
FS	74	6	2	82	16	2	0	18
PS	59	22	1	82	9	1	8	18
3V-GPS	65	18	0	83	16	1	0	17
3Ti-GPS	54	25	0	79	13	3	5	21
3Zr-GPS	59	22	3	84	12	0	4	16
3Ce-GPS	63	20	0	83	12	2	3	17
3Al-GPS	59	24	0	83	14	0	3	17
(3-3)VTi-GPS	65	20	0	85	13	0	2	15
(3-3)VZr-GPS	61	26	0	87	11	0	2	13
(3-3)VCe-GPS	58	27	0	85	12	0	3	15
(3-3)VAl-GPS	60	25	0	84	14	0	2	16

Comparing to the partial silylated sample PS, the fully silylated sample FS has a lower ratio of Q^3 peak and a higher ratio of Q^4 peak, this is reasonable as the fully silylated sample has less surface silanol (Table 2). The M^0 (20 ppm), M^1 (14 ppm), M^1-M^1 (9 ppm) peaks corresponding to the three types Si of EBDMS functional groups: [R_3SiOH] (M^0), [$R_3SiO(SiO_3)$] (M^1), and [$R_3SiOSiR_3$] (M^1-M^1), (R= -CH_3 / -CH_2-). After the grafting of metal ions, the ratio of each type of Si peaks does not change apparently, the EBDMS functional groups were stable on the silica matrix. The main existing form of grafted EBDMS groups were the bipedal pair species (M^1), there were few bridged bipedal species (M^1-M^1) and monopodial species (M^0). The two peaks at -3.4 ppm and 8.5 ppm in the ^{13}C NMR spectra of as-made VTi/Al/Zr/Ce-GPS (Appendix A7.2) corresponding to the methyl and methylene carbon atoms in EBDMS moieties.

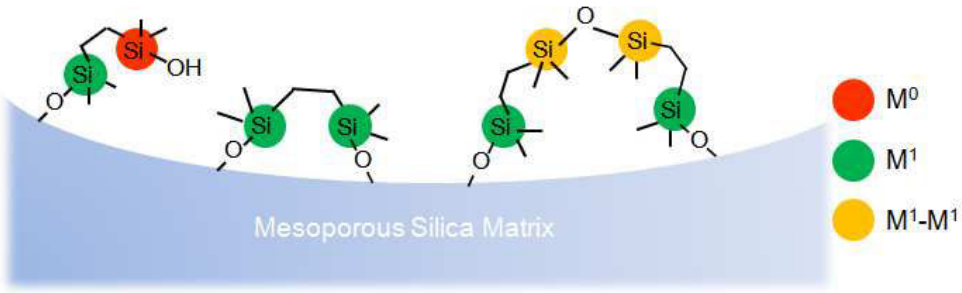

Figure 10. Possible existence form of grafted EBDMS on the surface of mesoporous silica.

Table 3. ^{27}Al quantitative NMR analysis of as-made Al-GPS and VAl-GPS.

Sample	Al (tet)	Al (oct)	Al (penta)
1Al-GPS	59	31	10
(1-1)VAl-GPS	55	35	10
3Al-GPS	70	22	8
(1-3)VAl-GPS	73	19	8
(3-3)VAl-GPS	61	31	8

The ^{27}Al quantitative NMR spectra of as-made Al-GPS and VAl-GPS (Appendix A7.2) and their quantitative analysis of NMR peaks (table 3) show that there are three types of Al in the low loading (1 % Al) samples: tetrahedral Al (~55 ppm), pentahedral Al (~35 ppm), and octahedral (~5 ppm) Al; while for the higher loading (3 % Al) samples, there were more tetrahedral Al species. In all these samples, the main existing form of grafted Al is tetrahedral Al.

5.3.3 Vanadium species

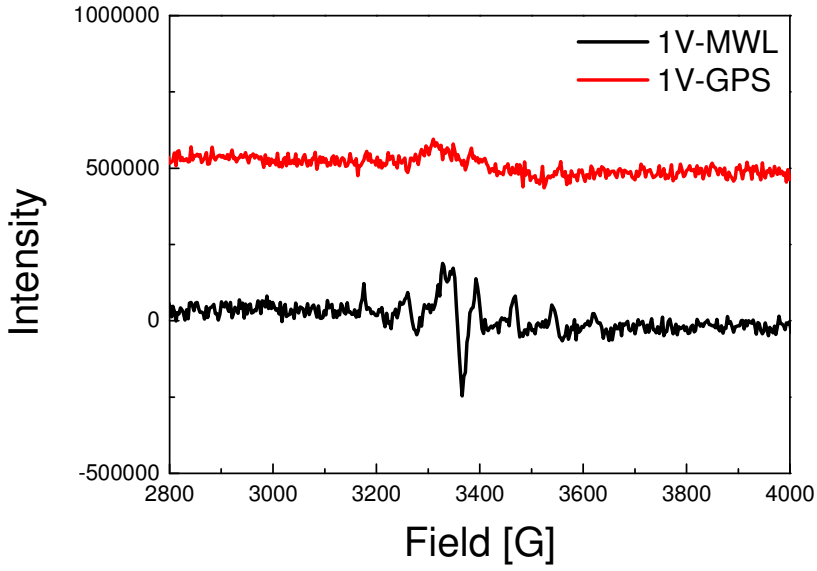

Figure 11. EPR spectra of 1V-MWL and 1V-GPS.

Figure 11 shows the EPR spectra of as-made samples of 1V-MWL and 1V-GPS. Unlike the hyperfine splitting signal of 1V-MWL, the grafted sample 1V-GPS has hardly any signal of vanadyl ions $(V^{IV}=O)^{2+}$, it means the vanadium ions in 1V-GPS were EPR silence $(V^{V}=O)^{3+}$, which was the same vanadium species as the vanadium precursor used for grafting.

UV-vis spectra of Ti/Zr/Ce/Al-GPS shows no obvious signal for Zr-GPS and Al-GPS, but shows high peaks for Ti-GPS and Ce-GPS, and the peak position of Ce overlapped with the peak position of vanadium (Figure 12). Comparing with the sample V-GPS-cal (Figure 13), the samples VTi/Zr/Ce/Al-GPS-cal (Figure 14) with anchor ions show an obvious blue shift of peaks in UV-vis spectra which means a better dispersion of vanadium. Different loading ratio of vanadium and anchor ions was compared (Figure 14), when the grafted anchor ions were three times ratio to the loading of vanadium, there is more blue shift than the sample with one to one ratio of anchor ions. So the 3:1 ratio of anchors to V was superior to the 1:1 ratio.

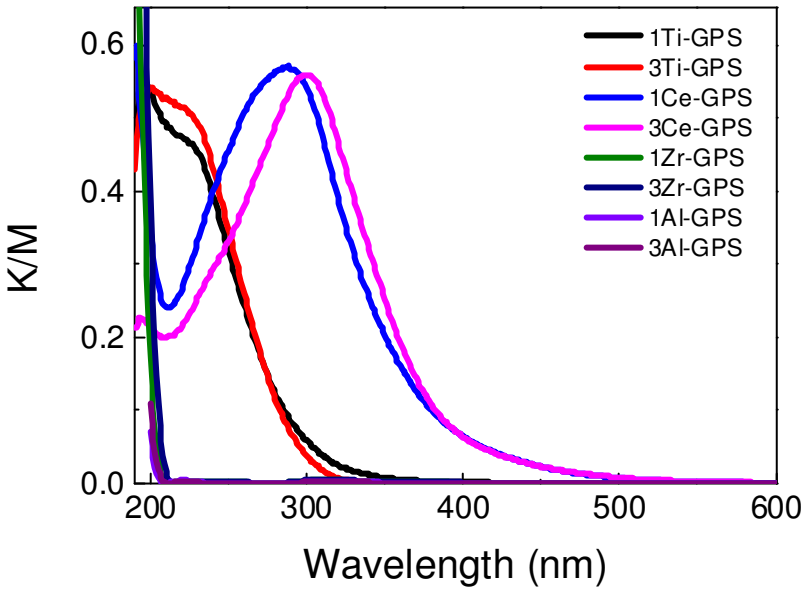

Figure 12. UV-vis spectra of Ti/Zr/Ce/Al-GPS. MWL-cal was used as blank, and before measurement, samples were diluted by MWL-cal to keep the spectra intensity in the range of 0.2-0.8 K/M.

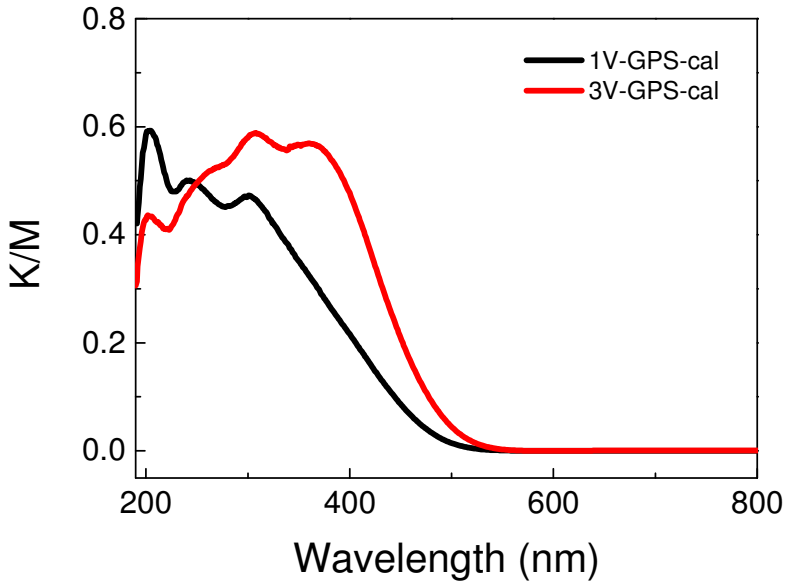

Figure 13. UV-vis spectra of V-GPS-cal. MWL-cal was used as blank, and before measurement, samples were diluted by MWL-cal to keep the spectra intensity in the range of 0.2-0.8 K/M.

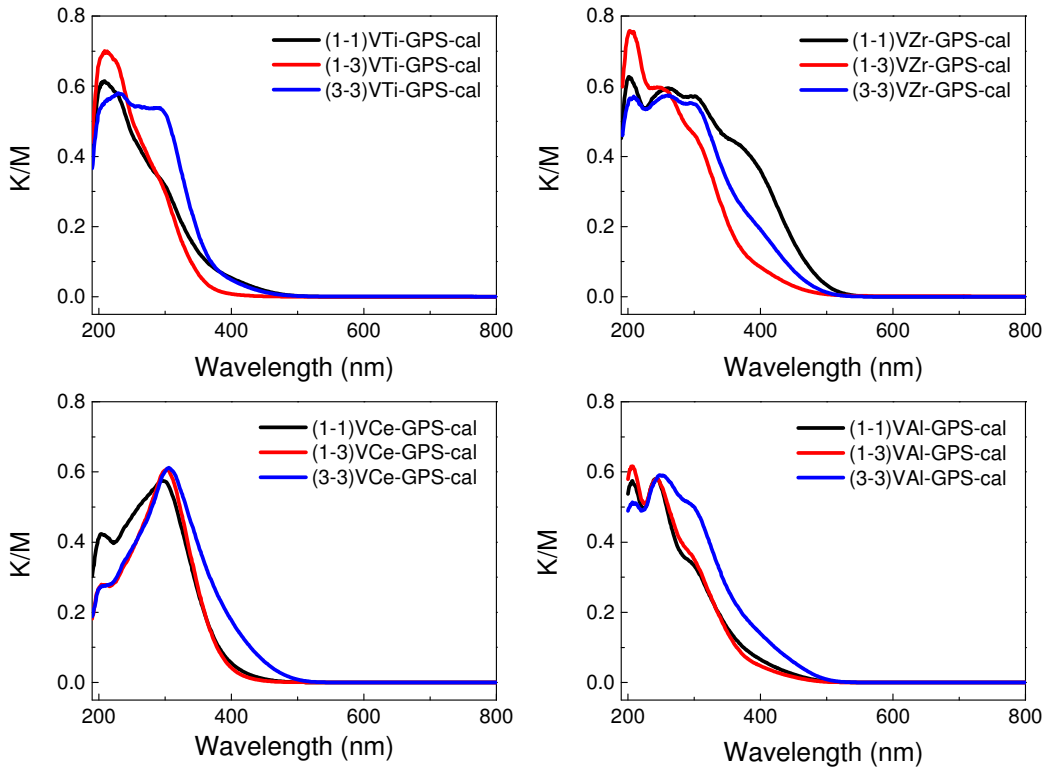

Figure 14. UV-vis spectra of V-Ti/Zr/Ce/Al-GPS. MWL-cal was used as blank, and before measurement, samples were diluted by MWL-cal to keep the spectra intensity in the range of 0.2-0.8 K/M.

The setting of 3 times molar ratio of anchors to vanadium was based on the model displayed in Figure 15. On the partial silylated surface of mesoporous silica, the anchor ions were grafted as targets to provide grappling sites of the vanadium and to avoid the aggregation of vanadium species. There are two level of isolation effects: the EBDMS groups facilitated the isolation of anchor ions and the anchors facilitated the isolation of vanadium species. In the idea structure model, one tetrahedron vanadium site needs three tetrahedron anchor ions as grappling, and the linkage between vanadium and anchor was expected to be stronger than the linkage between vanadium and silica surface. So there are two roles of anchor ions: to promote the dispersion of vanadium and to strengthen the grappling of vanadium thereby avoiding the leaching of vanadium.

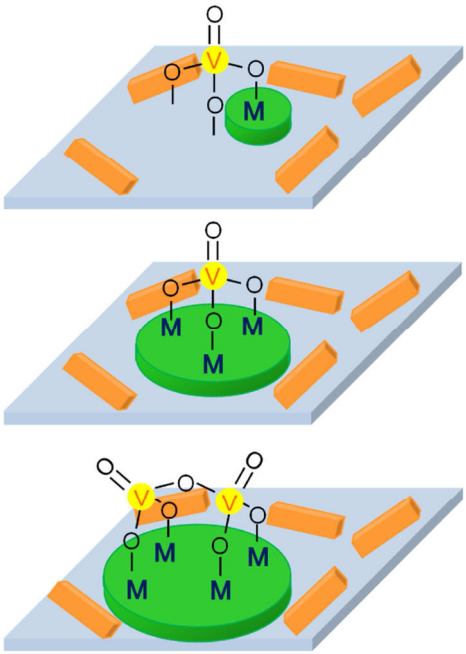

Figure 15. Schematic idealized models of anchoring effect on the surface of mesoporous silica modification with EBDMS functions (beige blocks): top, with single anchoring ion; middle, with three clustered anchoring ions; bottom, with four clustered anchoring ions; M=Ti/Al/Zr/Ce anchor ions, V = vanadium.

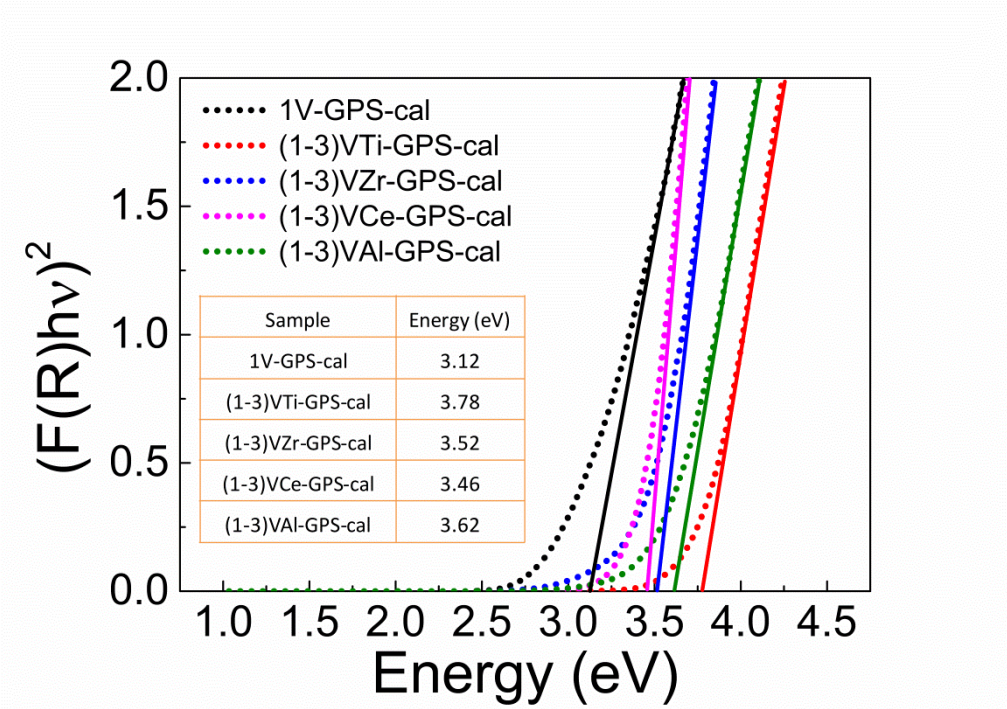

Figure 16. Tauc's plot and the corresponding edge energy of (1-3)VTi/Zr/Ce/Al-GPS-cal based on their UV-vis spectra.

Based on the UV-vis spectra of (1-3)VTi/Zr/Ce/Al-GPS-cal, Tauc's plot was drawn to compare the edge energy of different samples (Figure 16). Compared to 1V-GPS-cal, all the four samples of (1-3)VTi/Zr/Ce/Al-GPS-cal has a higher edge energy, which means the grafting of 3 times anchor ions is helpful for the better dispersion vanadium, and Ti/Al has a stronger anchor effect than Zr/Ce ions by grafted on the surface of mesoporous silica.

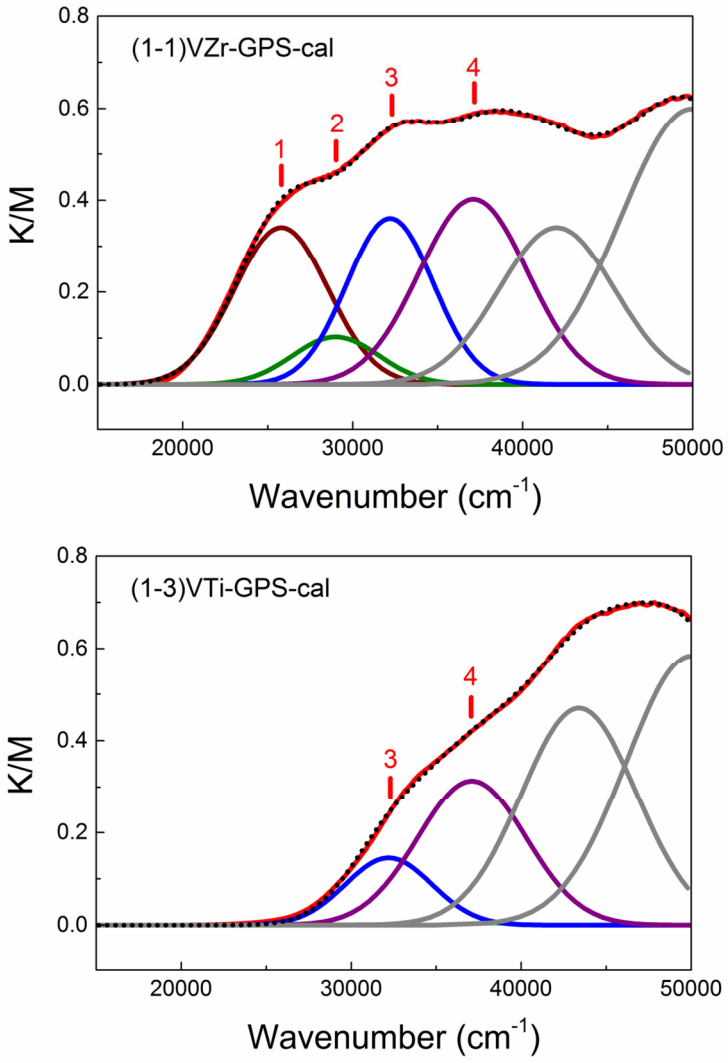

Figure 17. UV-vis spectra of (1-1)VZr-GPS-cal and (1-3)VTi-GPS-cal fitted with Gaussian curves. (MWL-cal was used as blank, and before measurement, samples were diluted by MWL-cal to keep the spectra intensity in the range of 0.2-0.8 K/M.) Peak 1, 2, 3, 4 pointing the center of Gaussian curves at 25800 cm^{-1}, 29000 cm^{-1}, 32200 cm^{-1} and 37100 cm^{-1} respectively (The Gaussian fitting data are collected in Table A5.2.2).

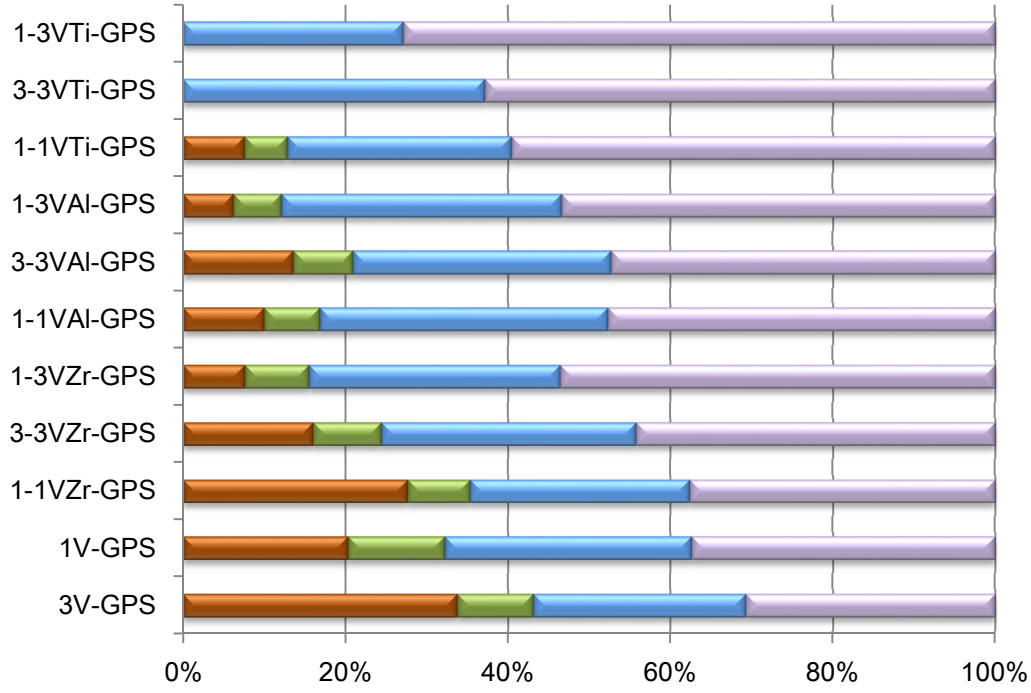

Figure 18. Composition of the relative intensities of Gaussian curves 1 (brown bars, center = 25800 cm^{-1}, FWHM = 6500 cm^{-1}, Ee = 2.7 eV), curves 2 (green bars, center = 29000 cm^{-1}, FWHM = 6000 cm^{-1}, Ee = 3.2 eV), curves 3 (blue bars, center = 32200 cm^{-1}, FWHM = 6000 cm^{-1}, Ee = 3.5 eV) and curves 4 (purple bars, center = 37100 cm^{-1}, FWHM = 7500 cm^{-1}, Ee = 4.1 eV) in the fitting of electron transfer band of V-Al/Ti/Zr/Ce-GPS-cal based on the UV-vis spectra.

The UV-vis spectra of V-Al/Ti/Zr/Ce-GPS-cal can be fitted by the Gaussian curves, and the fitting area of different peaks can provide the detail informations of the dispersion of each vanadium species (Figure 17). The peak at 25800 cm^{-1} corresponding to the 2D draft vanadium with the edge energy at about 2.7 eV, the peak at 29000 cm^{-1} corresponding to the 1D chains of vanadium with the optical gaps at about 3.2 eV, the peak at 32200 cm^{-1} corresponding to the vanadium dimers exhibit the optical gpas at about 3.5 eV and the peak at 37100 corresponding to the isolated vanadium species with the optical gaps at about 4.1 eV. Based on the relative intensities of the above fitting peaks, the bar chart (Figure 18) can be drown to compare the dispersion of different vanadium species in different samples. It is obvious that the samples with anchor ions has relatively smallar brown bars than the

samples without any anchor, especially the samples with 3 % Ti anchors has no brown bars, but have larger purple bars than the other samples, which means the Ti anchors have a stronge efficient to improve the ratio of isolated monomeric vanadium species.

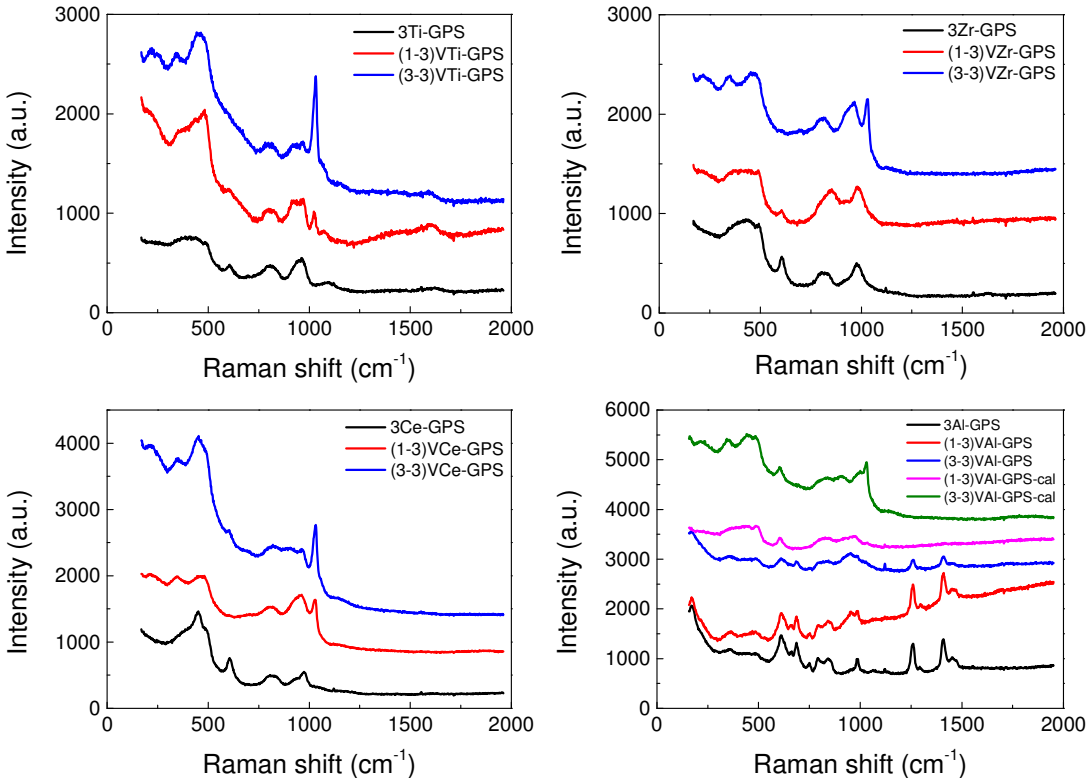

Figure 19. Raman spectra of VTi/Al/Zr/Ce-GPS.

In Figure 19, all the samples grafted with vanadium have a band at 1030 cm^{-1} which attributed to the V=O stretching vibration of monomeric species bond directly to the support (for the 3 % vanadium samples this band is more clear, while for some of the 1 % vanadium samples, this band is weak and overlapped with the bands nearby). The bands between 1100 cm^{-1} to 1500 cm^{-1} of as-made Al-GPS come from the ν(C–C) stretching vibration from the hydrocarbon chain in the Al precursor sodium bis(2-methoxyethoxy)aluminum hydride, which disappeared after the calcination. The band at 490 cm^{-1}, 610 cm^{-1}, 810 cm^{-1}, and 970 cm^{-1} come from the silica matrix.

Table 4. Elemental analysis of VTi/Zr/Ce/Al-GPS.

Sample	V (mol%)	M (mol%)
1V-GPS	1.07	0
(1-3)VTi-GPS-cal	1.04	3.28
(1-3)VAl-GPS-cal	0.99	3.21
(1-3)VZr-GPS-cal	1.1	2.76
(1-3)VCe-GPS-cal	1.05	2.29

The elemental analysis of VTi/Zr/Ce/Al-GPS (Table 4) indicated the stoichiometric vanadium was fully grafted on Ti/Zr/Ce/Al-GPS (data within experimental error); the difference loading of anchor ions indicated that Zr and Ce ions are more difficult to be grafted on GPS than the Ti and Al ions. The leaching test will be discussed in chapter 7.

5.4 Conclusion

Vanadium with different anchor ions (Al/Ti/Zr/Ce) were grafted on the surface of partially silylated mesoporous silica, EBDMS functional groups were incorporated as patterns to facilitate the isolation of metal ions, and the partial coverage of EBDMS groups was about 70 % of the total surface area of silica. After grafting, the EBDMS groups adopt three types of states (mono- or bipedal or engaged in a bipedal pairs), all characterized using solid state NMR. The anchored ions are grafted inside the patter of grafted EBDMS functions. The vanadium was then grafted on the anchored ions, forcing vanadium ions to disperse themselves avoiding the formation of large aggregate. All these surface modifications were obtained without modification of the hexagonal mesoporous structure. After each step of surface modification, one observed a systematic decrease of the pore diameter, specific surface area and pore volume consistent with a progressive occupation of internal space of the support. From UV-vis spectra and Tauc's plot, one measured the band gap that is correlated with the vanadium dispersion and found out that Al/Ti/Zr/Ce anchoring ions can effectively assist the vanadium species to have a better dispersion. A mol ratio of 3:1 anchoring ions to vanadium ions was found systematically better than the 1:1 mol ratio for a higher vanadium dispersion and Ti anchor ions have the strongest anchoring effect. The grafted vanadium exist as isolated V^{5+} species, no clusters of vanadium were observed.

5.5 References

1. Abry, S.; Albela, B.; Bonneviot, L. *C. R. Chim.* **2005,** 8, (3), 741-752.

2. Badiei, A.; Bonneviot, L.; Crowther, N.; Ziarani, G. M. *J. Organomet. Chem.* **2006,** 691, (26), 5911-5919.

3. Abry, S.; Lux, F.; Albela, B.; Artigas-Miquel, A.; Nicolas, S.; Jarry, B.; Perriat, P.; Lemercier, G.; Bonneviot, L. *Chem. Mater.* **2009,** 21, (12), 2349-2359.

4. Abry, S.; Thibon, A.; Albela, B.; Delichère, P.; Banse, F.; Bonneviot, L. *New J. Chem.* **2009,** 33, (3), 484-496.

5. Calmettes, S.; Albela, B.; Hamelin, O.; Menage, S.; Miomandre, F.; Bonneviot, L. *New J. Chem.* **2008,** 32, (4), 727-737.

6. Zhang, K.; Albela, B.; He, M.-Y.; Wang, Y.; Bonneviot, L. *PCCP* **2009,** 11, (16), 2912-2921.

7. Zhang, K.; Lam, K. F.; Albela, B.; Xue, T.; Khrouz, L.; Hou, Q. W.; Yuan, E. H.; He, M. Y.; Bonneviot, L. *Chem. Eur. J.* **2011,** 17, (50), 14258-14266.

8. Jollet, V.; Albela, B.; Sénéchal-David, K.; Jégou, P.; Kolodziej, E.; Sainton, J.; Bonneviot, L.; Banse, F. *Dalton Trans.* **2013,** 42, (32), 11607-11613.

9. Chaignon, J.; Stiriba, S.-E.; Lloret, F.; Yuste, C.; Pilet, G.; Bonneviot, L.; Albela, B.; Castro, I. *Dalton Trans.* **2014,** 43, (25), 9704-9713.

10. Zribi, S.; Albela, B.; Bonneviot, L.; Zina, M. S. *Appl. Catal., A* **2015,** 502, 195-203.

11. Zhang, K.; Zhang, Y.; Hou, Q.-W.; Yuan, E.-H.; Jiang, J.-G.; Albela, B.; He, M.-Y.; Bonneviot, L. *Microporous Mesoporous Mater.* **2011,** 143, (2), 401-405.

12. Chaignon, J.; Bouizi, Y.; Davin, L.; Calin, N.; Albela, B.; Bonneviot, L. *Green Chem.* **2015,** 17, (5), 3130-3140.

13. Zheng, Y. École Normale Supérieure de Lyon, Lyon, France, **2014**.

Chapter 6. Surface molecular engineering of vanadium containing MCM-41 with partial thermal treatment (PTT) technique

6.1 Introduction

Thermal treatment was widely used for removing the template in mesoporous silica or zeolites, the typical procedure was to do a calcination at 550 ^{o}C for 6 hours. Thermal gravity analysis (TGA) curves were applied to show the decomposition temperature of the organic constituent in mesoporous silica as well as to check the residual organic template in mesoporous silica after calcination or chemical extraction. MCM-41 can be functionalized by grafting of trimethylsilyl (TMS) groups, the coverage of TMS groups can be controlled by molecular stencil patterning (MSP) technique.[1-3]

In this chapter, we will apply a partial thermal treatment (PTT) to control the coverage of TMS groups and facilitate the following grafting of active metal sites. Inspired by the TGA curve of MCM-41 functionalized by total coverage of TMS groups, we set an appropriate temperature of calcination, when the tube furnace ramped up to the desired temperature, the heating will be stopped and the tube furnace will be opened immediately without any cooling segment. By this kind of partial calcination modification, the surface coverage of organic functional groups will be controlled and the exposure of Si-OH groups will provide good opportunities for high dispersion of vanadium particularly with the help of anchoring ions such as Ti(IV), Zr(IV), Ce(IV) and Al(III) ions. Herein, the structures and characterization of these grafted V-(Ti/Zr/Ce/Al)-MCM-41 catalysts based on PTT technique will be discussed in detail.

6.2 Experiments

6.2.1 Surface molecular engineering of MCM-41 with TMS

MWL-R was prepared as it was described in chapter 4.2.1.

1.0 g MWL-R was stirred at 130 ^{o}C in vacuum for 2 hours to remove the H_2O and air absorbed on the solid, then cooled down in argon to room temperature, after

that, 2.0 mL hexamethyldisilazane (HDMSA) was dissolved in 40 mL cyclohexane and added to the solid with stirring under argon. The mixture was stirred under argon for 0.5 hours at room temperature, then refluxed at 80 ^{o}C in argon for 16 hours. After filtration, the solid was washed with cyclohexane and dried at 80 ^{o}C overnight. The white powder was named MWL-TMS.[3]

6.2.2 Partial thermal treatment of modified MCM-41

1.0 g MWL-TMS was calcined in a tube furnace with flowing air, the calcination program was set as: 2 ^{o}C/min to ramp up from room temperature to 500 ^{o}C, then the heating was stopped and the tube furnace was opened immediately without the cooling segment. The product was named MWL-TMS-cal500, or PC (Partial Calcined MCM-41) for short.[4]

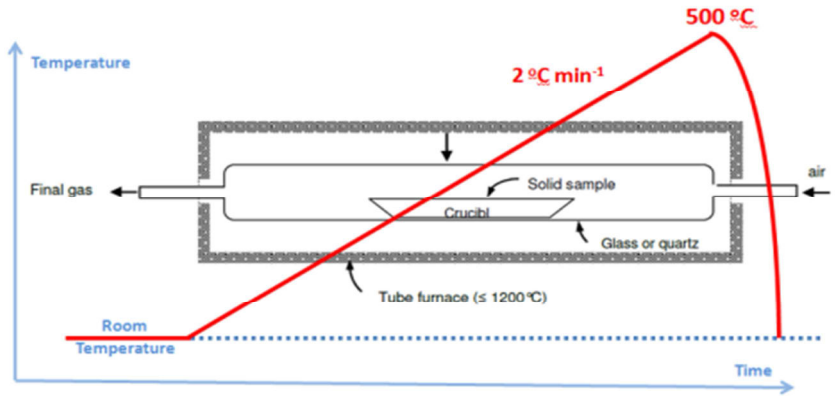

Figure 1. Schematic of fast thermal treatment of modified MCM-41 in a tube furnace

6.2.3 Grafting of Ti/Zr/Ce/Al on thermal treated MCM-41

The grafting of Ti/Zr/Ce/Al on PC followed the same procedure as it was described in chapter 5.2.2, the products were named Ti/Zr/Ce/Al-GPC (Grafted Partial Calcined MCM-41) respectively.

6.2.4 Grafting of vanadium on Ti/Zr/Ce/Al containing MCM-41

The grafting of vanadium on Ti/Zr/Ce/Al-GPC followed the same procedure as it was described in chapter 5.2.3, the products were named VTi/Zr/Ce/Al-GPC respectively.

6.3 Results and discussion

6.3.1 Characterization of the TMS functional groups

In chapter 5, it has been proved that the surface silylation on mesoporous silica does not change the structure of silica matrix, and the thermal treatment temperature did not exceed the temperature of conventional calcination of mesoporous silica, therefore the partial thermal treatment and surface modification of samples in this chapter do not influence the hexagonal structure of silica framework structure, the XRD characterization is omitted here, the XRD patterns of samples in chapter 5 can be used as references.

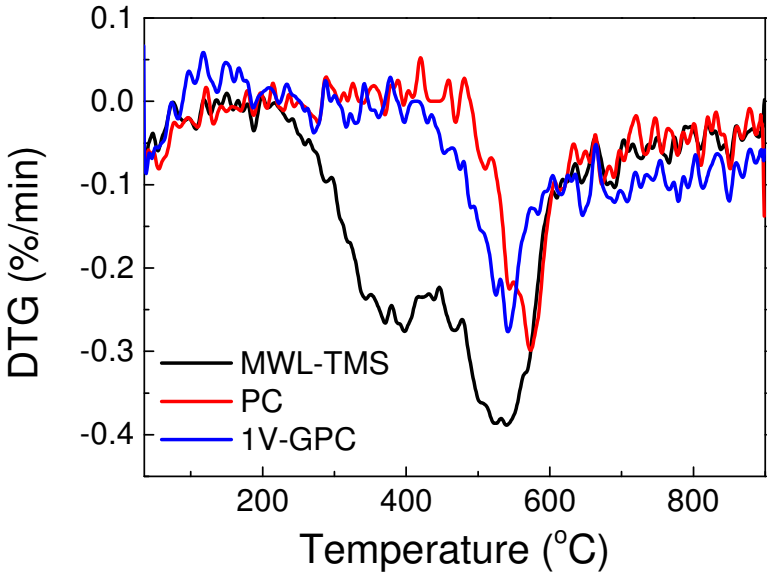

Figure 2. DTG analysis of as-made MWL-TMS, PC, and 1V-GPC.

The weight loss of MWL-TMS in the thermal gravity analysis comes from the thermal decomposition of methyl groups and the combustion of alkyl moieties. The weight loss in the region below 130 ^{o}C come from the desorption of H_2O, the peak between 200 ^{o}C to 500 ^{o}C come from the partial decomposition of methyl groups and the peak in the region above 500 ^{o}C come from the combustion of alkyl moieties. With the partial calcination, the heating was stopped at 500 ^{o}C, so only part of the methyl groups were decomposed or evolved, the alkyls were still maintained on the surface of mesoporous silica.[4] Comparing the samples before and after the partial

calcination, the differences of their DTG curves show that sample PC do not have weight loss in the region below 500 ^{o}C, the weight loss in the region of 500 ^{o}C to 700 ^{o}C is the same for the three samples in Figure 2, the grafting of vanadium did not change the alkyl on PC. The residual mass of V/Ti/Zr/Ce/Al-GPC from the TG analysis are very similar (Appendix 3.3), there was no loss of the alkyls during the grafting of metal ions.

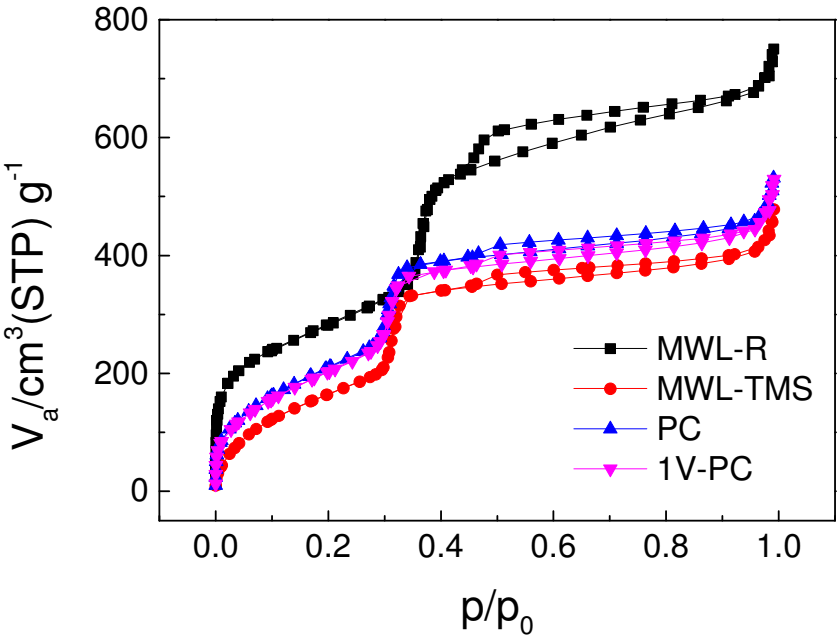

Figure 3. N_2 adsorption-desorption isotherms of MWL-R, MWL-TMS, PC (MWL-TMS-cal500), 1V-PC.

The N_2 adsorption-desorption isotherms of samples in Figure 3 exhibit the typical type IV isotherms of mesoporous silica, no destruction of the hexagonal structures during the silylation and thermal treatment. Among the four samples in Figure 3, after chemical extraction of surfactant, the mesoporous silica has the highest surface area and pores volumes (MWL-R), after a full silylation of TMS functional groups (MWL-TMS), the surface area decreased from 1024 $m^2 \cdot g^{-1}$ to 679 $m^2 \cdot g^{-1}$ and pores volume decreased from 0.92 $cm^3 \cdot g^{-1}$ to 0.53 $cm^3 \cdot g^{-1}$, this is because the TMS groups were grafted on the porous surface and occupied some space in the pores, the diameter of the pores has about 0.5 nm decrease as well. Due to the full coverage of

TMS groups on the surface of pores, the C parameter which corresponding to the silanol groups was very low after the silylation. After the partial thermal treatment, the surface area and pores volume of PC increased to 831 $m^2 \cdot g^{-1}$ and 0.61 $cm^3 \cdot g^{-1}$, which comes from the space released by the decomposition of some methyl groups in TMS during the thermal treatment. The porosity data of samples VTi/Zr/Ce/Al-GPC can be found in Table 1. After the grafting of low ratio (1~3 mol%) metal ions on the mesoporous surface, the porosity data of these metal grafted samples was very similar with the sample PC, about 3~20 % decrease of pore diameter, specific surface area and pore volume were observed due to the loading of metal species. All these surface modifications and their corresponding structure changes were controllable and monitored by the N_2 adsorption-desorption characterization very clearly.

Table 1. Porosity data derived from N_2 adsorption-desorption isotherms.

Sample	V_{total}[a] ($cm^3 \cdot g^{-1}$)	V_p[b] ($cm^3 \cdot g^{-1}$)	S_{BET}[c] ($m^2 \cdot g^{-1}$)	d_{HK}[d] (nm)	d_{BdB}[e] (nm)	C
MWL-TMS	0.72	0.53	679	2.9	3.5	22
PC	0.81	0.61	831	2.9	3.5	29
3Ti-GPC	0.75	0.57	806	2.8	3.4	30
3Zr-GPC	0.72	0.52	772	2.8	3.3	28
3Ce-GPC	0.74	0.55	793	2.9	3.5	31
3Al-GPC	0.6	0.47	683	2.8	3.4	33
(1-3)VTi-GPC	0.74	0.55	794	2.8	3.3	30
(1-3)VZr-GPC	0.72	0.52	761	2.7	3.3	29
(1-3)VCe-GPC	0.77	0.54	789	2.9	3.5	31
(1-3)VAl-GPC	0.6	0.47	679	2.8	3.4	34
1V-GPC-cal	0.69	0.57	811	2.9	3.5	104
1V-GPC	0.79	0.57	796	2.9	3.5	31

(a) V_{total} at $p/p_0 = 0.99$, accuracy ± 0.01 $cm^3 g^{-1}$; (b) V_p at $P/P_0 = 0$ on the adsorption plateau of t-plot, accuracy ± 0.01 $cm^3 g^{-1}$; (c) from BET equation at $0.05 \leq p/p_0 \leq 0.16$, accuracy ± 50 $m^2 g^{-1}$; (d) pore diameter extrapolated from Horvath-Kawazoe method, accuracy ± 0.1 nm; (e) pore diameter extrapolated from Broekhoff and De Boer method, accuracy ± 0.1 nm.

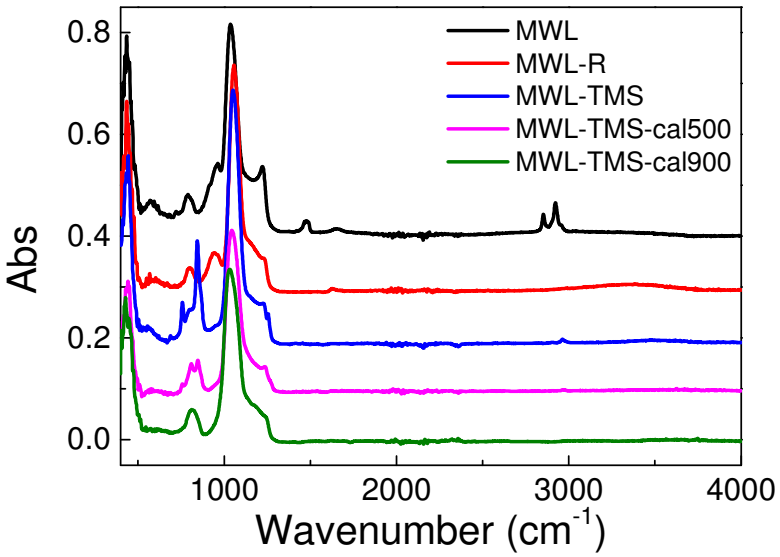

Figure 4. FT-IR spectra of MWL, MWL-R, MWL-TMS, MWL-TMS-cal500 (PC), and MWL-TMS-cal900.

In the FT-IR spectra of MWL (Figure 4), the bands in the region of 2800 cm^{-1} to 3000 cm^{-1} were derived from the C-H stretching vibrations of $-CH_3-$ and $-CH_2-$ in surfactant CTATos, which were nonexistent after the removal of surfactant by chemical extraction (MWL-R). After the grafting of TMS functional groups (MWL-TMS), due to the Si-C stretching vibrations of TMS on silica, two sharp peaks can be observed at 757 cm^{-1} and 845 cm^{-1}, and a weak band appeared at 2961 cm^{-1} is assigned to the asymmetric C-H stretching vibrations of TMS. By the partial thermal treatment at 500 ^oC (MWL-TMS-cal500), the peaks at 757 cm^{-1}, 845 cm^{-1}, and 2961 cm^{-1} were decreased, this is because part of the $-CH_3$ groups in TMS were consumed, there were less Si-C stretching vibrations but more groups as $=Si(CH_3)_2$ instead of $-Si(CH_3)_3$.[4] If the thermal treatment temperature was set as 900 ^oC, all the TMS functional groups can be removed, so the peaks at 757 cm^{-1}, 845 cm^{-1}, and 2961 cm^{-1} were disappeared (MWL-TMS-cal900). After the grafting of VTi/Zr/Ce/Al metal ions on the partial thermal treated mesoporous silica with TMS groups, the TMS bands at 757 cm^{-1} and 845 cm^{-1} did not change (Appendix A4.3), so there was no loss of TMS groups after the grafting of metal ions.

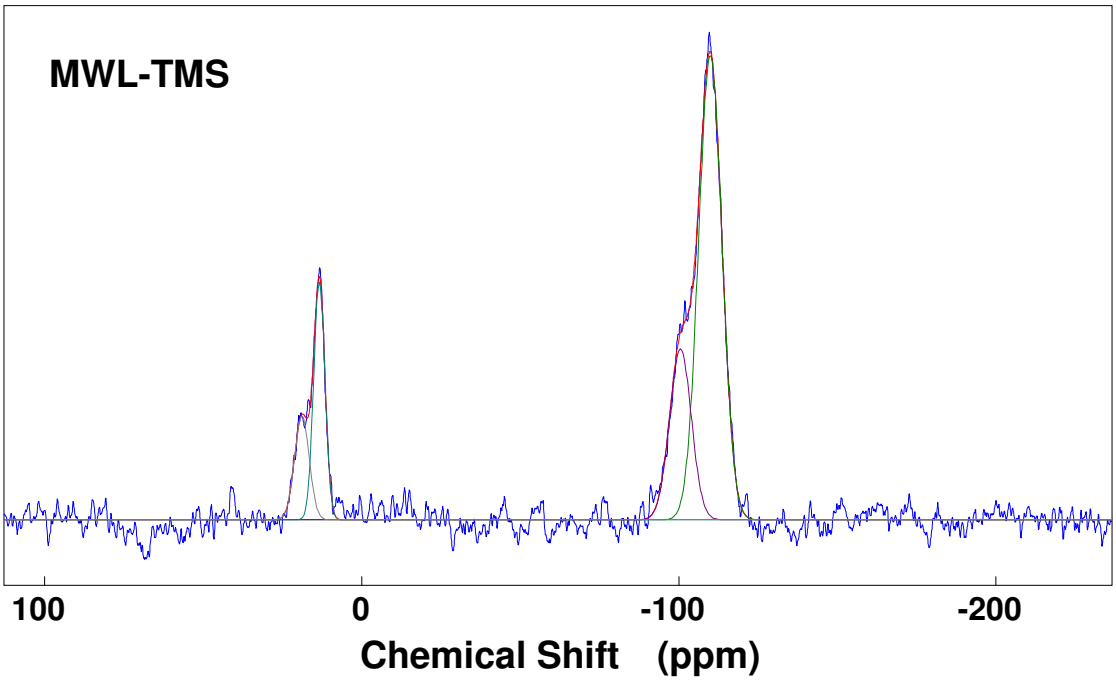

Figure 5. ^{29}Si quantitative NMR spectra of MWL-TMS.

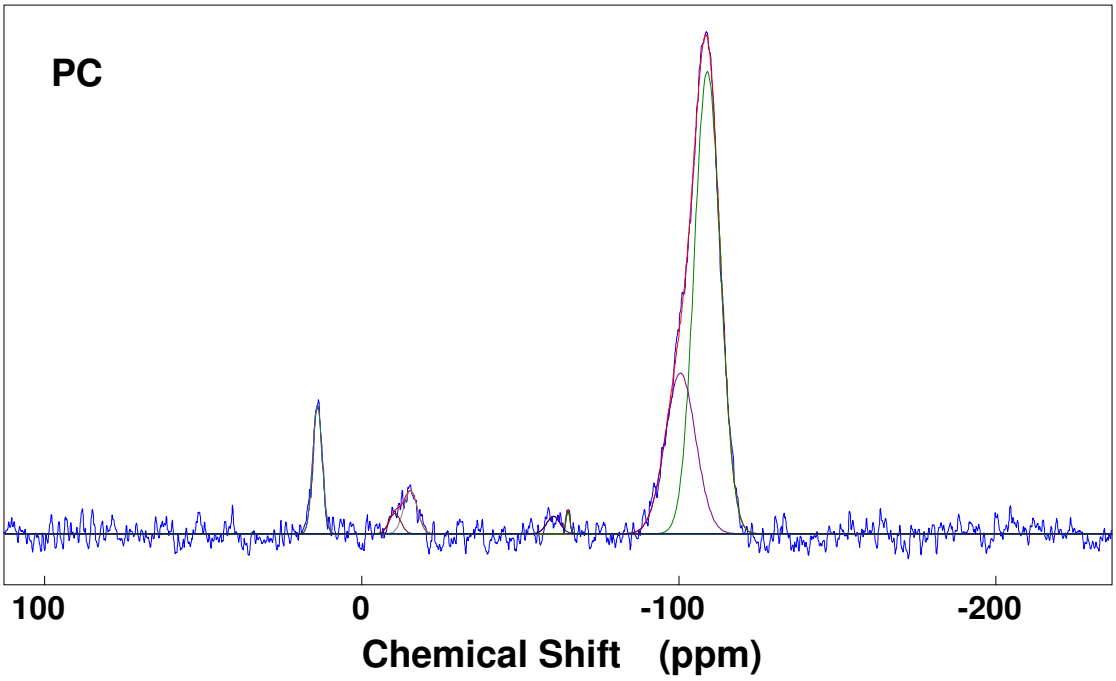

Figure 6. ^{29}Si quantitative NMR spectra of PC (MWL-TMS-cal500).

Table 2. ^{29}Si quantitative NMR analysis of MWL-TMS and PC.

Sample	**Q^4**	**Q^3**	**Q^2**	**Si (iorg)**
MWL-TMS	58	20	0	78
PC	62	26	0	88
Sample	**M^1**	**M^0**	**M^1-M^1**	**M**
MWL-TMS	14	8	0	22
PC	6	0	0	6
Sample	**T^1**	**T^2**	**T^3**	**T**
MWL-TMS	0	0	0	0
PC	0	1	1	2
Sample	**D^1**	**D^2**		**D**
MWL-TMS	0	0		0
PC	1	3		4

Figure 5 and Figure 6 show the ^{29}Si quantitative NMR spectra of MWL-TMS and PC, the quantitative analysis NMR peaks was summarized in Table 2. The ^{13}C NMR spectra of MWL-TMS and PC were collected in Appendix A7.3.

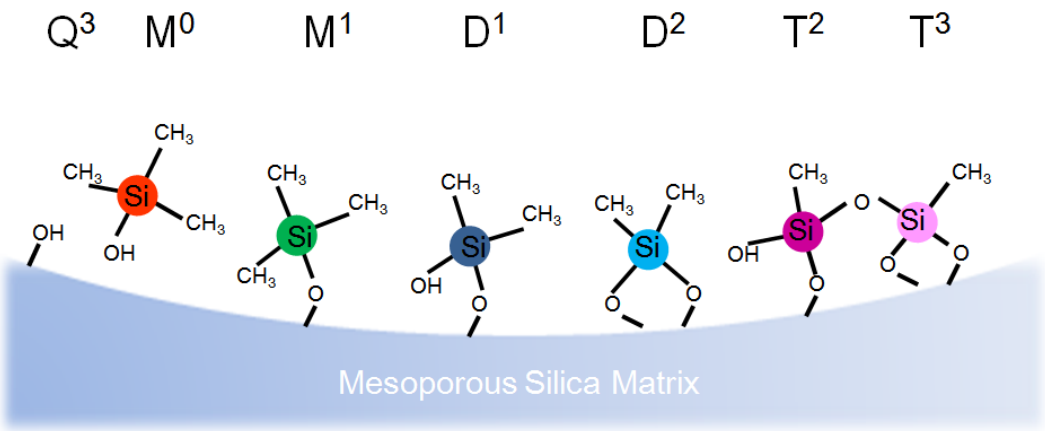

Figure 7. Different existence forms of grafted TMS functional groups on the surface of mesoporous silica.

There are four types of silica in MWL-TMS: Q^4 (-109 ppm), Q^3 (-100 ppm), M^0 (20 ppm), M^1(14 ppm) (Figure 5). M^1 was regarded as the characteristic peak of grafted TMS functional groups linked to the silica matrix, M^0 comes from the excess TMS precursors adsorbed in the solid. There was 22 % of the organic Si (derived from Table 2) in MWL-TMS. After the partial thermal treatment, the ratio of organic Si in PC decreased to 12 % (derived from Table 2). There were no free TMS precursors M^0 in PC, but four new types of Si species appeared: D^1 (-10 ppm), D^2 (-15 ppm), T^2 (-60 ppm), T^3 (-65 ppm) (Figure 6), these four new Si species come from the evolution of TMS functional groups during the partial thermal treatment:[4] as some of the methyls were decomposed, bi-bonded species and bridged dimer Si species were appeared (Figure 7), the total ratio of these four Si species was 6 %, and the ratio of Si kept as M^1 was 6% as well. The grafted TMS functional groups undertake the role as islands to isolate the hydroxy on mesoporous silica, while the hydroxy on D^1, T^2, and Q^3 Si were still available for the following grafting of metal ions. The grafting process was as mild as the grafting steps in chapter 5, and the alkyls can be kept as the state in PC before the grafting, this has been proved by the FT-IR spectra in Appendix A4.3.

Table 3. ^{27}Al quantitative NMR analysis of 3Al-GPC and (1-3)VAl-GPC.

Sample	**Al (tet)**	**Al (oct)**	**Al (penta)**
3Al-GPC	80	17	3
(1-3)VAl-GPC	70	23	7

The ^{27}Al quantitative NMR spectra of 3Al-GPC and (1-3)VAl-GPC (Appendix A7.3) and their quantitative analysis of NMR peaks (Table 3) show that there are two types of Al in the samples: tetrahedral Al (~55 ppm), and octahedral (~5 ppm) Al; the main existing form of grafted Al is tetrahedral Al (~80 %), which can serve as the anchor sites for the grafting of vanadium species.

6.3.2 Vanadium species

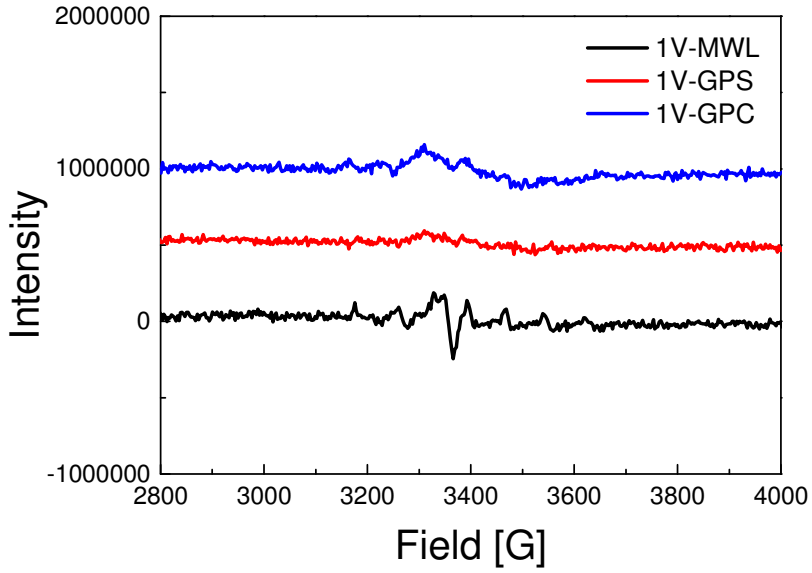

Figure 8. EPR spectra of 1V-MWL, 1V-GPS, and 1V-GPC.

Figure 8 shows the comparison of EPR spectra from the as-made samples of 1V-MWL and 1V-GPS. Only 1V-MWL has the hyperfine splitting signal of vanadyl ions $(V^{IV}=O)^{2+}$, the vanadium ions in 1V-GPS and 1V-GPC were EPR silence $(V^{V}=O)^{3+}$, which was the same vanadium species as the vanadium precursor used for grafting.

In Figure 9, the band at 490 cm^{-1}, 610 cm^{-1}, 810 cm^{-1}, and 970 cm^{-1} come from the silica matrix. All the three samples loading of 1 % vanadium have a band at 1030 cm^{-1} which attributed to the V=O stretching vibration of monomeric species bond directly to the support, the intensity of this peak in 1V-MWL is weaker than in 1V-GPS and 1V-GPC, because the grafted vanadium was on the surface of silica matrix, while in the one-pot incorporated sample 1V-MWL, part of the vanadium species was loading in the silica matrix walls. For the sample with anchor ions (Figure 10), the weak peak of V=O stretching vibration at 1030 cm^{-1} was overlapped by peaks nearby, and the sample with Al anchors has very strong fluorescence interference, so the signal of vanadium was difficult to be observed.

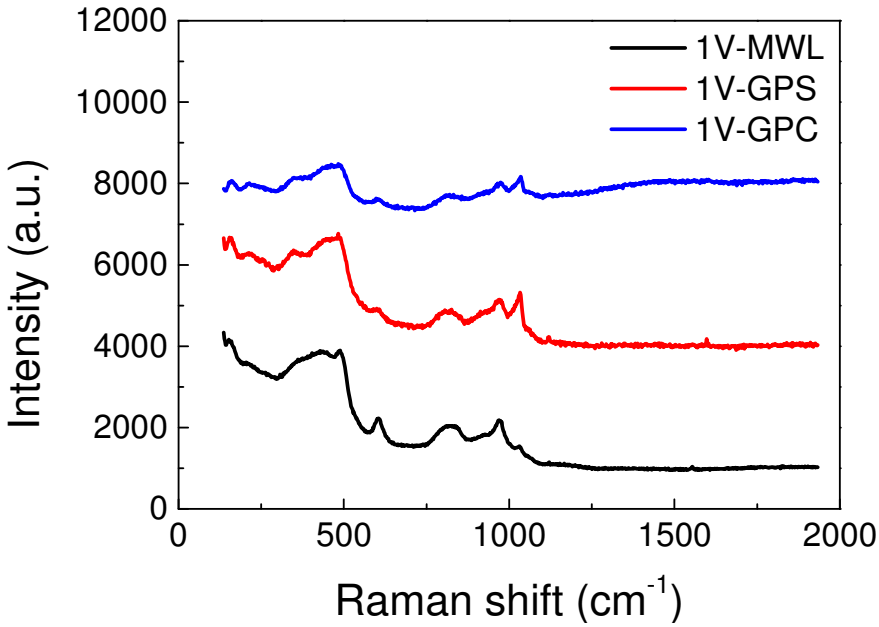

Figure 9. Raman spectra of 1V-MWL, 1V-GPS, and 1V-GPC.

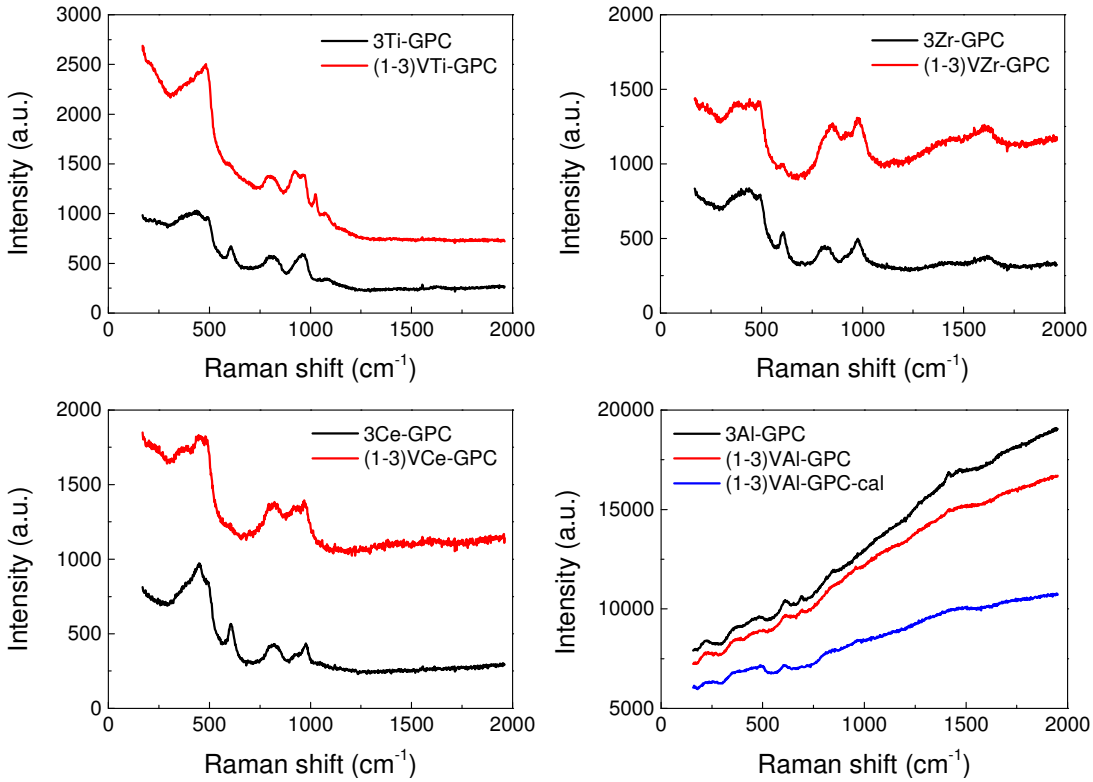

Figure 10. Raman spectra of VTi/Al/Zr/Ce-GPC.

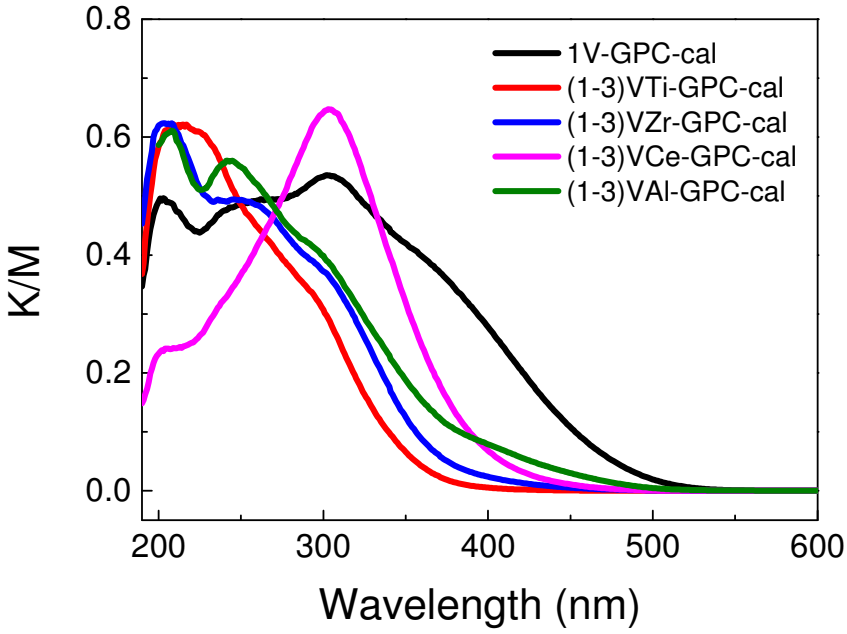

Figure 11. UV-vis spectra of VTi/Zr/Ce/Al-GPC-cal. MWL-cal was used as blank, and before measurement, samples were diluted by MWL-cal to keep the spectra intensity in the range of 0.2-0.8 K/M.

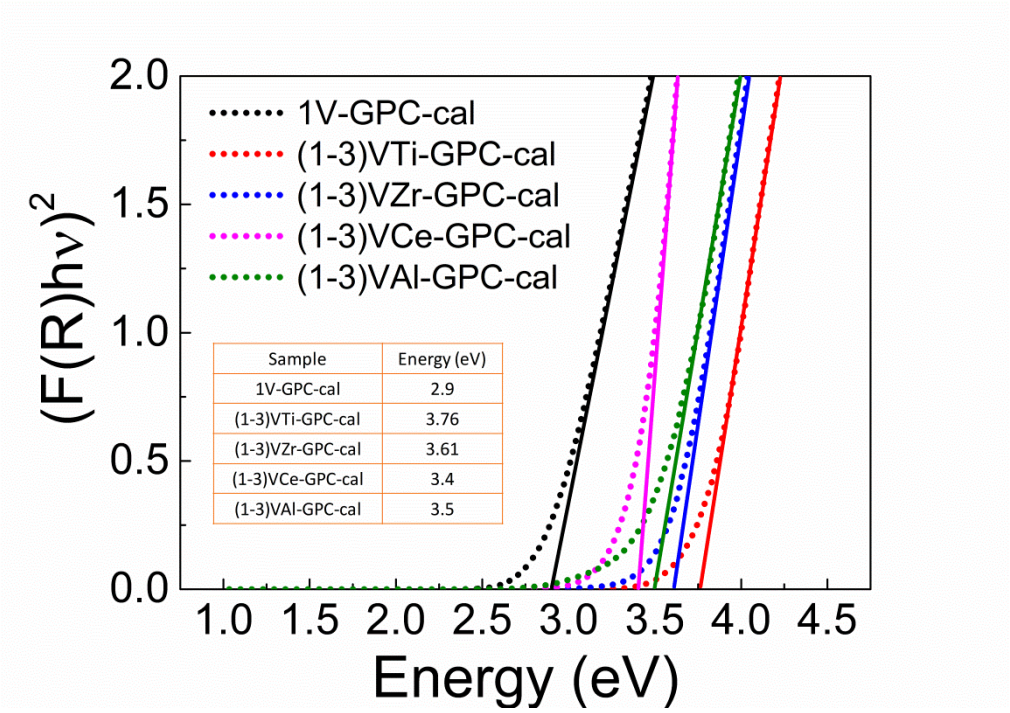

Figure 12. Tauc's plot and the corresponding edge energy of (1-3)VTi/Zr/Ce/Al-GPC-cal based on their UV-vis spectra.

Comparing with the UV-vis spectra of 1V-GPC-cal (Figure 11), the samples (1-3)VTi/Zr/Ce/Al-GPC-cal with anchor ions show an obvious blue shift in UV-vis spectra which means a better dispersion of vanadium. In order to show the effect of different anchor ions and to compare the edge energy of different samples clearly, Tauc's plot was drawn based on the UV-vis spectra of (1-3)VTi/Zr/Ce/Al-GPC-cal (Figure 12). All the four samples of (1-3)VTi/Zr/Ce/Al-GPC-cal have a higher edge energy than the sample 1V-GPC-cal, which means the grafting of 3 times anchor ions is helpful for the better dispersion of vanadium species, and Ti anchor ions have the most obvious anchor effect than Zr ions and Al ions by grafted on the surface of mesoporous silica. These results are compared with the data in chapter 5 in good agreement, so the partial thermal treatment with the TMS functional groups provide a comparable strategy to the molecular stencil patterning treatment with the EBDMS functions. The partial coverage of TMS groups provide the discrete sites for the grafting of anchor ions on the surface of mesoporous silica, the isolated anchors provide the grappling sites for the grafting of vanadium species. So the stronger linking and better dispersion of vanadium can be achieved.

Table 4. Elemental analysis of VTi/Zr/Ce/Al-GPC.

Sample	**V (mol%)**	**M (mol%)**
1V-GPC-cal	1.02	0
(1-3)VTi-GPC-cal	0.96	3.12
(1-3)VZr-GPC-cal	1.01	3.11
(1-3)VCe-GPC-cal	0.95	1.99
(1-3)VAl-GPC-cal	0.93	3.21

The elemental analysis of VTi/Zr/Ce/Al-GPC (Table 4) indicated the stoichiometric vanadium was fully grafted on Ti/Zr/Ce/Al-GPS (data within experimental error); comparing to the fully loading of anchor ions Ti/Zr/Al, Ce ions were more difficult to be grafted on GPC, this phenomenon may be aroused by the larger atom of Ce and less stable linkage between the Ce and SiO_2 matrix. The leaching test will be discussed in chapter 7.

6.4 Conclusion

Partial thermal treatment was applied to the TMS silylated mesoporous silica, by a simply programmed calcination, part of the methyl in TMS functional groups was decomposed, and the hydroxy which was available for the following grafting of metal ions can be isolated by the TMS islands, therefore the aggregation of grafted metal species can be avoided. Ti/Zr/Ce/Al anchors were grafted on the surface of TMS functionalized mesoporous silica before the incorporation of vanadium, a better dispersion of vanadium species with the TMS functions and anchor ions was confirmed by the UV-vis spectra and Tauc's plot with a 3:1 molar ratio of anchor ions to vanadium. All these modifications were on the surface of mesoporous silica without destruction of the hexagonal mesoporous structure of silica matrix, the regular decrease of the pores diameter, pores volume, and surface area can be observed due to the introduction of functional groups and metal species. The partial thermal treatment process is convenient and time-saving, which is on a par with the molecular stencil patterning technique for the obtaining of the controllable silylated mesoporous silica support, and it is a promising pervasive method to be applied to other supports such as silica nanoparticles, etc.

6.5 References

1. Abry, S.; Albela, B.; Bonneviot, L. *C. R. Chim.* **2005,** 8, (3), 741-752.
2. Badiei, A.; Bonneviot, L.; Crowther, N.; Ziarani, G. M. *J. Organomet. Chem.* **2006,** 691, (26), 5911-5919.
3. Zhang, K.; Albela, B.; He, M.-Y.; Wang, Y.; Bonneviot, L. *PCCP* **2009,** 11, (16), 2912-2921.
4. Fang, L. École Normale Supérieure de Lyon, Lyon, France, **2012**.

Chapter 7. Aerobic oxidation of lignin models with vanadium containing MCM-41 catalysts via high throughput screening (HTS)

7.1 Introduction

Selective transformation of lignin to value-added chemicals is a promising approach to take advantage of biomass. As lignin is a bulky polymer constituted by methoxylated phenoxy propanol units, the selective cleavage of carbon-carbon bond in lignin is an effective way to break lignin into small and utilizable molecules.[1] To facilitate the research of lignin transformation, some model molecules were chosen as substrates to represent the typical linkages (e.g. β-O-4) in lignin. Aerobic oxidation of lignin model molecule in a moderate reaction condition can be achieved with the assistance of transition metal catalysts.[2-6] As heterogeneous catalyst can be recycled and reused, it is imperative to develop the supported transition metal catalyst with high activity and less leaching for the oxidation of lignin models.

High throughput facility can allow the running of a large number of reactions at the same time, and the required sample quantity for each reaction is quite small. It provides a high efficient screening platform for the comparison of a series catalysts in a relative uniform condition.

In this chapter, the vanadium catalysts supported by mesoporous silica were applied for the aerobic oxidation of lignin models via high throughput screening, and the samples with high activity were picked out and were taken to run the lignin model oxidation reactions in high pressure autoclaves. Recycle test and leaching test were carried out to compare the stability of vanadium catalysts. Elemental analysis was carried out before and after the leaching test to compare the anchor effect of supported vanadium catalysts. The effects of the additional base and different solvents were compared and discussed as well.

7.2 Experiments

7.2.1 Synthesis of lignin model substrate 1,2-diphenyl-2-methoxyethanol (beta-methoxy-alpha-phenylphenethyl alcohol)

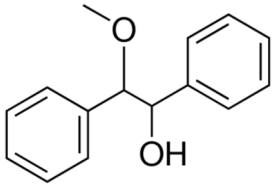

Figure 1. 1,2-diphenyl-2-methoxyethanol (beta-methoxy-alpha-phenylphenethyl alcohol) molecule.

Lignin model 1,2-diphenyl-2-methoxyethanol (β-methoxy-α-phenylphenethyl alcohol) was synthesized by the reducing of benzoin methyl ether, the preparation procedure was based on the method of Hanson.[2] 3.06 g benzoin methyl ether was dissolved in 50 mL dry ethanol and stirred at room temperature until clear, then 2.03 g sodium borohydride was added slowly into the above solution and stirred at room temperature (be careful of the large number of H_2 bubbles generated during the addition of sodium borohydride). After refluxing at 85 ^oC overnight, the solution was cooled in an ice bath, then 50 mL saturated solution of ammonium chloride was slowly added and the mixture was stirred for 1 hour (a lot of white solids appeared). Diethyl ether was added to the mixture, then filtration was carried out to remove the solid. The organic layer was extracted and washed with H_2O for 3 times, then washed with 0.1 M HCl for 2 times. After removing the solvent in a rotary evaporator, the white solid was obtained as the target product.

7.2.2 Synthesis of VCu/Fe-MWL

7.2.2.1 Preparation of Cu/Fe-MWL

Cu-MWL and Fe-MWL were prepared in a similar way as V-MWL except that copper(II) nitrate or iron(III) nitrate was dissolved in the deionized water before the adding of CTATos in the surfactant solution. After calcination, the light blue-green powder with 1 mol% Cu was named as 1Cu-MWL-cal, the earthy-yellow powder

with 1 mol% Fe was named as 1Fe-MWL-cal, and the grey-yellow powder with 0.5 mol % Cu and 0.5 mol % Fe was named as (0.5-0.5)CuFe-MWL-cal.

7.2.2.2 Preparation of VCu/Fe-GMW

The grafting of vanadium on Cu/Fe-MWL followed the same way as the preparation of VTi-GPS: Cu/Fe-MWL-cal was stirred in vacuum, then vanadium(V) triisopropoxide was dissolved in cyclohexane and added to the solid then reflux in argon, after filtration, washing, drying, and calcination, the product with 1 mol% V and 1 mol% Cu was named as (1-1)VCu-GMW-cal, and the product with 1 mol% V with 0.5 mol% Cu and 0.5 mol% Fe was named as (1-0.5-0.5)VCuFe-GMW-cal.

7.2.3 Oxidation reactions of lignin models with vanadium containing MCM-41 catalysts

7.2.3.1 High throughput screening (HTS)

The oxidation reactions of lignin models were carried out in a high-throughput experimentation facility equipment system in catalysis research and innovation center in university of Ottawa.

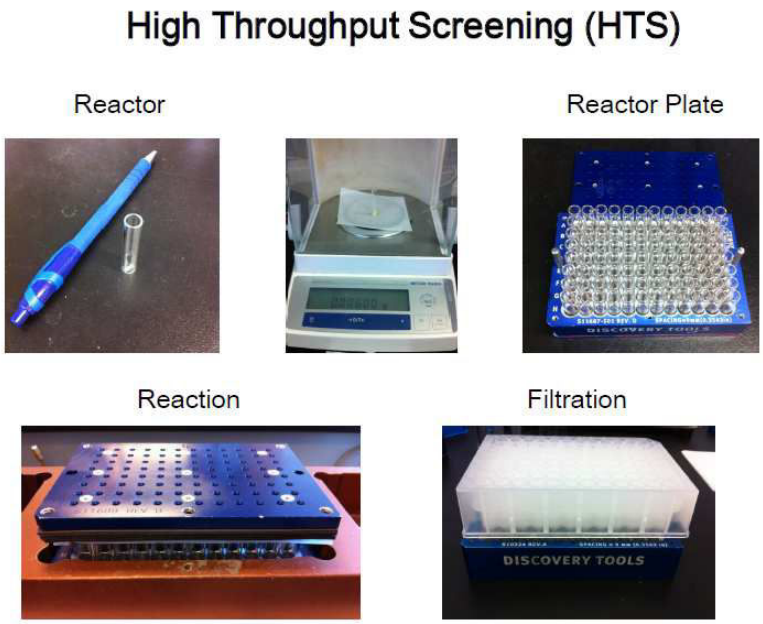

Figure 2. High throughput screening reaction facility.

The reactor was a glass test tube of 1 mL capacity, each reactor plate can hold 96

reactors at the same time. To prepare for the reaction, in each reactor, 6 mg vanadium supported catalyst was weighted and put inside the tube carefully with a magnet rotor, then 0.5 mL substrate solution (0.5 mL solvent with 25 mmol/L mesitylene as internal standard and 50 mmol/L substrate included) was injected, the reactors were covered by a polyfluoroalkoxy copolymer resin (PFA) membrane and closed tightly to hold the pressure during the reaction. After stirring and heating at 100 ^{o}C for 18 hours, the reactor plate was cooled down to room temperature. The mixture in reactors was taken out, filtrated and washed with acetonitrile separately, then the solution was taken for analysis in a gas chromatography system.

7.2.3.2 High pressure reactions

12 mg 3V-GPS-cal was put into a 25 mL autoclave, then 10 mL substrate solution (10 mL acetonitrile with 25 mmol/L mesitylene as internal standard and 50 mmol/L substrate included) was added. The reaction was carried out at 100 ^{o}C for 4 hours or 18 hours in O_2 (8 % O_2 in Ar) with stirring. The reaction pressure was set as 110 PSI (758.4 kPa), while the actual pressure at 100 ^{o}C was 140 PSI (965.27 kPa). Then the reactor was cooled to room temperature overnight. After the mixture was taken out, filtrated and washed with acetonitrile, the solution was taken for analysis in a gas chromatography system.

7.2.3.3 Recycle test of catalyst

1st Run: 48 mg (2.5-2.5)VAl-MWL-cal was put into a 50 mL glass flask, then 4 mL substrate solution (4 mL acetonitrile with 25 mmol/L mesitylene as internal standard and 50 mmol/L substrate included) was added. The flask was sealed and heated in an oil bath at 100 ^{o}C for 18 hours. After cooled to room temperature, the mixture was filtrated and washed with acetonitrile. The solution was taken for analysis in a gas chromatography system, while the solid was collected, dried at 120 ^{o}C for 6 hours, and named as (2.5-2.5)VAl-MWL-1st.

2nd Run: 30 mg (2.5-2.5)VAl-MWL-1st powder was put into a 50 mL glass flask, then 2.5 mL substrate solution (2.5 mL acetonitrile with 25 mmol/L mesitylene

as internal standard and 50 mmol/L substrate included) was added. The reaction was carried out as the 1st Run. The solid after the reaction was collected, dried at 120 ^{o}C for 6 hours, and named as (2.5-2.5)VAl-MWL-2nd.

3rd Run: 18 mg (2.5-2.5)VAl-MWL-2nd powder was put into a 50 mL glass flask, then 1.5 mL substrate solution (1.5 mL acetonitrile with 25 mmol/L mesitylene as internal standard and 50 mmol/L substrate included) was added. The reaction was carried out as the 2nd Run. The solid after the reaction was collected, dried at 120 ^{o}C for 6 hours, and named as (2.5-2.5)VAl-MWL-3rd.

4th Run: 6 mg (2.5-2.5)VAl-MWL-2nd powder was put into a 50 mL glass flask, then 0.5 mL substrate solution (0.5 mL acetonitrile with 25 mmol/L mesitylene as internal standard and 50 mmol/L substrate included) was added. The reaction was carried out as the 3rd Run. The solid after the reaction was collected, dried at 120 ^{o}C for 6 hours, and named as (2.5-2.5)VAl-MWL-4th.

7.2.4 Leaching test of vanadium containing MCM-41 catalysts

0.2 g catalyst powder was put into a flask, then 40 mL methanol was added. The mixture was stirred at room temperature for 1 hour. After filtration and washed with 40 mL methanol, the solid was dried at 80 ^{o}C overnight. Then the samples were sent for elemental analysis.

7.3 Results and discussion

7.3.1 Oxidation of the lignin model substrate 1,2-diphenyl-2-methoxyethanol (beta-methoxy-alpha-phenylphenethyl alcohol)

7.3.1.1 High throughput screening (HTS)

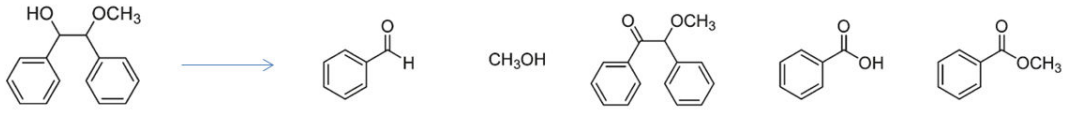

Figure 3. Oxidation of the lignin model substrate 1,2-diphenyl-2-methoxyethanol and the products. Reaction conditions: 6 mg catalyst in 0.5 ml acetonitrile with 0.025 mmol substrate, 18 hours at 100 ^{o}C.

Table 1. High throughput screening of 1,2-diphenyl-2-methoxyethanol oxidation via one pot synthesized vanadium catalyst (with Ti anchor ions).

Catalysts	**Conversion**	**Selectivity (%)**				
	(%)	Benzaldehyde	Methyl benzoate	Methanol	Benzoic acid	Benzoin methyl ether
1Ti-MWT-cal	0	-	-	-	-	-
(1-1)VTi-MWT-cal	<1	-	-	-	-	-
(2.5-1)VTi-MWT-cal	42	77	11	0	0	12
(5-1)VTi-MWT-cal	52	79	8	6	0	7
2.5Ti-MWT-cal	0	-	-	-	-	-
(1-2.5)VTi-MWT-cal	<1	-	-	-	-	-
(2.5-2.5)VTi-MWT-cal	8	100	0	0	0	0
(5-2.5)VTi-MWT-cal	50	81	6	6	0	7
5Ti-MWT-cal	0	-	-	-	-	-
(1-5)VTi-MWT-cal	<1	-	-	-	-	-
(2.5-5)VTi-MWT-cal	<1	-	-	-	-	-
(5-5)VTi-MWT-cal	31	90	0	0	0	10
10Ti-MWT-cal	0	-	-	-	-	-
(1-10)VTi-MWT-cal	<1	-	-	-	-	-
(2.5-10)VTi-MWT-cal	<1	-	-	-	-	-
(5-10)VTi-MWT-cal	7	100	0	0	0	0

Table 2. High throughput screening of 1,2-diphenyl-2-methoxyethanol oxidation via one pot synthesized vanadium catalyst (with Al anchor ions).

Catalysts	**Conversion**	**Selectivity (%)**				
	(%)	Benzaldehyde	Methyl benzoate	Methanol	Benzoic acid	Benzoin methyl ether
1Al-MWL-cal	0	-	-	-	-	-
(1-1)VAl-MWL-cal	14	100	0	0	0	0
(2.5-1)VAl-MWL-cal	53	86	7	7	0	0
(5-1)VAl-MWL-cal	72	89	5	6	0	0
2.5Al-MWL-cal	0	-	-	-	-	-
(1-2.5)VAl-MWL-cal	31	89	0	0	0	11
(2.5-2.5)VAl-MWL-cal	49	84	10	6	0	0
(5-2.5)VAl-MWL-cal	63	88	6	6	0	0
5Al-MWL-cal	0	-	-	-	-	-
(1-5)VAl-MWL-cal	7	100	0	0	0	0
(2.5-5)VAl-MWL-cal	35	93	0	0	0	7
(5-5)VAl-MWL-cal	43	85	8	7	0	0
10Al-MWL-cal	0	-	-	-	-	-
(1-10)VAl-MWL-cal	5	100	0	0	0	0
(2.5-10)VAl-MWL-cal	33	83	10	0	0	7
(5-10)VAl-MWL-cal	41	94	0	0	0	6

Table 3. High throughput screening of 1,2-diphenyl-2-methoxyethanol oxidation via one pot synthesized vanadium catalyst (with Zr anchor ions).

Catalysts	**Conversion**	**Selectivity (%)**				
	(%)	Benzaldehyde	Methyl benzoate	Methanol	Benzoic acid	Benzoin methyl ether
2.5Zr_B-MWT-cal	0	-	-	-	-	-
(1-2.5)VZr_B-MWT-cal	6	100	0	0	0	0
(2.5-2.5)VZr_B-MWT-cal	42	90	10	0	0	0
(5-2.5)VZr_B-MWT-cal	38	92	8	0	0	0
5Zr_B-MWT-cal	0	-	-	-	-	-
(1-5)VZr_B-MWT-cal	4	100	0	0	0	0
(2.5-5)VZr_B-MWT-cal	39	82	12	0	0	6
(5-5)VZr_B-MWT-cal	46	86	7	7	0	0
2.5Zr_N-MWL-cal	0	-	-	-	-	-
(1-2.5)VZr_N-MWL-cal	<1	-	-	-	-	-
(2.5-2.5)VZr_N-MWL-cal	29	100	0	0	0	0
(5-2.5)VZr_N-MWL-cal	68	89	0	6	0	5
5Zr_N-MWL-cal	0	-	-	-	-	-
(1-5)VZr_N-MWL-cal	<1	-	-	-	-	-
(2.5-5)VZr_N-MWL-cal	4	100	0	0	0	0
(5-5)VZr_N-MWL-cal	39	94	0	0	0	6

Table 4. High throughput screening of 1,2-diphenyl-2-methoxyethanol oxidation via one pot synthesized vanadium catalyst (with Ce anchor ions).

Catalysts	Conversion	Selectivity (%)				
	(%)	Benzaldehyde	Methyl benzoate	Methanol	Benzoic acid	Benzoin methyl ether
$2.5Ce_A$-MWL-cal	0	-	-	-	-	-
(1-2.5)VCe_A-MWL-cal	<1	-	-	-	-	-
(2.5-2.5)VCe_A-MWL-cal	5	100	0	0	0	0
(5-2.5)VCe_A-MWL-cal	8	100	0	0	0	0
$2.5Ce_N$-MWL-cal	0	-	-	-	-	-
(1-2.5)VCe_N-MWL-cal	<1	-	-	-	-	-
(2.5-2.5)VCe_N-MWL-cal	<1	-	-	-	-	-
(5-2.5)VCe_N-MWL-cal	16	100	0	0	0	0
$2.5Ce_A$-MWT-cal	0	-	-	-	-	-
(1-2.5)VCe_A-MWT-cal	4	100	0	0	0	0
(2.5-2.5)VCe_A-MWT-cal	20	100	0	0	0	0
(5-2.5)VCe_A-MWT-cal	50	87	6	7	0	0
$2.5Ce_N$-MWT-cal	0	-	-	-	-	-
(1-2.5)VCe_N-MWT-cal	<1	-	-	-	-	-
(2.5-2.5)VCe_N-MWT-cal	12	100	0	0	0	0
(5-2.5)VCe_N-MWT-cal	44	100	0	0	0	0

The main product of lignin model 1,2-diphenyl-2-methoxyethanol oxidation via supported vanadium catalysts is benzaldehyde, while the benzoin methyl ether percentage in products is quite low. The preponderant selectivity to benzaldehyde indicated the cleavage of C-C bond in β-O-4 linkage is the main reaction during the oxidation process.

Without vanadium sites, the mesoporous silica with anchor ion Ti/Al/Zr/Ce did not show any activity for this oxidation reaction, so the anchor ions do not act as active sites. In each group of samples above, the catalysts with higher loading of vanadium correspond to higher conversion of the substrate. A high incorporation of anchor ions leads to the decreasing of substrate conversion. To compare the four groups of catalysts with different anchor ions, the samples with Al anchor ions gave the highest activity, and (5-1)VAl-MWL-cal show a 72 % conversion of the substrate.

Table 5. High throughput screening of 1,2-diphenyl-2-methoxyethanol oxidation via grafted vanadium catalyst (with Ti/Al/Zr/Ce anchor ions).

Catalysts	Conversion	Selectivity (%)				
	(%)	Benzaldehyde	Methyl benzoate	Methanol	Benzoic acid	Benzoin methyl ether
1Ti-GPS	0	-	-	-	-	-
3Ti-GPS	0	-	-	-	-	-
(1-1)VTi-GPS-cal	31	80	11	0	0	9
(1-3)VTi-GPS-cal	7	100	0	0	0	0
(3-3)VTi-GPS-cal	29	100	0	0	0	0
1Al-GPS	0	-	-	-	-	-
3Al-GPS	0	-	-	-	-	-
(1-1)VAl-GPS-cal	28	80	9	6	0	5
(1-3)VAl-GPS-cal	10	77	13	0	0	10
(3-3)VAl-GPS-cal	51	90	4	2	0	4
1Zr-GPS	0	-	-	-	-	-
3Zr-GPS	2	0	0	0	0	100
(1-1)VZr-GPS-cal	32	87	13	0	0	0
(1-3)VZr-GPS-cal	10	100	0	0	0	0
(3-3)VZr-GPS-cal	32	100	0	0	0	0
1Ce-GPS	5	77	0	0	0	23
3Ce-GPS	5	71	0	0	0	29
(1-1)VCe-GPS-cal	22	100	0	0	0	0
(1-3)VCe-GPS-cal	10	100	0	0	0	0
(3-3)VCe-GPS-cal	57	93	0	7	0	0
3Ti-GPC	0	-	-	-	-	-
3Al-GPC	0	-	-	-	-	-
3Zr-GPC	5	0	0	0	0	100
3Ce-GPC	1	100	0	0	0	0
(1-3)VTi-GPC-cal	9	100	0	0	0	0
(1-3)VAl-GPC-cal	2	100	0	0	0	0
(1-3)VZr-GPC-cal	9	100	0	0	0	0
(1-3)VCe-GPC-cal	6	100	0	0	0	0

The grafted samples with Ti or Al anchors without vanadium loading have no activity, but the grafted samples of Zr/Ce-GPS and Zr/Ce GPC have weak activity for the oxidation of the substrate. One thing to be noted is that Zr-GPS and Zr-GPC promoted the oxidation of hydroxy other than the C-C cleavage. After the grafting of

vanadium with anchor ions, the catalysts of VTi-GPS-cal and VZr-GPS-cal have a similar conversion of substrate, meanwhile, VAl-GPS-cal and VCe-GPS-cal have a much higher conversion of the substrate. The GPC samples have very similar results to the GPS samples.

Table 6. High throughput screening of 1,2-diphenyl-2-methoxyethanol oxidation via supported vanadium catalyst synthesized by different methods.

Catalysts	**Conversion**	**Selectivity (%)**				
	(%)	Benzaldehyde	Methyl benzoate	Methanol	Benzoic acid	Benzoin methyl ether
1V-MWL-cal	21	100	0	0	0	0
1V-GPS-cal	37	88	12	0	0	0
3V-GPS-cal	46	91	9	0	0	0
1V-GPC-cal	34	86	14	0	0	0

To compare the supported vanadium catalysts without anchor ions which were prepared by different synthesis methods, the grafted samples with molecular stencil pattering technique (1V-GPS-cal) and partial thermal treatment technique (1V-GPC-cal) have very parallel activity, which are higher than the one-pot synthesized sample (1V-MWL-cal). This is because the one-pot incorporated vanadium active sites were partially loaded in the wall of silica, not all the active sites can contact with the substrate molecules, while the grafted vanadium active sites were all exposed on the surface of silica, which can have adequate contact with the substrate.

7.3.1.2 Leaching test

Table 7. Residual elemental percentage of vanadium and anchor ions in different catalysts after leaching test in methanol. (M corresponding to Ti/Al/Zr/Ce respectively)

No.	Catalyst	V (%)	M (%)
1	(2.5-2.5)VTi-MWT-cal	83	100
2	(2.5-2.5)VAl-MWL-cal	49	93
3	(2.5-2.5)VZr_N-MWL-cal	50	100
4	(2.5-2.5)VCe_N-MWT-cal	79	98
5	(1-3)VTi-GPS-cal	94	100
6	(1-3)VAl-GPS-cal	18	97
7	(1-3)VZr-GPS-cal	62	100
8	(1-3)VCe-GPS-cal	83	100
9	(1-3)VTi-GPC-cal	86	96
10	(1-3)VAl-GPC-cal	19	95
11	(1-3)VZr-GPC-cal	65	98
12	(1-3)VCe-GPC-cal	78	96
13	1V-MWL-cal	27	-
14	1V-GPS-cal	25	-
15	1V-GPC-cal	29	-

V (%) = $(V/Si)_{after\ leaching}$ / $(V/Si)_{before\ leaching}$, M (%) = $(M/Si)_{after\ leaching}$ / $(M/Si)_{before\ leaching}$, M = Al/Ti/Zr/Ce.

Methanol is a very strong polar solvent, the leaching test of samples in methanol can indicate the stability of loaded sites in supported catalyst. Elemental analysis was carried out before and after the leaching test in methanol. Table 7 shows the residual percentage of vanadium and anchor ions in different catalysts after leaching test. For all the samples, there was almost no leaching of anchor ions, while the leaching of vanadium depends on the different anchor ions and different loading methods. Without anchor ions, 1V-MWL-cal, 1V-GPS-cal and 1V-GPC-cal have serious leaching in methanol, about 70 % of vanadium sites were lost during the test. With anchor ions, the samples can hold vanadium sites stronger and there were less leaching of vanadium in methanol. Ti has the most strong anchor effect for all the three groups of samples with different synthesis methods.

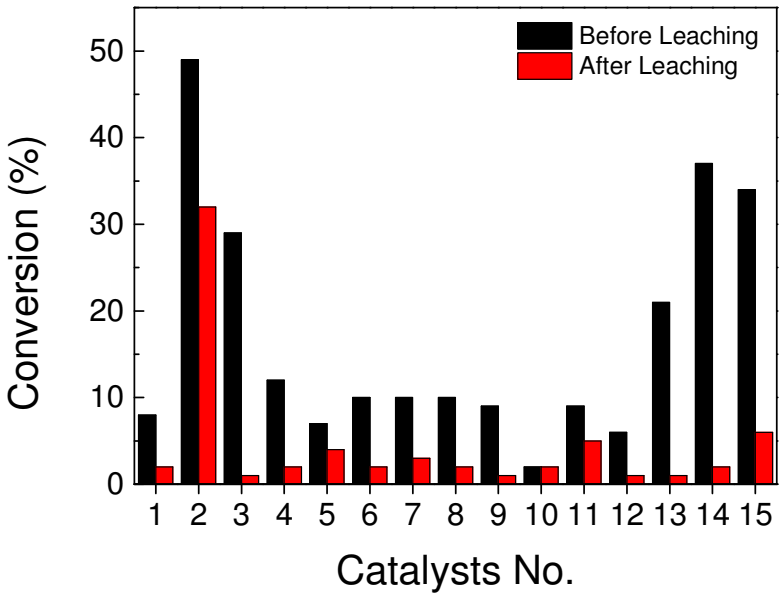

Figure 4. Conversion of 1,2-diphenyl-2-methoxyethanol substrate via different catalyst samples before and after the leaching test in methanol. (The catalysts number and their corresponding samples names were summarized in Table 7.)

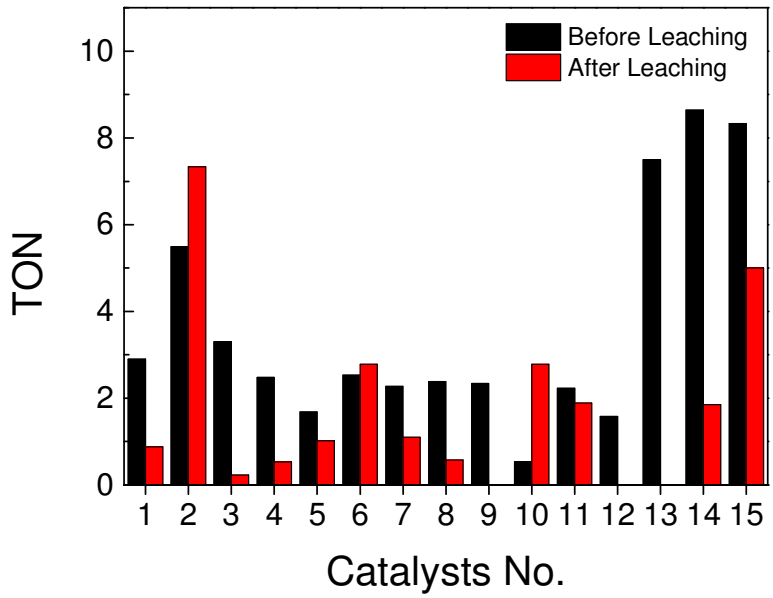

Figure 5. TON of 1,2-diphenyl-2-methoxyethanol substrate via different catalyst samples before and after the leaching test in methanol. (The catalysts number and their corresponding samples names were summarized in Table 7.)

Figure 4 and Figure 5 compared the conversion and TON of 1,2-diphenyl-2-methoxyethanol substrate via different catalyst samples before and after the leaching test in methanol (the full table of data is in appendix A11.1). (2.5-5)VAl-MWL-cal is the most active catalyst in all these samples whether before or after leaching test. Though the samples without anchor ions have high activity before leaching, but their activities are very low after leaching (Figure 4. No. 13, 14, 15). After leaching, there were less vanadium active sites in all the samples, but the samples with Al anchor ions have higher TON than themselves before leaching (Figure 5. No. 2, 6, 10).

Table 8. Residual elemental percentage of vanadium and anchor ions in different samples after stirring in acetonitrile at 100 ^{o}C for 18 hours. (M corresponding to Ti/Al/Zr/Ce respectively)

Catalyst	**V (%)**	**M (%)**
(2.5-5)VAl-MWL-cal	89	96
1V-MWL-cal	96	-

Two samples were chosen for another leaching test in acetonitrile, which is the solvent for the 1,2-diphenyl-2-methoxyethanol oxidation reaction, the temperature and stirring duration were set as same as the oxidation reaction conditions. The elemental analysis was carried out before and after this leaching test. Table 8 indicate that the leaching of vanadium of these two samples in acetonitrile was much less than in methanol. This is because acetonitrile was not so polar as methanol, so the vanadium active sites were stably incorporated on the support even with longer stirring time and higher temperature.

7.3.1.3 Recycling test

Table 9. Recycling test of (2.5-5)VAl-MWL-cal for 1,2-diphenyl-2-methoxyethanol oxidation in acetonitrile.

Catalysts	Conversion (%)	Selectivity (%)				
		Benzaldehyde	Methyl benzoate	Methanol	Benzoic acid	Benzoin methyl ether
(2.5-2.5)VAl-MWL-1st	49	84	10	6	0	0
(2.5-2.5)VAl-MWL-2nd	46	81	12	4	0	3
(2.5-2.5)VAl-MWL-3rd	43	79	13	5	0	3
(2.5-2.5)VAl-MWL-4th	39	78	14	5	0	3
(2.5-2.5)VAl-MWL-cal After leaching in MeOH	32	76	19	0	0	5

Figure 6. Conversion of 1,2-diphenyl-2-methoxyethanol via (2.5-5)VAl-MWL-cal catalyst in acetonitrile.

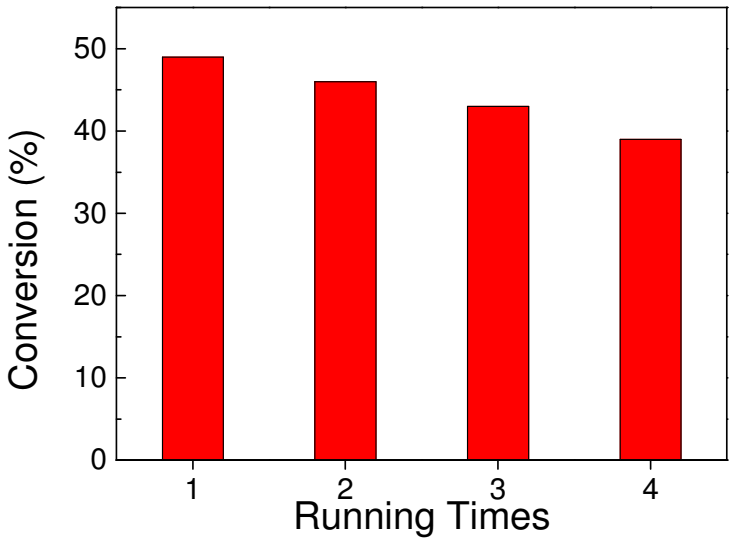

The sample (2.5-5)VAl-MWL-cal has high activity for the oxidation of 1,2-diphenyl-2-methoxyethanol substrate, the recovery and recycles test was run at the same reaction conditions. Though after each recovery, the activity of (2.5-5)VAl-MWL-cal was decreased slightly, the conversion of the substrate with the 4th run is still higher than with the sample after leaching in methanol. Compare to the 1st run, the catalyst after three times of recycling was still keeping 80 % of the initial activity, reminding that the recovery was just a classical filtration followed by a drying step.

7.3.1.4 Addition of base

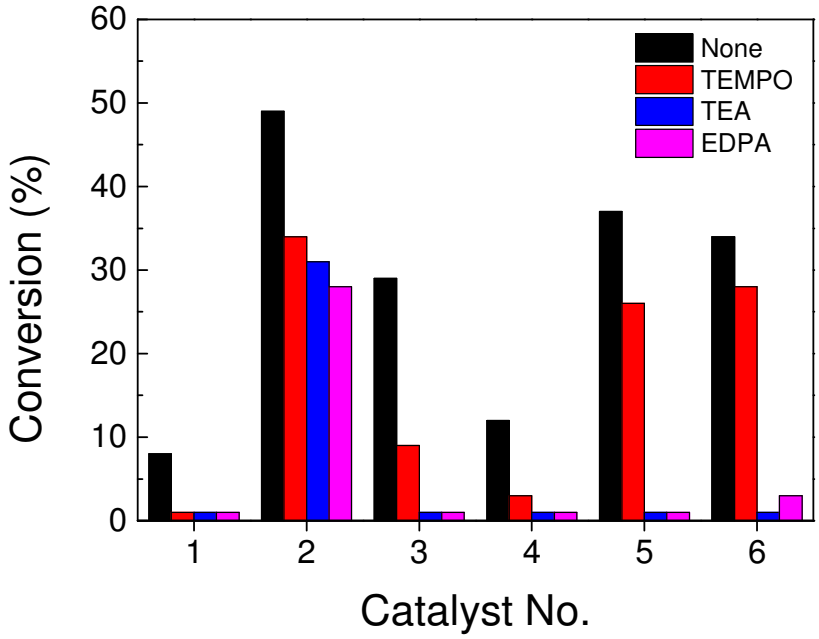

Figure 7. Conversion of 1,2-diphenyl-2-methoxyethanol substrate via different supported vanadium catalysts. Catalyst No: 1, (2.5-2.5)VTi-MWT-cal; 2, (2.5-2.5)VAl-MWL-cal; 3, (2.5-2.5)VZr_N-MWL-cal; 4, (2.5-2.5)VCe_N-MWT-cal; 5, 1V-GPS-cal; 6, 1V-GPC-cal. 6 mg catalyst in 0.5 mL acetonitrile with 0.025 mmol substrate to reacted at 100 ^oC for 18 hours. Additional of base: 0.00125 mmol, TEMPO (2,2,6,6-Tetramethyl-1-piperidinyloxy), TEA (Triethylamine), EDPA (N-Ethyldiisopropylamine).

Three types of base (TEMPO, TEA, EDPA) were added in substrate solutions respectively. To compare the reaction results (Figure 7, the full table of data is in appendix A11.2), the additional of the base in these heterogeneous catalysts reactions is not helpful, on the contrary, the conversion of the substrate was decreased with the base. It means the reaction mechanism and pathway of these supported vanadium catalysts is quite different from the homogeneous vanadium catalysts.[3, 4]

7.3.1.5 Effect of copper or iron additives

Table 10. High throughput screening of 1,2-diphenyl-2-methoxyethanol oxidation via supported vanadium catalyst incorporated with Cu/Fe assistant ions.

Catalysts	Conversion	Selectivity (%)				
	(%)	Benzaldehyde	Methyl benzoate	Methanol	Benzoic acid	Benzoin methyl ether
1Cu-MWL-cal	5	70	30	0	0	0
1Fe-MWL-cal	2	0	0	0	100	0
(0.5-0.5)CuFe-MWL-cal	6	66	34	0	0	0
(1-0.5-0.5)VCuFe-MWL-cal	4	100	0	0	0	0
(1-1)VCu-MWL-cal	7	69	31	0	0	0
(1-0.5-0.5)VCuFe-MWL-cal add: TEMPO	5	57	0	0	0	43
(1-1)VCu-MWL-cal add :TEMPO	<1	-	-	-	-	-

Mottweiler et al.[7] have tested a series of catalysts for the oxidative cleavage of lignin, the bimetal catalysts with two types of active sites (e.g. Cu-V, Fe-V) displayed higher activity and better selectivity than the monometallic catalysts. Here, the mesoporous silica was incorporated with V/Cu/Fe with the synthesis method combined with one-pot synthesis and grafting (characterization of catalysts in Table 10 are collected in Appendix). The 1Cu-MWL-cal and 1Fe-MWL-cal catalysts are active for the oxidation of 1,2-diphenyl-2-methoxyethanol substrate, but their activities are very low, and their selectivities are not good. When the catalysts combined with two or three types of metal active sites ((1-1)VCu-MWL-cal and (1-0.5-0.5)VCuFe-MWL-cal), their conversion of the substrate is still much less than 1V-MWL-cal. The additional base TEMPO is not helpful for these groups of catalysts.

7.3.1.6 Different solvents

Table 11. Oxidation of 1,2-diphenyl-2-methoxyethanol in different solvents via vanadium catalyst (5-1)VAl-MWL-cal and 3V-GPS-cal respectively.

No.	Solvent	Boiling Point (°C)	Polarity	Conversion (%)		Selectivity to Benzaldehyde(%)	
				(5-1)VAl-MWL-cal	3V-GPS-cal	(5-1)VAl-MWL-cal	3V-GPS-cal
1	Chloroform	61	4.4	93	90	65	78
2	Benzene	80	3	92	91	79	78
3	EtOAc	77	4.3	83	79	> 95	> 95
4	Toluene	111	2.4	70	58	> 95	> 95
5	MeCN	82	6.2	72	46	89	91
6	CH_2Cl_2	40	3.4	69	75	63	63
7	Dioxane	101	4.8	27	32	72	86
8	THF	66	4.2	23	23	57	53
9	DMSO	189	7.2	14	16	49	68
10	Pyridine	115	5.3	< 5	< 5	-	-
11	Ethanol (95 %)	78	4.3	< 5	< 5	-	-
12	H2O (+MeCN)	100	10.2 (6.2)	< 5	< 5	-	-

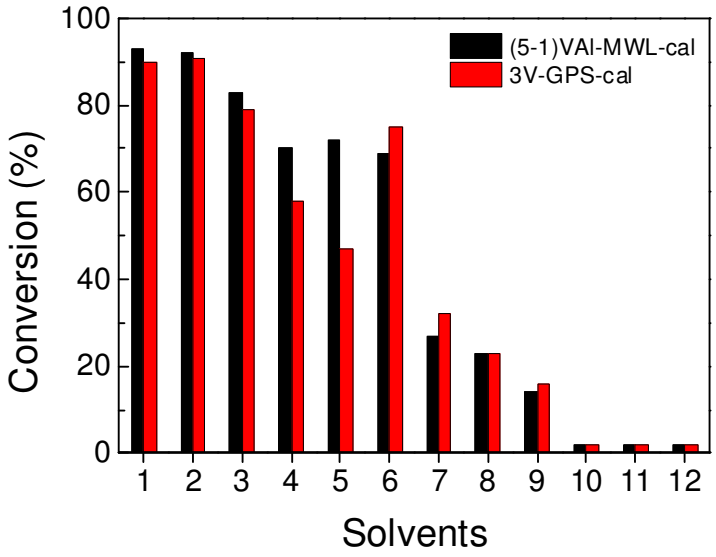

Figure 8. Conversion of 1,2-diphenyl-2-methoxyethanol in different solvents via (5-1)VAl-MWL-cal and 3V-GPS-cal catalysts. (The solvent number corresponding to the solvent list in Table 11)

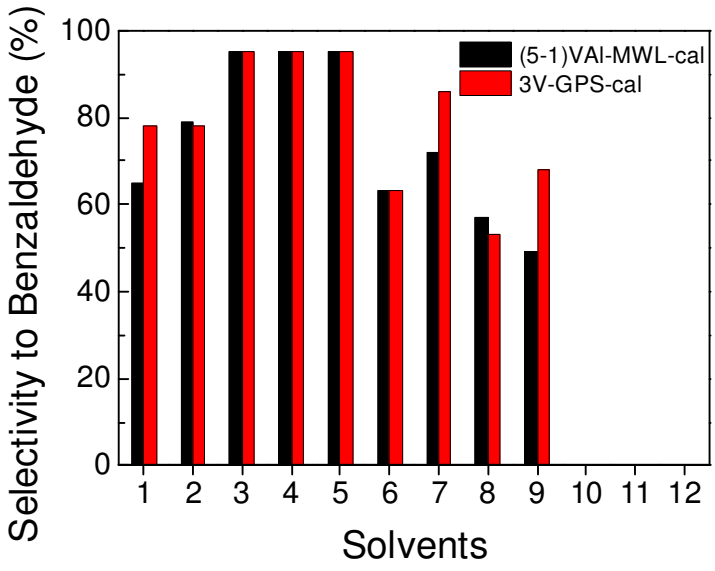

Figure 9. Selectivity to benzaldehyde in different solvents via (5-1)VAl-MWL-cal and 3V-GPS-cal catalysts. (The abscissa corresponds to the solvent listed in Table 11).

The oxidation reactions of 1,2-diphenyl-2-methoxyethanol were run in different solvents via vanadium catalyst (5-1)VAl-MWL-cal and 3V-GPS-cal respectively. In chloroform, benzene and EtOAc, the conversion of the substrate is quite high (Figure 8. No. 1, 2, 3), while in EtOAc, toluene and MeCN, the reaction has good selectivity (Figure 9. No. 3, 4, 5). So EtOAc is a very good solvent for the oxidation reactions of 1,2-diphenyl-2-methoxyethanol via supported vanadium catalyst, and it is nontoxic as a "green" solvent. In MeCN, the difference between the activity of two catalyst samples is the maximum (Figure 8. No. 5), so it is a good choice for the high throughput screening to see the difference in a series of catalyst samples.

7.3.2 Oxidation of the cellulose model substrate meso-hydrobenzoin

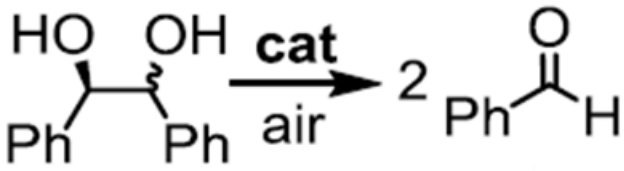

Figure 10. Aerobic oxidation of meso-hydrobenzoin with supported vanadium catalysts. 6 mg catalyst in 0.5 mL acetonitrile with 0.025 mmol substrated to stir at 100 ^{o}C for 18 hours.

Table 12. Conversion and theoretical TON of meso-hydrobenzoin with different supported vanadium catalysts.

Catalysts	Conversion (%)	TON (theoretical)
(5-1)VTi-MWT-cal	69	3.5
(5-1)VAl-MWL-cal	82	4.1
(5-2.5)VZr_N-MWL-cal	74	3.7
(5-2.5)VCe_A-MWT-cal	77	3.9
1V-GPS-cal	72	18.0
1V-GPC-cal	53	13.3

Diols are important cellulose biomass models. Meso-hydrobenzoin was chosen as a substrate to test the activity of supported vanadium catalysts, it can be converted into different products to reveal the catalyst selectivity to C-C bond cleavage or dehydrogenation, and it is commercially available. For the aerobic oxidation of meso-hydrobenzoin in acetonitrile, all the catalyst samples in Table 12 have a 100 % selectivity to benzaldehyde, which indicates that the C-C bond cleavage is the dominating reaction promoted by these supported vanadium catalysts (Figure 10). For the one-pot samples with anchor ions, sample (5-1)VAl-MWL-cal shows the highest activity with a substrate conversion of 82 %. The grafted vanadium catalyst 1V-GPS-cal has a lower conversion but a much higher TON.

7.3.3 Oxidation of cellulose model substrate pinacol

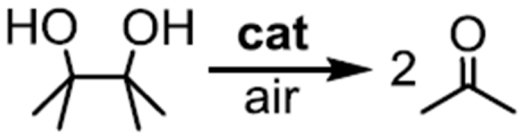

Figure 11. Aerobic oxidation of pinacol with supported vanadium catalysts. 6 mg catalyst in 0.5 mL acetonitrile with 0.025 mmol substrate to stir at 100 ^{o}C for 18 hours.

Table 13. Conversion and theoretical TON of pinacol with different supported vanadium catalysts.

Catalysts	Conversion (%)	TON (theoretical)
(5-1)VTi-MWT-cal	55	2.8
(5-1)VAl-MWL-cal	68	3.4
(5-2.5)VZr_N-MWL-cal	66	3.3
(5-2.5)VCe_A-MWT-cal	38	1.9
1V-GPS-cal	61	15.3
1V-GPC-cal	59	14.8

Pinacol was chosen as another diol substrate to test the activity of supported vanadium catalysts, with the catalysts in Table 13. the pinacol substrate was converted into acetone (Figure 11). Sample (5-1)VAl-MWL-cal shows the highest activity with a substrate conversion of 68 %, and 1V-GPS-cal has a lower conversion but a much higher TON. The results in Table 13 are consistent with the results of in Table 12. The lower conversion of pinacol is because the aromatic group in meso-hydrobenzoin make its C-C bond easier to break than the pinacol.

7.3.4 Reaction in high pressure autoclaves

Table 14. Aerobic oxidation of lignin model 1,2-diphenyl-2-methoxyethanol and cellulose model meso-hydrobenzoin in high pressure autoclaves via 3V-MSP-cal.

Catalysts	**Conversion**	**Selectivity (%)**					**TON**
3V-MSP-cal	**(%)**	Benzaldehyde	Methyl benzoate	Methanol	Benzoic acid	Benzoin methyl ether	(theoretical)
1,2-diphenyl-2-methoxyethanol, in glass vial, 18 h	46	91	9	0	0	0	3.8
1,2-diphenyl-2-methoxyethanol, in autoclave, 4 h	18	90	4	6	0	0	15.0
1,2-diphenyl-2-methoxyethanol, in autoclave, 18 h	59	87	6	6	0	1	49.2
Meso-hydrobenzoin, in autoclave, 4 h	24	100	-	-	-	-	20.0
Meso-hydrobenzoin, in autoclave, 18 h	100	99.2	-	-	-	-	83.3

Sample 3V-MSP-cal was taken as an example to test the influence of reaction conditions, the concentration of substrate and internal standard was kept the same as it was in the high throughput screening reactions (chapter 7.3.1.1), but the catalyst concentration in autoclaves was set as one-tenth compared to the catalyst concentration in the glass vial. When 1,2-diphenyl-2-methoxyethanol was chosen as a substrate, in the high throughput screening vial, after 18 hours reaction, the conversion of the substrate was 46 %. In the autoclave, the pressure was much higher than in the glass vial, and the O_2 concentration was higher as well. After 4 hours of reaction in the autoclave, the conversion of the substrate was 18 %, and after 18 hours of reaction in the autoclave, the conversion of the substrate was 59 %, which is higher than the conversion in the glass vial. In autoclaves, the concentration of catalyst was much lower, and the TON was much higher compared to the reaction in the vial. When meso-hydrobenzoin was chosen as a substrate, after 4 hours of reaction in the autoclave, the conversion of the substrate was 24 %, and after 18 hours of reaction in the autoclave, the substrate was totally converted into benzaldehyde, the TON was up

to 83.3. The selectivity changes can be ignored with the different reaction conditions. So for the C-C cleavage of lignin model 1,2-diphenyl-2-methoxyethanol and cellulose model meso-hydrobenzoin, high pressure, high O_2 concentration, and long reaction time was necessary for the total conversion of the substrate. In autoclaves, with the same reaction conditions, the conversion of the substrate was time dependent, the C-C bond in cellulose model meso-hydrobenzoin was easier to break than the one in lignin model 1,2-diphenyl-2-methoxyethanol, so the total conversion of 1,2-diphenyl-2-methoxyethanol would need a longer reaction time.

7.4 Conclusion

Aerobic oxidation of the lignin model substrate 1,2-diphenyl-2-methoxyethanol via supported vanadium catalysts was carried out using a high throughput screening facility. The activity of one-pot synthesized and grafted vanadium catalysts with different anchor ions (Ti/Al/Zr/Ce) were compared. Like in the catalysts prepared according to the one pot approach, the catalysts prepared by grafting showed all a good selectivity to the C-C bond cleavage at the β-O-4 position. The samples with a higher loading of vanadium active sites gave a higher conversion of substrate, and the samples of vanadium incorporated with Al anchor ions showed the highest activity. Globally, the grafted vanadium catalysts had a higher activity than the one-pot samples where metal ion embedding was unfavorable for both optimal anchoring effect and vanadium accessibility. Practically, the catalytic activity was compared in twelve different solvents. The best were apolar with EtOAc being the best as it combines both very high C-C cleavage activity and selectivity. The worst were the polar ones combined with ligand properties favoring vanadium solvation and leaching, like alcohols or pyridine. Methanol, the more polar alcohol, was indeed chosen for leaching test. Acetonitrile keeping an excellent selectivity in C-C bond cleavage produced an average effect on catalytic activity and was therefore chosen to compare the anchoring effect. As expected, all the anchors were found resistant to leaching while vanadium behavior was highly anchor-dependent. Among anchor ions, Ti(IV) were the best to prevent leaching though a worse catalytic promoter than Al(III) ions. Effectively, the robustness of the catalysts during recycling was rather good even with Al(III) anchor ions as leaching was rather small in acetonitrile. In complement, a basic media known to promote the homogeneous catalytic pathway was detrimental in the present conditions. All these data are consistent with a true heterogeneous pathway that totally differs from the homogeneous one and would take place on a cluster of vanadium and better when Al(III) ions are nearby the vanadium. Contrary to other heterogeneous catalysts, the introduction of Cu(II) or Fe(III) ions as additives was not promoting the catalytic activity of vanadium. Our preliminary study confirms

that the catalytic C-C cleavage in meso-hydrobenzoin or pinacol used as model for oxidant degradation of cellulose is easier than in 1,2-diphenyl-2-methoxyethanol for supported vanadium catalysts like in homogeneous catalysis.

7.5 References

1. Reale, S.; Di Tullio, A.; Spreti, N.; De Angelis, F. *Mass Spectrom. Rev.* **2004,** 23, (2), 87-126.

2. Hanson, S. K.; Baker, R. T.; Gordon, J. C.; Scott, B. L.; Thorn, D. L. *Inorg. Chem.* **2010,** 49, (12), 5611-5618.

3. Sedai, B.; Díaz-Urrutia, C.; Baker, R. T.; Wu, R.; Silks, L. P.; Hanson, S. K. *ACS Catal.* **2011,** 1, (7), 794-804.

4. Sedai, B.; Díaz-Urrutia, C.; Baker, R. T.; Wu, R.; Silks, L. P.; Hanson, S. K. *ACS Catal.* **2013,** 3, (12), 3111-3122.

5. Díaz-Urrutia, C.; Chen, W.-C.; Crites, C.-O.; Daccache, J.; Korobkov, I.; Baker, R. T. *RSC Adv.* **2015,** 5, (86), 70502-70511.

6. Díaz-Urrutia, C.; Sedai, B.; Leckett, K. C.; Baker, R. T.; Hanson, S. K. *ACS Sustain. Chem. Eng.* **2016,** 4, (11), 6244-6251.

7. Mottweiler, J.; Puche, M.; Räuber, C.; Schmidt, T.; Concepción, P.; Corma, A.; Bolm, C. *ChemSusChem* **2015,** 8, (12), 2106-2113.

Chapter 8. Conclusions and perspectives

8.1 Conclusions

Large scale production of biosourced organic molecule has to be produced from non nutritive vegetal biomass, i.e., from lignin or cellulose. However, the degradation of these oxygen reach natural and renewable polymers is very challenging and for economical reason requires a low temperature catalytic process to recover valuable molecules. This is the societal context of the present thesis where supported vanadium catalysts were developed for C-C bond cleavage of molecules considered as model for the catalytic oxidative degradation of these natural polymers.

Efforts were devoted to optimize all the parameters of the catalysts such as high surface area, accessibility to the catalytic sites, fast, clean and energy saving catalyst syntheses, in the view of practical large-scale applications. Mesoporous silica MCM-41 was chosen as a support as it provides good opportunities for high surface area and high metal dispersion of active sites for an optimum site accessibility. Vanadium was preferred as catalytic metal ions as it allows us to operate oxidation on relatively large substrates using O_2 as oxidant at moderate temperatures. The drawback of vanadium being its leaching into the catalytic media, an emphasis was brought on improving its retention using anchoring ions such as Al(III), Ti(IV), Zr(IV) and Ce(IV) ions. To find the most efficient anchoring effect compatible with a decent catalytic productivity, both metal concentration and relative ratio between vanadium and anchors was varied. A fast and easy one-pot microwave assisted synthesis was developed to efficiently screen most of the significant combinations. While sequential graftings on a pre-synthesized support were preferred to further document the anchoring effect. These more sophisticated post-synthesis treatments using either the molecular stencil patterning (MSP) and the partial thermal treatment (PTT) techniques were shown to improve vanadium dispersion with or without anchoring ions. Among the panel of characterization tools, Diffuse Reflectance UV-visible spectroscopy was found particularly useful to evidence the effect of anchoring ions on the dispersion of vanadium(V) ions. Despite the very large number of catalysts produced, most of them were tested thanks to a high throughput reaction facility applied here to aerobic oxidation of 1,2-diphenyl-2-methoxyethanol. This substrate was chosen as it is a good model to predict the reactivity and the selectivity in C-C cleavage in the β-O-4 linkage that characterizes lignin substrates. Among the catalysts those involving the

aluminium anchors were found the best for the highest loading. Some preliminary tests were also made showing that these catalysts are also very active in the C-C cleavage of molecules mimicking the degradation key path of cellulose degradation.

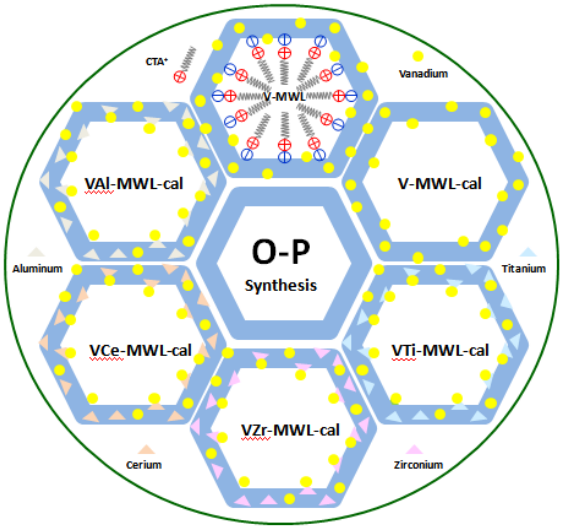

Figure 1. One-pot microwave assisted synthesis of the V(Ti/Zr/Ce/Al)-MWL series.

In more details, Chapter 4 was devoted to the ultra fast one-pot synthesis approach. The vanadium as well as the anchoring aluminium, titanium, zirconium, or cerium salts were added together with the precursors of the mesoporous silica and treated in a Teflon autoclave under a microwave irradiation for 10 minutes at 180 ^{o}C. The so-obtained powders present a rather well-ordered hexagonal pore array containing vanadium anchored to the mesoporous silica walls. (Figure 1)

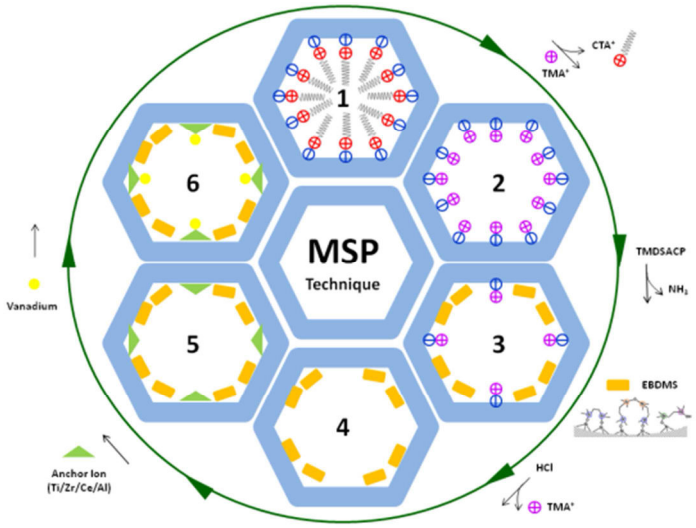

Figure 2. Post grafting of V(Ti/Zr/Ce/Al)-GPS based on MSP technique.

The multistep synthesis via sequential grafting was described in Chapter 5. It starts with an already-made silica pure mesoporous support of the MCM-41 type of structure, on which is a first grafting is applied. It consisted to cap selectively some surface silanol groups in the presence of tetramethyl ammonium partly covering the surface and acting as a masking pattern. After removing the ammonium ion, the anchoring ions take their places as grafted nanoclusters, the size of which depends on the loading. The vanadium ions are finally anchored on these nanoislands adopting, therefore, the molecular pattern of the masking ammonium partially covering the surface in the first step of the synthesis. (Figure 2).

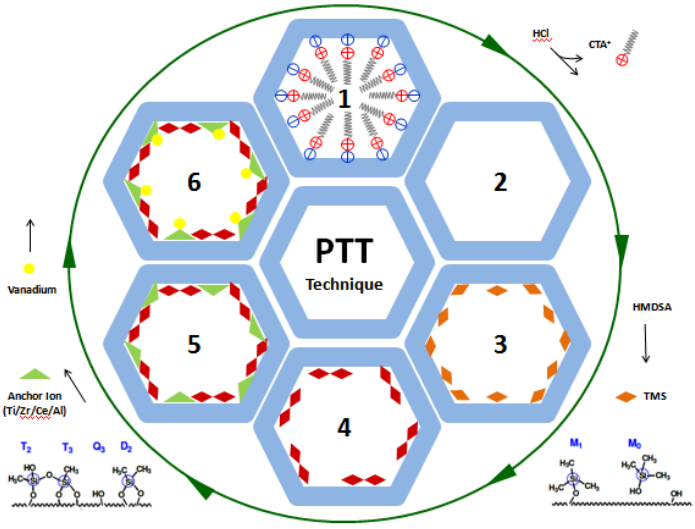

Figure 3. Post grafting of V(Ti/Zr/Ce/Al)-GPS based on PTT technique.

Chapter 6 deals also with the principle of partial surface silanol capping before grafting any of the metal ions. However, it was designed to be is easier to operate as it requires much fewer steps and skills as compared with the MSP technique described in Chapter 7. It starts from a full surface silanol capping of a preformed MCM-41 type of silica by trimethylsilyl (TMS) functions followed by a controlled thermal degradation. The partial degradation of the trimethyl function is operated at a temperature determined from the TGA mass loss profile. It produced dimethyl- and monomethylsilyl functions that are 2 of 3 fold binded to the silica surface. Contrary the previous method, the silanol patches were produced according to a thermally controlled surface reconstruction. Indeed, the so-generated FTT catalyst series was improving the vanadium dispersion but not as much as the GPS series though anchoring ions were decreasing slightly the difference (Figure 3).

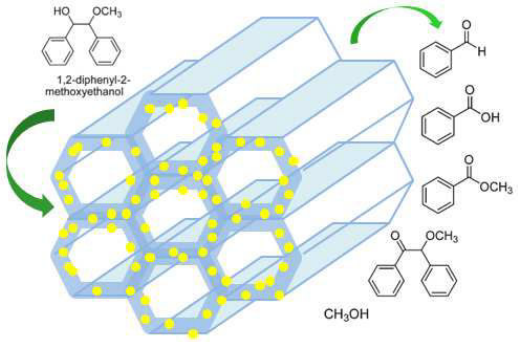

Figure 4. Schematic of 1,2-diphenyl-2-methoxyethanol aerobic oxidation with mesoporous

A panel of characterization techniques described in chapter 3 and used in chapter 4, 5 and 6 was devoted to get information on the solid support itself and on the anchoring and anchored metal ions. Therefore, regular solid state techniques were systematically applied such as X-ray diffraction for the control on the hexagonal pore array of the mesoporous silica, thermal gravimetry analysis for the determination of the organic content, nitrogen physisorption for surface area and porosity control, ^{27}Al and ^{29}Si solid state NMR for the coordination of Al anchors and silanol capping. In addition, reflectance IR spectroscopy and in some particular case Raman spectroscopy was also applied to characterize the functional groups including vanadium sites. For instance, we were able to follow the progressive occupation of the internal porosity monitoring the decrease of surface area and pore volume in parallel with the appearance of the specific NMR and IR signatures of the grafted species for the catalysts prepared according to the post-synthesis routes (GPS and FTT series). However, to rank the catalysts according to the distribution of vanadium species the best technique was diffuse reflectance UV-visible spectroscopy. This ranking was based on the blue shift of the ligand to metal charge transfer band (LMCT). It was measured in terms of edge energy, E_e also called optical gap obtained by linear extrapolation of the low energy side of the band using Tauc plots. This rather simple analysis was further refined adopting a complete shape analysis of the LMCT band using Gaussian curve fittings. The originality of our fits was the use of the same set of six Gaussian curves for all the LMCT fits, whatever the presence or the absence of anchors. The relative intensity was the only change, except for the to two most blue

shifted curves when Ti was the anchor. This was explained by the presence of LMCT transitions of the Ti(VI) anchoring ions in this region of the spectrum. We were less lucky with Ce(IV) ions the LMCT transition of which was interfering in most of the energy range of interes. Nonetheless, the first four Gaussian curves on the low energy side were safely determined and, corresponded to E_e of 2.7, 3.2, 3.6 and 3.9 eV known to be typical of the first LMCT of vanadium ions in 2D raft, chains, pairs or monomeric species, respectively. As a consequence, we were able to confirm the absence of 3D clusters (E_e at 2.3 eV) even in the samples containing the highest level of 2D vanadium oxide rafts. The relatively low intensity of the Gaussian centered at 3.2 eV reveals the quasi absence of vanadium oxide chain, though not excluding the presence of some linear trimers. Dimers and monomers present in all our catalysts were the only species formed in the best cases obtained solely using Ti anchors. As a general trend we indeed observed a higher dispersion when the anchoring ion loading was increased up to 5 mol% Anchor/Si. Not surprisingly, lower vanadium loading generated better dispersions (tested down to 1 mol%). Ranking the anchoring efficiency according to a higher vanadium dispersion lead to the following sequence: none < Zr < Ce < Al < Ti mirroring the oxides sequence for vanadium dispersion: SiO_2< ZrO_2 < CeO_2 < Al_2O_3 < TiO_2. More precisely, a ratio close to 1 vanadium for 3 anchoring ions was preferable to favor the formation of dimer and monomers according to both GPS and FTT series where all the anchoring ions and vanadium ions were grafted on the surface. It allowed us to anticipate that these two ultimate states of dispersion might need two and even three anchoring ions clustered together, likely to favor the formation of bi- or tripodal vanadium(V) covalently linked to these nano islands. Notably, we estimated that the weaker anchoring efficiency of aluminium over titanium ions was related to its tendency to be stabilized as isolated tetrahedral species into silica surfaces according to ^{27}Al NMR spectroscopy. In some extent, the anchoring nano islands possessed some of the surface properties of the bulk oxide support but certainly not the bulky ones as shown for instance by the blue shift of the optical gap of the Ti oxide nano-islands.

Finally, the chapter 7 dealing with the catalytic reactivity was focused on the high throughput screening for aerobic oxidation. The reaction was run in parallel inside 96 mini reactors that were indeed small wells drilled in the same steel plate. Each well was filled with few mg of catalyst and few mL of the reaction media both

precisely measured. After undergoing to the same reaction temperature, pressure and time, each content was analyzed using gas chromatography allowing a comparison of a large number of catalysts (Figure 4). The oxidative carbon-carbon bond cleavage of 1,2-diphenyl-2-methoxyethanol run with dioxygen (O_2) produced mainly benzaldehyde and methyl benzoate attesting for a very high selectivity to the C-C bond cleavage. Higher conversions were systematically obtained with higher vanadium loadings and preferably using aluminium ions as anchors. It was verified that leaching was not a problem. Among, thirteen solvents tested, the best were rather apolar, ethyl acetate being the best. The metal leaching that was a main concern for vanadium was rather negligible according to recycling tests in the relatively high polar acetonitrile. The solvent had to be a better ligand to dissolve vanadium into the reaction media as shown using methanol. Furthermore, the catalytic activity of the vanadium supported catalysts did not require a basic media as it is required for the homogeneous vanadium based catalysts that also presents a different selectivity. These independent criteria fully support the idea that the specific selectivity for C-C bond cleavage is the fingerprint of a true heterogeneous catalytic pathway.

8.2 Perspectives

In a general point of view, the three type of synthesis proposed here can serve as a model to design multicomponent metal supported catalysts first focusing on fast and coarse synthetic protocols, then moving a more sophisticated one to move into more insights on the true catalytic site and to adopt *in fine* a more practical synthesis route for eventual application.

More particularly, it is shown that the actual vanadium based catalysts are selective for C-C bond cleavage in oxidative liquid phase reaction conditions in a relatively clean solvent as Ethylacetate. It now important to check whether this selectivity and the recycling properties can be maintained in this particular solvent, at larger scale and at higher pressure.

The application of this catalysts to C-C bond cleavage of other diols than those tested here is important as leaching might become in some cases a crucial problem to solve particularly in the view of industrial application where a high concentration of reactant is preferred.

At last, vanadium that is obviously not the preferred metal ion when environmental concerns are at stake, one may try other metal. Copper dimers known

to intervene in enzyme for C-C bond cleavage in diols might be one of the candidates to replace vanadium, for instance.

Appendix

A 8.1 Raman spectra of Chapter 7

Appendix 9 TEM images

A 9.1 TEM images of Chapter 7

Appendix 10 Elemental analysis

A10.1 Elemental analysis of Chapter 7

Appendix 11 Conversion and selectivity tables

A 11.1 High throughput screening of 1,2-diphenyl-2-methoxyethanol oxidation via supported vanadium catalyst before and after leaching test.

A11.2 High throughput screening of 1,2-diphenyl-2-methoxyethanol oxidation via supported vanadium catalyst with additional base.

Appendix 1 XRD patterns

A1.1 XRD patterns of Chapter 4

Figure A1.1.1 Low-angle XRD patterns of as-made VTi-MWT and VTi-MWT-cal.

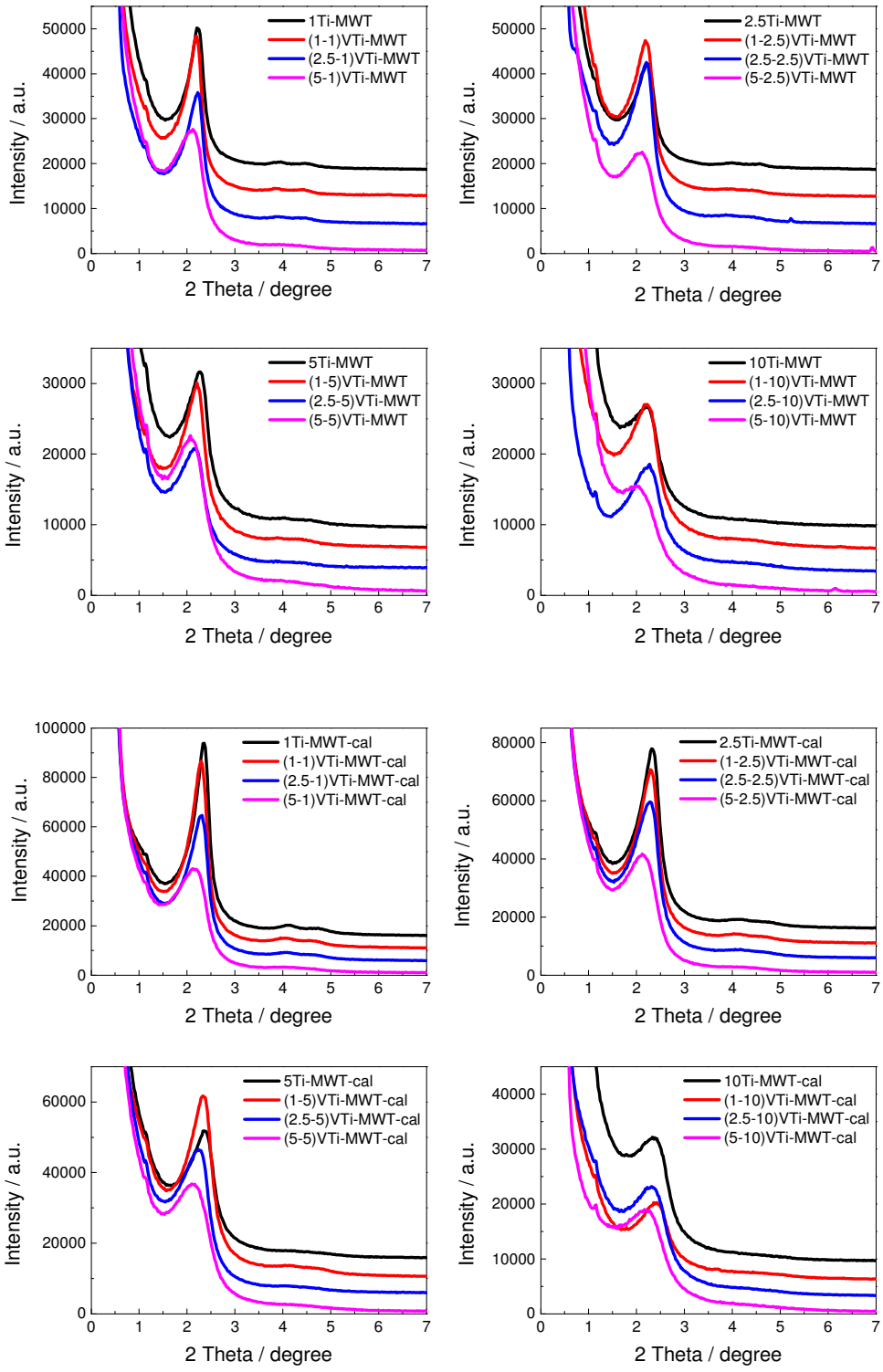

Figure A1.1.2 Low-angle XRD patterns of as-made VAl-MWL and VAl-MWL-cal.

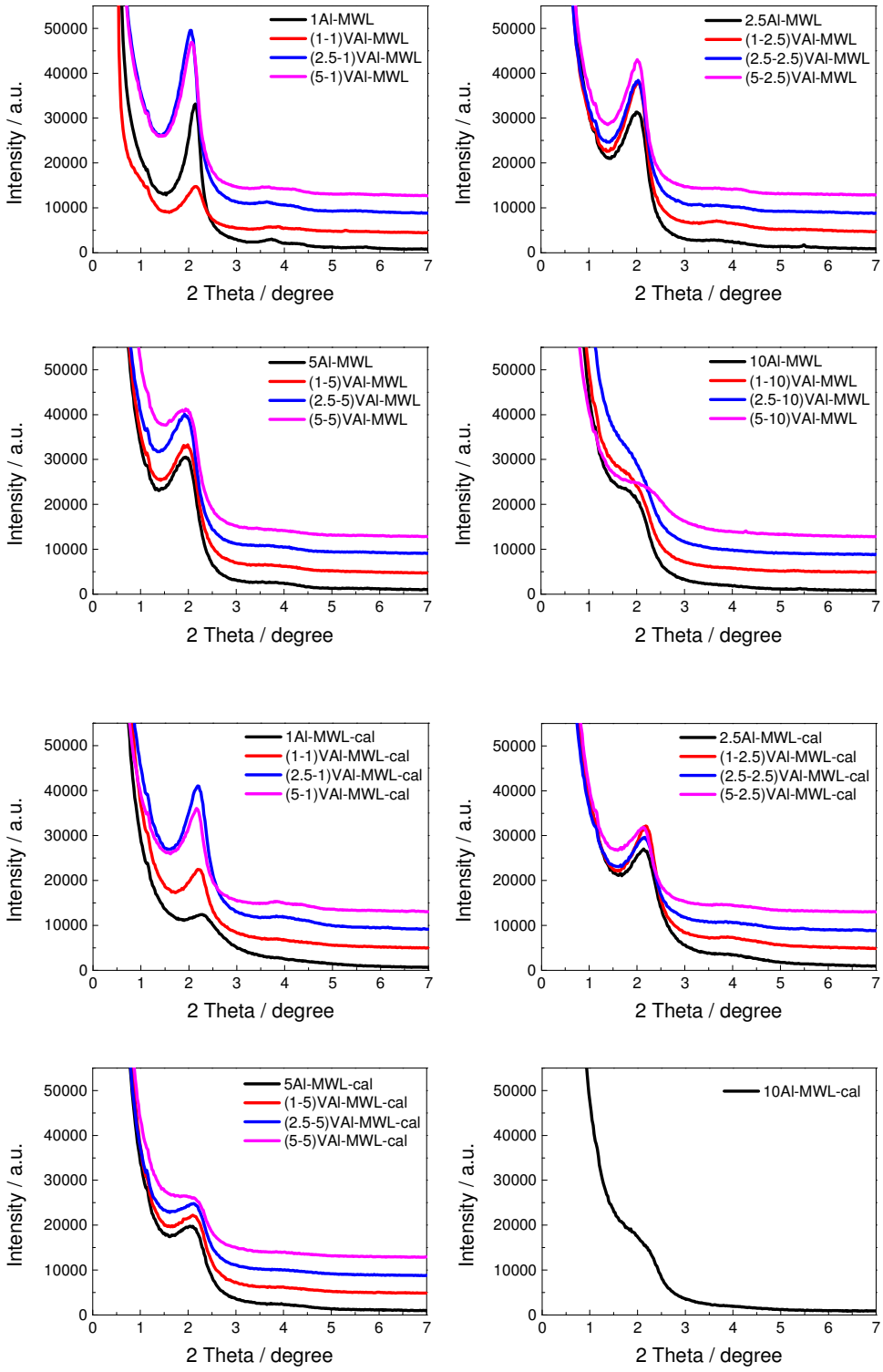

Figure A1.1.3 Low-angle XRD patterns of VZr-MWT/MWL-cal.

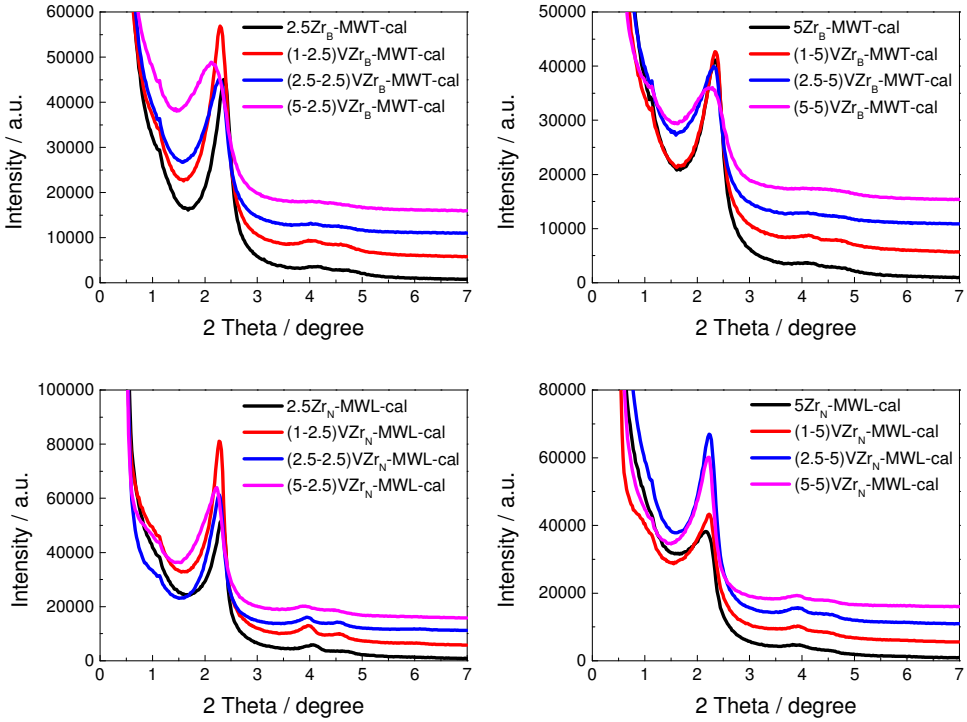

Figure A1.1.4 Low-angle XRD patterns of VCe-MWL/MWT-cal.

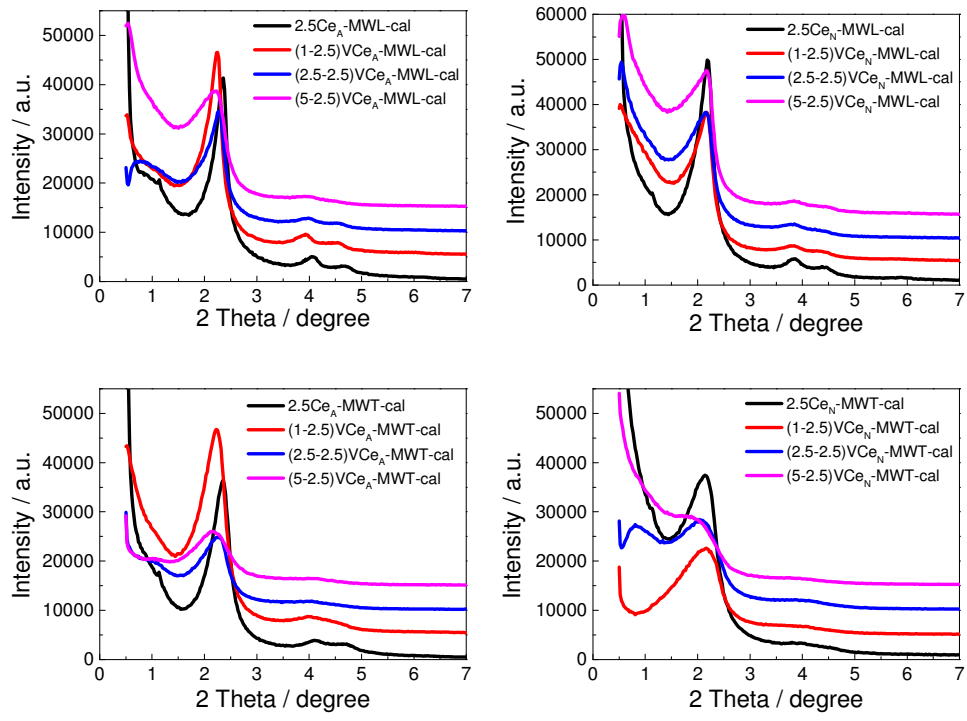

A1.2 XRD patterns of Chapter 5

Figure A1.2.1 Low-angle XRD patterns GPS and V-GPS.

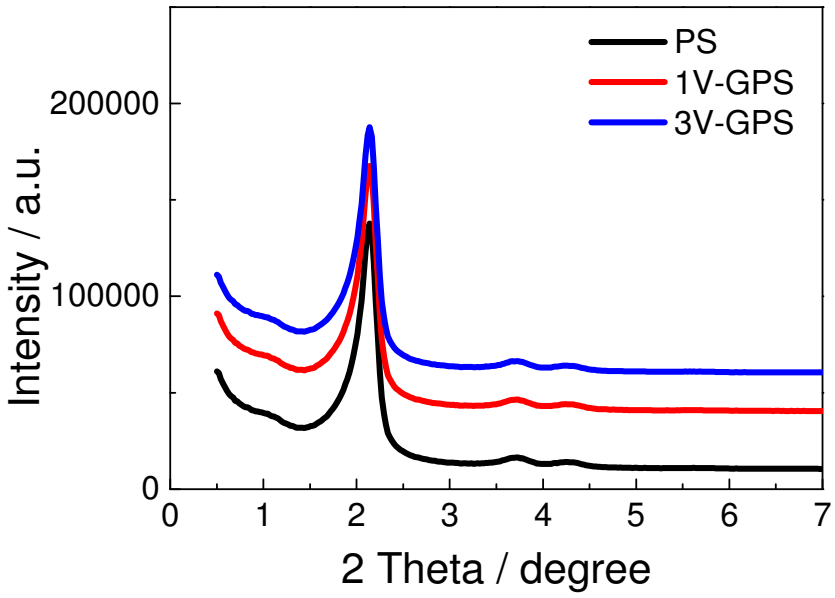

Figure A1.2.2 Low-angle XRD patterns of V-Ti/Al/Zr/Ce-GPS.

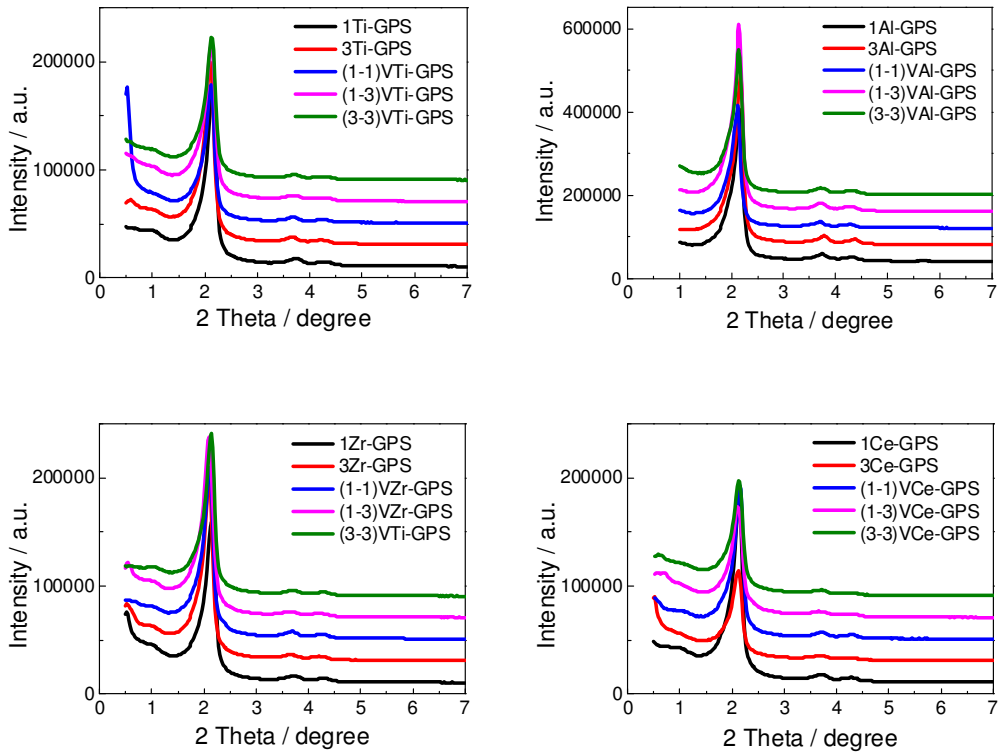

A1.3 XRD patterns of Chapter 7

Figure A1.3.1 Low-angle XRD patterns of Cu/Fe-MWL-cal, VCuFe-GMW-cal.

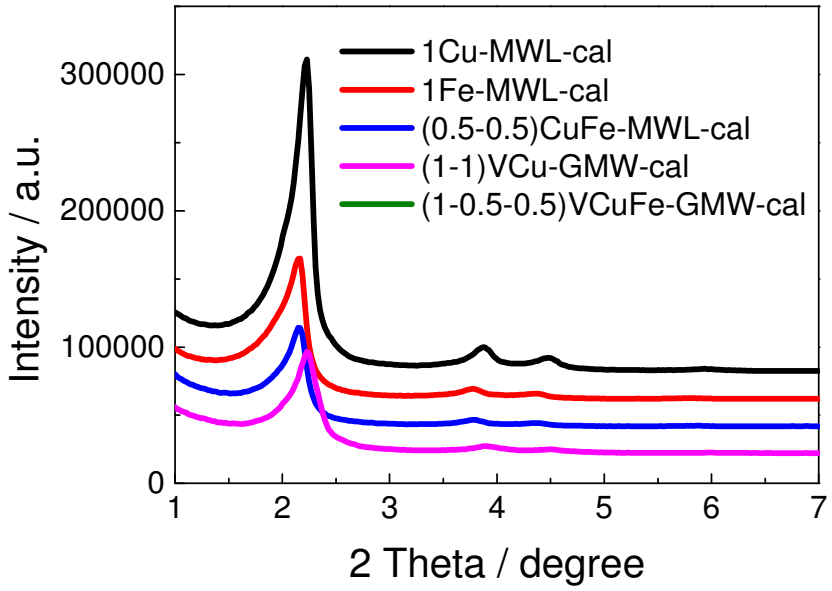

Appendix 2 N_2 adsorption-desorption isotherms and porosity data

A2.1 N_2 adsorption-desorption isotherms and porosity data of Chapter 4

Figure A2.1.1 N_2 adsorption-desorption isotherms of VTi-MWT-cal.

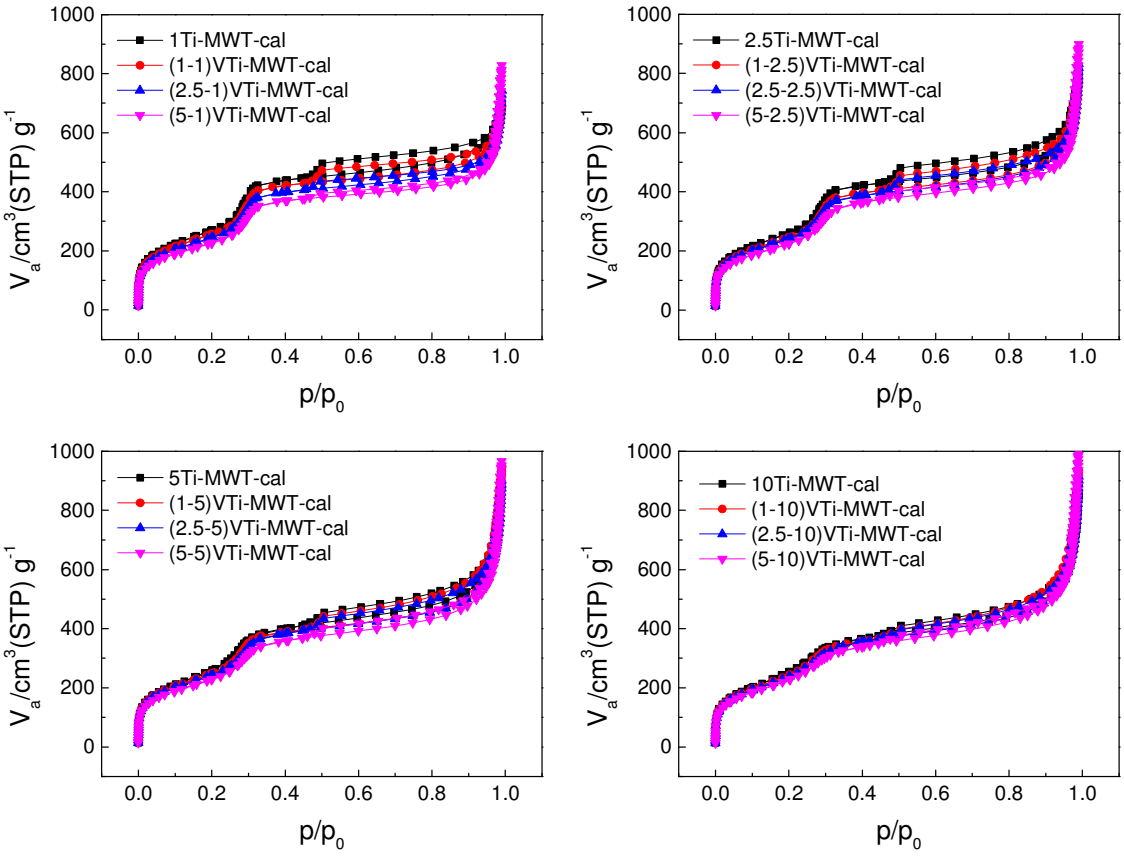

Figure A2.1.2 N_2 adsorption-desorption isotherms of VAl-MWL-cal.

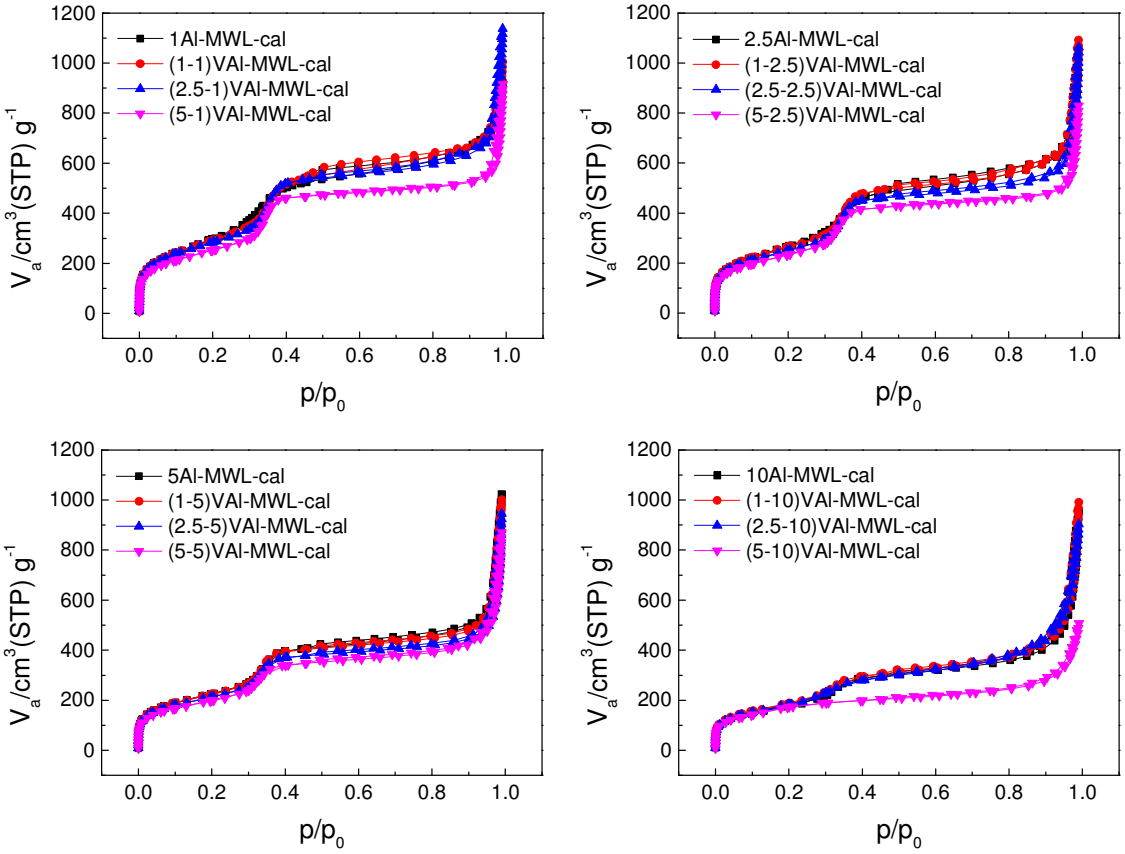

Figure A2.1.3 N_2 adsorption-desorption isotherms of VZr-MWT/MWL-cal.

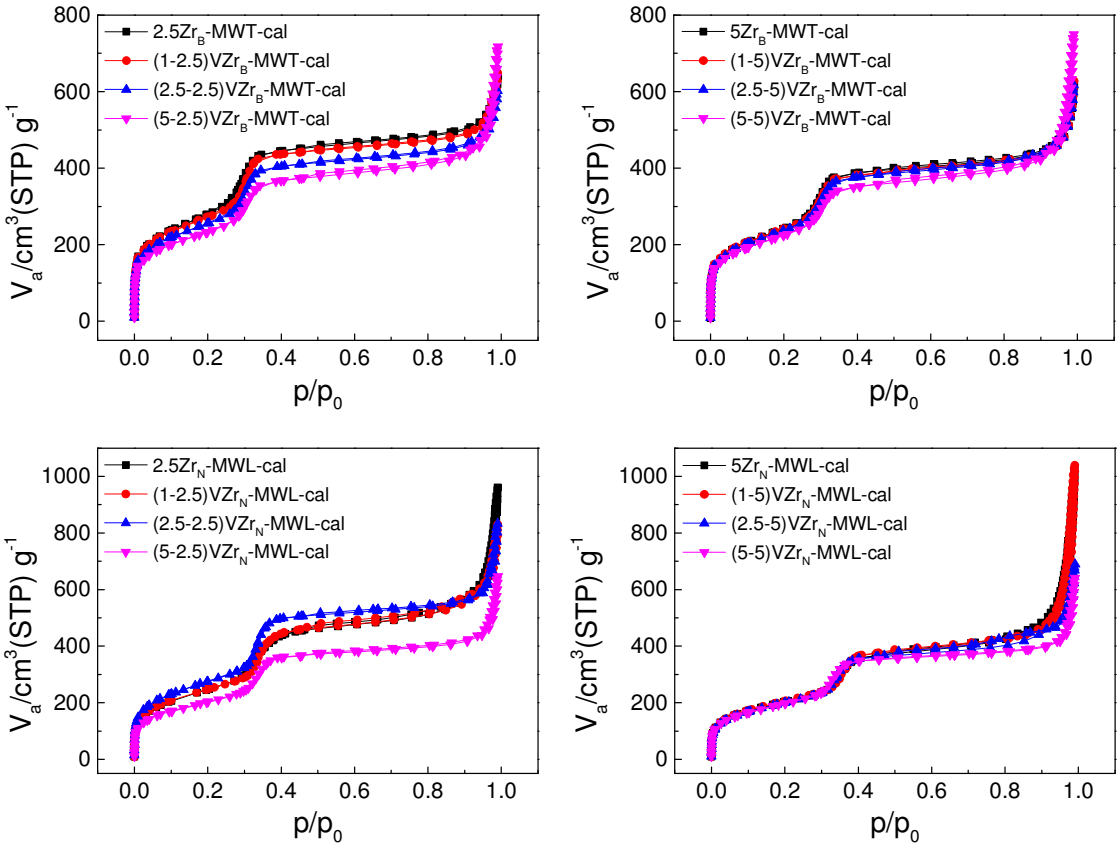

Figure A2.1.4 N_2 adsorption-desorption isotherms of VCe-MWL/MWT-cal.

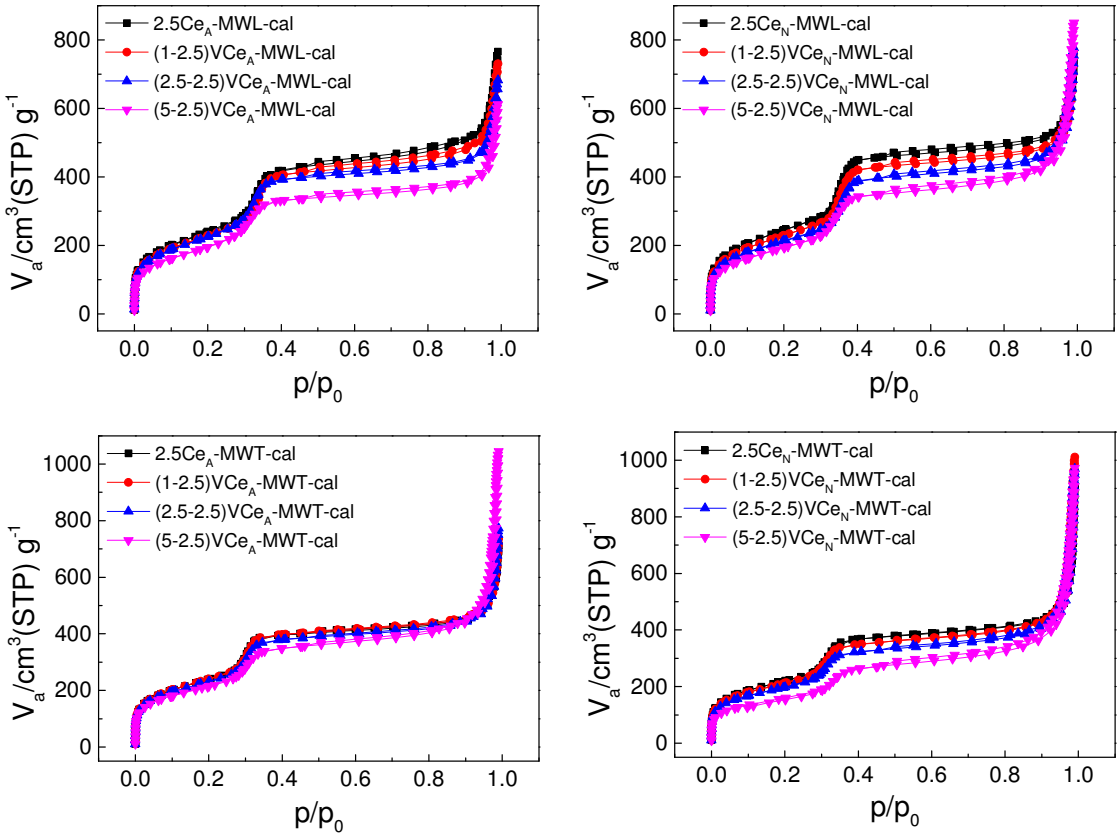

Table A2.1.1 Porosity data of VTi-MWT-cal derived from N_2 adsorption-desorption isotherms.

Sample	a_0[a] (nm)	V_{total}[b] ($cm^3 \cdot g^{-1}$)	V_p[c] ($cm^3 \cdot g^{-1}$)	S_{BET}[d] ($m^2 \cdot g^{-1}$)	d_{HK}[e] (nm)	d_{BdB}[f] (nm)	$T_{w\ BdB}$[g] (nm)	C
1Ti-MWT-cal	4.3	1.07	0.62	987	2.8	3.3	1.0	74
(1-1)VTi-MWT-cal	4.4	1.05	0.60	939	2.8	3.3	1.1	80
(2.5-1)VTi-MWT-cal	4.4	1.13	0.58	893	2.8	3.3	1.1	84
(5-1)VTi-MWT-cal	4.8	1.26	0.53	825	2.8	3.4	1.4	89
2.5Ti-MWT-cal	4.4	1.23	0.58	961	2.8	3.3	1.1	68
(1-2.5)VTi-MWT-cal	4.4	1.20	0.54	900	2.8	3.3	1.1	77
(2.5-2.5)VTi-MWT-cal	4.5	1.28	0.53	879	2.8	3.3	1.2	81
(5-2.5)VTi-MWT-cal	4.8	1.39	0.52	814	2.8	3.3	1.5	82
5Ti-MWT-cal	4.3	1.37	0.54	952	2.7	3.2	1.1	62
(1-5)VTi-MWT-cal	4.4	1.45	0.51	919	2.7	3.3	1.1	68
(2.5-5)VTi-MWT-cal	4.4	1.38	0.50	890	2.8	3.3	1.1	71
(5-5)VTi-MWT-cal	4.9	1.47	0.47	837	2.8	3.3	1.6	76
10Ti-MWT-cal	4.3	1.31	0.47	939	2.6	3.1	1.2	51
(1-10)VTi-MWT-cal	4.2	1.43	0.44	897	2.7	3.3	0.9	57
(2.5-10)VTi-MWT-cal	4.4	1.41	0.45	867	2.7	3.3	1.1	62
(5-10)VTi-MWT-cal	4.7	1.54	0.43	831	2.7	3.3	1.4	64

(a) Hexagonal lattice parameter calculated from XRD, $a_0 = 2d_{100}/1.732$, accuracy ± 0.1 nm; (b) V_{total} at $p/p_0 = 0.99$, accuracy ± 0.01 cm^3g^{-1}; (c) V_p at $P/P_0 = 0$ on the adsorption plateau of t-plot, accuracy ± 0.01 cm^3g^{-1}; (d) from BET equation at $0.05 \leq p/p_0 \leq 0.16$, accuracy ± 50 m^2g^{-1}; (e) pore diameter extrapolated from Horvath-Kawazoe method, accuracy ± 0.1 nm; (f) pore diameter extrapolated from Broekhoff and De Boer method, accuracy ± 0.1 nm; (g) pore wall thickness calculated from a_0-d_{BdB}, accuracy ± 0.2 nm.

Table A2.1.2 Porosity data of VAl-MWL-cal derived from N_2 adsorption-desorption isotherms.

Sample	a_0[a] (nm)	V_{total}[b] ($cm^3 \cdot g^{-1}$)	V_p[c] ($cm^3 \cdot g^{-1}$)	S_{BET}[d] ($m^2 \cdot g^{-1}$)	d_{HK}[e] (nm)	d_{BdB}[f] (nm)	$T_{w\ BdB}$[g] (nm)	C
1Al-MWL-cal	4.5	1.41	0.76	1108	3.2	3.6	0.9	57
(1-1)VAl-MWL-cal	4.6	1.54	0.83	1082	3.3	3.7	0.9	68
(2.5-1)VAl-MWL-cal	4.7	1.74	0.74	1044	3.3	3.7	1.0	79
(5-1)VAl-MWL-cal	4.7	1.34	0.70	926	3.2	3.7	1.0	82
2.5Al-MWL-cal	4.7	1.62	0.67	985	3.2	3.7	1.0	68
(1-2.5)VAl-MWL-cal	4.6	1.67	0.66	975	3.2	3.7	0.9	80
(2.5-2.5)VAl-MWL-cal	4.7	1.62	0.64	916	3.2	3.7	1.0	89
(5-2.5)VAl-MWL-cal	4.8	1.26	0.62	852	3.2	3.6	1.2	90
5Al-MWL-cal	4.9	1.57	0.56	827	3.2	3.7	1.2	84
(1-5)VAl-MWL-cal	4.9	1.52	0.57	822	3.2	3.6	1.3	87
(2.5-5)VAl-MWL-cal	4.8	1.45	0.53	776	3.2	3.6	1.2	92
(5-5)VAl-MWL-cal	5.0	1.34	0.48	725	3.1	3.6	1.4	92
10Al-MWL-cal	#	1.46	0.34	652	3.0	3.5	#	86
(1-10)VAl-MWL-cal	#	1.51	0.34	690	3.0	3.5	#	78
(2.5-10)VAl-MWL-cal	#	1.39	0.30	672	2.9	3.4	#	74
(5-10)VAl-MWL-cal	#	0.77	0.23	640	#	#	#	64

(a) Hexagonal lattice parameter calculated from XRD, $a_0 = 2d_{100}/1.732$, accuracy ± 0.1 nm; (b) V_{total} at $p/p_0 = 0.99$, accuracy ± 0.01 cm^3g^{-1}; (c) V_p at $P/P_0 = 0$ on the adsorption plateau of t-plot, accuracy ± 0.01 cm^3g^{-1}; (d) from BET equation at $0.05 \leq p/p_0 \leq 0.16$, accuracy ± 50 m^2g^{-1}; (e) pore diameter extrapolated from Horvath-Kawazoe method, accuracy ± 0.1 nm; (f) pore diameter extrapolated from Broekhoff and De Boer method, accuracy ± 0.1 nm; (g) pore wall thickness calculated from a_0-d_{BdB}, accuracy ± 0.2 nm.

Table A2.1.3 Porosity data of VZr-MWL/MWT-cal derived from N_2 adsorption-desorption isotherms.

Sample	a_0[a] (nm)	V_{total}[b] ($cm^3 \cdot g^{-1}$)	V_p[c] ($cm^3 \cdot g^{-1}$)	S_{BET}[d] ($m^2 \cdot g^{-1}$)	d_{HK}[e] (nm)	d_{BdB}[f] (nm)	$T_{w\ BdB}$[g] (nm)	C
2.5Zr_B-MWT-cal	4.3	0.96	0.67	1010	2.8	3.4	0.9	110
(1-2.5)VZr_B-MWT-cal	4.4	1.00	0.66	984	2.9	3.5	0.9	130
(2.5-2.5)VZr_B-MWT-cal	4.5	0.93	0.60	919	2.9	3.5	1.0	130
(5-2.5)VZr_B-MWT-cal	4.8	1.08	0.53	836	2.9	3.5	1.3	139
5Zr_B-MWT-cal	4.4	0.92	0.58	872	2.8	3.4	1.0	115
(1-5)VZr_B-MWT-cal	4.3	0.96	0.57	870	2.8	3.4	0.9	127
(2.5-5)VZr_B-MWT-cal	4.6	0.95	0.55	852	2.8	3.5	1.1	121
(5-5)VZr_B-MWT-cal	4.6	1.15	0.50	805	2.8	3.5	1.1	132
2.5Zr_N-MWL-cal	4.4	1.47	0.59	905	2.9	3.6	0.8	78
(1-2.5)VZr_N-MWL-cal	4.5	1.26	0.62	907	3.2	3.7	0.8	80
(2.5-2.5)VZr_N-MWL-cal	4.5	1.28	0.75	1009	3.2	3.7	0.8	79
(5-2.5)VZr_N-MWL-cal	4.6	0.97	0.54	745	3.2	3.7	0.9	80
5Zr_N-MWL-cal	4.7	1.59	0.45	747	3.2	3.7	1.0	84
(1-5)VZr_N-MWL-cal	4.6	1.58	0.51	751	3.3	3.7	0.9	86
(2.5-5)VZr_N-MWL-cal	4.6	1.03	0.47	732	3.2	3.7	0.9	82
(5-5)VZr_N-MWL-cal	4.6	0.97	0.52	720	2.9	3.6	1.0	82

(a) Hexagonal lattice parameter calculated from XRD, $a_0 = 2d_{100}/1.732$, accuracy ± 0.1 nm; (b) V_{total} at $p/p_0 = 0.99$, accuracy ± 0.01 cm^3g^{-1}; (c) V_p at $P/P_0 = 0$ on the adsorption plateau of t-plot, accuracy ± 0.01 cm^3g^{-1}; (d) from BET equation at $0.05 \leq p/p_0 \leq 0.16$, accuracy ± 50 m^2g^{-1}; (e) pore diameter extrapolated from Horvath-Kawazoe method, accuracy ± 0.1 nm; (f) pore diameter extrapolated from Broekhoff and De Boer method, accuracy ± 0.1 nm; (g) pore wall thickness calculated from a_0-d_{BdB}, accuracy ± 0.2 nm.

Table A2.1.4 Porosity data of VCe-MWL/MWT-cal derived from N_2 adsorption-desorption isotherms.

Sample	a_0[a] (nm)	V_{total}[b] ($cm^3 \cdot g^{-1}$)	V_p[c] ($cm^3 \cdot g^{-1}$)	S_{BET}[d] ($m^2 \cdot g^{-1}$)	d_{HK}[e] (nm)	d_{BdB}[f] (nm)	$T_{w\ BdB}$[g] (nm)	C
$2.5Ce_A$-MWL-cal	4.3	1.17	0.59	881	2.9	3.6	0.7	76
(1-2.5)VCe_A-MWL-cal	4.6	1.10	0.58	837	3.2	3.7	0.9	77
(2.5-2.5)VCe_A-MWL-cal	4.5	1.02	0.58	822	2.9	3.6	0.9	80
(5-2.5)VCe_A-MWL-cal	4.6	0.92	0.49	716	2.9	3.5	1.1	70
$2.5Ce_N$-MWL-cal	4.7	1.11	0.67	894	3.3	3.8	0.9	85
(1-2.5)VCe_N-MWL-cal	4.7	1.16	0.63	838	3.3	3.8	0.9	83
(2.5-2.5)VCe_N-MWL-cal	4.7	1.19	0.57	780	3.3	3.8	0.9	85
(5-2.5)VCe_N-MWL-cal	4.7	1.30	0.48	705	3.2	3.7	1.0	82
$2.5Ce_A$-MWT-cal	4.3	1.08	0.58	870	2.8	3.5	0.8	91
(1-2.5)VCe_A-MWT-cal	4.6	1.12	0.58	876	2.8	3.5	1.1	90
(2.5-2.5)VCe_A-MWT-cal	4.5	1.19	0.54	838	2.8	3.5	1.0	94
(5-2.5)VCe_A-MWT-cal	4.7	1.60	0.47	781	2.8	3.5	1.2	92
$2.5Ce_N$-MWT-cal	4.7	1.38	0.53	799	2.8	3.5	1.2	100
(1-2.5)VCe_N-MWT-cal	4.7	1.55	0.49	772	2.9	3.5	1.2	100
(2.5-2.5)VCe_N-MWT-cal	4.9	1.50	0.44	717	2.9	3.5	1.4	101
(5-2.5)VCe_N-MWT-cal	#	1.50	0.31	577	2.9	3.6	#	106

(a) Hexagonal lattice parameter calculated from XRD, $a_0 = 2d_{100}/1.732$, accuracy ± 0.1 nm; (b) V_{total} at $p/p_0 = 0.99$, accuracy ± 0.01 cm^3g^{-1}; (c) V_p at $P/P_0 = 0$ on the adsorption plateau of t-plot, accuracy ± 0.01 cm^3g^{-1}; (d) from BET equation at $0.05 \leq p/p_0 \leq 0.16$, accuracy ± 50 m^2g^{-1}; (e) pore diameter extrapolated from Horvath-Kawazoe method, accuracy ± 0.1 nm; (f) pore diameter extrapolated from Broekhoff and De Boer method, accuracy ± 0.1 nm; (g) pore wall thickness calculated from a_0-d_{BdB}, accuracy ± 0.2 nm.

A2.2 Porosity data of Chapter 5

Table A2.2.1 Porosity data of VTi/Zr/Ce/Al-GPS derived from N_2 adsorption-desorption isotherms.

Sample	a_0[a] (nm)	V_{total}[b] ($cm^3 \cdot g^{-1}$)	V_p[c] ($cm^3 \cdot g^{-1}$)	S_{BET}[d] ($m^2 \cdot g^{-1}$)	d_{HK}[e] (nm)	d_{BdB}[f] (nm)	$T_{w\ BdB}$[g] (nm)	C
1V-GPS	4.8	0.80	0.58	818	2.8	3.3	1.5	32
3V-GPS	4.9	0.76	0.56	778	2.8	3.3	1.6	33
1Ti-GPS	4.8	0.75	0.56	781	2.7	3.3	1.5	31
3Ti-GPS	4.9	0.74	0.55	766	2.6	3.2	1.7	30
1Zr-GPS	4.8	0.77	0.58	799	2.6	3.2	1.6	33
3Zr-GPS	4.9	0.68	0.51	725	2.6	3.1	1.8	29
1Ce-GPS	4.8	0.77	0.59	809	2.7	3.3	1.5	34
3Ce-GPS	4.8	0.69	0.51	739	2.7	3.3	1.5	34
1Al-GPS	4.8	0.77	0.58	803	2.8	3.3	1.5	32
3Al-GPS	4.7	0.72	0.53	733	2.7	3.3	1.4	31
(1-3)VTi-GPS	4.8	0.73	0.54	754	2.6	3.2	1.6	31
(3-3)VTi-GPS	4.8	0.70	0.51	723	2.6	3.1	1.7	31
(1-3)VZr-GPS	4.9	0.69	0.50	706	2.6	3.1	1.8	32
(3-3)VZr-GPS	4.8	0.65	0.48	677	2.6	3.1	1.7	31
(1-3)VCe-GPS	4.9	0.75	0.54	774	2.7	3.3	1.6	33
(3-3)VCe-GPS	4.9	0.70	0.50	722	2.7	3.3	1.6	33
(1-3)VAl-GPS	4.8	0.70	0.50	722	2.7	3.3	1.5	30
(3-3)VAl-GPS	4.8	0.66	0.48	689	2.7	3.3	1.5	31
(1-1)VTi-GPS	4.8	0.74	0.56	773	2.7	3.3	1.5	32
(1-1)VZr-GPS	4.8	0.75	0.56	775	2.6	3.2	1.6	32
(1-1)VCe-GPS	4.8	0.76	0.57	782	2.7	3.3	1.5	32
(1-1)VAl-GPS	4.8	0.75	0.55	769	2.7	3.3	1.5	32

(a) Hexagonal lattice parameter calculated from XRD, $a_0 = 2d_{100}/1.732$, accuracy ± 0.1 nm; (b) V_{total} at $p/p_0 = 0.99$, accuracy ± 0.01 cm^3g^{-1}; (c) V_p at $P/P_0 = 0$ on the adsorption plateau of t-plot, accuracy ± 0.01 cm^3g^{-1}; (d) from BET equation at $0.05 \leq p/p_0 \leq 0.16$, accuracy ± 50 m^2g^{-1}; (e) pore diameter extrapolated from Horvath-Kawazoe method, accuracy ± 0.1 nm; (f) pore diameter extrapolated from Broekhoff and De Boer method, accuracy ± 0.1 nm; (g) pore wall thickness calculated from a_0-d_{BdB}, accuracy ± 0.2 nm.

A2.3 Porosity data of Chapter 7

Table A2.3.1 Porosity data of Cu/Fe-MWL-cal and VCu/Fe-GMW-cal derived from N_2 adsorption-desorption isotherms.

Sample	a_0[a] (nm)	V_{total}[b] ($cm^3 \cdot g^{-1}$)	V_p[c] ($cm^3 \cdot g^{-1}$)	S_{BET}[d] ($m^2 \cdot g^{-1}$)	d_{HK}[e] (nm)	d_{BdB}[f] (nm)	$T_{w\ BdB}$[g] (nm)	C
1Cu-MWL-cal	4.6	0.99	0.74	974	3.1	3.6	1.0	81
(0.5-0.5)CuFe-MWL-cal	4.8	1.13	0.74	970	3.2	3.7	1.1	88
1Fe-MWL-cal	4.7	1.10	0.77	985	3.2	3.7	1.0	87
(1-0.5-0.5)VCuFe-GMW-cal	4.7	1.12	0.65	905	2.9	3.5	1.2	83
(1-1)VCu-GMW-cal	4.6	0.91	0.63	894	2.9	3.5	1.1	79

(a) Hexagonal lattice parameter calculated from XRD, $a_0 = 2d_{100}/1.732$, accuracy ± 0.1 nm; (b) V_{total} at $p/p_0 = 0.99$, accuracy ± 0.01 cm^3g^{-1}; (c) V_p at $P/P_0 = 0$ on the adsorption plateau of t-plot, accuracy ± 0.01 cm^3g^{-1}; (d) from BET equation at $0.05 \leq p/p_0 \leq 0.16$, accuracy ± 50 m^2g^{-1}; (e) pore diameter extrapolated from Horvath-Kawazoe method, accuracy ± 0.1 nm; (f) pore diameter extrapolated from Broekhoff and De Boer method, accuracy ± 0.1 nm; (g) pore wall thickness calculated from a_0-d_{BdB}, accuracy ± 0.2 nm.

Appendix 3 TGA

A3.1 TGA of Chapter 4

Figure A3.1.1 DTG curves of VTi-MWT.

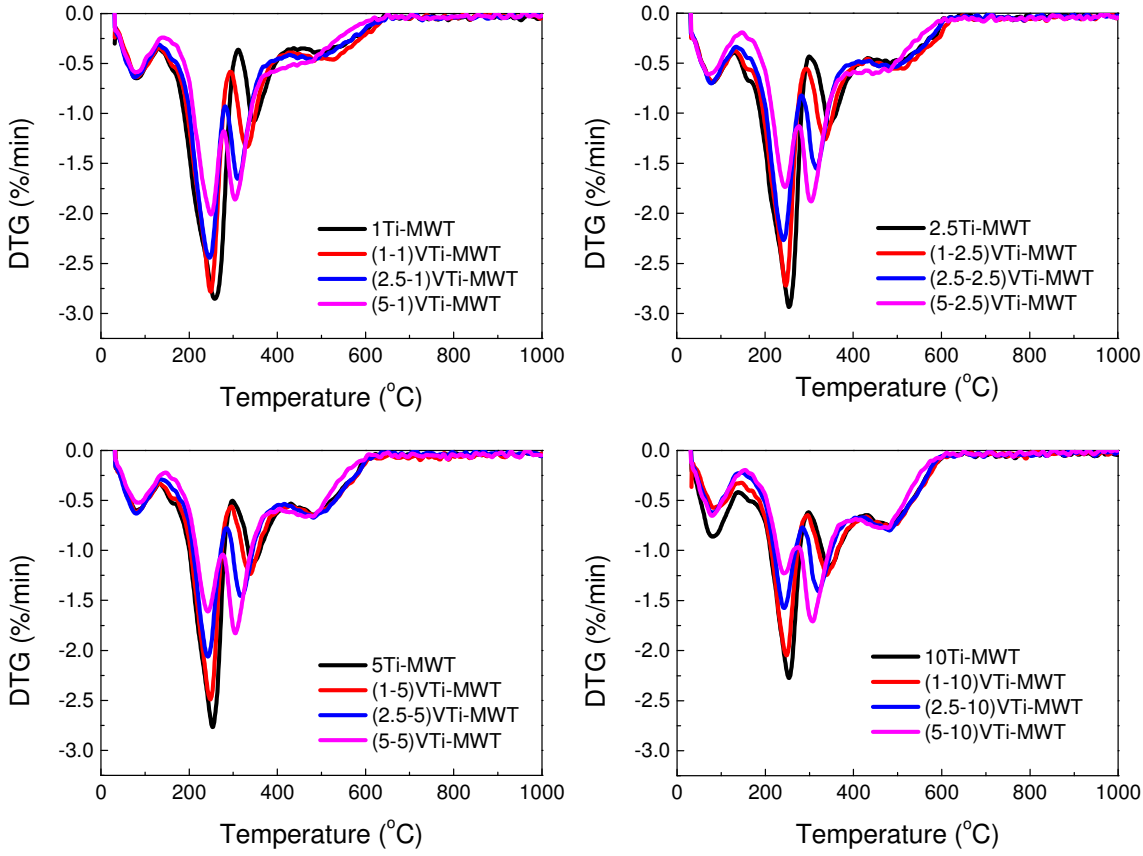

Figure A3.1.2 DTG curves of VAl-MWL.

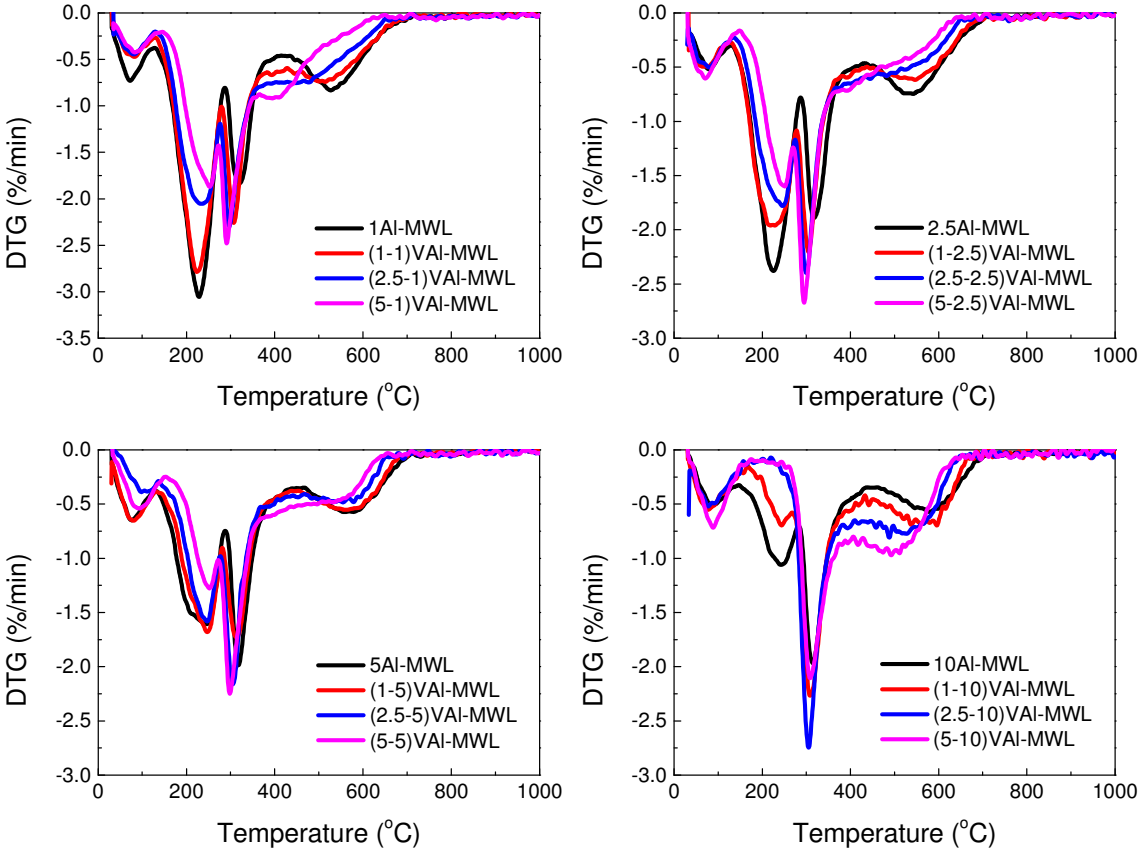

Figure A3.1.3 DTG curves of VZr-MWT/MWL.

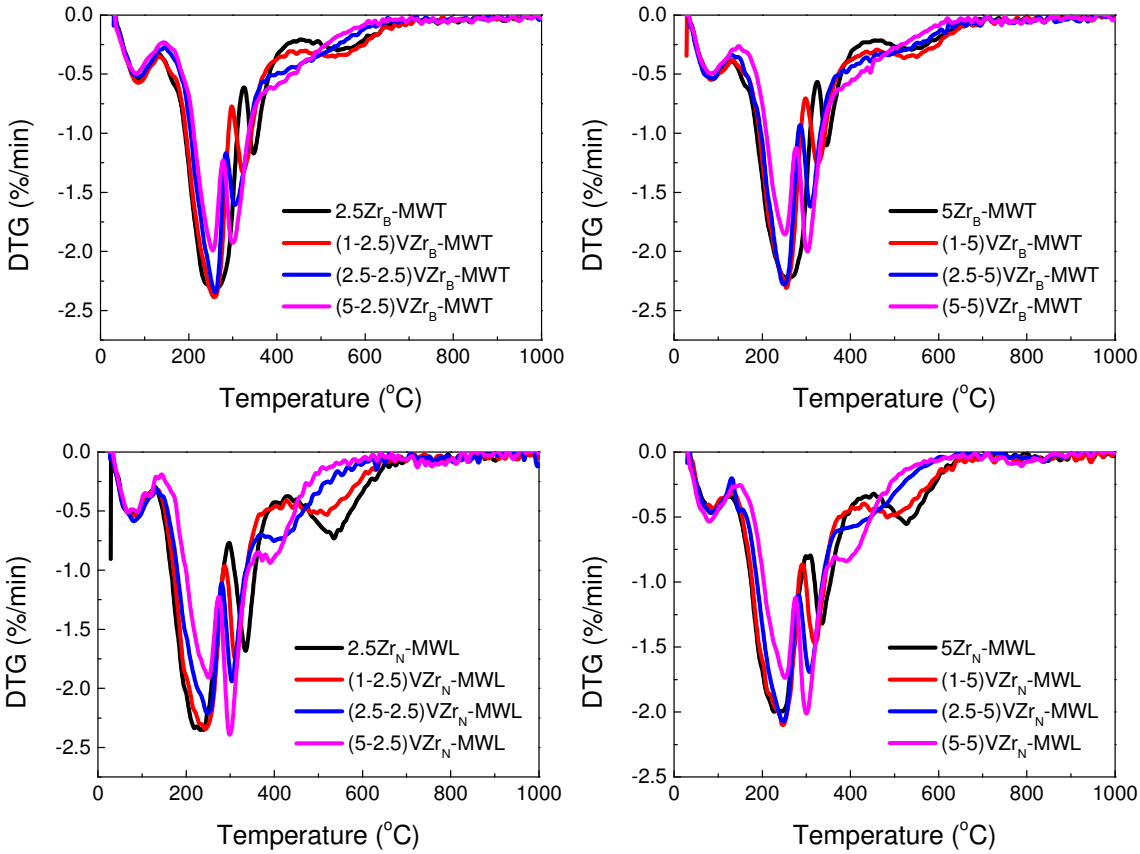

Figure A3.1.4 DTG curves of VCe.MWL/MWT.

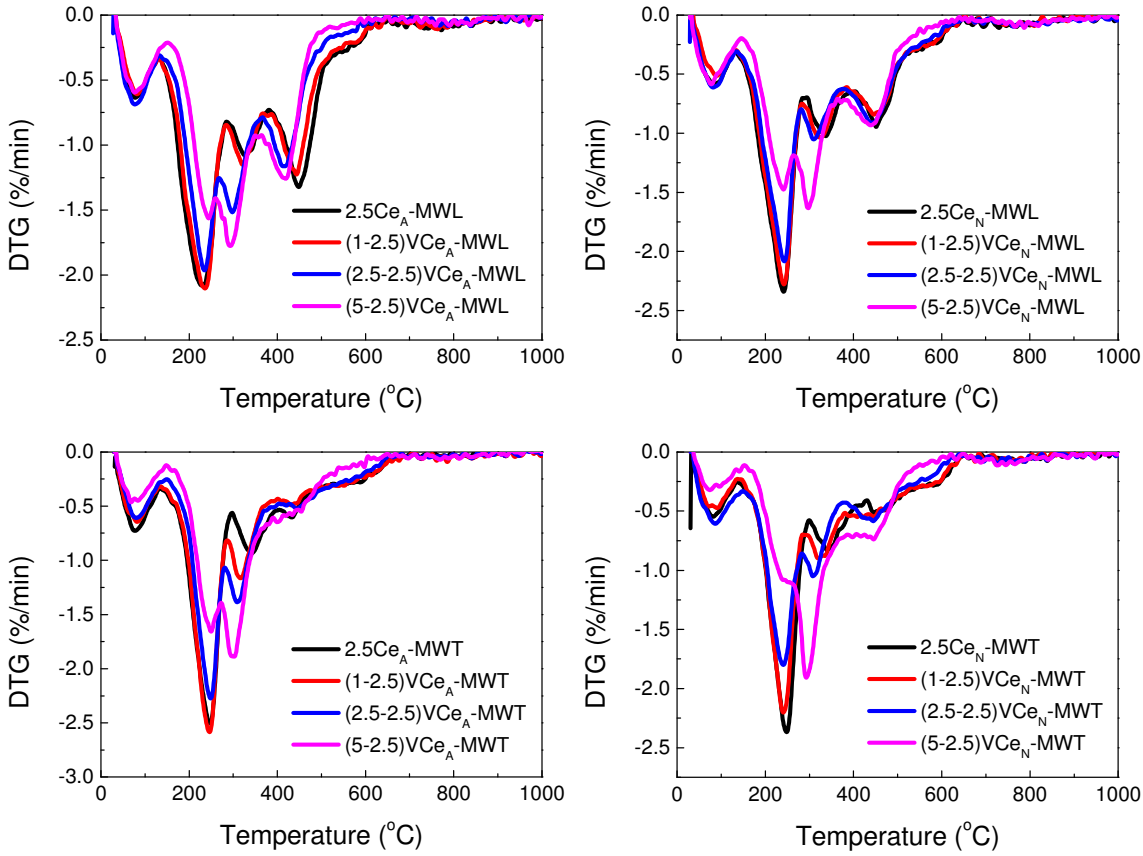

Table A3.1.1 DTG analysis of VTi-MWT.

Sample	PEAK 1	PEAK 2	PEAK 3	PEAK 4	Residual Mass
	mass change from DTG (%)				(%)
1Ti-MWT-cal	4.59	24.87	7.78	6.00	55.18
(1-1)VTi-MWT-cal	4.16	19.65	10.02	7.81	57.09
(2.5-1)VTi-MWT-cal	4.23	17.29	11.89	7.33	58.12
(5-1)VTi-MWT-cal	4.18	13.47	13.16	7.60	60.32
2.5Ti-MWT-cal	4..85	23.05	9.30	7.13	54.42
(1-2.5)VTi-MWT-cal	5.01	18.97	9.85	9.10	55.28
(2.5-2.5)VTi-MWT-cal	4.90	15.80	11.24	8.81	57.65
(5-2.5)VTi-MWT-cal	4.61	11.19	13.22	9.14	59.94
5Ti-MWT-cal	4.25	20.00	9.74	8.74	55.45
(1-5)VTi-MWT-cal	4.32	17.31	10.29	9.50	56.34
(2.5-5)VTi-MWT-cal	4.39	14.11	10.87	10.31	58.91
(5-5)VTi-MWT-cal	3.88	10.87	12.27	10.50	60.64
10Ti-MWT-cal	5.80	16.45	10.94	9.53	55.75
(1-10)VTi-MWT-cal	4.34	14.15	11.72	9.81	58.66
(2.5-10)VTi-MWT-cal	4.19	10.69	11.43	11.41	61.22
(5-10)VTi-MWT-cal	4.63	7.88	13.97	10.45	62.28

Table A3.1.2 DTG analysis of VAl-MWL.

Sample	PEAK 1	PEAK 2	PEAK 3	PEAK 4	Residual Mass
	mass change from DTG (%)				(%)
1Al-MWL-cal	4.87	25.39	12.50	14.57	41.91
(1-1)VAl-MWL-cal	3.38	22.96	15.82	13.28	43.66
(2.5-1)VAl-MWL-cal	3.53	18.64	14.66	14.36	47.59
(5-1)VAl-MWL-cal	3.31	13.74	13.88	13.48	54.40
2.5Al-MWL-cal	3.85	21.17	13.84	13.35	46.96
(1-2.5)VAl-MWL-cal	4.48	19.16	15.71	11.62	48.24
(2.5-2.5)VAl-MWL-cal	3.80	15.54	16.91	10.18	52.82
(5-2.5)VAl-MWL-cal	4.56	10.77	19.34	7.75	56.87
5Al-MWL-cal	4.48	16.90	13.78	10.43	53.66
(1-5)VAl-MWL-cal	4.50	15.20	13.77	10.36	55.57
(2.5-5)VAl-MWL-cal	2.05	12.84	14.93	8.79	60.49
(5-5)VAl-MWL-cal	3.98	8.52	16.66	8.71	61.29
10Al-MWL-cal	3.91	9.51	14.13	10.46	61.24
(1-10)VAl-MWL-cal	4.51	4.29	17.05	12.56	60.88
(2.5-10)VAl-MWL-cal	5.05	0.00	18.21	15.02	60.49
(5-10)VAl-MWL-cal	4.78	0.00	17.20	16.79	60.61

Table A3.1.3 DTG analysis of VZr-MWT/MWL.

Sample	PEAK 1	PEAK 2	PEAK 3	PEAK 4	Residual Mass
	mass change from DTG (%)				(%)
2.5Zr_B-MWT-cal	3.15	26.58	6.91	4.95	57.23
(1-2.5)VZr_B-MWT-cal	3.50	21.14	9.35	6.68	58.11
(2.5-2.5)VZr_B-MWT-cal	3.47	16.79	11.08	7.19	60.37
(5-2.5)VZr_B-MWT-cal	3.37	13.25	12.28	7.89	61.98
5Zr_B-MWT-cal	3.03	26.07	6.61	4.74	58.51
(1-5)VZr_B-MWT-cal	3.06	20.61	9.64	6.07	59.68
(2.5-5)VZr_B-MWT-cal	3.20	18.21	9.11	7.92	60.28
(5-5)VZr_B-MWT-cal	3.07	12.95	11.65	8.36	62.77
2.5Zr_N-MWL-cal	3.28	24.41	10.20	12.00	48.82
(1-2.5)VZr_N-MWL-cal	3.34	22.90	10.54	9.78	51.85
(2.5-2.5)VZr_N-MWL-cal	3.56	19.32	11.01	10.46	54.72
(5-2.5)VZr_N-MWL-cal	3.32	13.87	13.07	10.07	58.41
5Zr_N-MWL-cal	2.71	21.87	9.95	7.54	57.06
(1-5)VZr_N-MWL-cal	2.77	20.31	9.49	9.02	57.12
(2.5-5)VZr_N-MWL-cal	2.85	17.75	10.19	8.42	60.19
(5-5)VZr_N-MWL-cal	3.37	12.76	11.70	9.82	61.20

Table A3.1.4 DTG analysis of VCe-MWL/MWT.

Sample	PEAK 1	PEAK 2	PEAK 3	PEAK 4	PEAK 5	Residual Mass
	mass change from DTG (%)					(%)
2.5Ce_A-MWL-cal	3.79	19.04	8.75	12.40	2.72	51.49
(1-2.5)VCe_A-MWL-cal	3.56	18.23	8.20	12.04	2.40	54.07
(2.5-2.5)VCe_A-MWL-cal	4.04	14.05	11.76	10.85	1.36	56.93
(5-2.5)VCe_A-MWL-cal	3.90	9.13	13.19	11.86	0.91	59.76
2.5Ce_N-MWL-cal	3.30	18.93	8.73	8.67	2.96	55.75
(1-2.5)VCe_N-MWL-cal	2.89	17.60	8.06	9.12	2.75	58.28
(2.5-2.5)VCe_N-MWL-cal	3.77	15.66	7.99	9.90	2.47	58.45
(5-2.5)VCe_N-MWL-cal	3.99	9.94	11.35	10.47	2.03	60.73
2.5Ce_A-MWT-cal	4.84	19.08	7.69	4.79	3.96	58.94
(1-2.5)VCe_A-MWT-cal	3.89	18.33	7.85	5.06	4.10	59.72
(2.5-2.5)VCe_A-MWT-cal	4.07	14.70	9.85	5.63	3.58	61.26
(5-2.5)VCe_A-MWT-cal	3.23	10.13	12.85	6.92	2.09	64.02
2.5Ce_N-MWT-cal	3.55	17.66	8.16	4.18	3.01	62.22
(1-2.5)VCe_N-MWT-cal	3.03	15.51	6.69	6.93	2.92	64.09
(2.5-2.5)VCe_N-MWT-cal	3.83	13.03	7.26	6.46	2.67	65.48
(5-2.5)VCe_N-MWT-cal	1.98	20.91		8.17	1.29	66.06

A3.2 TGA of Chapter 5

Figure A3.2.1 DTG curves of VTi/Zr/Ce/Al-GPS.

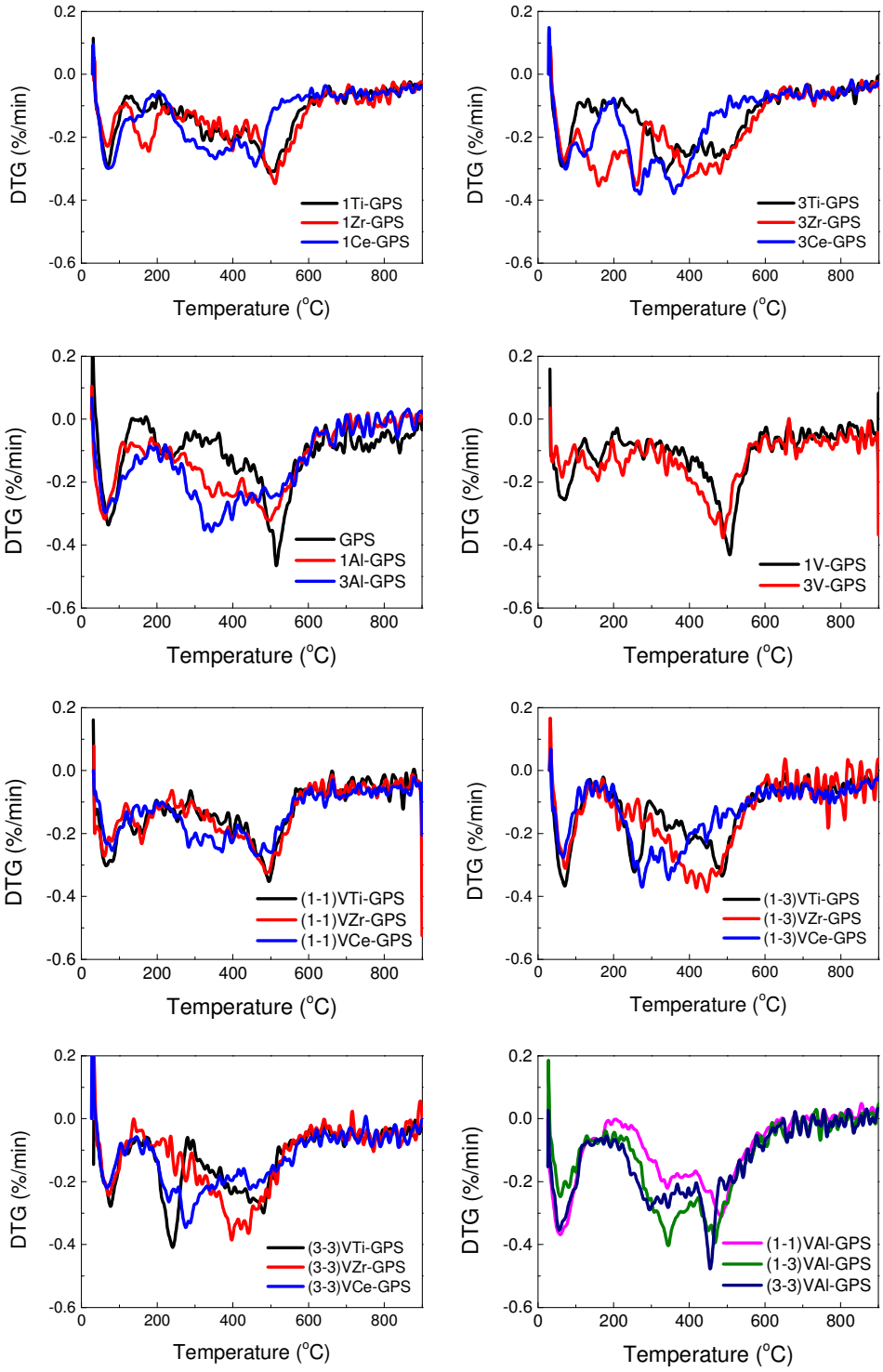

A3.3 TGA of Chapter 6

Figure A3.3.1 DTG curves of VTi/Zr/Ce/Al-GPC.

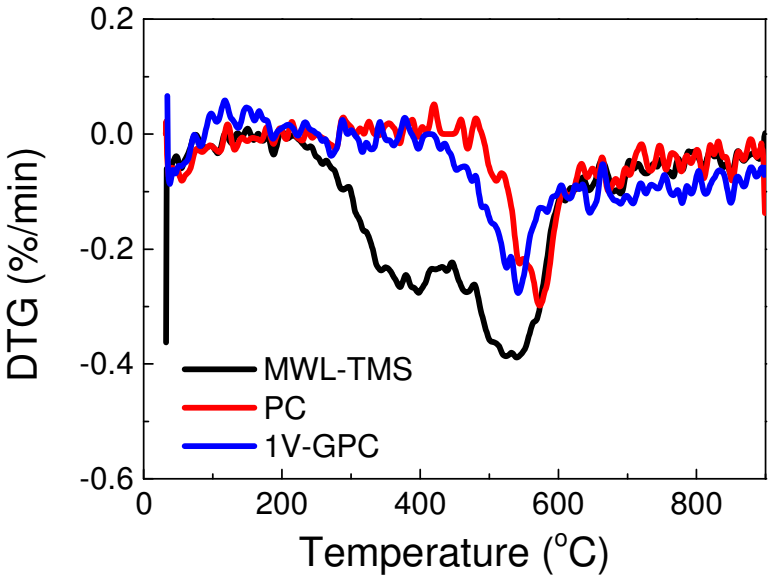

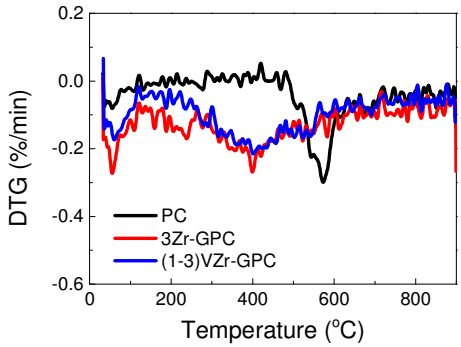

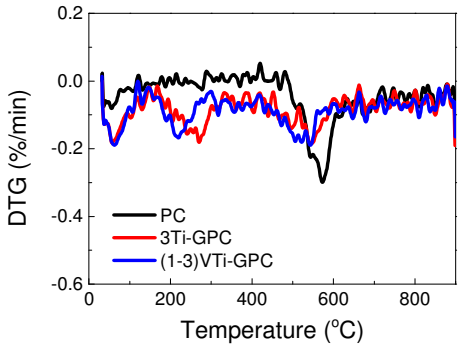

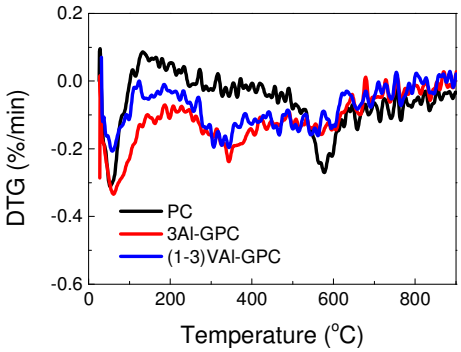

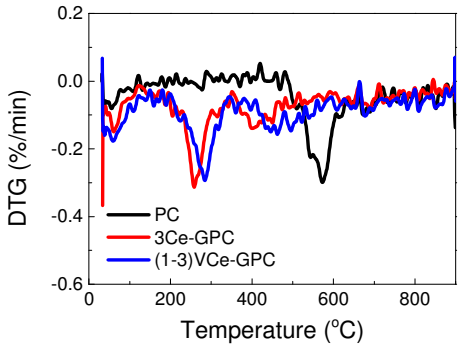

Table A3.3.1 TG analysis of MWL-TMS, PC, and VTi/Zr/Ce/Al-GPC.

Sample	Residual Mass (%)
MWL-TMS	89.29
PC	96.30
3Ti-GPC	92.71
3Zr-GPC	88.57
3Ce-GPC	93.77
3Al-GPC	90.34
(1-3)VTi-GPC	92.32
(1-3)VZr-GPC	91.19
(1-3)VCe-GPC	92.00
(1-3)VAl-GPC	92.97
1V-GPC	94.72

A3.4 TGA of Chapter 7

Figure A3.4.1 DTG curves of Cu/Fe-MWL.

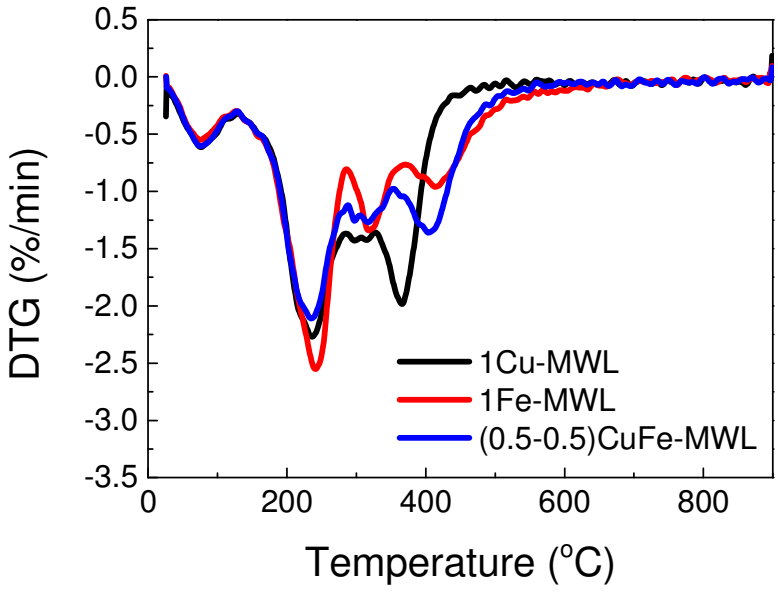

Table A3.4.1 TG analysis of Cu/Fe-MWL.

Sample	Residual Mass (%)
1Cu-MWL	55.77
(0.5-0.5)CuFe-MWL	55.34
1Fe-MWL	56.17

Appendix 4 FT-IR spectra

A4.1 FT-IR spectra of Chapter 4

Figure A4.1.1 FT-IR spectra of as-made VTi-MWT.

A: 1Ti-MWT, B: (1-1)VTi-MWT, C: (2.5-1)VTi-MWT, D: (5-1)VTi-MWT,

E: 2.5Ti-MWT, F: (1-2.5)VTi-MWT, G: (2.5-2.5)VTi-MWT, H: (5-2.5)VTi-MWT,

I: 5Ti-MWT, J: (1-5)VTi-MWT, K: (2.5-5)VTi-MWT, L: (5-5)VTi-MWT,

M: 10Ti-MWT, N: (1-10)VTi-MWT, O: (2.5-10)VTi-MWT, P: (5-10)VTi-MWT.

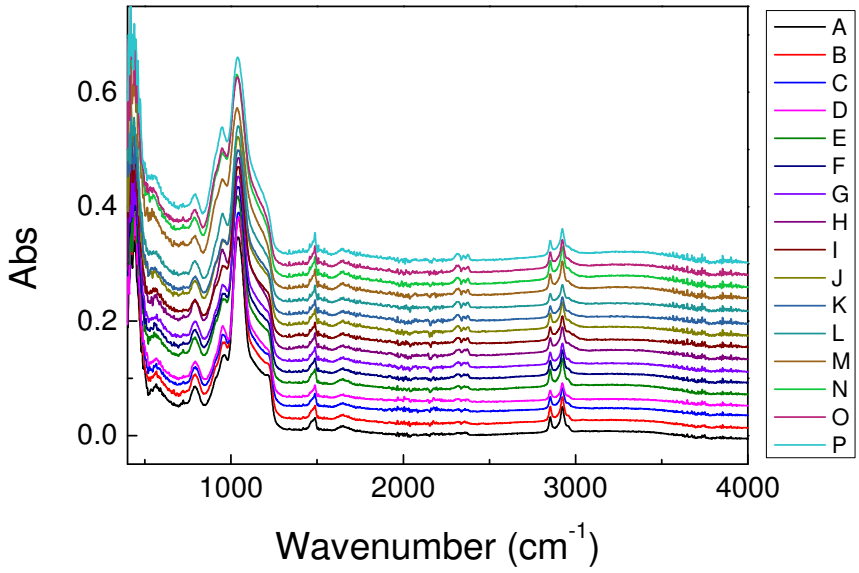

Figure A4.1.2 FT-IR spectra of VTi-MWT-cal.

a: 1Ti-MWT-cal, b: (1-1)VTi-MWT-cal, c: (2.5-1)VTi-MWT-cal, d: (5-1)VTi-MWT-cal,

e: 2.5Ti-MWT-cal, f: (1-2.5)VTi-MWT-cal, g: (2.5-2.5)VTi-MWT-cal, h: (5-2.5)VTi-MWT-cal,

i: 5Ti-MWT-cal, j: (1-5)VTi-MWT-cal, k: (2.5-5)VTi-MWT-cal, l: (5-5)VTi-MWT-cal,

m: 10Ti-MWT-cal, n: (1-10)VTi-MWT-cal, o: (2.5-10)VTi-MWT-cal, p: (5-10)VTi-MWT-cal.

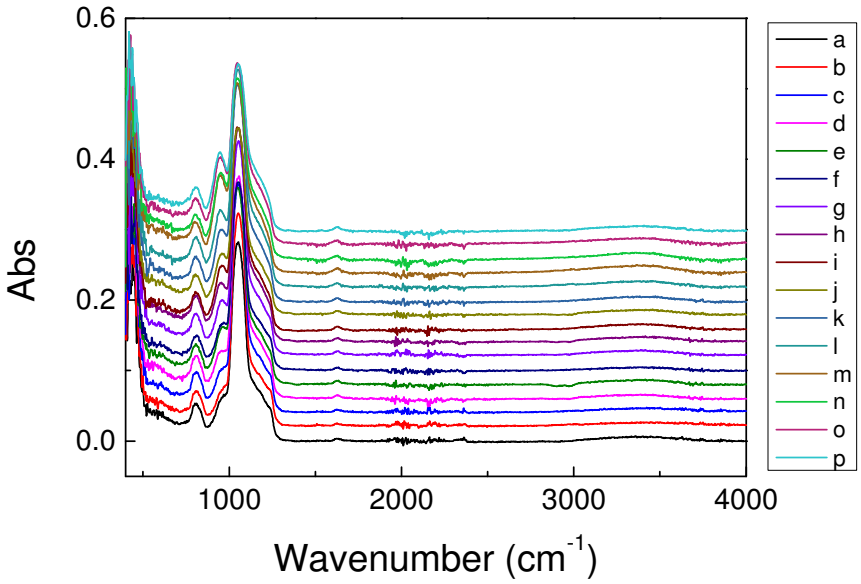

Figure A4.1.3 FT-IR spectra of as-made VAl-MWL.

A: 1Al-MWL, B: (1-1)VAl-MWL, C: (2.5-1)VAl-MWL, D: (5-1)VAl-MWL,

E: 2.5Al-MWL, F: (1-2.5)VAl-MWL, G: (2.5-2.5)VAl-MWL, H: (5-2.5)VAl-MWL,

I: 5Al-MWL, J: (1-5)VAl-MWL, K: (2.5-5)VAl-MWL, L: (5-5)VAl-MWL,

M: 10Al-MWL, N: (1-10)VAl-MWL, O: (2.5-10)VAl-MWL, P: (5-10)VAl-MWL.

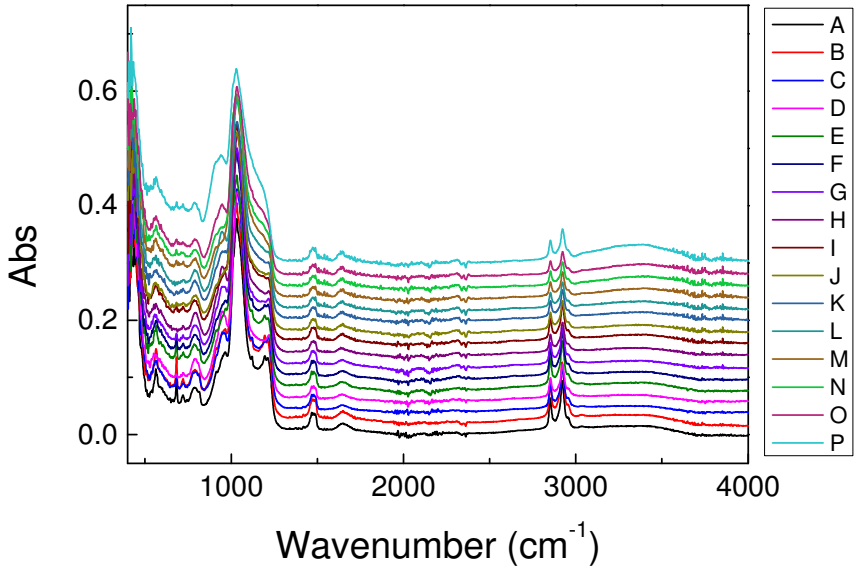

Figure A4.1.4 FT-IR spectra of VAl-MWL-cal.

a: 1Al-MWL-cal, b: (1-1)VAl-MWL-cal, c: (2.5-1)VAl-MWL-cal, d: (5-1)VAl-MWL-cal,

e: 2.5Al-MWL-cal, f: (1-2.5)VAl-MWL-cal, g: (2.5-2.5)VAl-MWL-cal, h: (5-2.5)VAl-MWL-cal,

i: 5Al-MWL-cal, j: (1-5)VAl-MWL-cal, k: (2.5-5)VAl-MWL-cal, l: (5-5)VAl-MWL-cal,

m: 10Al-MWL-cal, n: (1-10)VAl-MWL-cal, o: (2.5-10)VAl-MWL-cal, p: (5-10)VAl-MWL-cal.

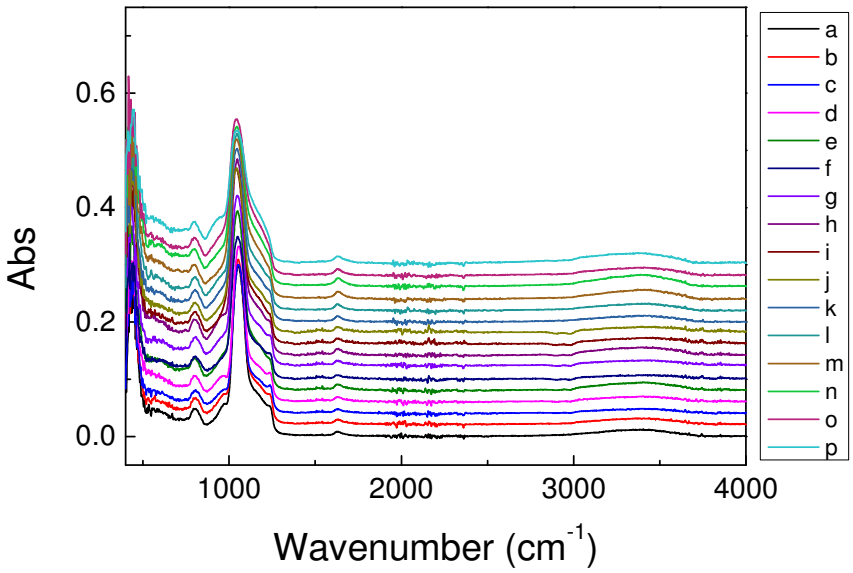

Figure A4.1.5 FT-IR spectra of as-made VZr-MWL/MWT.

A: 2.5Zr_B-MWT, B: (1-2.5)VZr_B-MWT, C: (2.5-2.5)VZr_B-MWT, D: (5-2.5)VZr_B-MWT,

E: 5Zr_B-MWT, F: (1-5)VZr_B-MWT, G: (2.5-5)VZr_B-MWT, H: (5-5)VZr_B-MWT,

I: 2.5Zr_N-MWL, J: (1-2.5)VZr_N-MWL, K: (2.5-2.5)VZr_N-MWL, L: (5-2.5)VZr_N-MWL,

M: 5Zr_N-MWL, N: (1-5)VZr_N-MWL, O: (2.5-5)VZr_N-MWL, P: (5-5)VZr_N-MWL.

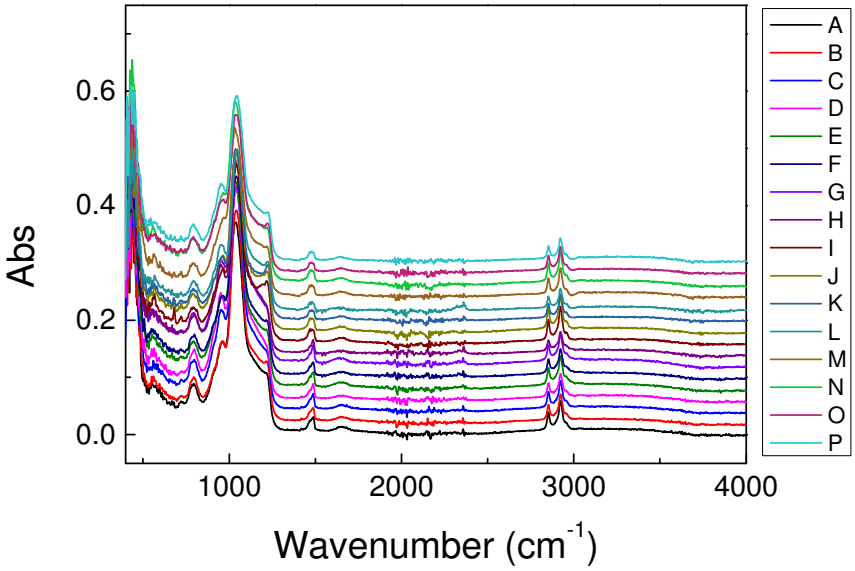

Figure A4.1.6 FT-IR spectra of VZr-MWL/MWT-cal.

a: 2.5Zr_B-MWT-cal, b: (1-2.5)VZr_B-MWT-cal, c: (2.5-2.5)VZr_B-MWT-cal, d: (5-2.5)VZr_B-MWT-cal, e: 5Zr_B-MWT-cal, f: (1-5)VZr_B-MWT-cal, g: (2.5-5)VZr_B-MWT-cal, h: (5-5)VZr_B-MWT-cal, i: 2.5Zr_N-MWL-cal, j: (1-2.5)VZr_N-MWL-cal, k: (2.5-2.5)VZr_N-MWL-cal, l: (5-2.5)VZr_N-MWL-cal, m: 5Zr_N-MWL-cal, n: (1-5)VZr_N-MWL-cal, o: (2.5-5)VZr_N-MWL-cal, p: (5-5)VZr_N-MWL-cal.

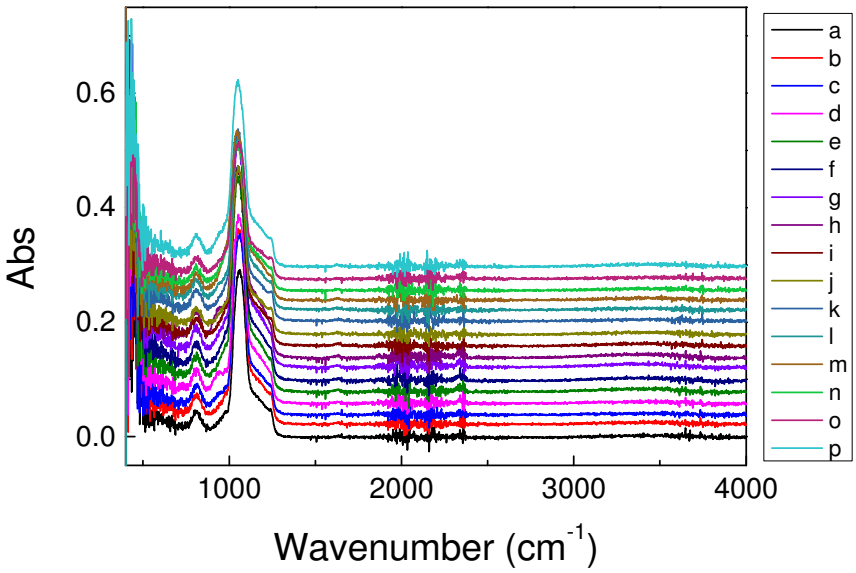

Figure A4.1.7 FT-IR spectra of as-made VCe-MWL/MWT.

A: 2.5Ce_A-MWL, B: (1-2.5)VCe_A-MWL, C: (2.5-2.5)VCe_A-MWL, D: (5-2.5)VCe_A-MWL,

E: 2.5Ce_N-MWL, F: (1-2.5)VCe_N-MWL, G: (2.5-2.5)VCe_N-MWL, H: (5-2.5)VCe_N-MWL,

I: 2.5Ce_A-MWT, J: (1-2.5)VCe_A-MWT, K: (2.5-2.5)VCe_A-MWT, L: (5-2.5)VCe_A-MWT,

M: 2.5Ce_N-MWT, N: (1-2.5)VCe_N-MWT, O: (2.5-2.5)VCe_N-MWT, P: (5-2.5)VCe_N-MWT.

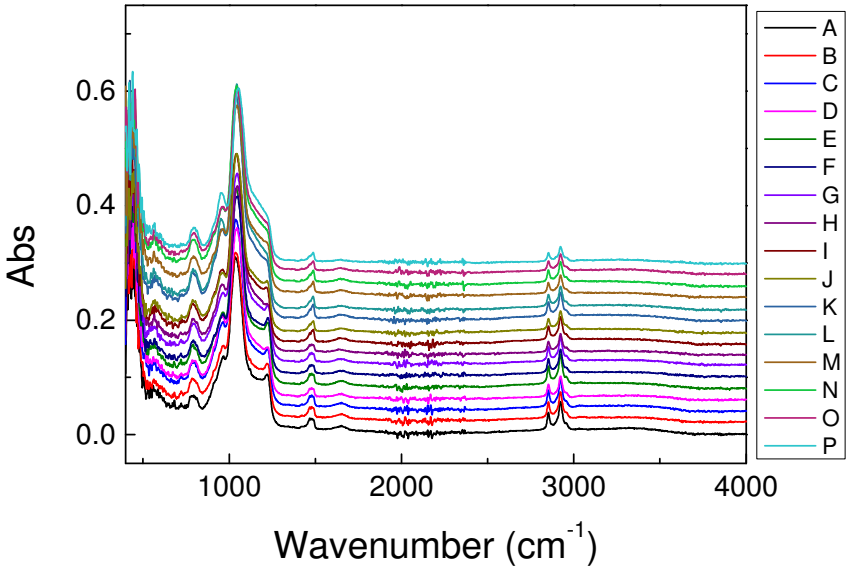

Figure A4.1.8 FT-IR spectra of as-made VCe-MWL/MWT-cal.

a: 2.5Ce_A-MWL, b: (1-2.5)VCe_A-MWL, c: (2.5-2.5)VCe_A-MWL, d: (5-2.5)VCe_A-MWL,

e: 2.5Ce_N-MWL, f: (1-2.5)VCe_N-MWL, g: (2.5-2.5)VCe_N-MWL, h: (5-2.5)VCe_N-MWL,

i: 2.5Ce_A-MWT, j: (1-2.5)VCe_A-MWT, k: (2.5-2.5)VCe_A-MWT, l: (5-2.5)VCe_A-MWT,

m: 2.5Ce_N-MWT, n: (1-2.5)VCe_N-MWT, o: (2.5-2.5)VCe_N-MWT, p: (5-2.5)VCe_N-MWT.

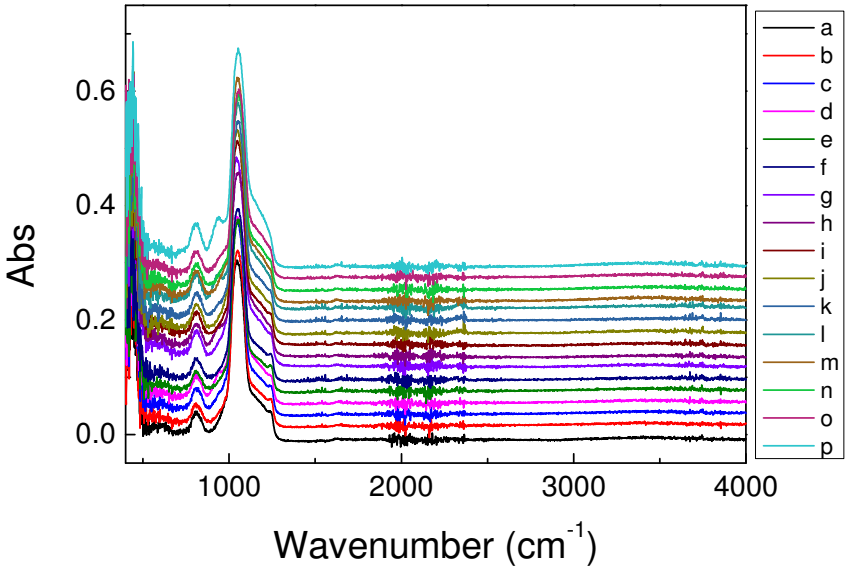

A4.2 FT-IR spectra of Chapter 5

Figure A4.2.1 FT-IR spectra of VTi/Zr/Ce/Al-GPS.

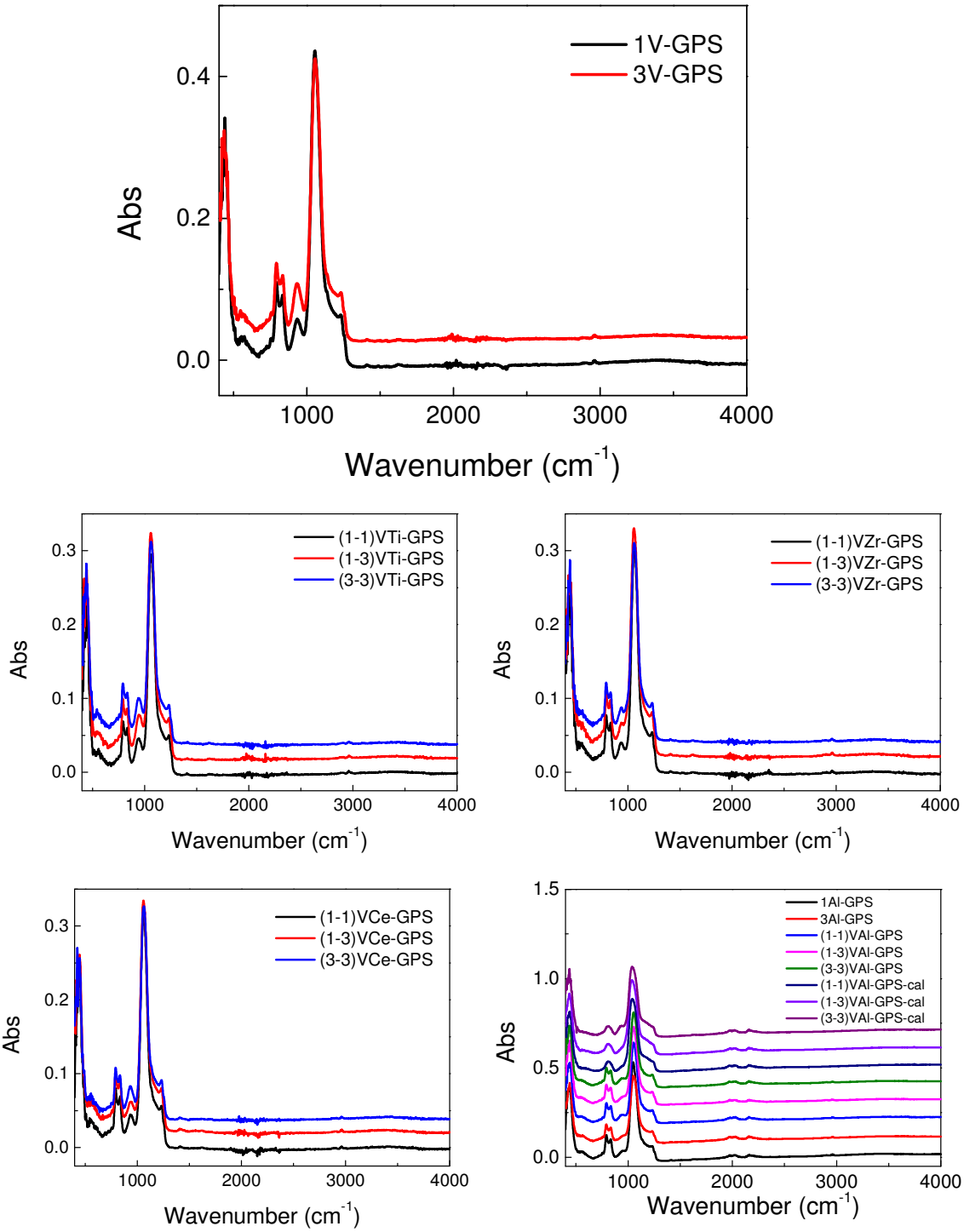

A4.3 FT-IR spectra of Chapter 6

Figure A4.3.1 FT-IR spectra of VTi/Zr/Ce/Al-GPC(cal).

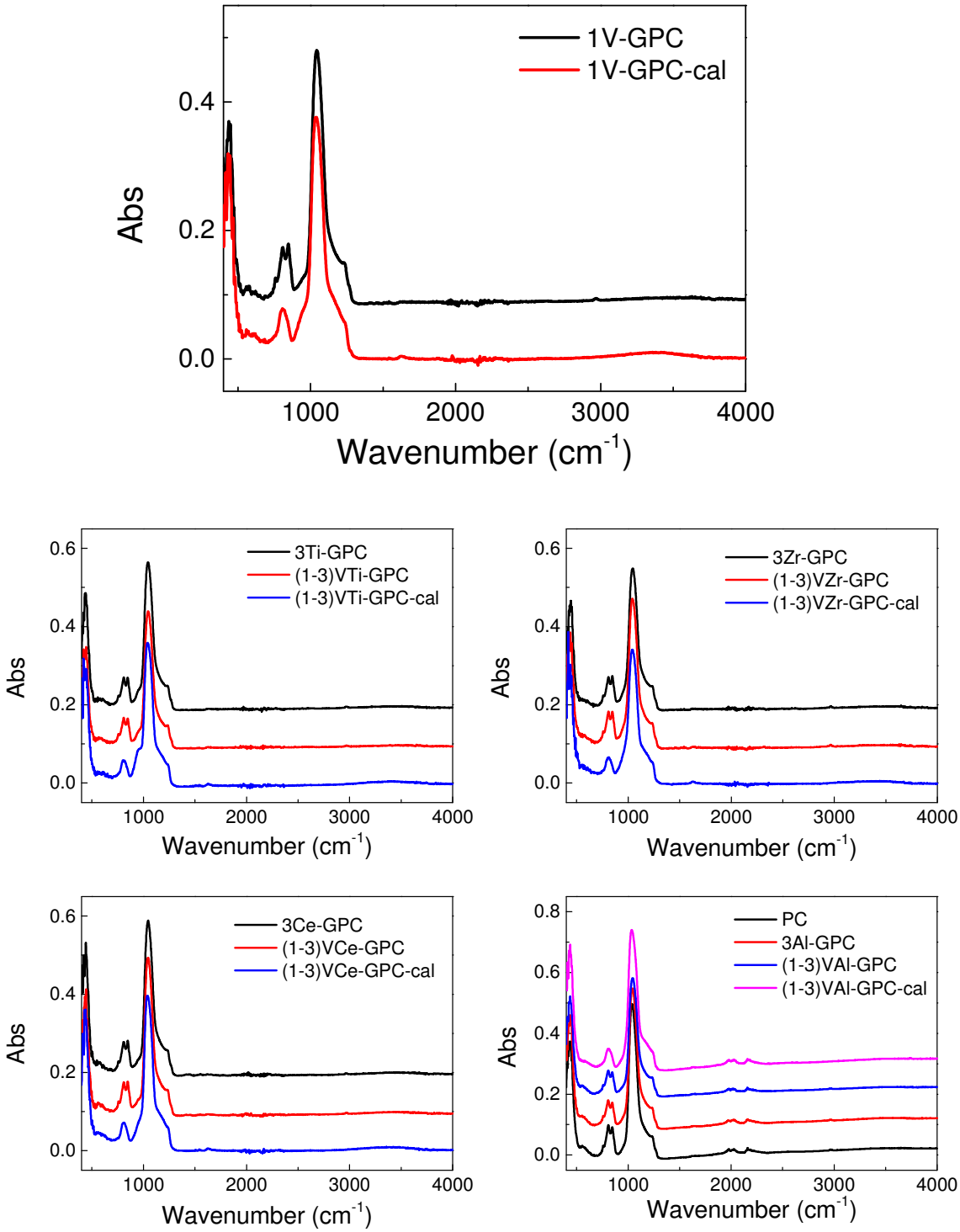

A4.4 FT-IR spectra of Chapter 7

Figure A4.4.1 FT-IR spectra of Cu/Fe-MWL(cal) and VCu/Fe-GMW(cal).

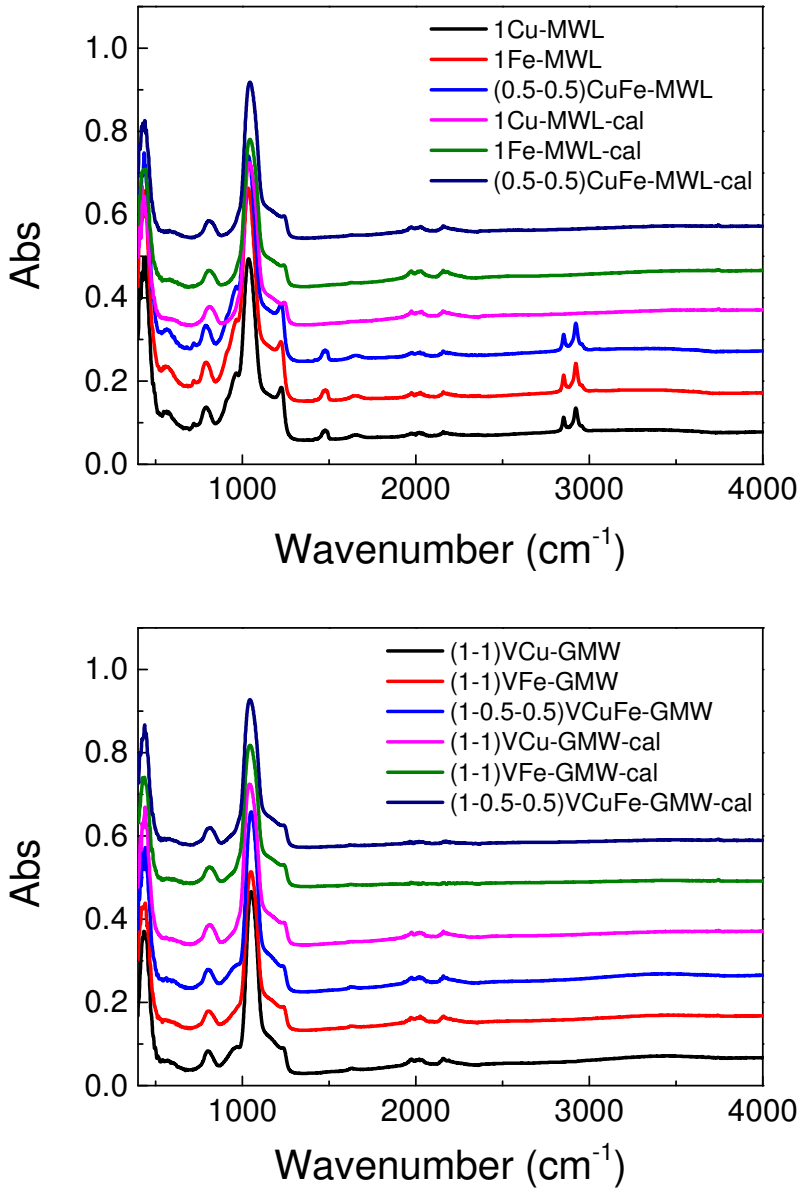

Appendix 5 UV-vis spectra

A5.1 UV-vis spectra of Chapter 4

Figure A5.1.1 UV-vis spectra of VAl-MWL-cal. MWL-cal was used as blank, and before measurement, samples were diluted by MWL-cal to keep the spectra intensity in the range of 0.2-0.8 K/M.

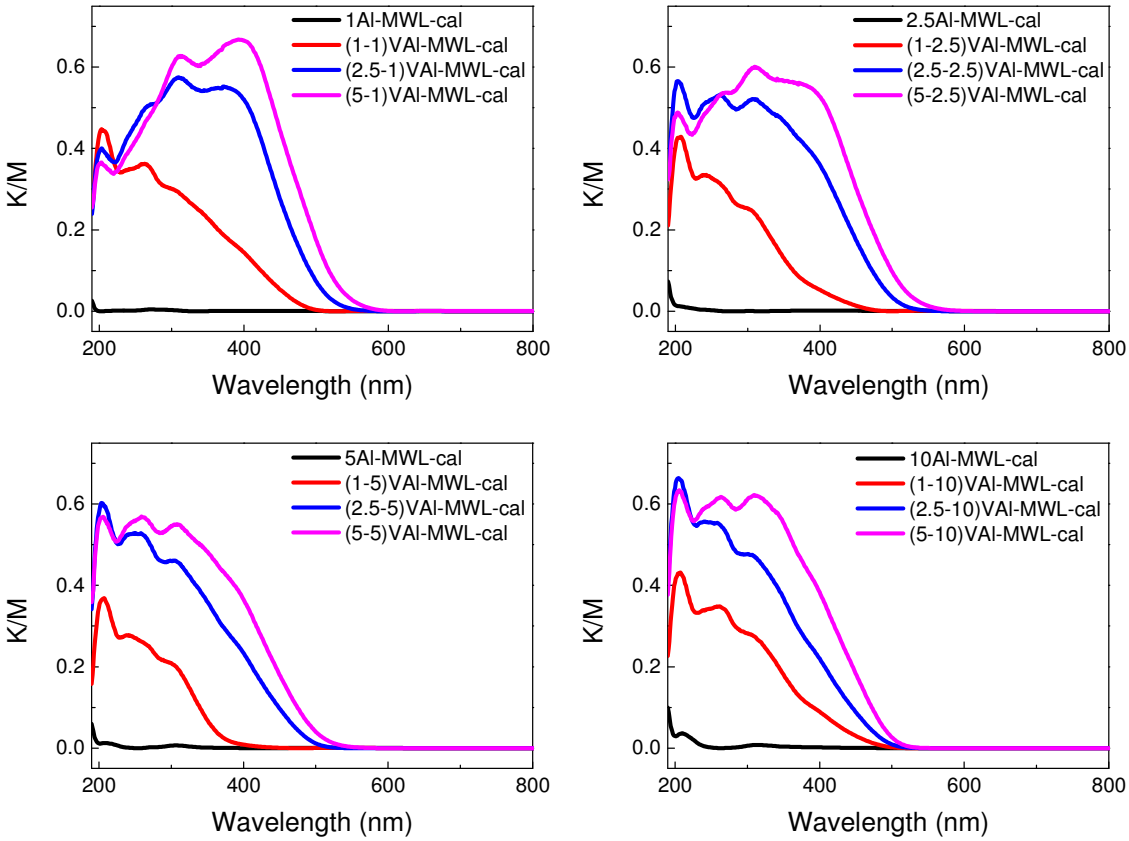

Figure A5.1.2 UV-vis spectra of VZr_B-MWT-cal and VZr_N-MWL-cal. MWL-cal was used as blank, and before measurement, samples were diluted by MWL-cal to keep the spectra intensity in the range of 0.2-0.8 K/M.

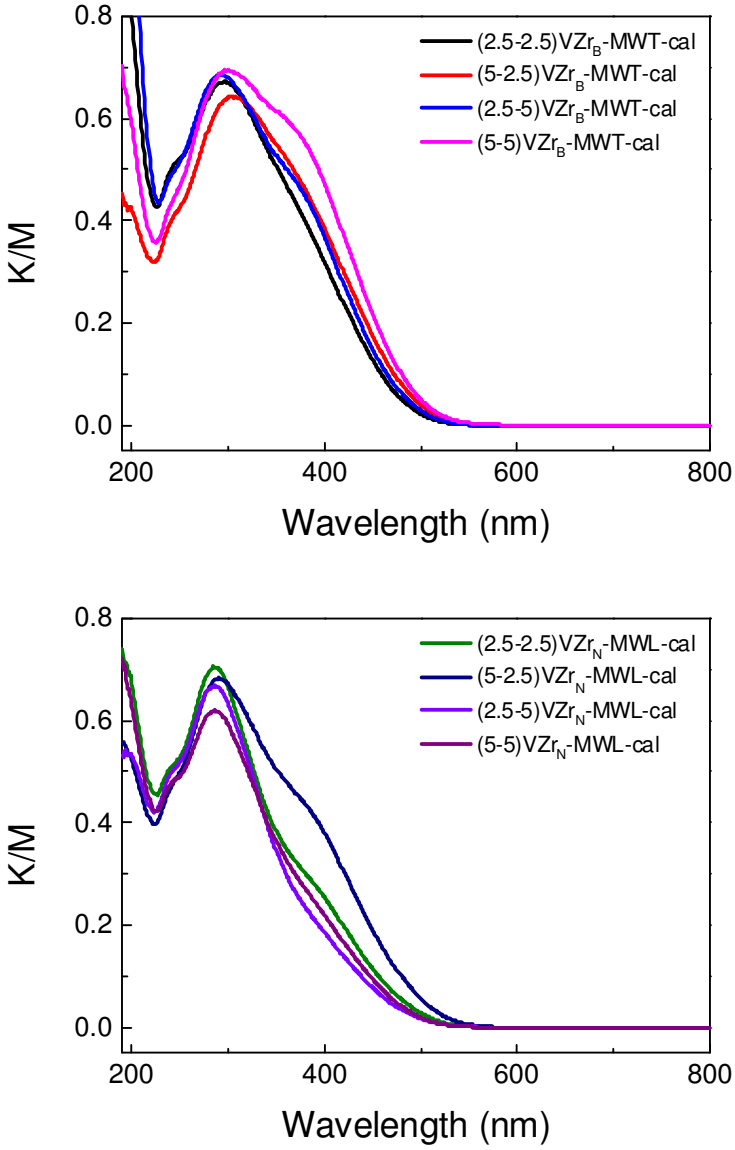

Figure A5.1.3 UV-vis spectra of VCe_A-MWL-cal, VCe_N-MWL-cal, VCe_A-MWT-cal, VCe_N-MWT-cal. MWL-cal was used as blank, and before measurement, samples were diluted by MWL-cal to keep the spectra intensity in the range of 0.2-0.8 K/M.

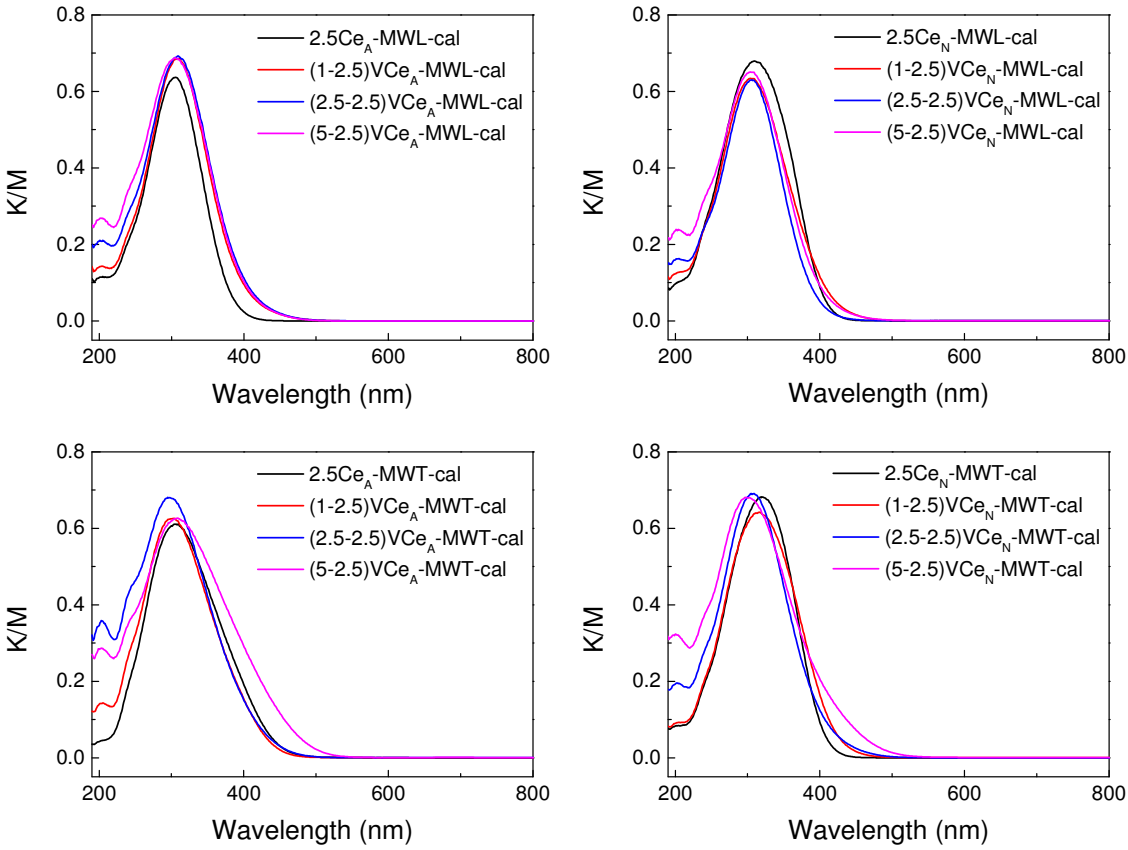

A5.2 UV-vis spectra of Chapter 5

Figure A5.2.1 UV-vis spectra of VTi/Zr/Ce/Al-GPS. MWL-cal was used as blank, and before measurement, samples were diluted by MWL-cal to keep the spectra intensity in the range of 0.2-0.8 K/M.

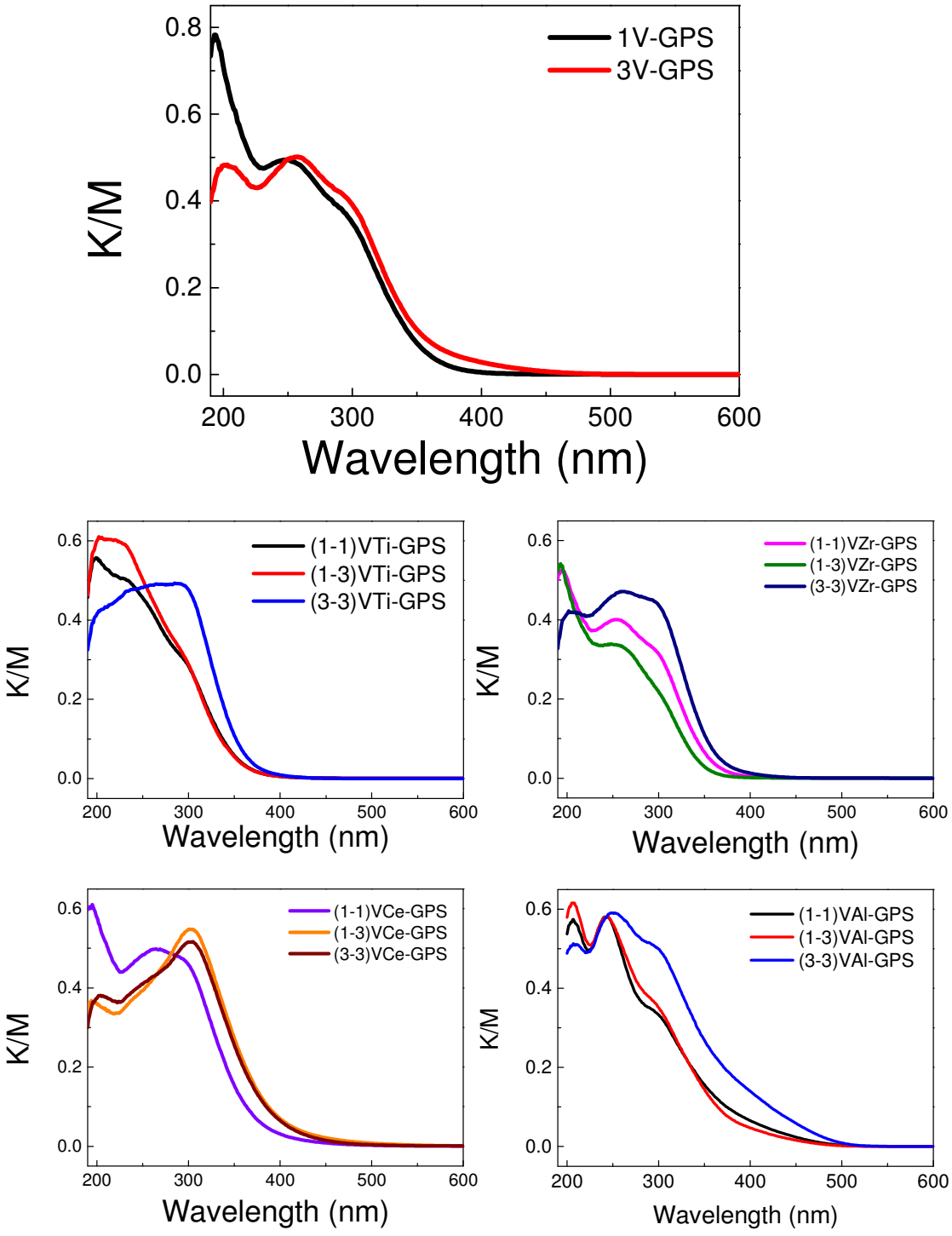

Table A5.2.2 Gaussian curves fitting data based on the UV-vis spectra of V-Al/Ti/Zr/Ce-GPS-cal. (FWHM: full width at half maximum, the units of center and FWHM are cm^{-1}).

1V-GPS-cal			3V-GPS-cal		
Center	FWHM	Area	Center	FWHM	Area
25800	6500	1284.388	25800	6500	3141.66
29000	6000	753.6854	29000	6000	871.453
32200	6000	1921.062	32200	6000	2437.56
37100	7500	2367.785	37100	7500	2861.8
42000	8000	2771.478	42000	8000	2380.8
49675.51535	8838.4	2842.957	49937	9815	2177.8

1-1VZr-GPS-cal			1-3VZr-GPS-cal			3-3VZr-GPS-cal		
Center	FWHM	Area	Center	FWHM	Area	Center	FWHM	Area
25800	6500	2356.294	25800	6500	425.887	25800	6500	1135.7605
29000	6000	654.7622	29000	6000	440.557	29000	6000	597.12367
32200	6000	2301.172	32200	6000	1732.77	32200	6000	2225.7099
37100	7500	3209.574	37100	7500	3000.16	37100	7500	3138.6682
42000	8000	2871.301	42000	8000	3120.17	42000	8000	2550.5329
49937.22846	9815.6	3166.474	49289.28438	8843	3904.17	49457.36578	10306	3212.4268

1-1VAl-GPS-cal			1-3VAl-GPS-cal			3-3VAl-GPS-cal		
Center	FWHM	Area	Center	FWHM	Area	Center	FWHM	Area
25800	6500	368.9303	25800	6500	239.145	25800	6500	835.74028
29000	6000	253.941	29000	6000	229.265	29000	6000	453.1257
32200	6000	1311.947	32200	6000	1338.45	32200	6000	1959.8539
37100	7500	1763.993	37100	7500	2071.61	37100	7500	2919.5652
42000	8000	4066.713	42000	8000	3875.11	42000	8000	3362.5118
49158.48494	6428	2198.235	49151.51516	6703	2479.92	49395.44657	8122	2288.4809

1-1VTi-GPS-cal			1-3VTi-GPS-cal			3-3VTi-GPS-cal		
Center	FWHM	Area	Center	FWHM	Area	Center	FWHM	Area
25800	6500	294.8077	25800	0	0	25800	0	0
29000	6000	204.8094	29000	0	0	29000	0	0
32200	6000	1074.773	32200	6000	927.231	32200	6000	1848.1562
37100	7500	2320.509	37100	7500	2498.1	37100	7500	3125.4862
43400	8000	3693.888	43400	8000	3897.46	43512.56054	8000	3005.4158
50000	8000	2208.137	50000	9000	2795.03	51019.58878	9000	1419.0855

A5.3 UV-vis spectra of Chapter 7

Figure A5.3.1 UV-vis spectra of Cu/Fe-MWL-cal and VCu/Fe-GMW-cal. MWL-cal was used as blank, and before measurement, samples were diluted by MWL-cal to keep the spectra intensity in the range of 0.2-0.8 K/M

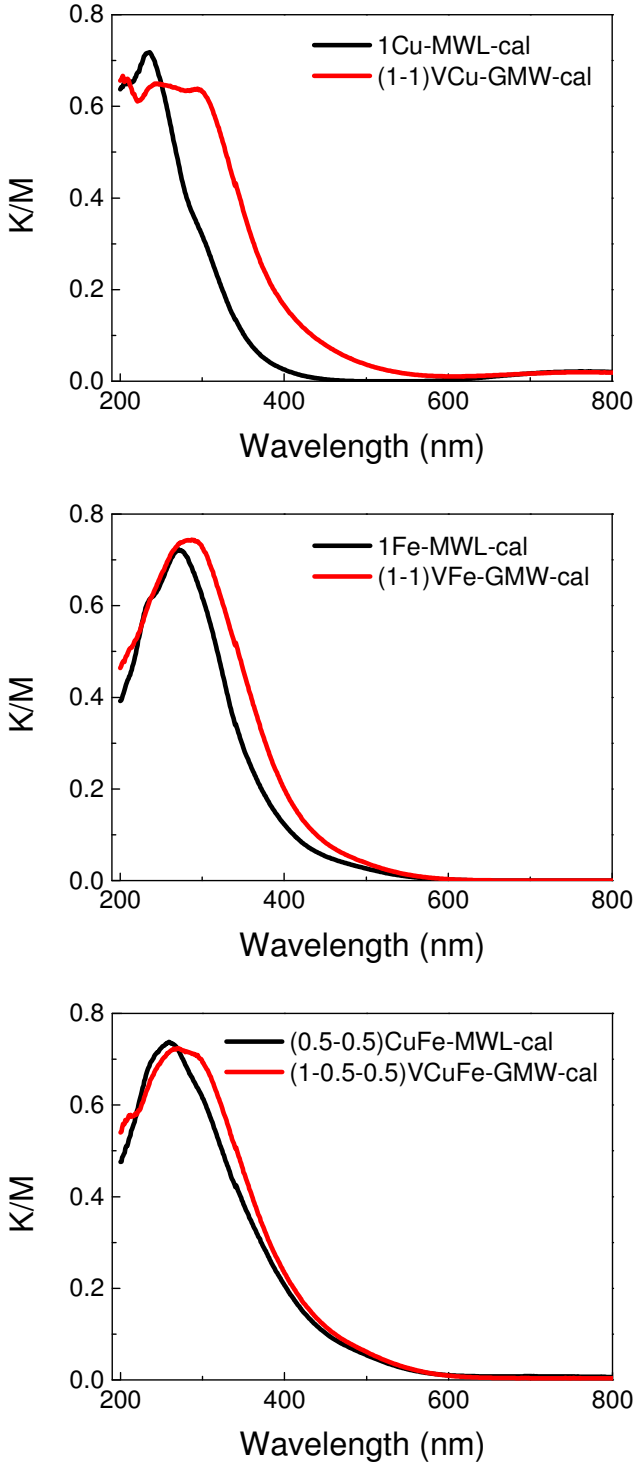

Appendix 6 Tauc's plot

A6.1 Tauc's plot of Chapter 4

Figure A6.1.1 Tauc's plot and the corresponding edge energy of VTi-MWT-cal based on their UV-vis spectra.

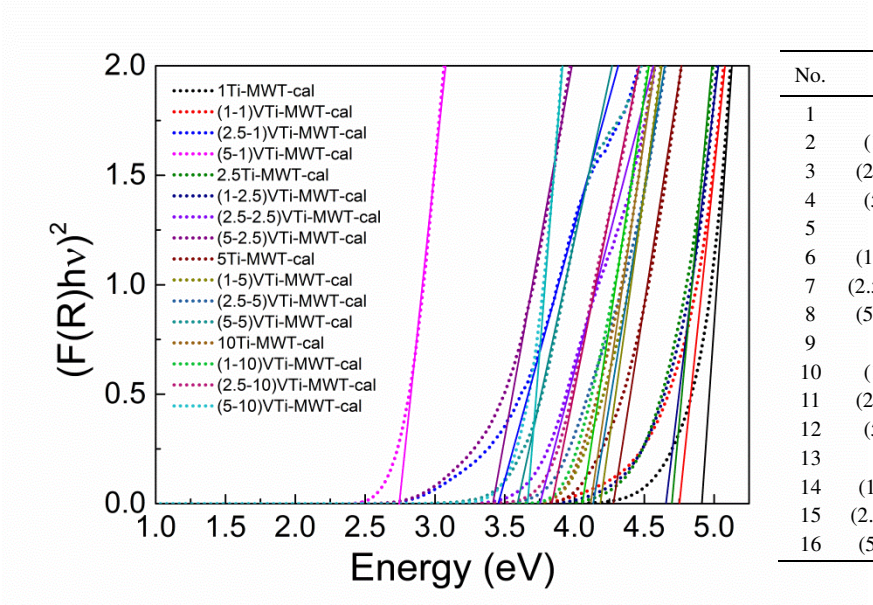

No.	Sample	Energy (eV)
1	1Ti-MWT-cal	4.91
2	(1-1)VTi-MWT-cal	4.75
3	(2.5-1)VTi-MWT-cal	3.46
4	(5-1)VTi-MWT-cal	2.75
5	2.5Ti-MWT-cal	4.7
6	(1-2.5)VTi-MWT-cal	4.65
7	(2.5-2.5)VTi-MWT-cal	3.75
8	(5-2.5)VTi-MWT-cal	3.42
9	5Ti-MWT-cal	4.28
10	(1-5)VTi-MWT-cal	4.19
11	(2.5-5)VTi-MWT-cal	4.13
12	(5-5)VTi-MWT-cal	3.58
13	10Ti-MWT-cal	4.11
14	(1-10)VTi-MWT-cal	4.06
15	(2.5-10)VTi-MWT-cal	3.84
16	(5-10)VTi-MWT-cal	3.66

Figure A6.1.2 Tauc's plot and the corresponding edge energy of VAl-MWL-cal based on their UV-vis spectra.

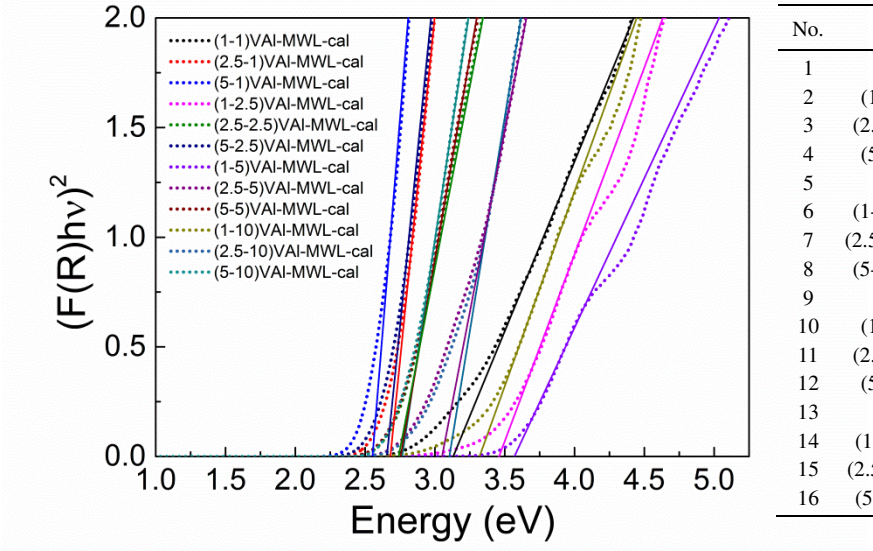

No.	Sample	Energy (eV)
1	1Al-MWL-cal	-
2	(1-1)VAl-MWL-cal	3.13
3	(2.5-1)VAl-MWL-cal	2.68
4	(5-1)VAl-MWL-cal	2.55
5	2.5Al-MWL-cal	-
6	(1-2.5)VAl-MWL-cal	3.46
7	(2.5-2.5)VAl-MWL-cal	2.74
8	(5-2.5)VAl-MWL-cal	2.66
9	5Al-MWL-cal	-
10	(1-5)VAl-MWL-cal	3.57
11	(2.5-5)VAl-MWL-cal	3.05
12	(5-5)VAl-MWL-cal	2.76
13	10Al-MWL-cal	-
14	(1-10)VAl-MWL-cal	3.32
15	(2.5-10)VAl-MWL-cal	3.1
16	(5-10)VAl-MWL-cal	2.77

Figure A6.1.3 Tauc's plot and the corresponding edge energy of VZr-MWT/MWL-cal based on their UV-vis spectra.

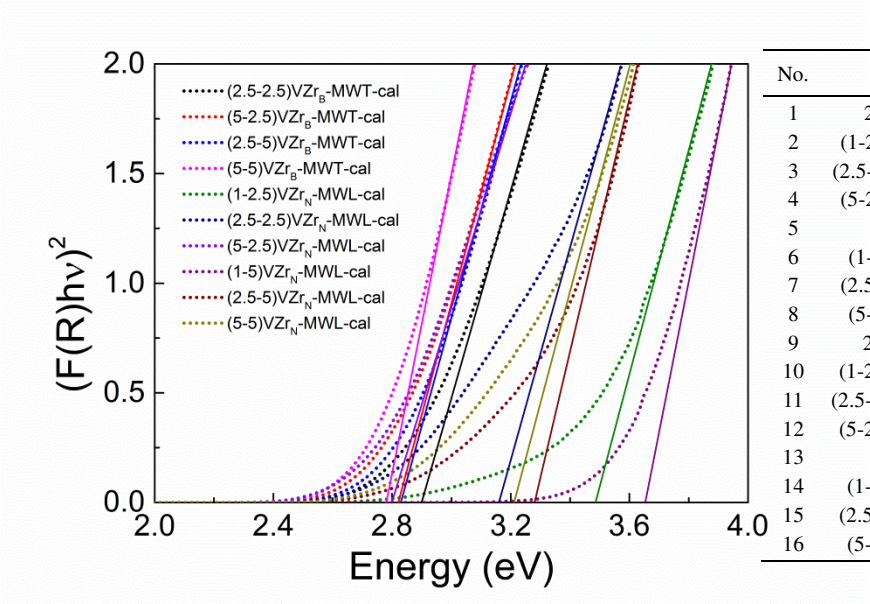

No.	Sample	Energy (eV)
1	2.5Zr$_B$-MWT-cal	-
2	(1-2.5)VZr$_B$-MWT-cal	-
3	(2.5-2.5)VZr$_B$-MWT-cal	2.9
4	(5-2.5)VZr$_B$-MWT-cal	2.82
5	5Zr$_B$-MWT-cal	-
6	(1-5)VZr$_B$-MWT-cal	-
7	(2.5-5)VZr$_B$-MWT-cal	2.83
8	(5-5)VZr$_B$-MWT-cal	2.78
9	2.5Zr$_N$-MWL-cal	-
10	(1-2.5)VZr$_N$-MWL-cal	3.49
11	(2.5-2.5)VZr$_N$-MWL-cal	3.16
12	(5-2.5)VZr$_N$-MWL-cal	2.8
13	5Zr$_N$-MWL-cal	-
14	(1-5)VZr$_N$-MWL-cal	3.65
15	(2.5-5)VZr$_N$-MWL-cal	3.28
16	(5-5)VZr$_N$-MWL-cal	3.21

Figure A6.1.4 Tauc's plot and the corresponding edge energy of VCe-MWL/MWT-cal based on their UV-vis spectra.

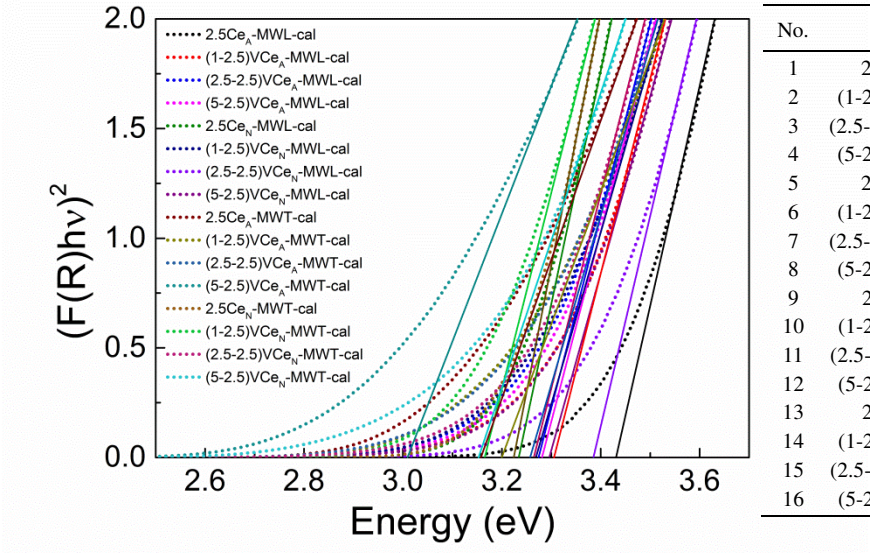

No.	Sample	Energy (eV)
1	2.5Ce$_A$-MWL-cal	3.43
2	(1-2.5)VCe$_A$-MWL-cal	3.31
3	(2.5-2.5)VCe$_A$-MWL-cal	3.27
4	(5-2.5)VCe$_A$-MWL-cal	3.28
5	2.5Ce$_N$-MWL-cal	3.23
6	(1-2.5)VCe$_N$-MWL-cal	3.27
7	(2.5-2.5)VCe$_N$-MWL-cal	3.39
8	(5-2.5)VCe$_N$-MWL-cal	3.3
9	2.5Ce$_A$-MWT-cal	3.16
10	(1-2.5)VCe$_A$-MWT-cal	3.2
11	(2.5-2.5)VCe$_A$-MWT-cal	3.26
12	(5-2.5)VCe$_A$-MWT-cal	3.01
13	2.5Ce$_N$-MWT-cal	3.22
14	(1-2.5)VCe$_N$-MWT-cal	3.17
15	(2.5-2.5)VCe$_N$-MWT-cal	3.26
16	(5-2.5)VCe$_N$-MWT-cal	3.15

Appendix 7 NMR spectra

A7.1 NMR spectra of Chapter 4

Figure A7.1.1 ^{29}Si quantitative NMR spectra of as-made 2.5V-MWL.

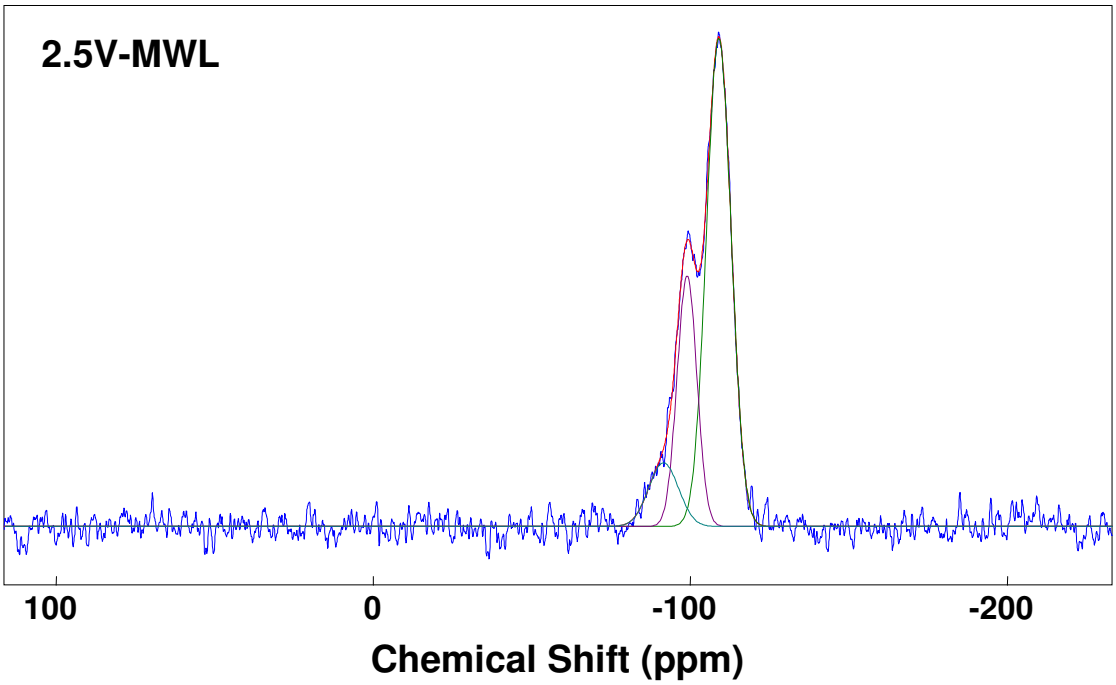

Figure A7.1.2 ^{29}Si quantitative NMR spectra of as-made 2.5Ti-MWT.

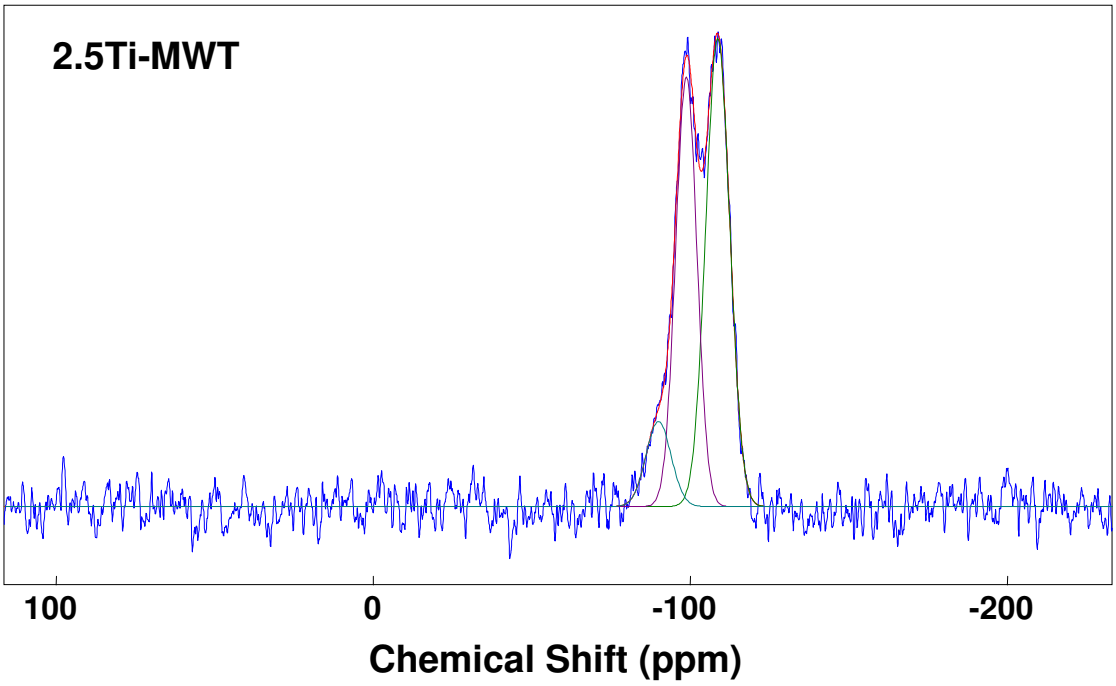

Figure A7.1.3 ^{29}Si quantitative NMR spectra of as-made 2.5Al-MWL.

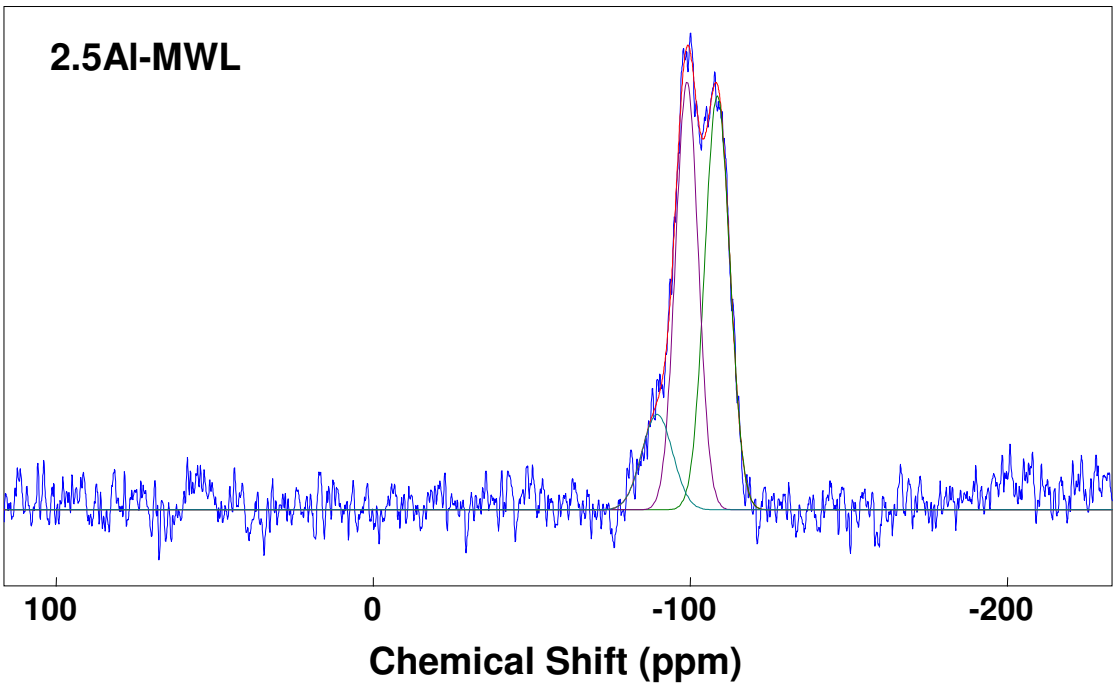

Figure A7.1.4 ^{29}Si quantitative NMR spectra of as-made 2.5Zr_N-MWL.

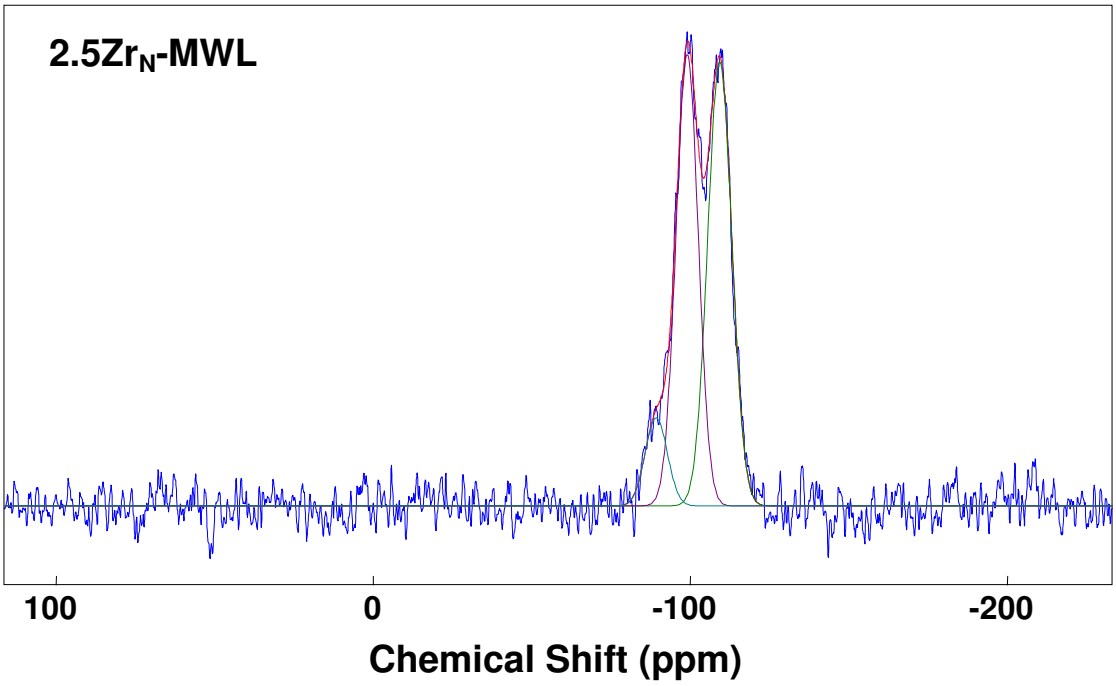

Figure A7.1.5 ^{29}Si quantitative NMR spectra of as-made 2.5Ce_A-MWT.

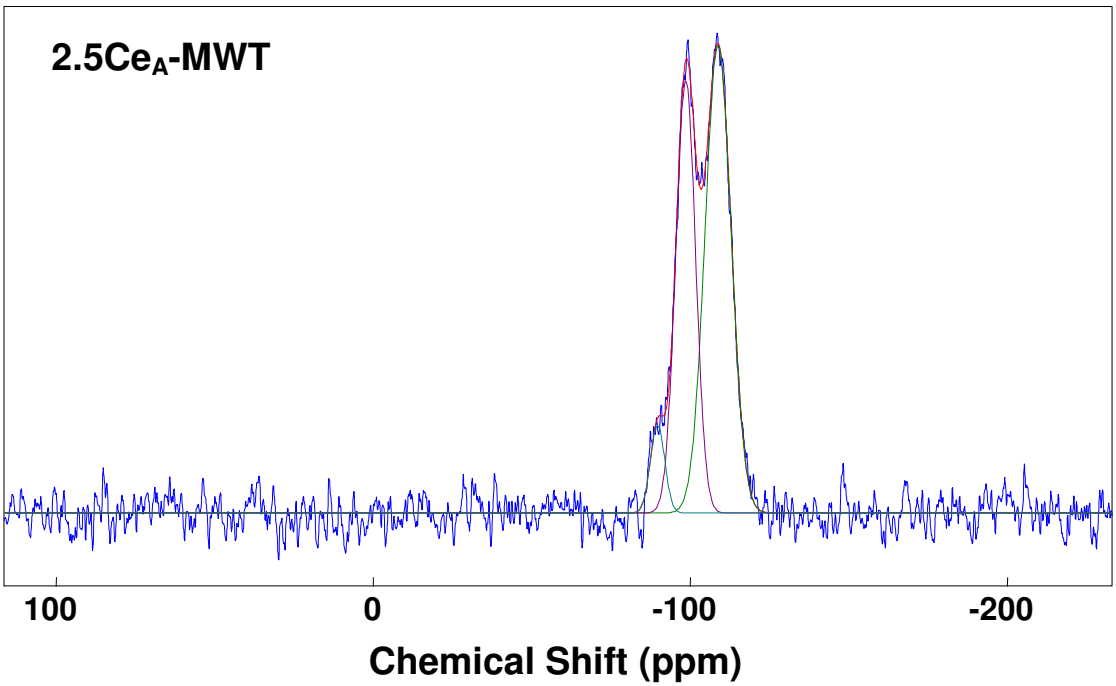

Figure A7.1.6 ^{29}Si quantitative NMR spectra of as-made (2.5-2.5)VTi-MWT.

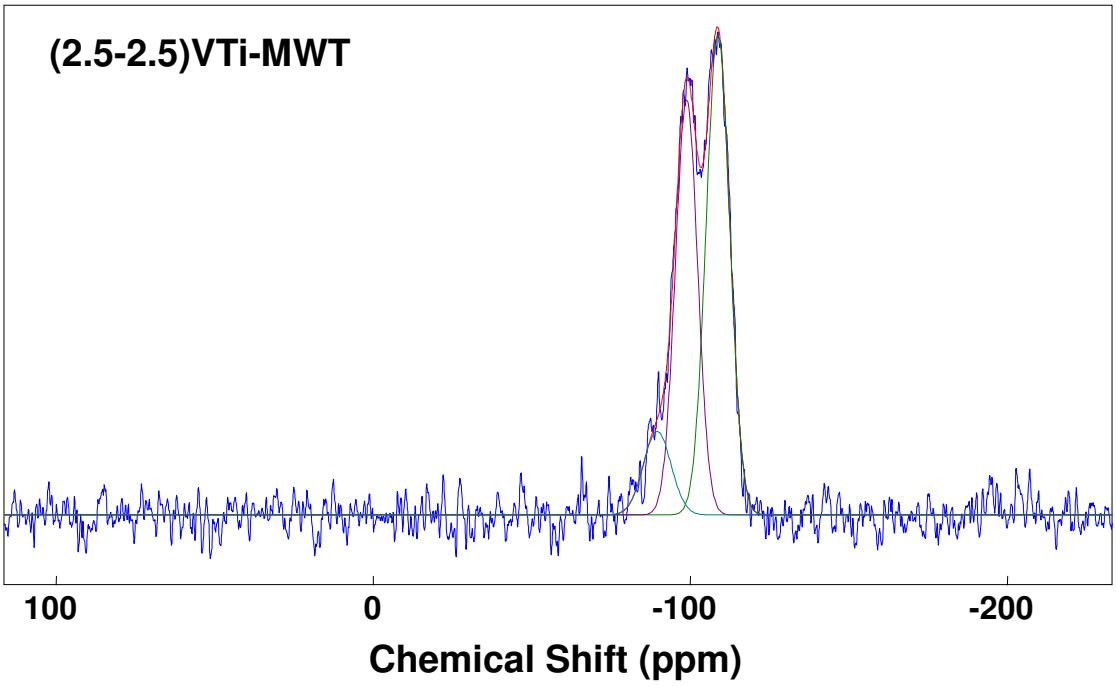

Figure A7.1.7 ^{29}Si quantitative NMR spectra of as-made (2.5-2.5)VAl-MWL.

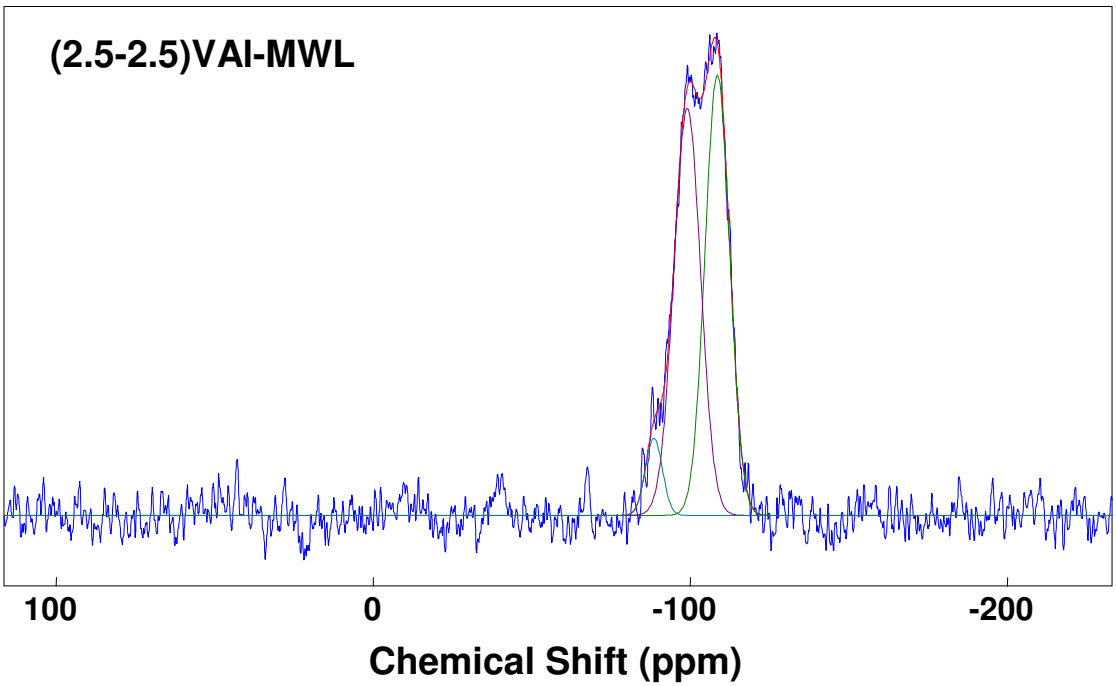

Figure A7.1.8 ^{29}Si quantitative NMR spectra of as-made (2.5-2.5)VZr$_N$-MWL.

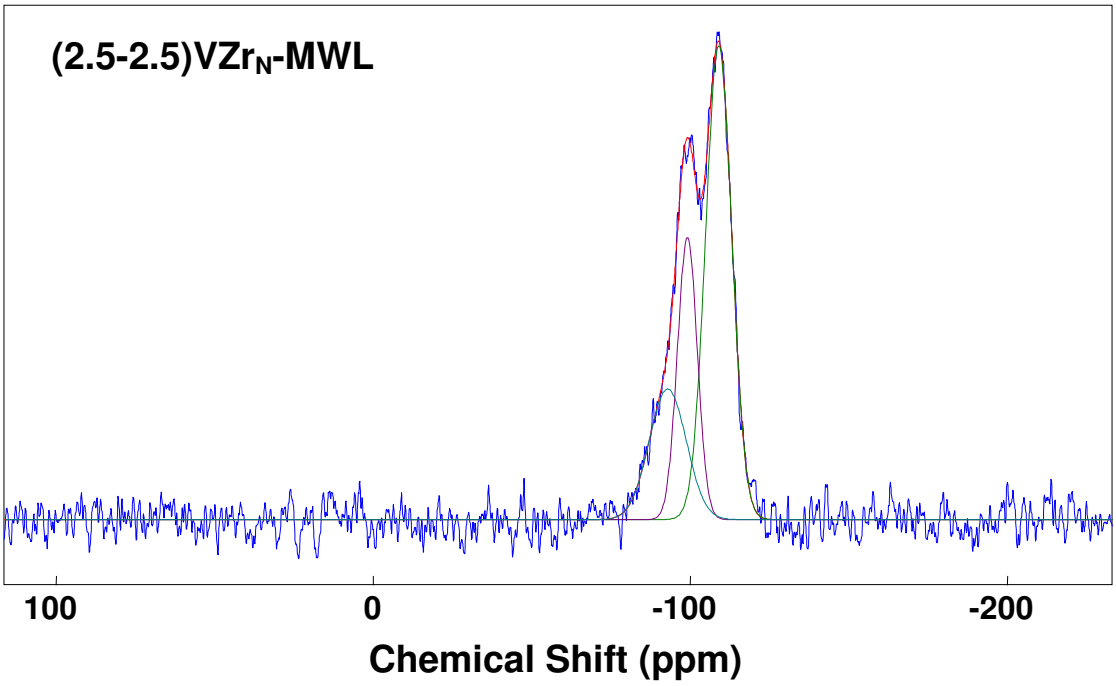

Figure A7.1.9 ^{29}Si quantitative NMR spectra of as-made (2.5-2.5)VCe$_A$-MWT.

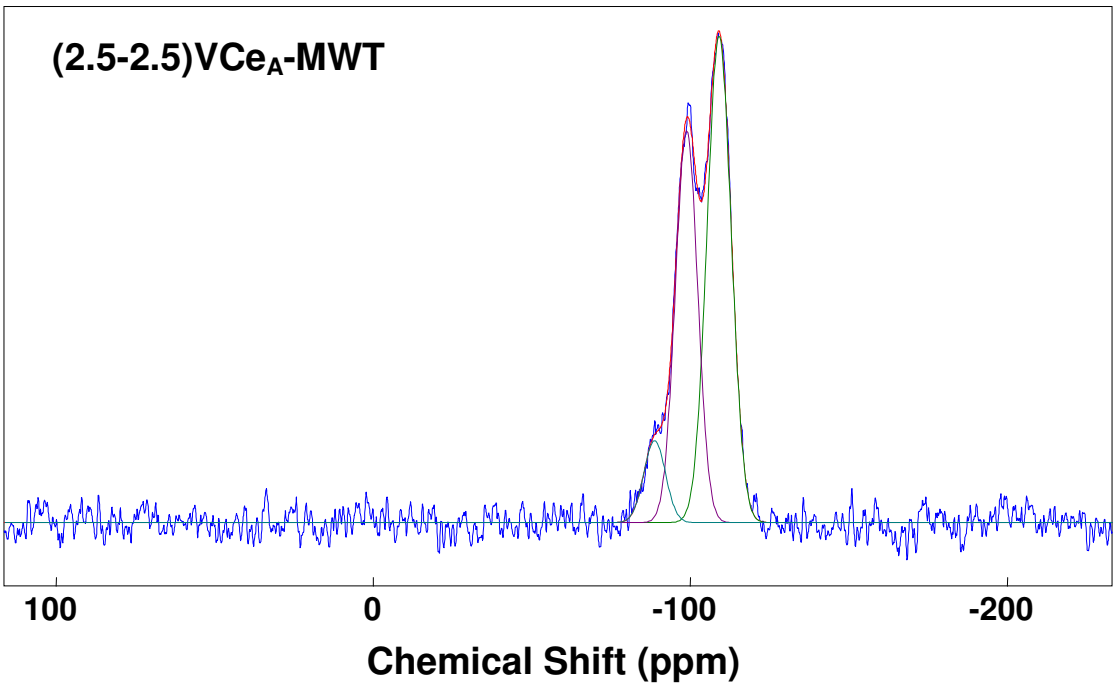

Figure A7.1.10 ^{27}Al quantitative NMR spectra of as-made 1Al-MWL.

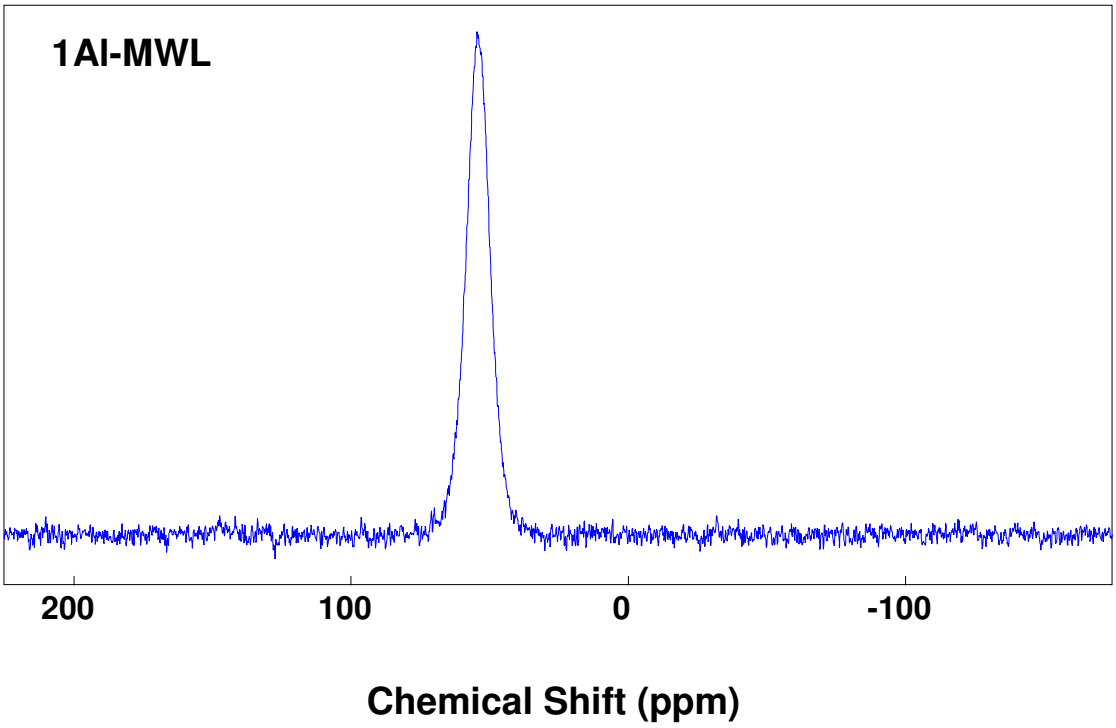

Figure A7.1.11 ^{27}Al quantitative NMR spectra of as-made (1-1)VAl-MWL.

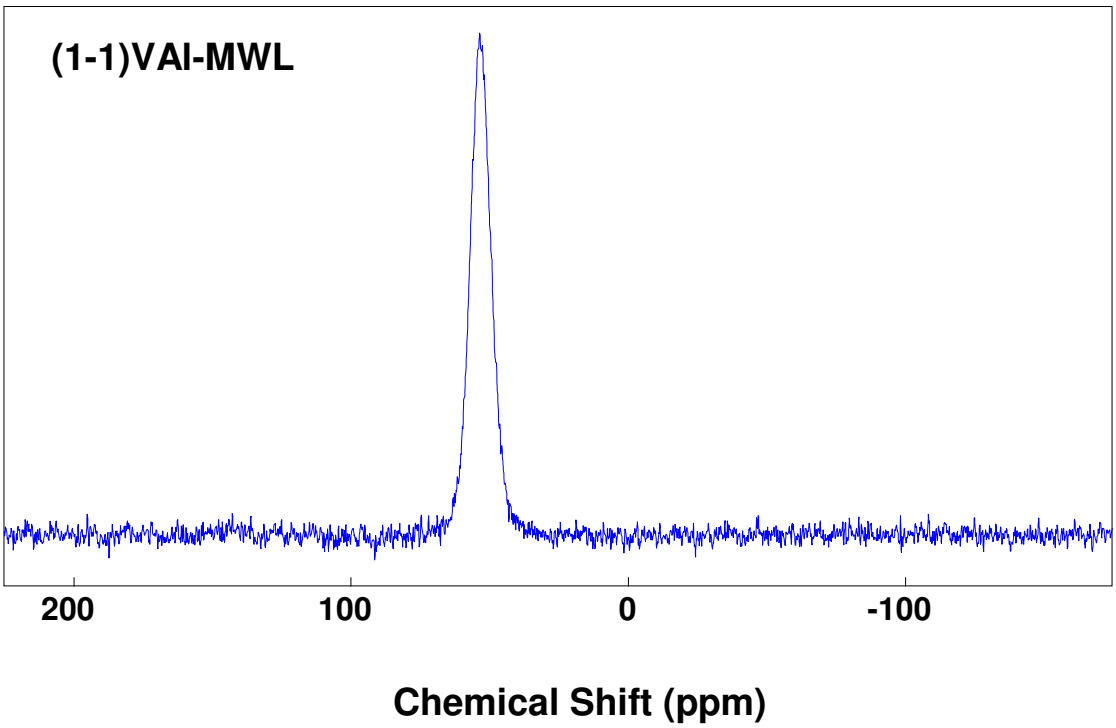

Figure A7.1.12 ^{27}Al quantitative NMR spectra of as-made 2.5Al-MWL.

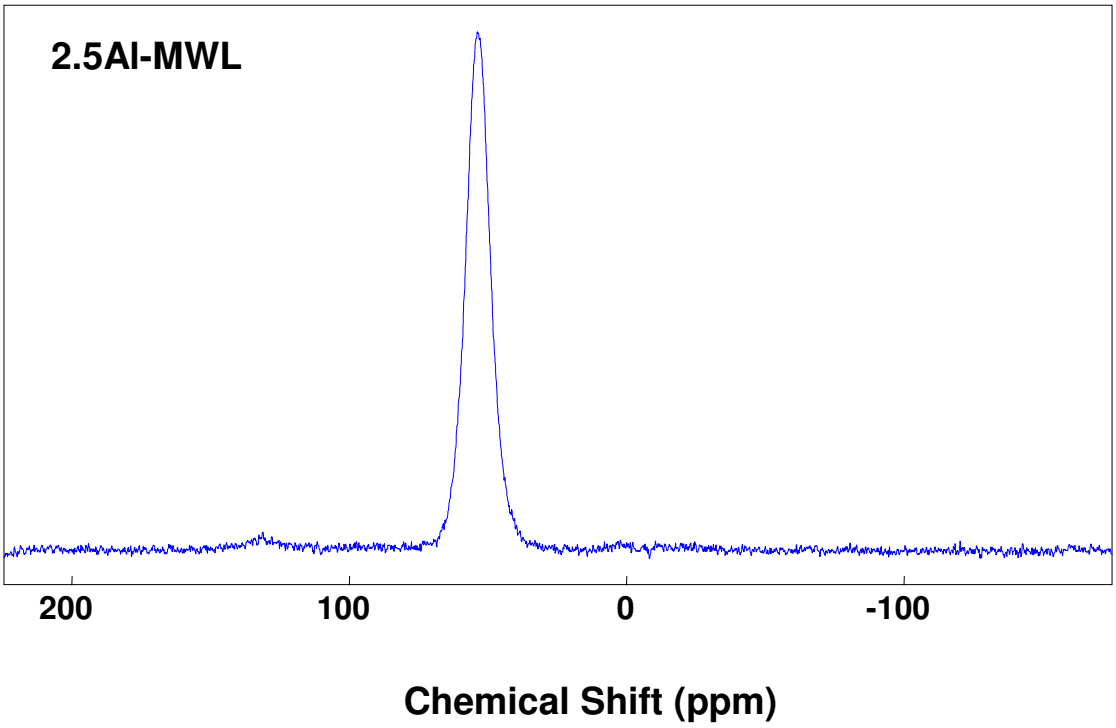

Figure A7.1.13 ^{27}Al quantitative NMR spectra of as-made (1-2.5)VAl-MWL.

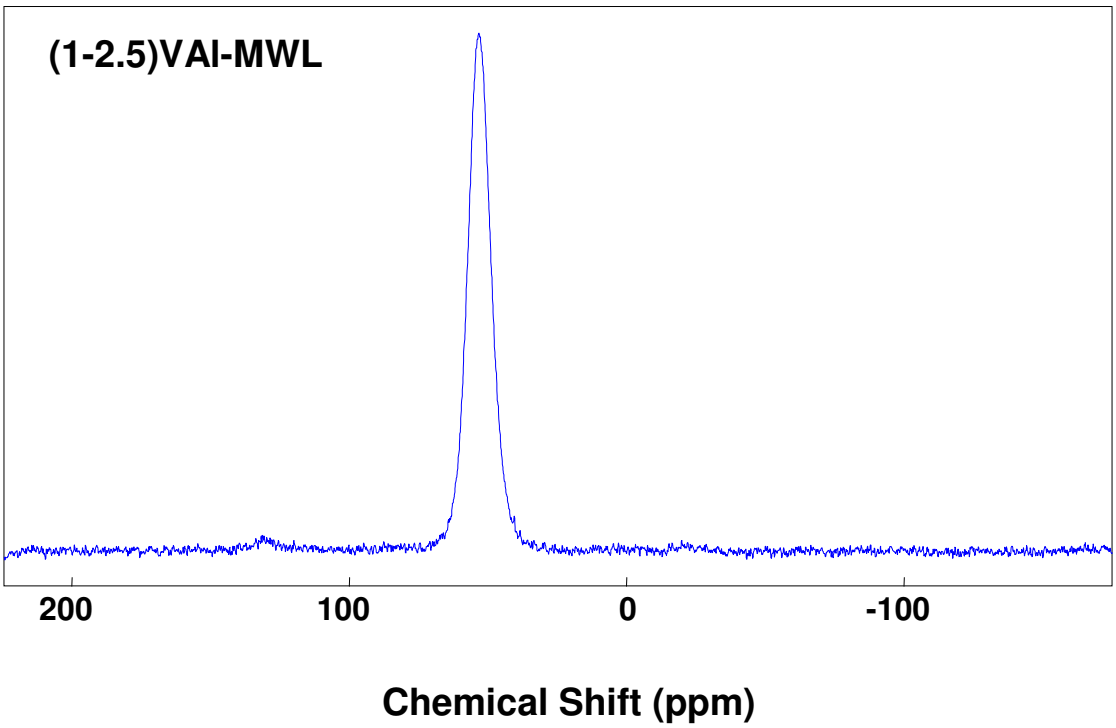

Figure A7.1.14 ^{27}Al quantitative NMR spectra of as-made 5Al-MWL.

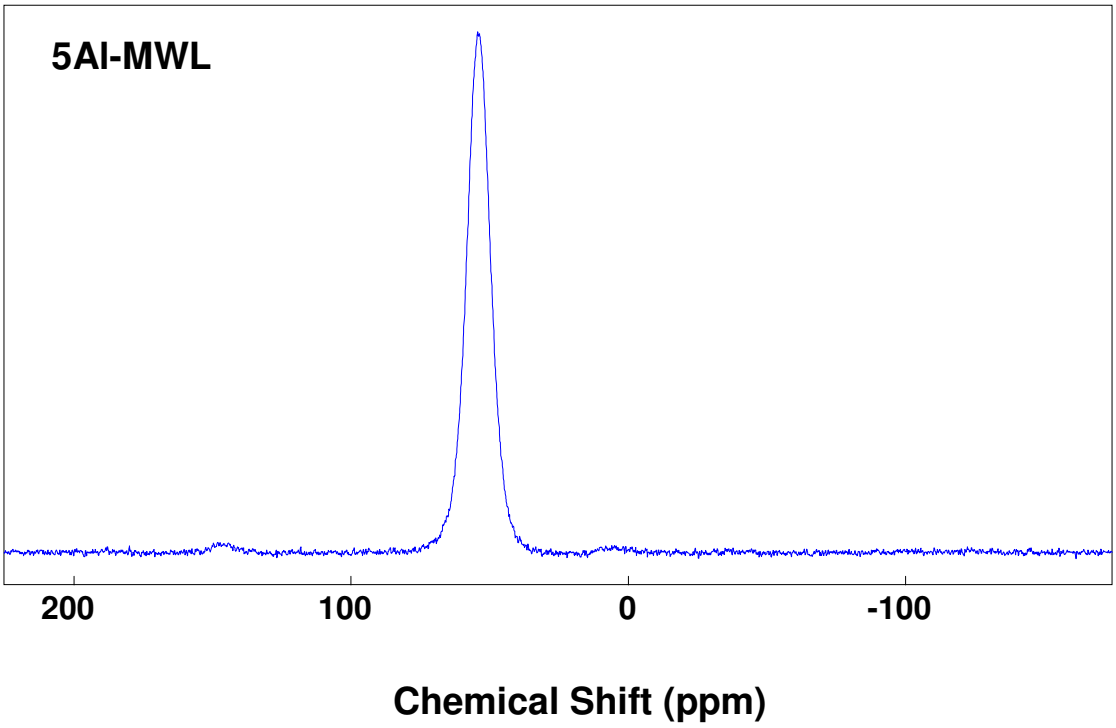

Figure A7.1.15 ^{27}Al quantitative NMR spectra of as-made (1-5)Al-MWL.

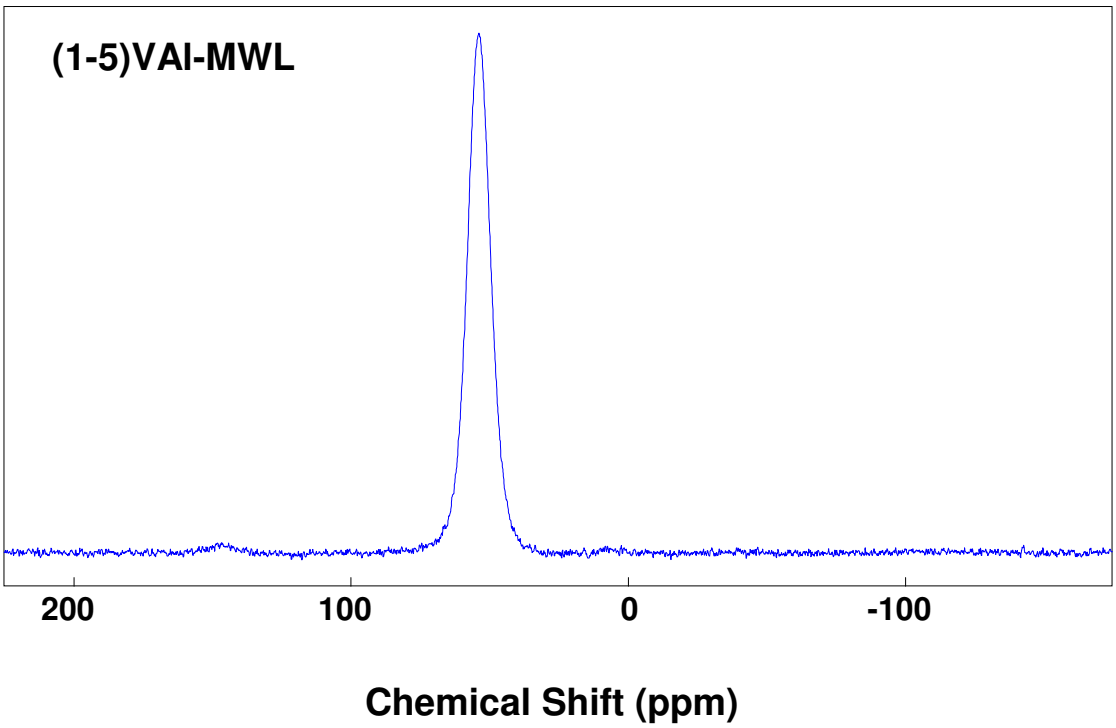

Figure A7.1.16 ^{27}Al quantitative NMR spectra of as-made 10Al-MWL.

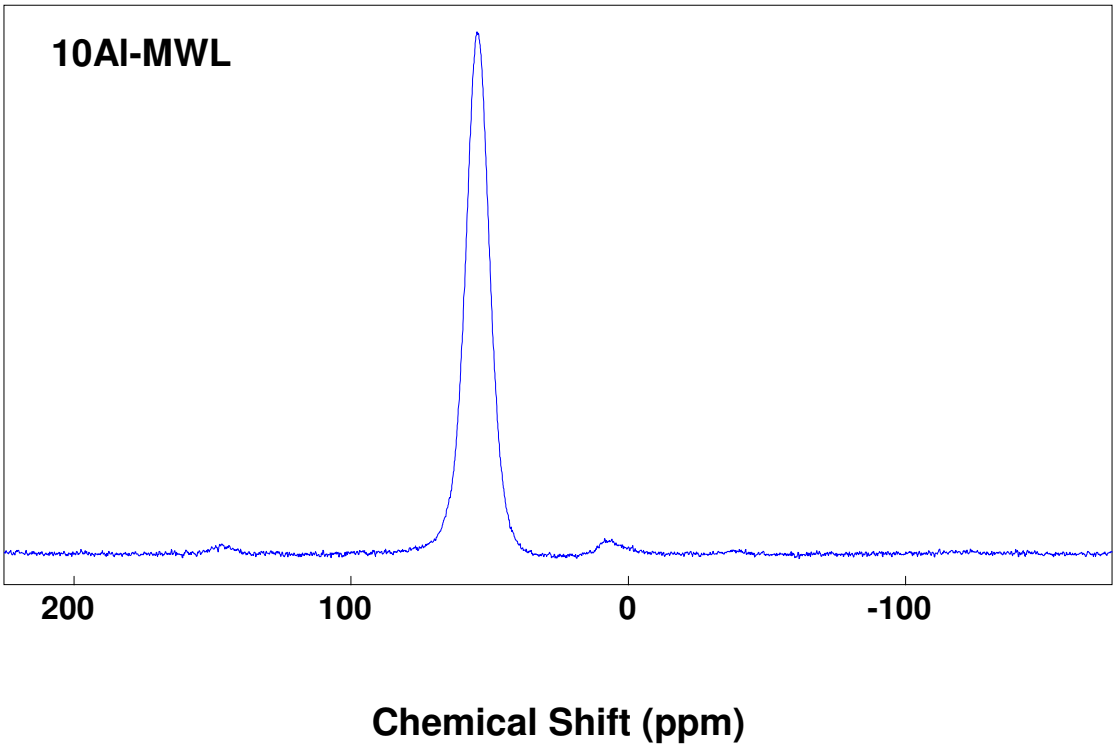

Figure A7.1.17 ^{27}Al quantitative NMR spectra of as-made (1-10)VAl-MWL.

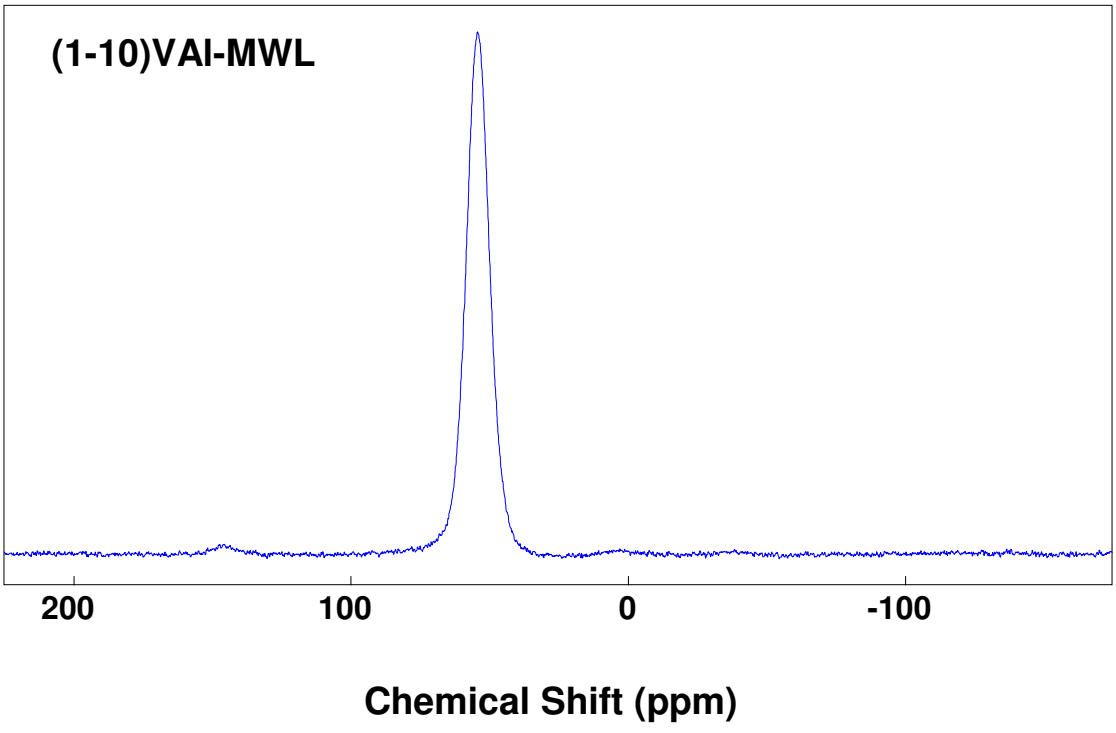

A7.2 NMR spectra of Chapter 5

Figure A7.2.1 ^{13}C NMR spectra of MWL-TMA-EBDMS.

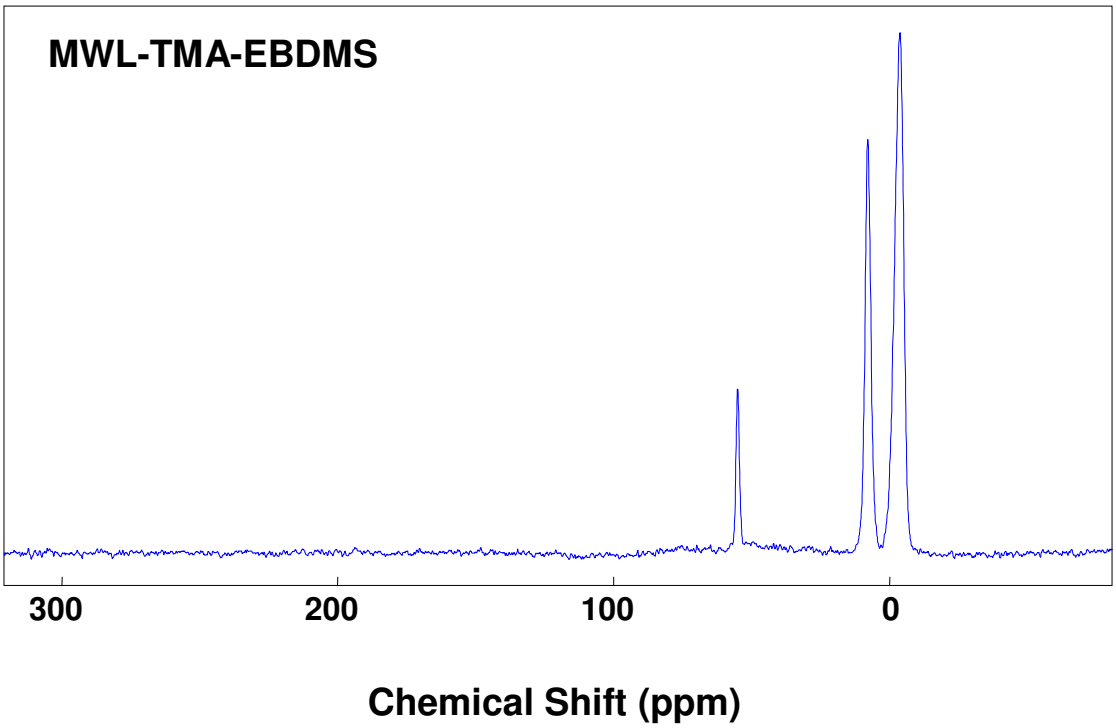

Figure A7.2.2 ^{29}Si quantitative NMR spectra of MWL-TMA-EBDMS.

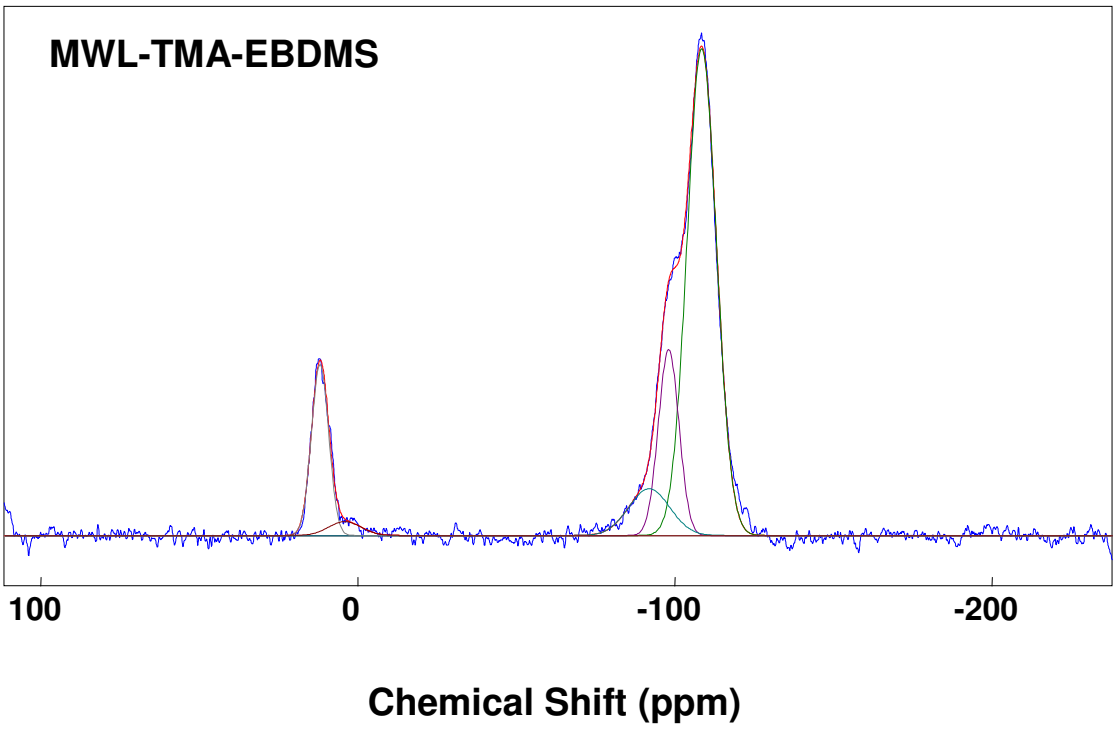

Figure A7.2.3 ^{13}C NMR spectra of FS.

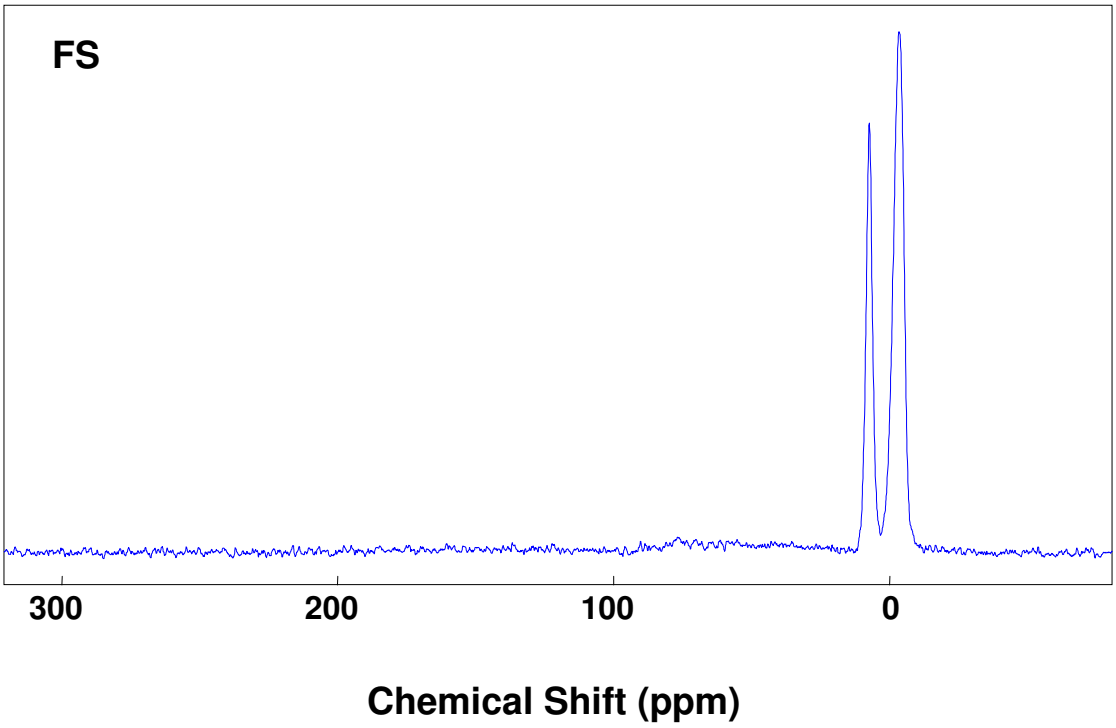

Figure A7.2.4 ^{29}Si quantitative NMR spectra of FS.

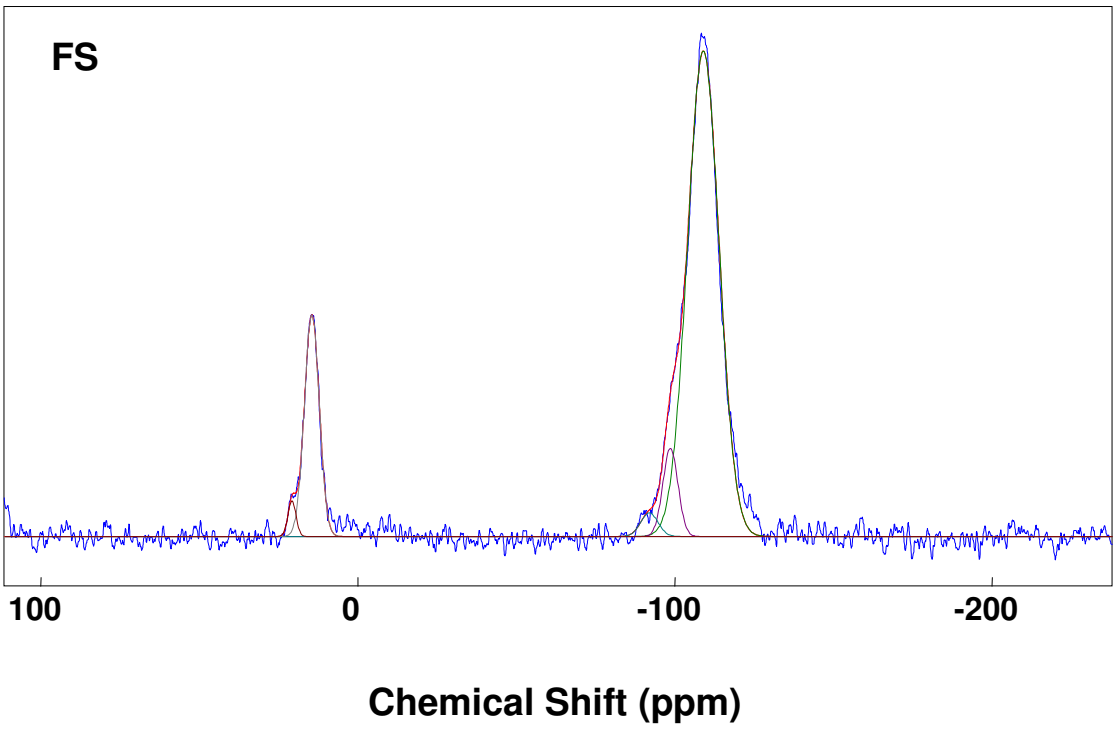

Figure A7.2.5 ^{13}C NMR spectra of PS.

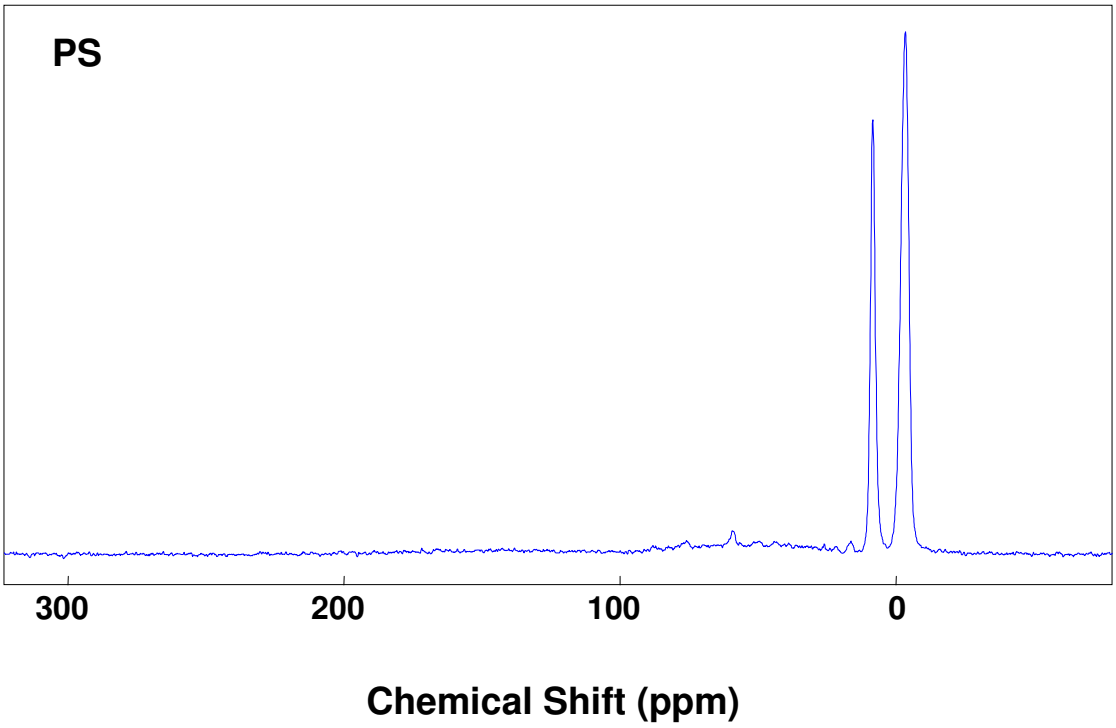

Figure A7.2.6 ^{29}Si quantitative NMR spectra of PS.

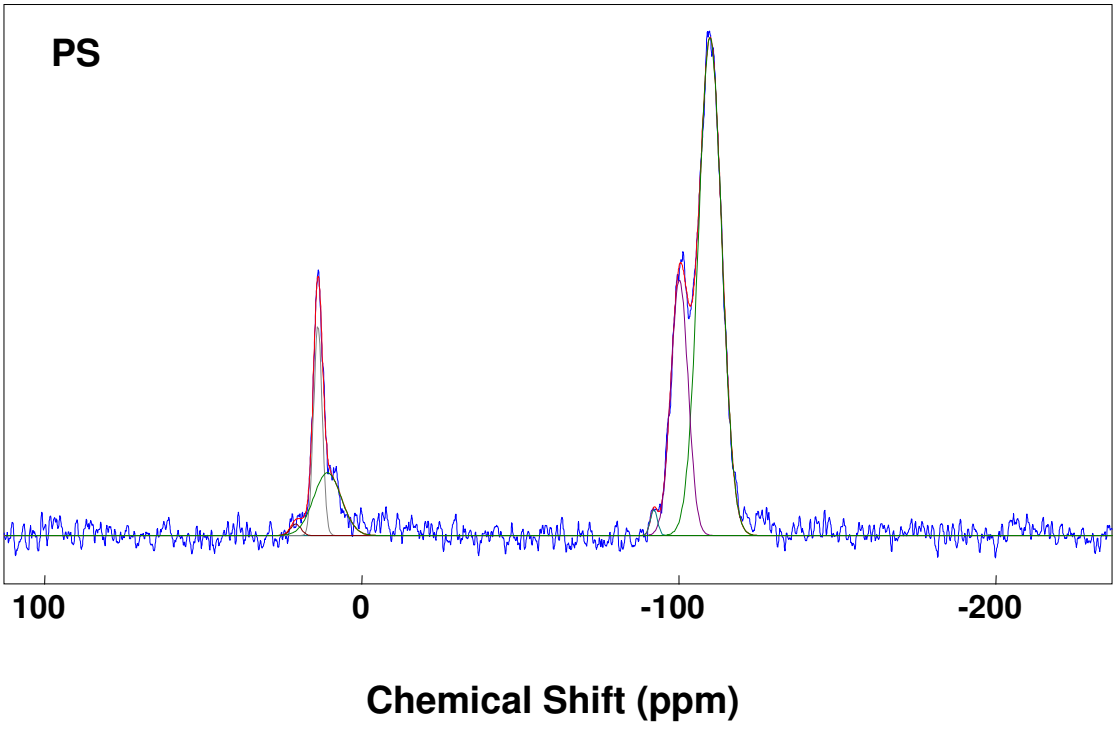

Figure A7.2.7 ^{13}C NMR spectra of 3V-GPS.

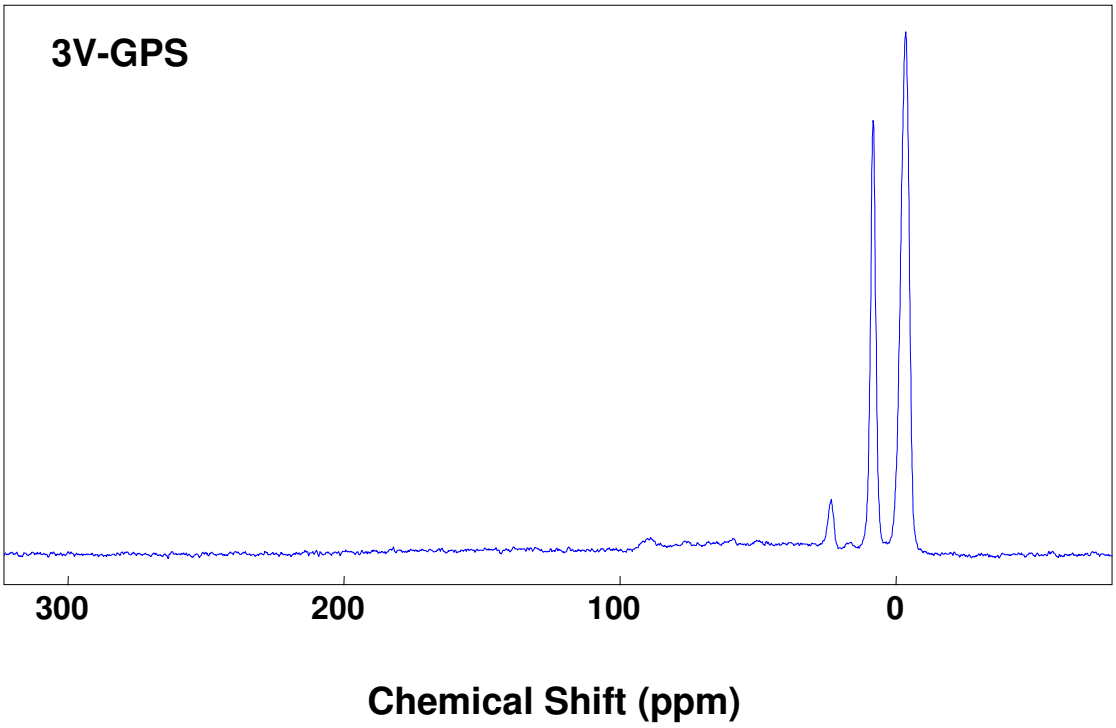

Figure A7.2.8 ^{29}Si quantitative NMR spectra of 3V-GPS.

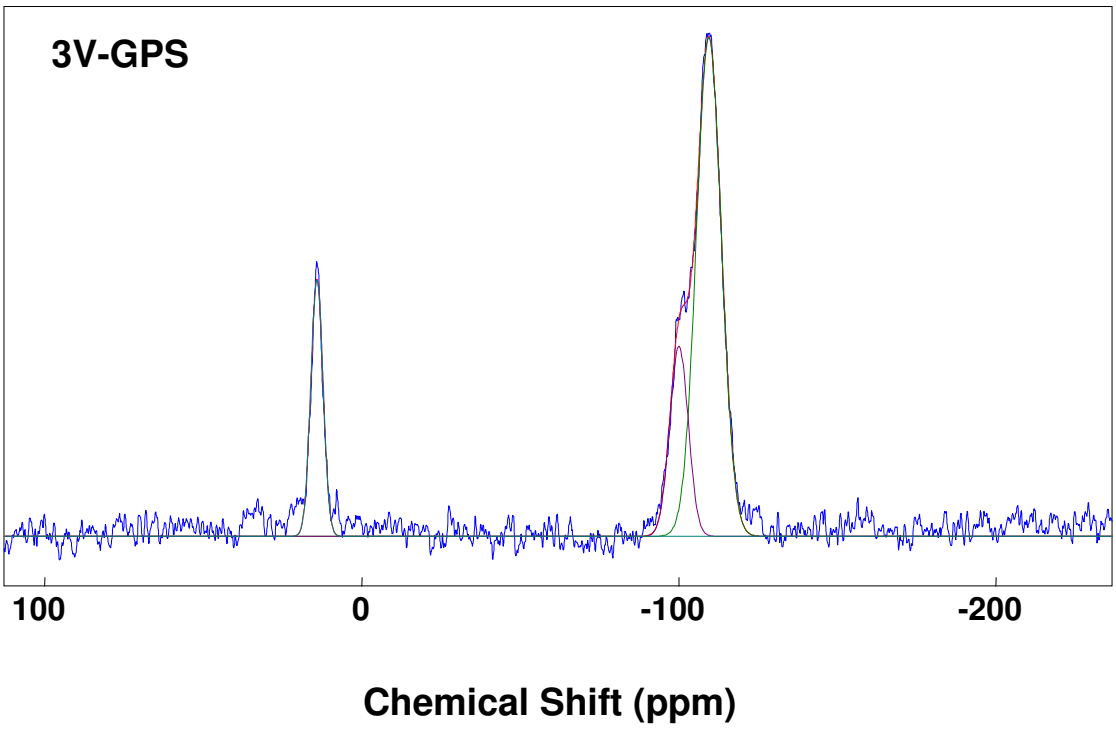

Figure A7.2.9 ^{13}C NMR spectra of 3Ti-GPS.

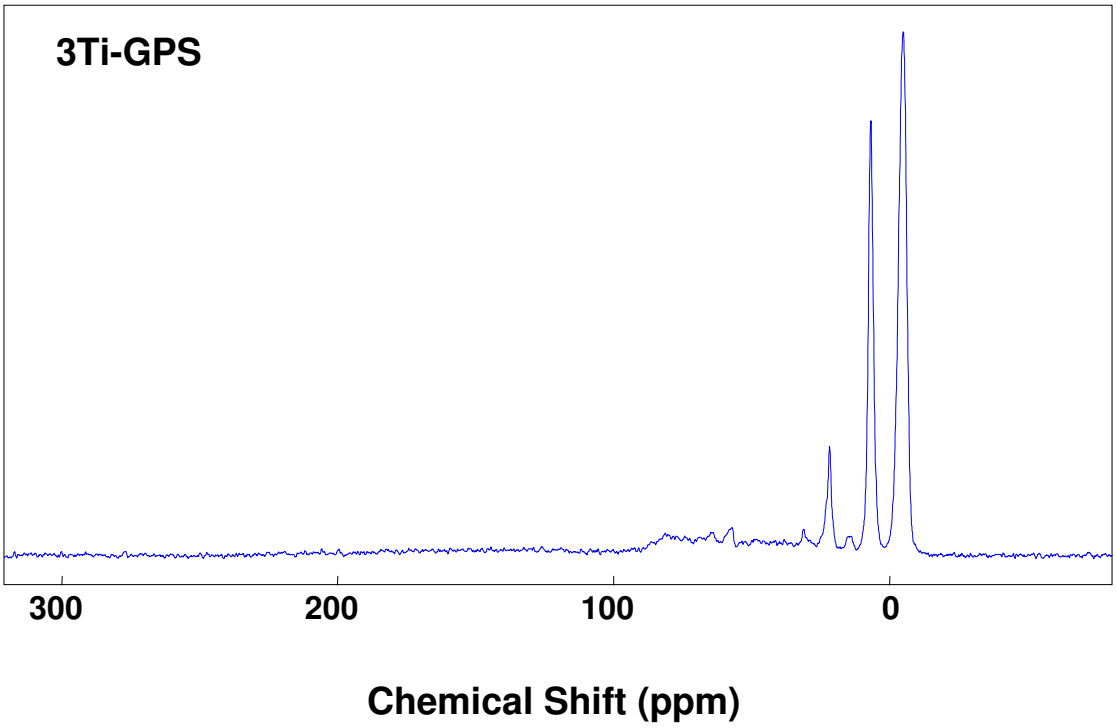

Figure A7.2.10 ^{29}Si quantitative NMR spectra of 3Ti-GPS.

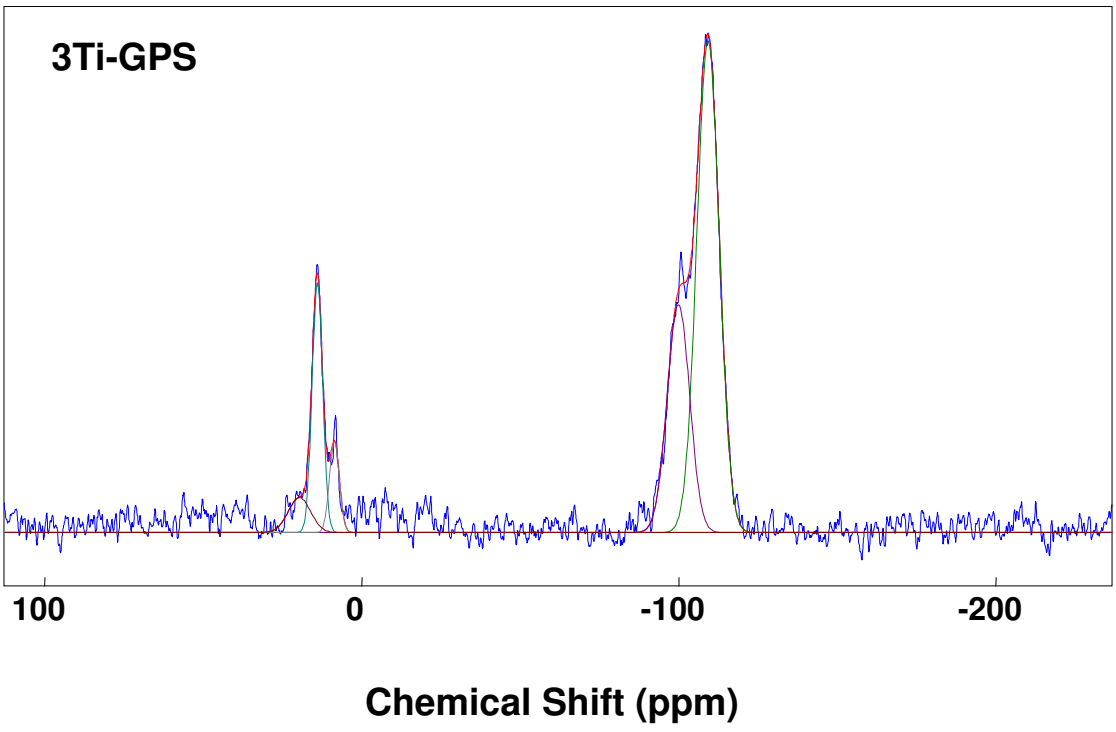

Figure A7.2.11 ^{13}C NMR spectra of 3Zr-GPS.

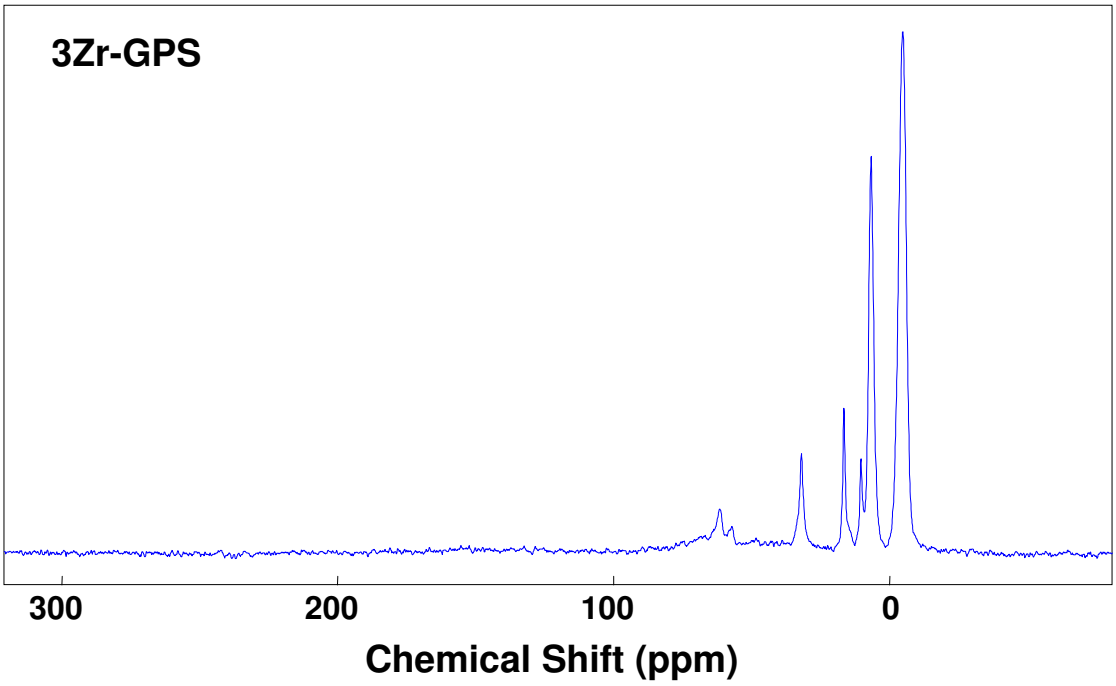

Figure A7.2.12 ^{29}Si quantitative NMR spectra of 3Zr-GPS.

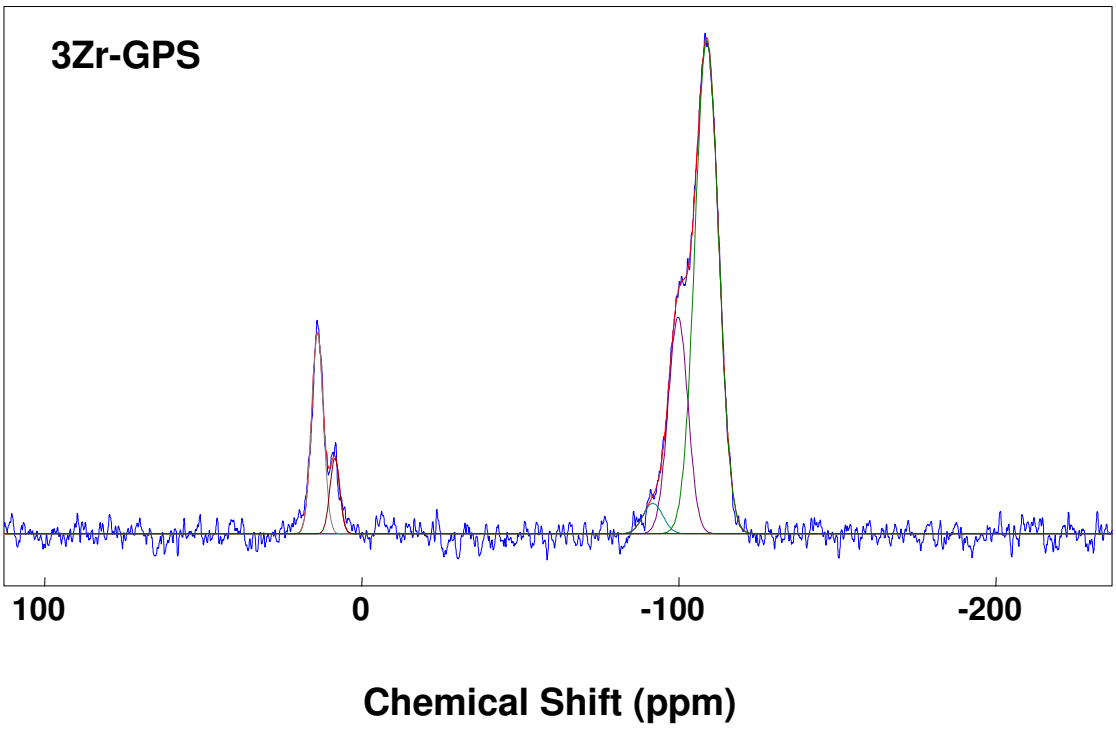

Figure A7.2.13 ^{13}C NMR spectra of 3Ce-GPS.

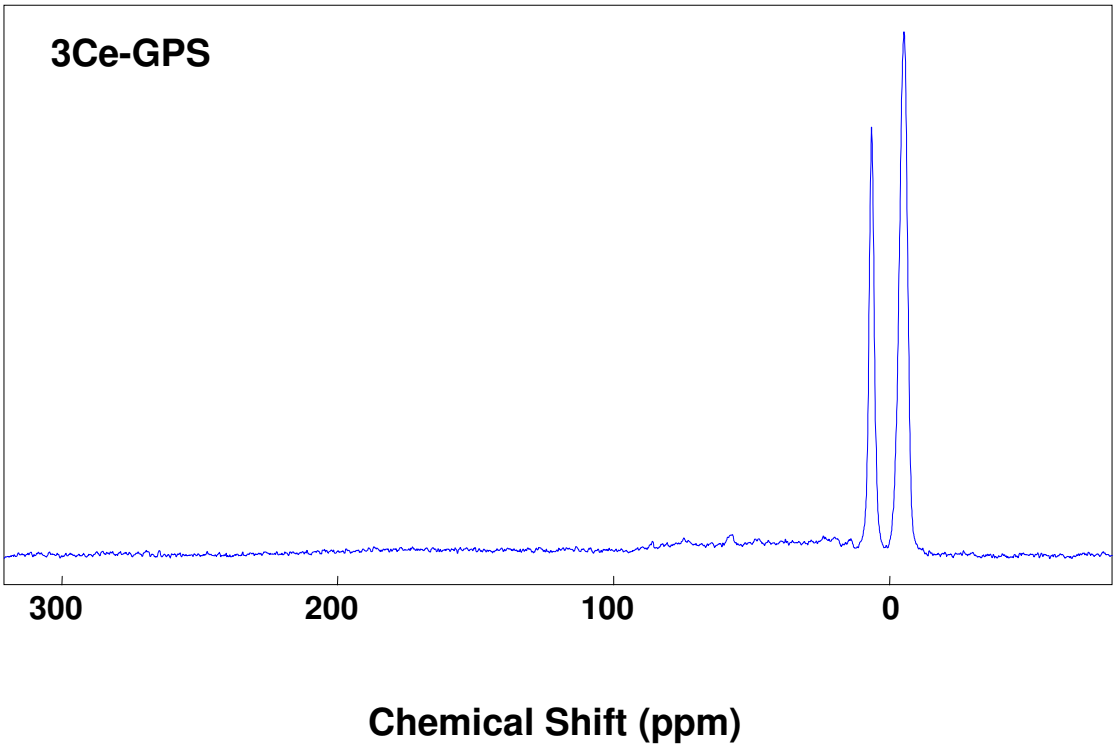

Figure A7.2.14 ^{29}Si quantitative NMR spectra of 3Ce-GPS.

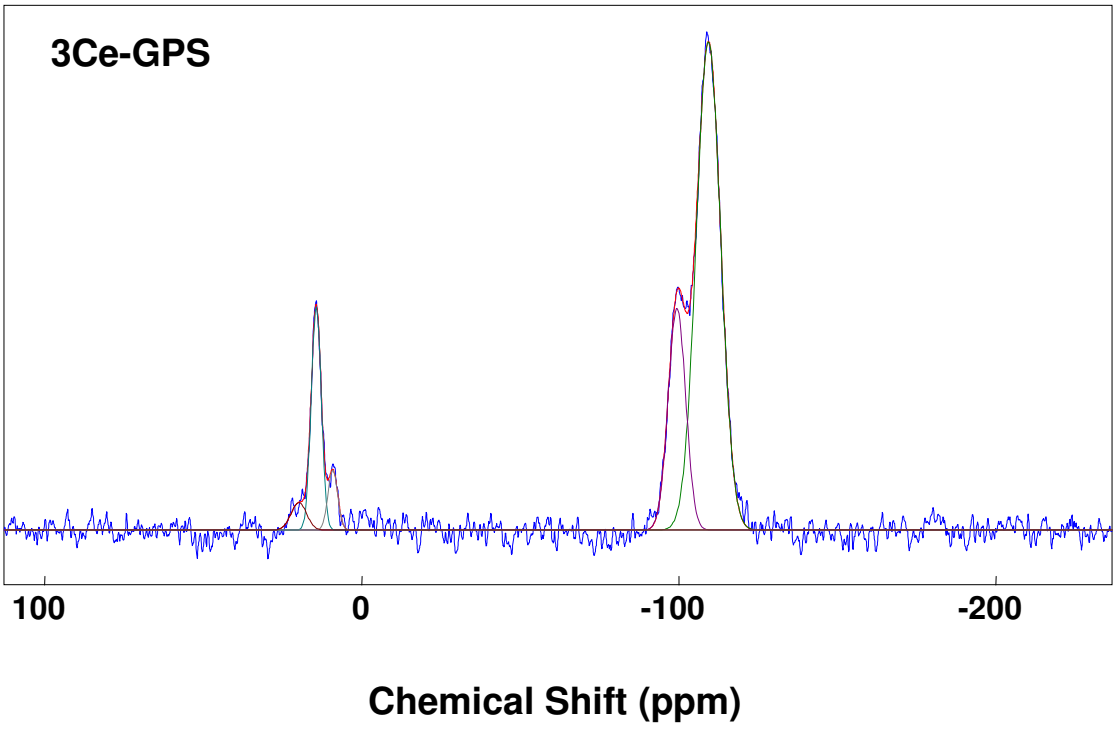

Figure A7.2.15 ^{13}C NMR spectra of (3-3)VTi-GPS.

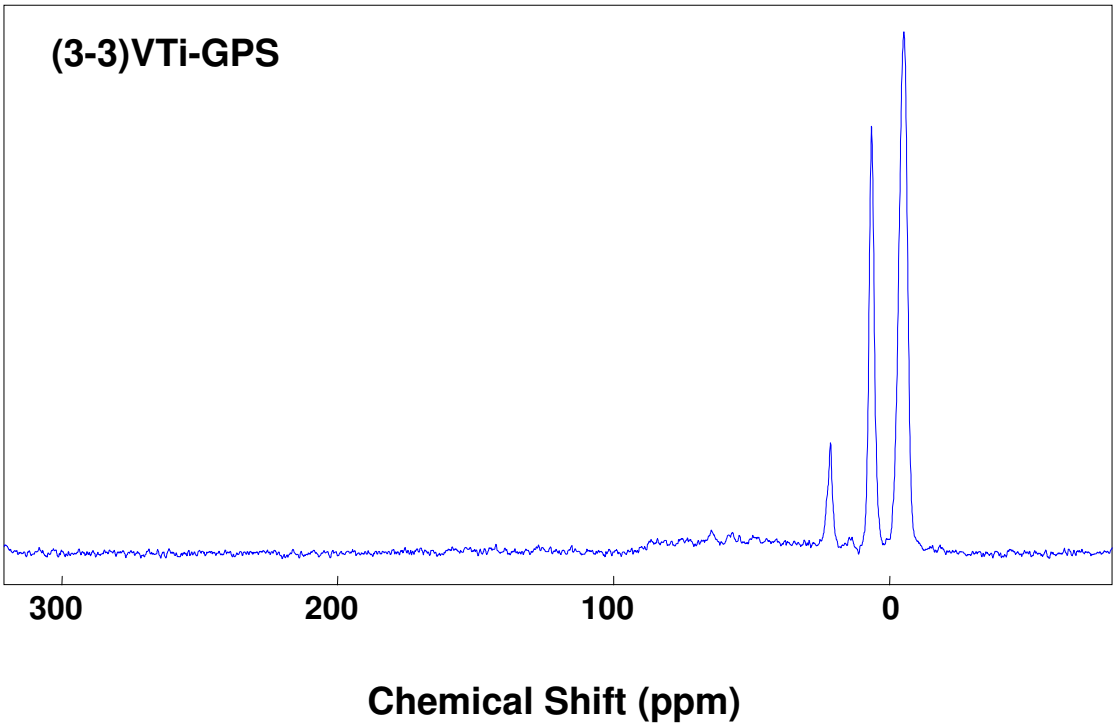

Figure A7.2.16 ^{29}Si quantitative NMR spectra of (3-3)VTi-GPS.

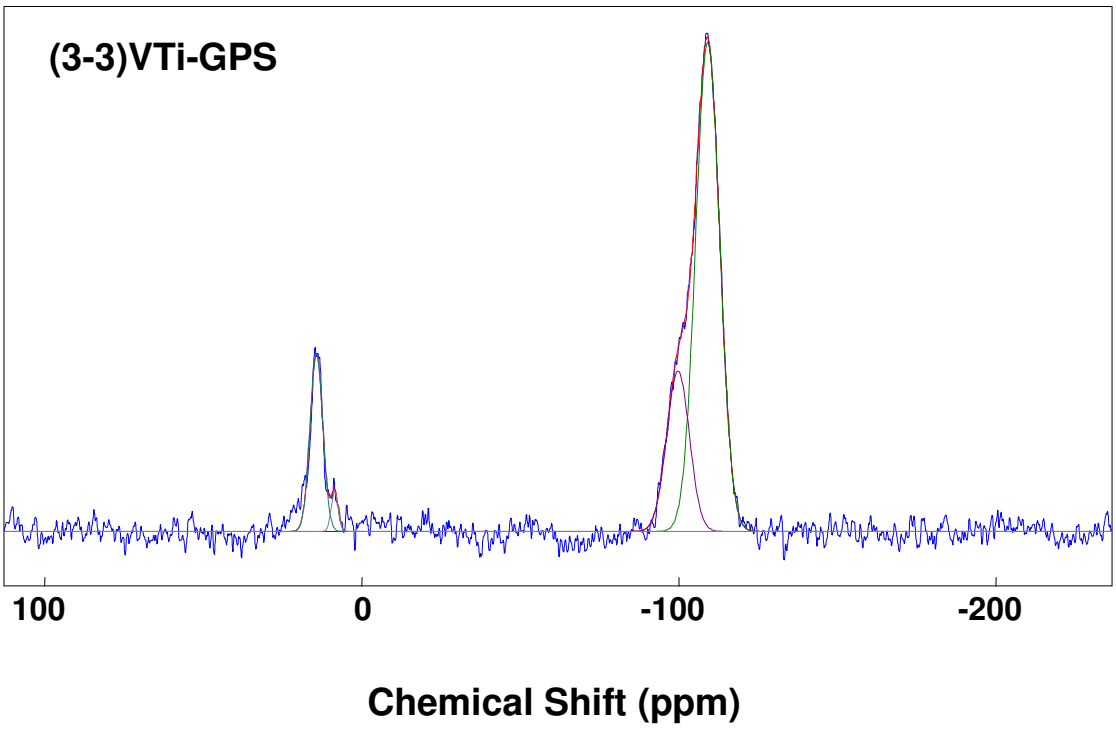

Figure A7.2.17 ^{13}C NMR spectra of (3-3)VZr-GPS.

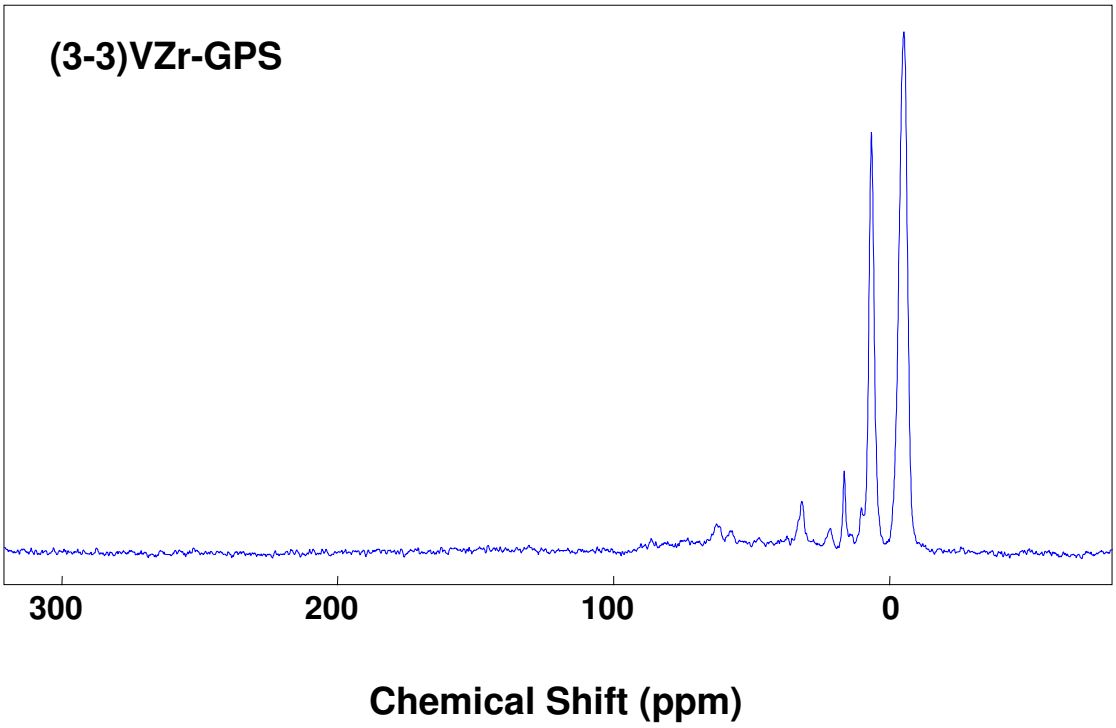

Figure A7.2.18 ^{29}Si quantitative NMR spectra of (3-3)VZr-GPS.

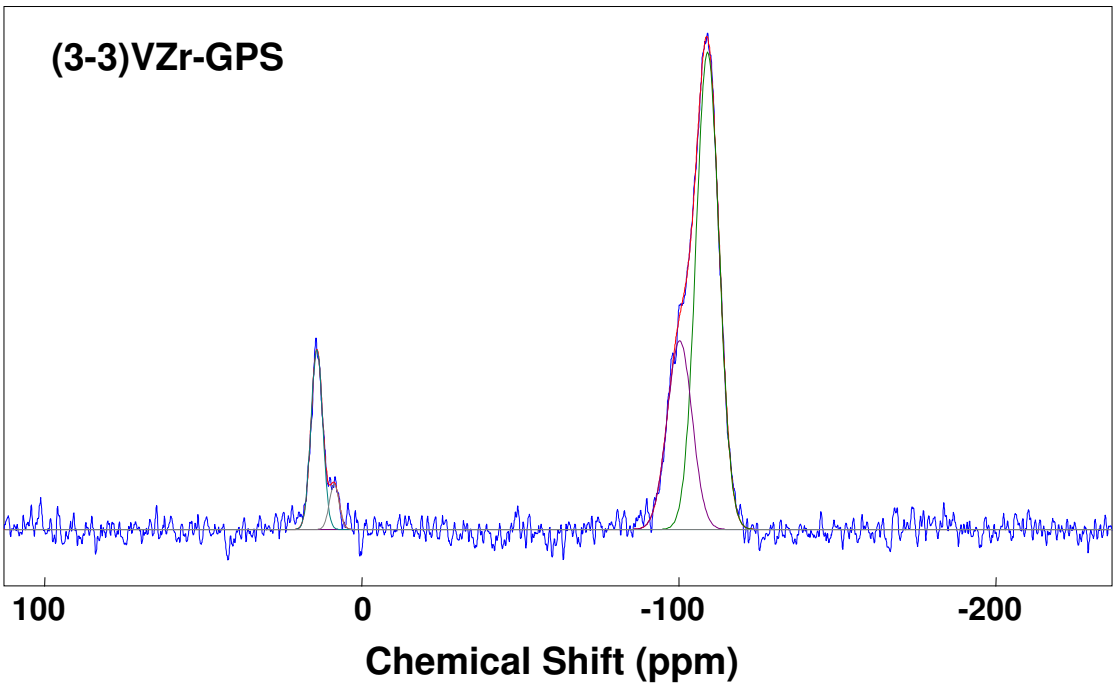

Figure A7.2.19 ^{13}C NMR spectra of (3-3)VCe-GPS.

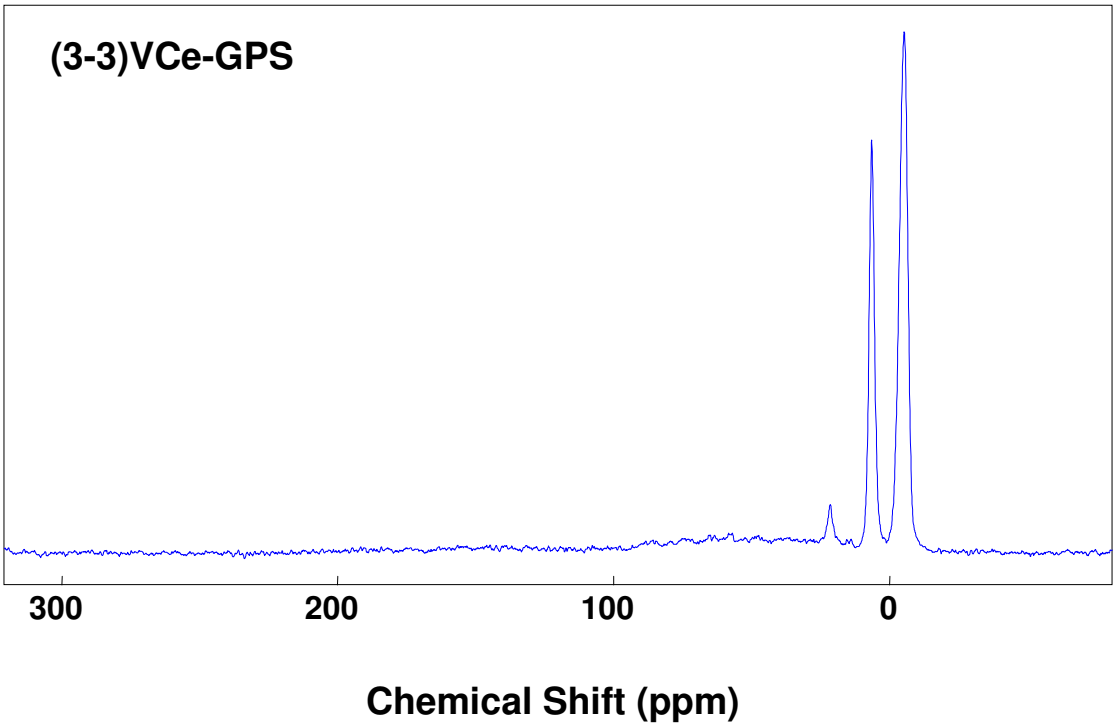

Figure A7.2.20 ^{29}Si quantitative NMR spectra of (3-3)VCe-GPS.

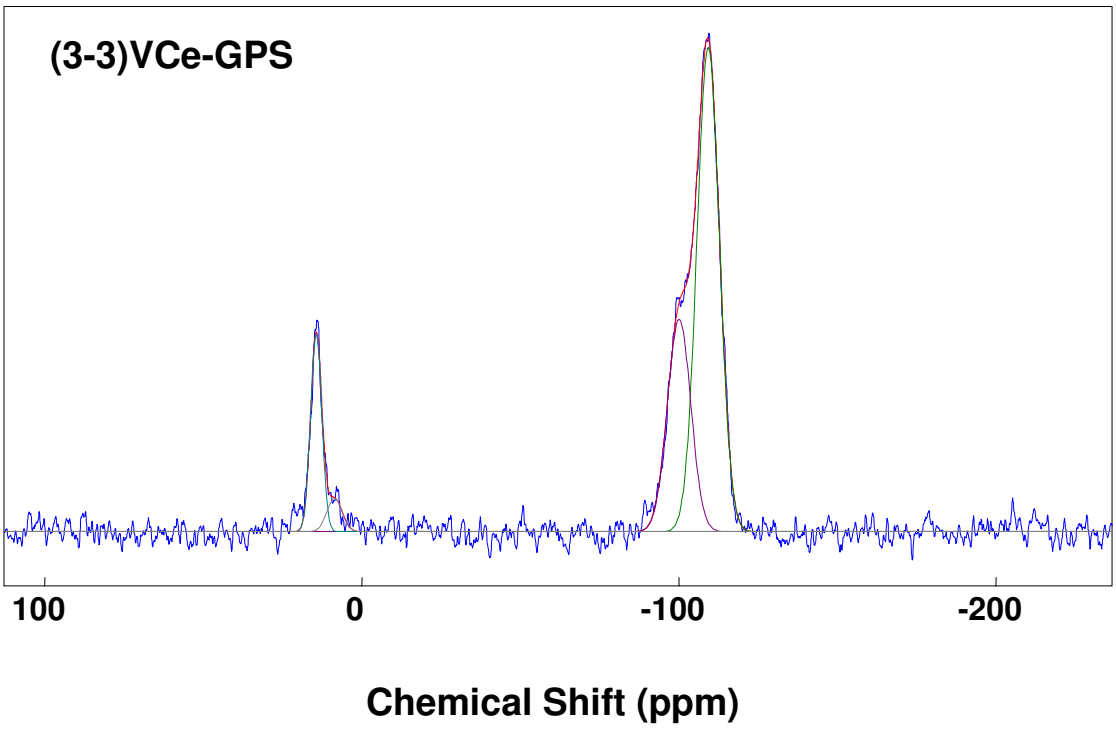

Figure A7.2.21 ^{13}C quantitative NMR spectra of 3Al-GPS.

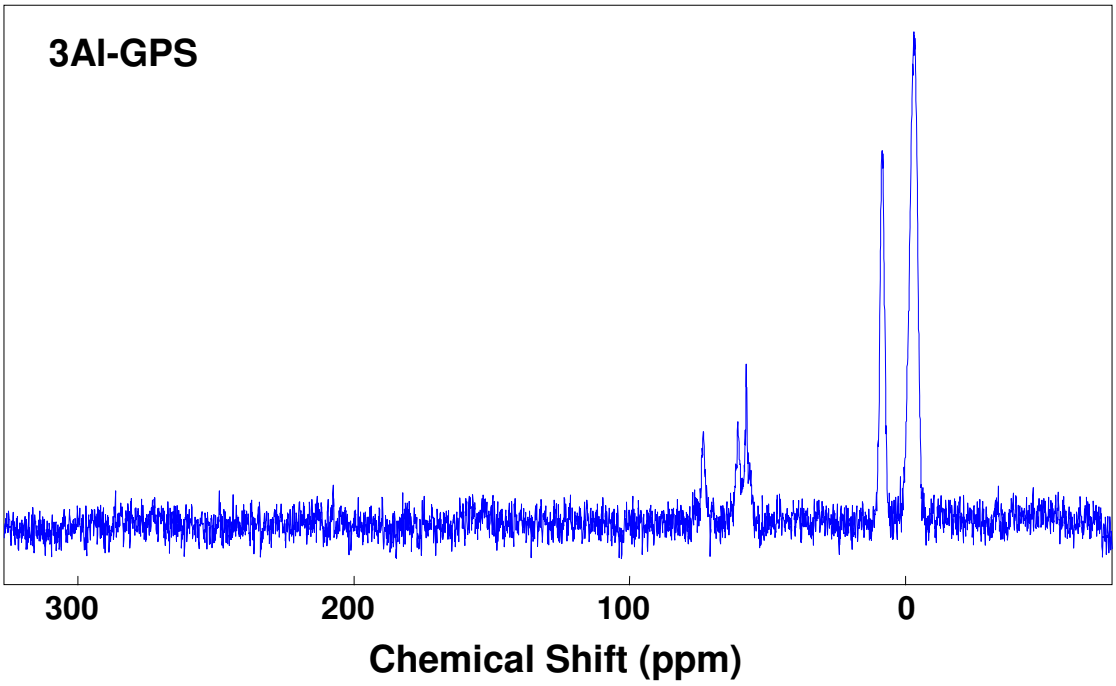

Figure A7.2.22 ^{29}Si quantitative NMR spectra of 3Al-GPS.

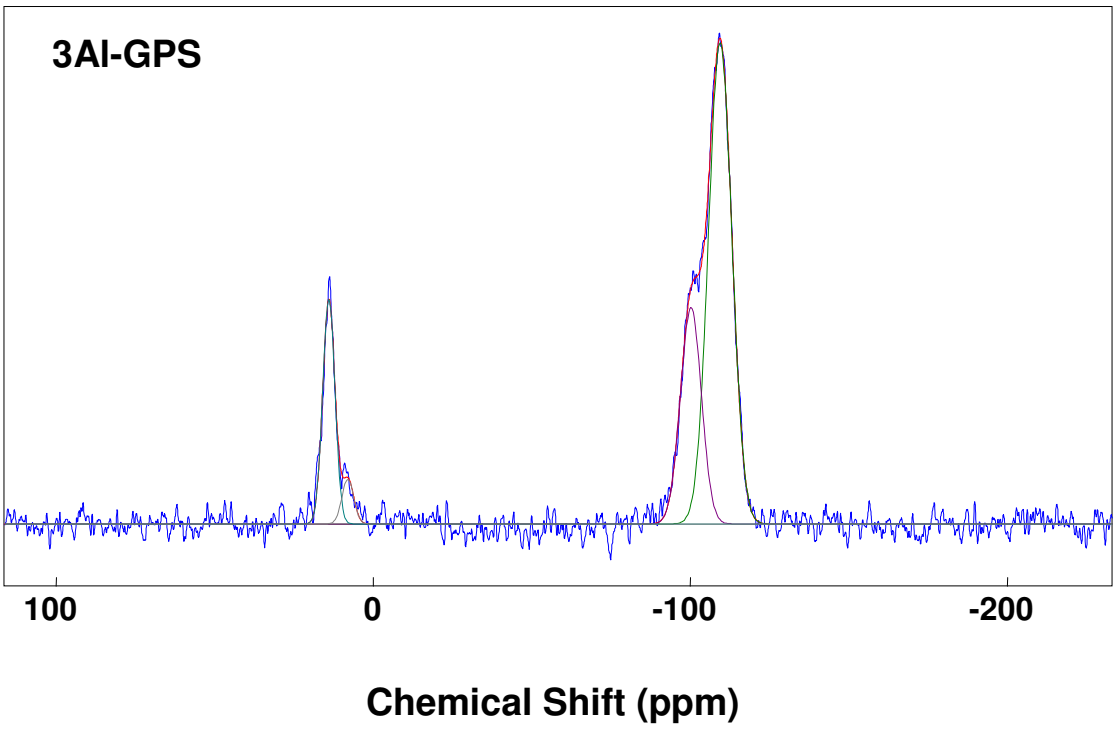

Figure A7.2.23 ^{13}C quantitative NMR spectra of (3-3)VAl-GPS.

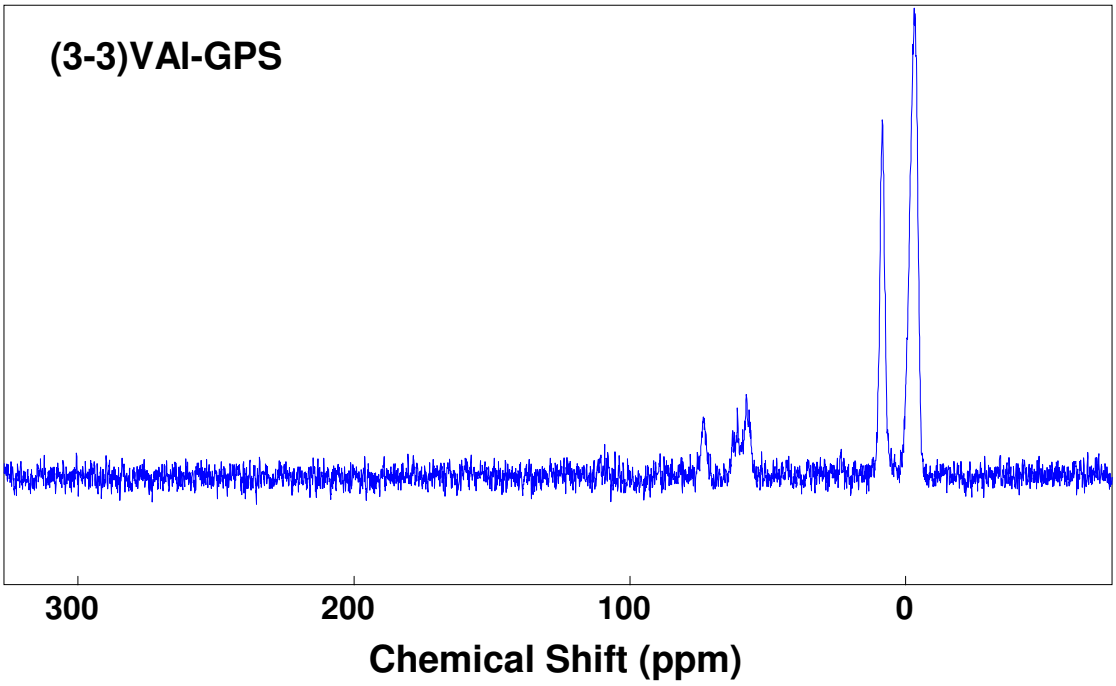

Figure A7.2.24 ^{29}Si quantitative NMR spectra of (3-3)VAl-GPS.

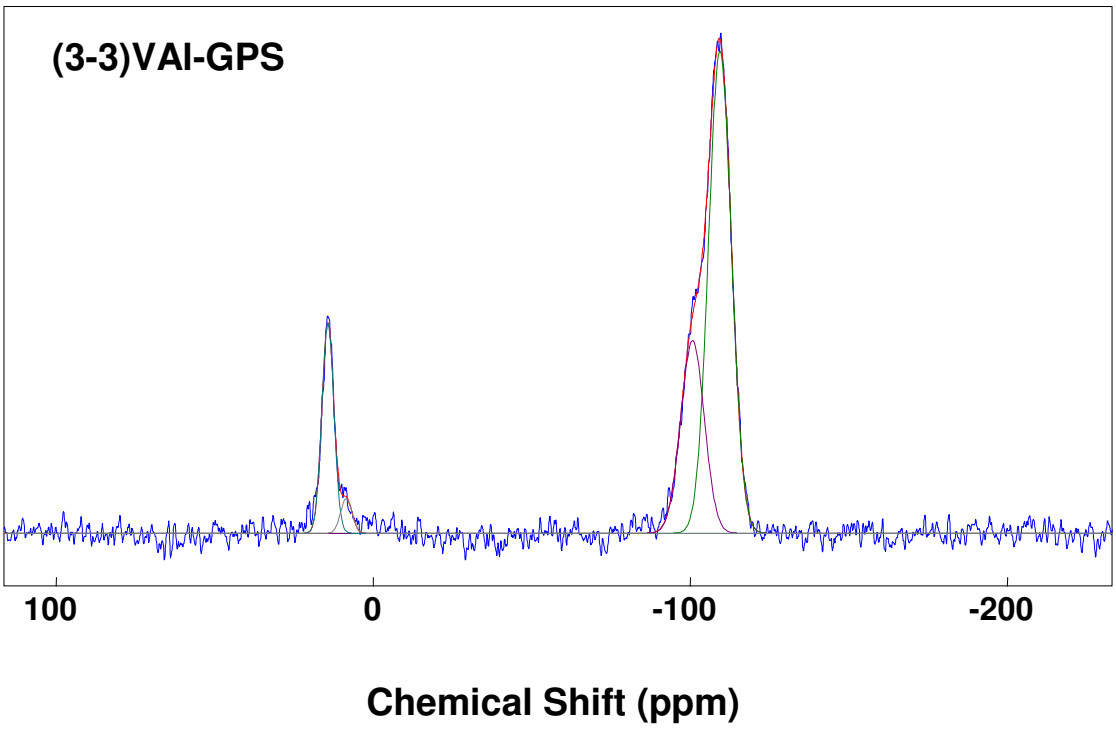

Figure A7.2.25 ^{27}Al quantitative NMR spectra of 1Al-GPS.

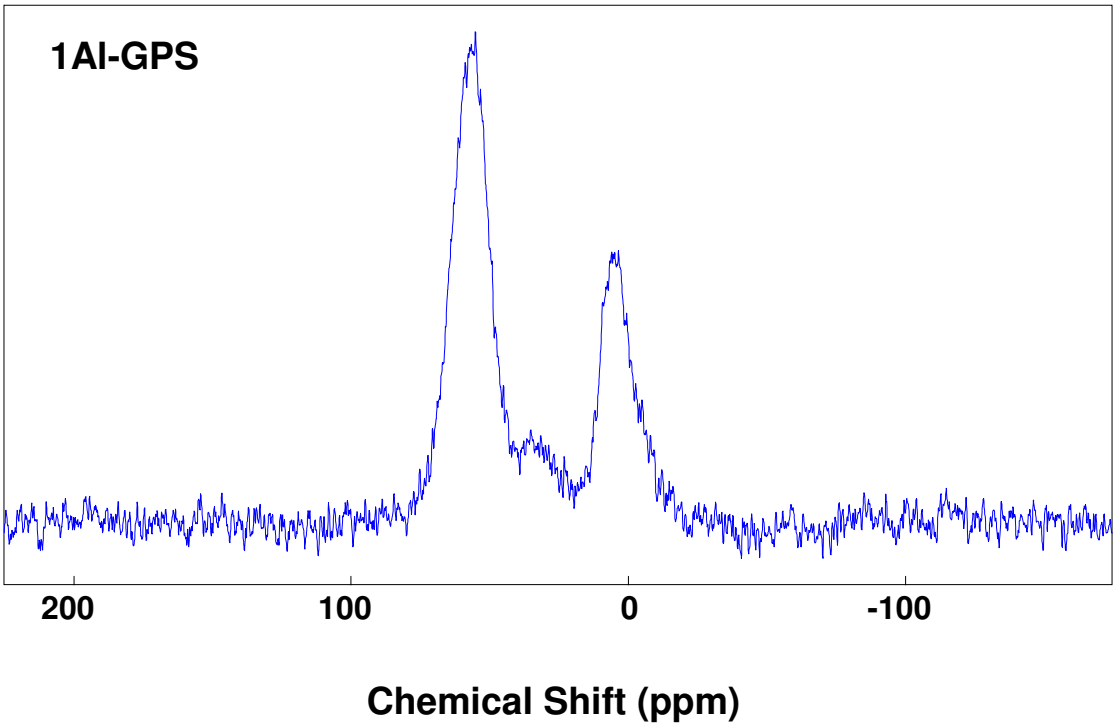

Figure A7.2.26 ^{27}Al quantitative NMR spectra of (1-1)VAl-GPS.

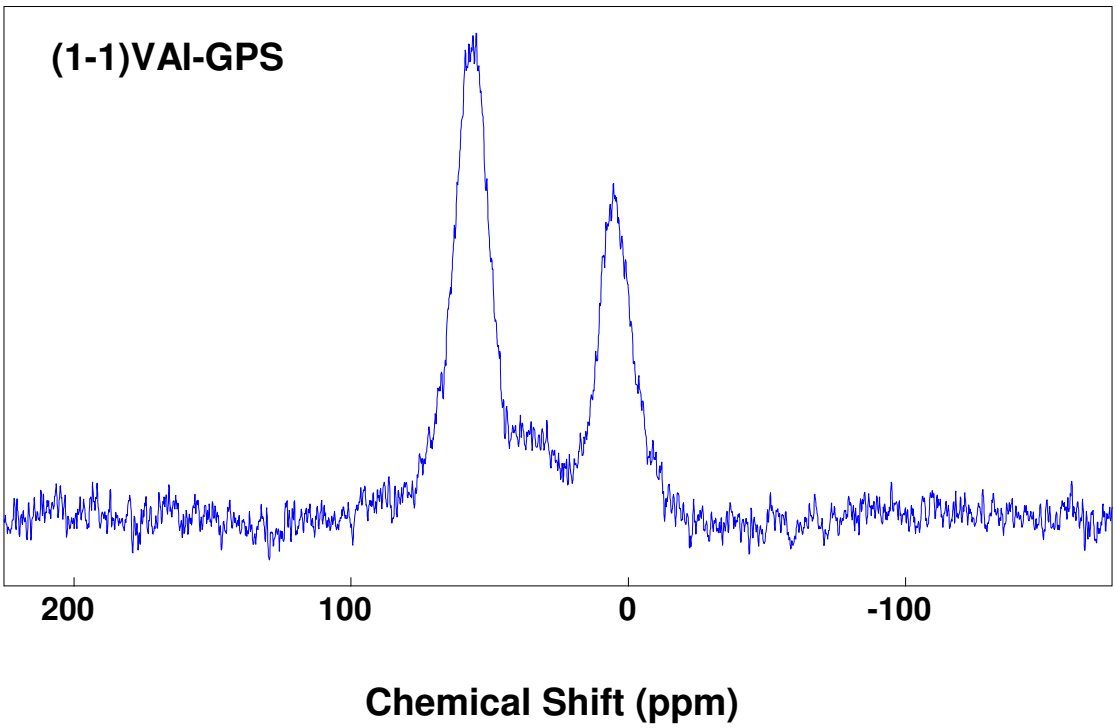

Figure A7.2.27 ^{27}Al quantitative NMR spectra of 3Al-GPS.

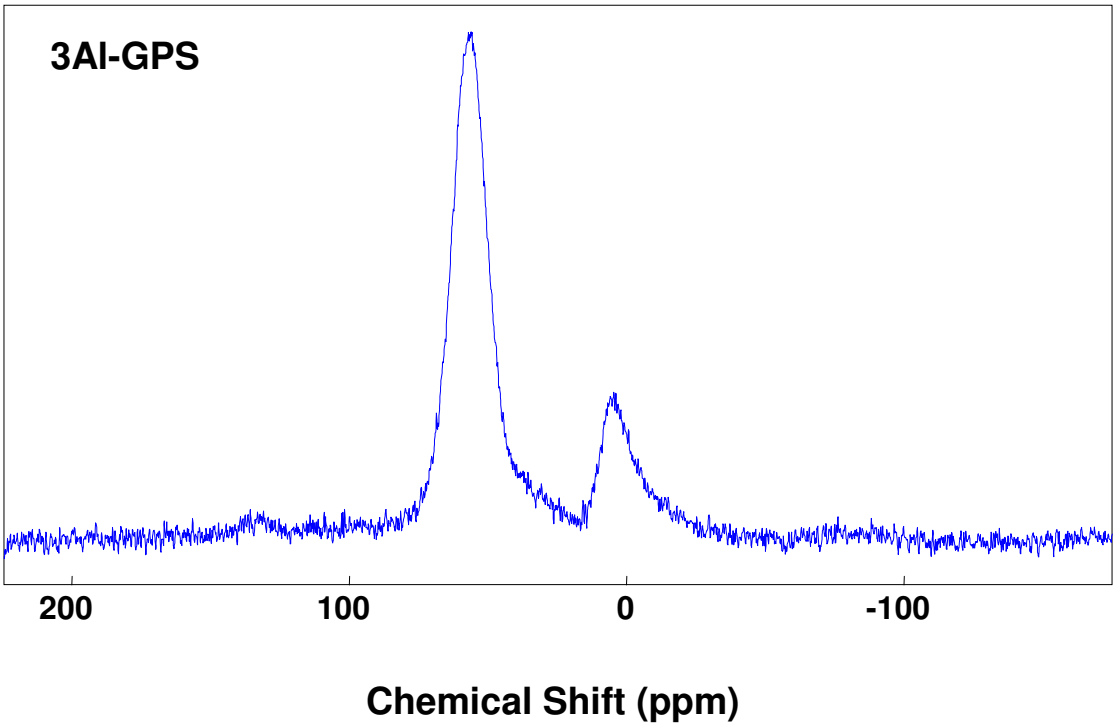

Figure A7.2.28 ^{27}Al quantitative NMR spectra of (1-3)VAl-GPS.

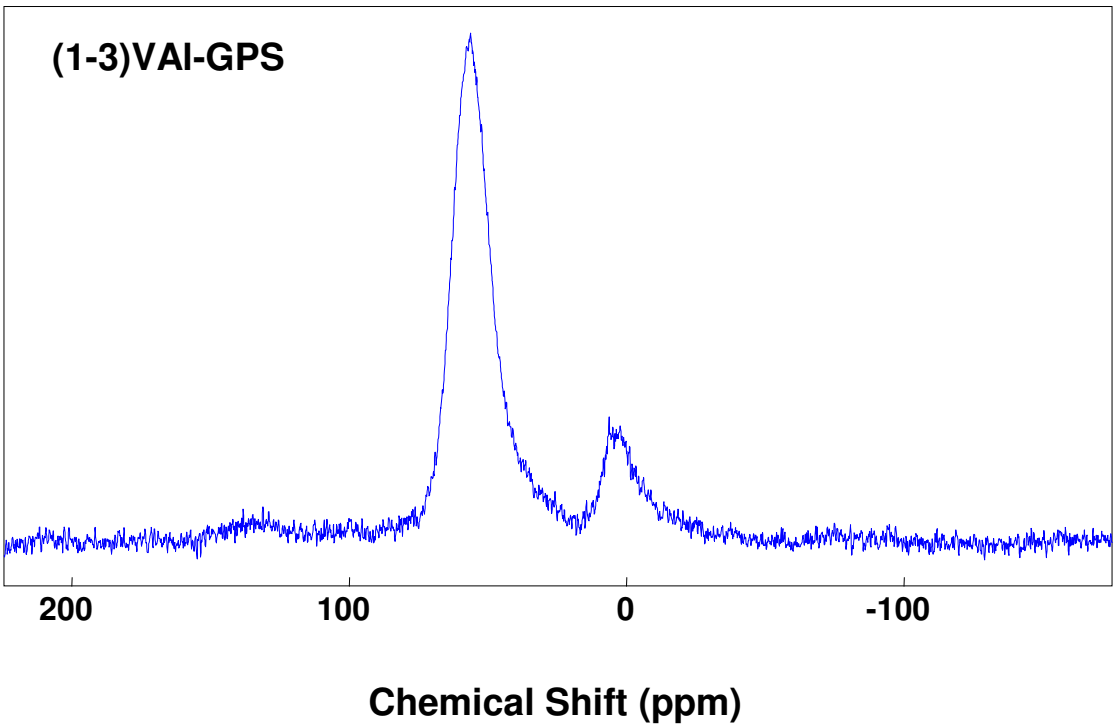

Figure A7.2.29 ^{27}Al quantitative NMR spectra of (3-3)VAl-GPS.

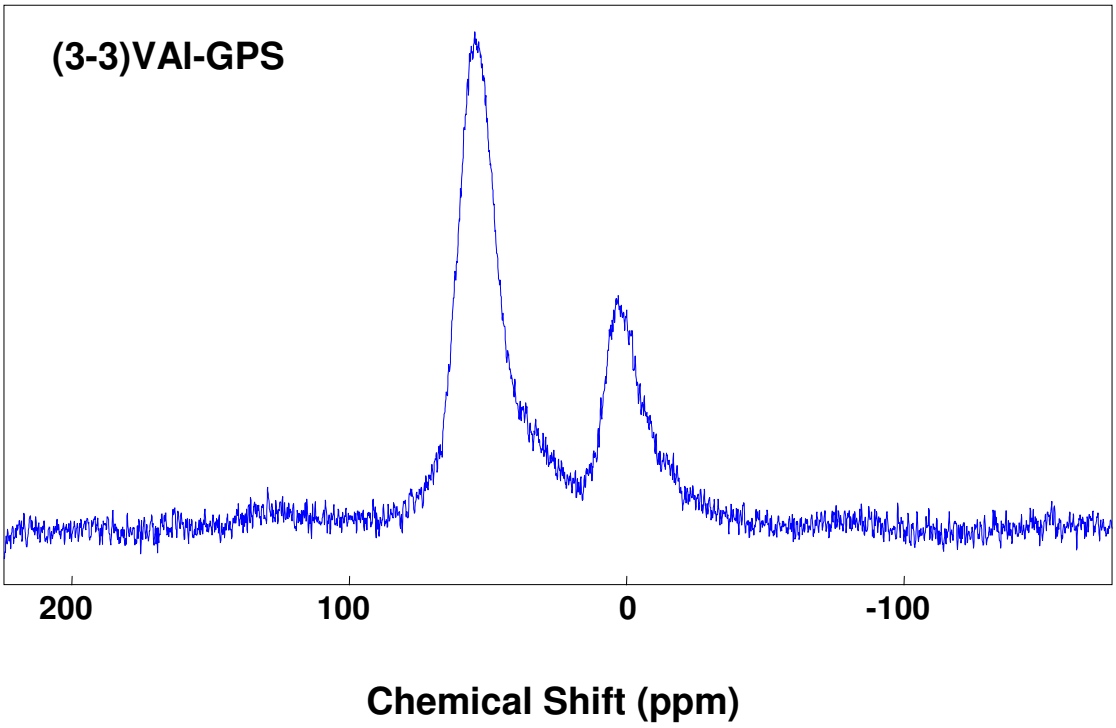

A7.3 NMR spectra of Chapter 6

Figure A7.3.1 ^{13}C NMR spectra of MWL-TMS.

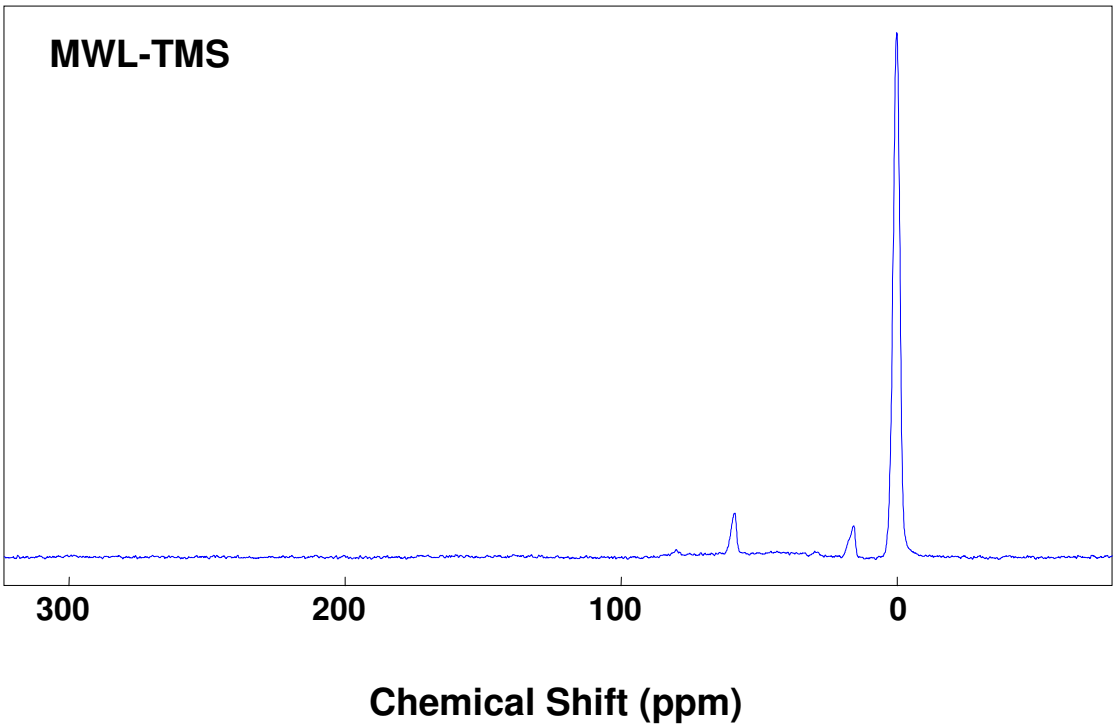

Figure A7.3.2 ^{13}C NMR spectra of PC.

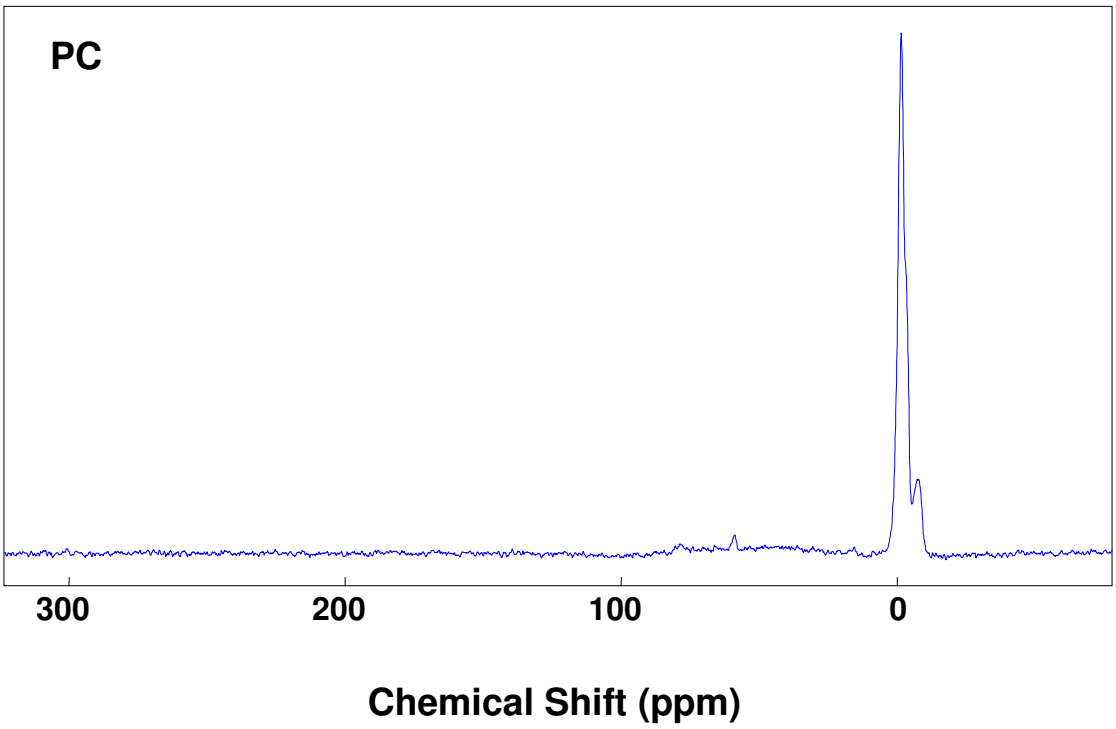

Figure A7.3.3 ^{27}Al quantitative NMR spectra of 3Al-GPC.

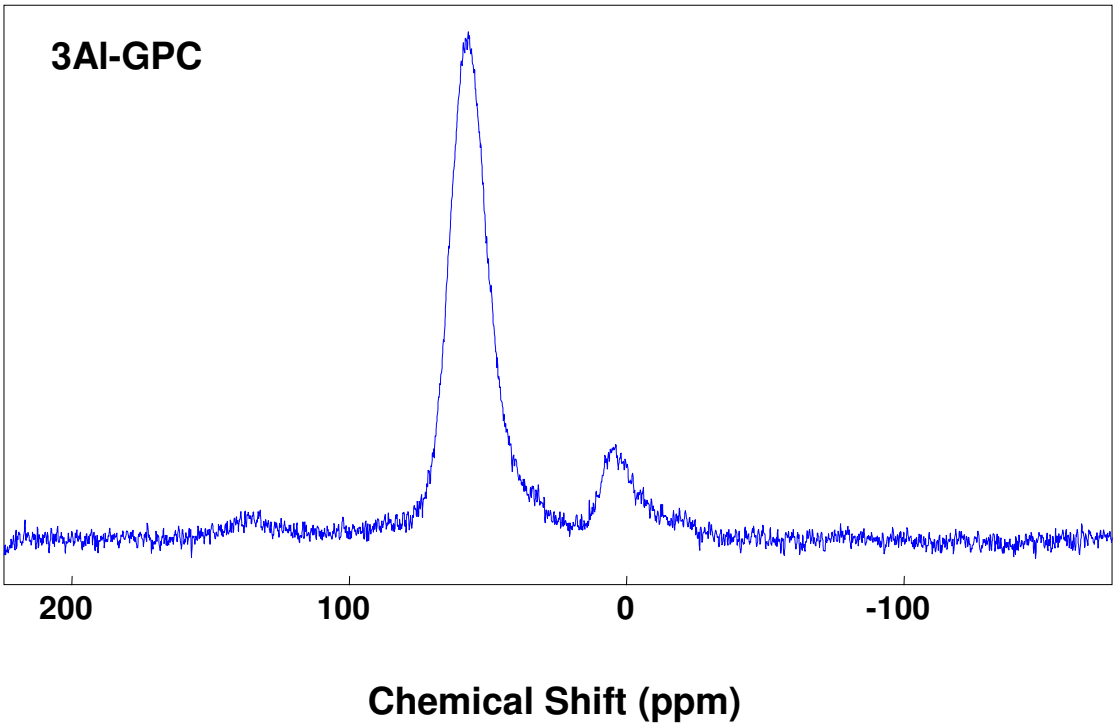

Figure A7.3.4 ^{27}Al quantitative NMR spectra of (1-3)VAl-GPC.

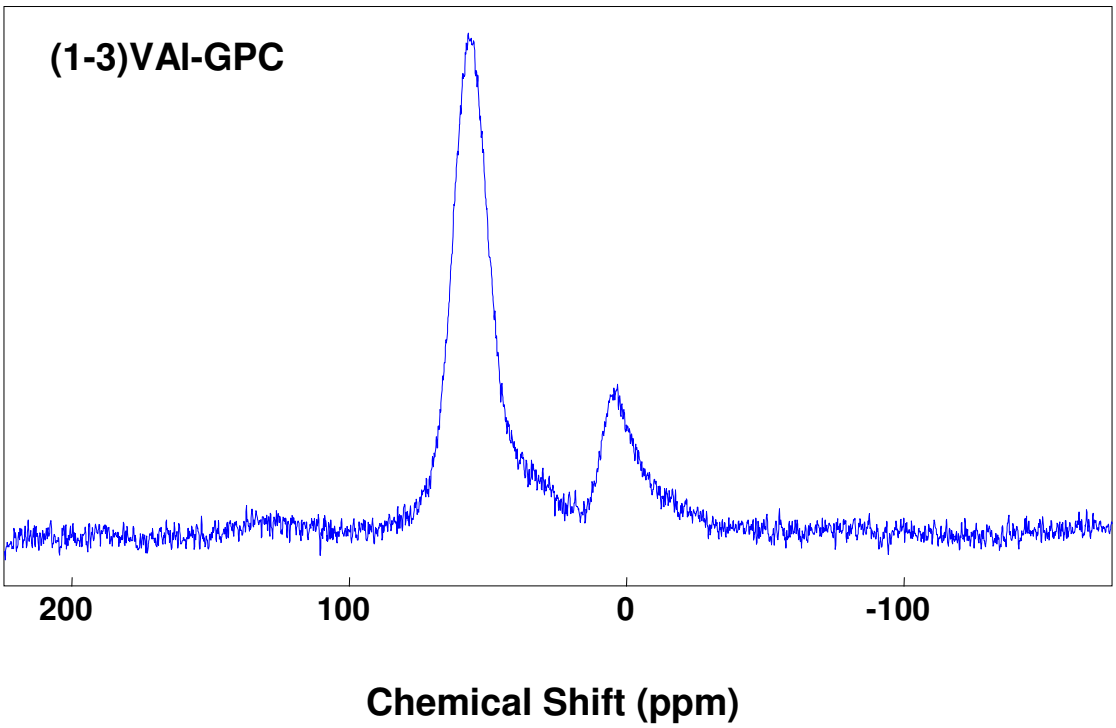

Appendix 8 Raman spectra

A 8.1 Raman spectra of Chapter 7

Figure A8.1.1 Raman spectra of Cu/Fe-MWL-cal and VCu/Fe-GMW-cal.

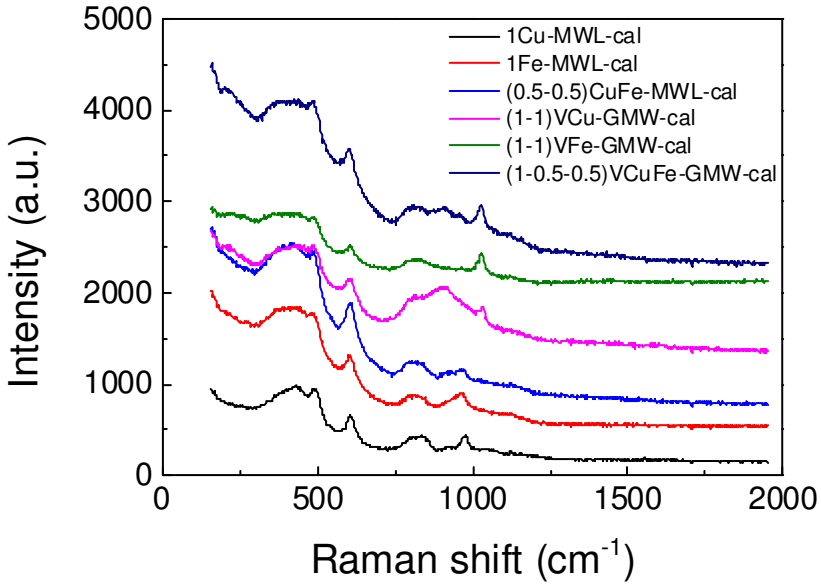

Appendix 9 TEM images

A 9.1 TEM images of Chapter 7

Figure A9.1.1 TEM image of 1Cu-MWL-cal

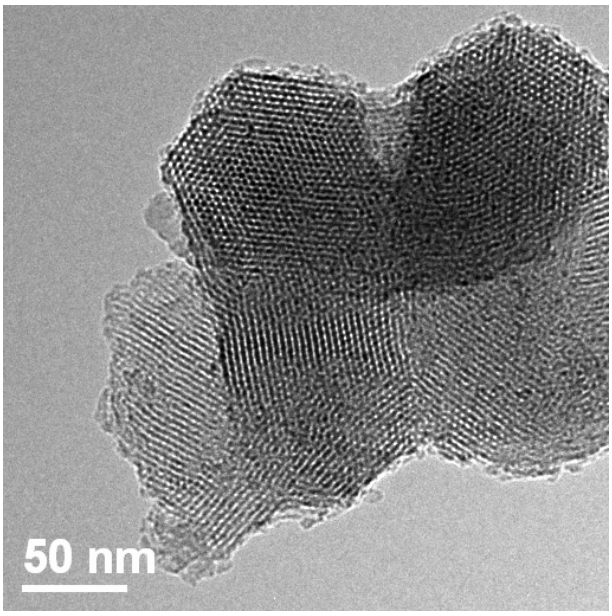

Figure A9.1.2 TEM image of 1Fe-MWL-cal

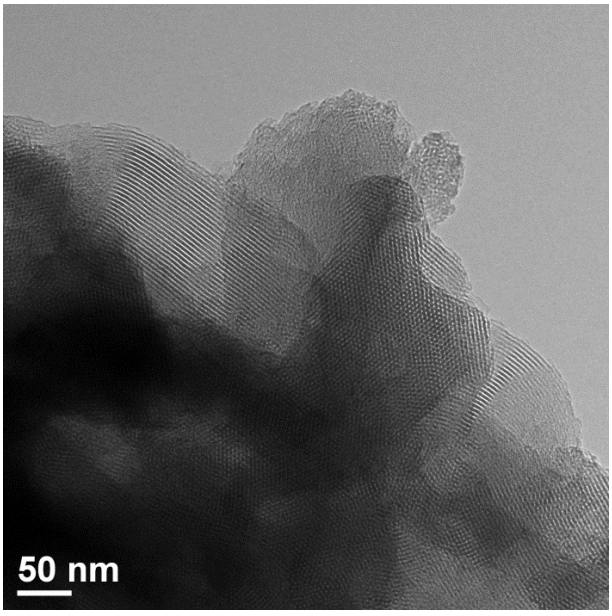

Appendix 10 Elemental analysis

A10.1 Elemental analysis of Chapter 7

Table A10.1.1 Elemental analysis of vanadium incorporated MCM-41 with Cu/Fe ions.

Sample	V (mol %)	Cu (mol %)	Fe (mol %)
1Cu-MWL-cal	0.00	2.92	0.00
(0.5-0.5)CuFe-MWL-cal	0.00	1.38	1.47
1Fe-MWL-cal	0.00	0.00	2.77
(1-0.5-0.5)VCuFe-MWL-cal	1.00	1.39	1.46
(1-1)VCu-MWL-cal	0.96	2.88	0.00

Appendix 11 Conversion and selectivity tables

Table A 11.1 High throughput screening of 1,2-diphenyl-2-methoxyethanol oxidation via supported vanadium catalyst before and after leaching test.

Catalysts		Conversion (%)	Selectivity (%)					TON	
			Benzaldehyde	Methyl benzoate	Methanol	Benzoic acid	Benzoin methyl ether	(ICP)	(actual)
(2.5-2.5)VTi-MWT-cal	RAW	8	100	0	0	0	0	0.00069	2.90
	Leaching	2	100	0	0	0	0	0.00057	0.88
(2.5-5)VAl-MWL-cal	RAW	49	84	10	6	0	0	0.00223	5.49
	Leaching	32	76	19	0	0	5	0.00109	7.34
(2.5-2.5)VZr_N-MWL-cal	RAW	29	100	0	0	0	0	0.00220	3.30
	Leaching	1	100	0	0	0	0	0.00109	0.23
(2.5-2.5)VCe_N-MWT-cal	RAW	12	100	0	0	0	0	0.00121	2.48
	Leaching	2	0	0	0	0	100	0.00095	0.53
(1-3)VTi-GPS-cal	RAW	7	100	0	0	0	0	0.00104	1.68
	Leaching	4	100	0	0	0	0	0.00098	1.02
(1-3)VAl-GPS-cal	RAW	10	77	13	0	0	10	0.00099	2.53
	Leaching	2	100	0	0	0	0	0.00018	2.78
(1-3)VZr-GPS-cal	RAW	10	100	0	0	0	0	0.00110	2.27
	Leaching	3	71	0	0	0	29	0.00068	1.10
(1-3)VCe-GPS-cal	RAW	10	100	0	0	0	0	0.00105	2.38
	Leaching	2	100	0	0	0	0	0.00087	0.57
(1-3)VTi-GPC-cal	RAW	9	100	0	0	0	0	0.00096	2.34
	Leaching	<1	-	-	-	-	-	0.00083	-
(1-3)VAl-GPC-cal	RAW	2	100	0	0	0	0	0.00093	0.54
	Leaching	2	100	0	0	0	0	0.00018	2.78
(1-3)VZr-GPC-cal	RAW	9	100	0	0	0	0	0.00101	2.23
	Leaching	5	64	36	0	0	0	0.00066	1.89
(1-3)VCe-GPC-cal	RAW	6	100	0	0	0	0	0.00095	1.58
	Leaching	<1	-	-	-	-	-	0.00074	-
1V-MWL-cal	RAW	21	100	0	0	0	0	0.00070	7.50
	Leaching	<1	-	-	-	-	-	0.00019	-
1V-GPS-cal	RAW	37	88	12	0	0	0	0.00107	8.64
	Leaching	2	100	0	0	0	0	0.00027	1.85
1V-GPC-cal	RAW	34	86	14	0	0	0	0.00102	8.33
	Leaching	6	100	0	0	0	0	0.0003	5.00

Table A 11.2 High throughput screening of 1,2-diphenyl-2-methoxyethanol oxidation via supported vanadium catalyst with additional base.

(RAW: no additional base; TEMPO: 2,2,6,6-Tetramethyl-1-piperidinyloxy; TEA: Triethylamine; EDPA: N-Ethyldiisopropylamine.)

Catalysts		Conversion (%)	Selectivity (%)				
			Benzaldehyde	Methyl benzoate	Methanol	Benzoic acid	Benzoin methyl ether
(2.5-2.5)VTi-MWT-cal	RAW	8	100	0	0	0	0
	TEMPO	<1	-	-	-	-	-
	TEA	<1	-	-	-	-	-
	EDPA	<1	-	-	-	-	-
(2.5-2.5)VAl-MWL-cal	RAW	49	84	10	6	0	0
	TEMPO	34	89	0	6	0	5
	TEA	31	78	5	11	0	6
	EDPA	28	93	0	0	0	7
(2.5-2.5)VZr$_N$-MWL-cal	RAW	29	100	0	0	0	0
	TEMPO	9	100	0	0	0	0
	TEA	<1	-	-	-	-	-
	EDPA	<1	-	-	-	-	-
(2.5-2.5)VCe$_N$-MWT-cal	RAW	12	100	0	0	0	0
	TEMPO	3	100	0	0	0	0
	TEA	<1	-	-	-	-	-
	EDPA	<1	-	-	-	-	-
1V-GPS-cal	RAW	37	88	12	0	0	0
	TEMPO	26	94	0	6	0	0
	TEA	<1	-	-	-	-	-
	EDPA	<1	-	-	-	-	-
1V-GPC-cal	RAW	34	86	14	0	0	0
	TEMPO	28	92	0	8	0	0
	TEA	<1	-	-	-	-	-
	EDPA	3	100	0	0	0	0

List of Abbreviations

(in alphabetical order)

AAS: Atomic Absorption Spectroscopy

AES: Auger Electron Spectroscopy

ALD: Atomic Layer Deposition

-cal: calcination

CTA: Cetyltrimethylammonium

CTATos: Hexadecyltrimethylammonium p-toluenesulfonate

CTMS: Chlorotrimethylsilane

CVD: Chemical Vapor Deposition

DTG: Derivative Thermogravimetric

EBDMS: Ethyl-1,2-bis(dimethylsilyl)

EDPA: N-Ethyldiisopropylamine

EDX: Energy Dispersive X-ray analysis

Eg: Edge energy

EPR: Electron Paramagnetic Resonance spectroscopy

FS: Fully Silylated mesoporous silica

FTIR: Fourier Transform Infrared spectroscopy

GC: Gas Chromatography analysis

GMW: Grafting following the Microwave incorporation

GPC: Grafted Partially Calcined mesoporous silica

GPS: Grafted Partially Silylated mesoporous silica

HCl: Hydrochloric acid in water

HMDSA: Hexamethyldisilazane

HTS: High Throughput Screening

ICP: Inductively Coupled Plasma spectrometer

InGASE: Internal/ Grafted/ Anchored/ Surfacing/ Embedded nomenclature

IUPAC: International Union of Pure and Applied Chemistry

LCT: Liquid Crystal Templating

LMCT: Ligand to Metal Charge Transfer

Ludox®: HS-40 colloidal silica

MCM-41: Mobil Composition of Matter No. 41

MSNs: Mesoporous Silica Nanoparticles

MSP: Molecular Stencil Patterning

MWL: Microwave synthesis with Ludox as silica source

MWL-R: "R" means "surfactant removed by chemical extraction"

MWT: Microwave synthesis with TEOS as silica source

NMR: Nuclear Magnetic Resonance spectroscopy

PFA: Polyfluoroalkoxy copolymer resin

PS: Partially Silylated mesoporous silica

PSI: Pounds per Square Inch

PTT: Partial Thermal Treatment

Red-Al®: Sodium bis(2-methoxyethoxy)aluminum hydride solution

RS: Raman Spectroscopy

SEM: Scanning Electron Microscopy

SOMC: Surface Organometallic Chemistry

TBOT: Titanium (IV) n-butoxide

TEA: Triethylamine

TEM: Transmission Electron Microscopy

TEMPO: 2,2,6,6-Tetramethyl-1-piperidinyloxy

TEOS: Tetraethyl Orthosilicate

TGA: Thermogravimetric Analysis

TMA^+: Trimethyl Ammonium

TMABr: Tetramethylammonium Bromide

TMAOH: Tetramethylammonium Hydroxide

TMDSACP: 2,2,5,5-tetramethyl-2,5-disila-1-azacyclopentane

TMS: Trimethylsilyl

TON: Turn Over Number

UV-vis DRS: Ultraviolet Visible Diffuse Reflectance Spectroscopy

XAS: X-ray Absorption Spectroscopy

XPS: X-ray Photoelectron Spectroscopy

XRD: X Ray Diffraction

Acknowledgements

Firstly, I would like to express my sincere gratitude to my supervisors: Professor Laurent BONNEVIOT (ENS-Lyon, France), Professor Belén ALBELA (ENS-Lyon, France), and Professor Yong LU (ECNU, China). The guidance of Professor Laurent BONNEVIOT helped me in all the time of my research and the writing of this thesis. I was greatly touched by his patience, motivation, and immense knowledge. He led me with his inspiration and enthusiasm to explore the magic and profoundness scientific truth behind the experimental phenomenon, his optimistic spirit and his encouragement are the strong impetus to help me overcome the difficulties in my study. He is modest and genial as a friend to his students, and he is also a great model for students with his wisdom and spirit both in science and in life. Professor Belén ALBELA also gave me a lot of supports in my research and writing, her positive and cheerful spirit is like the sunshine to warm everyone around her. She is always ready to help students, not only for their research but also in their life. With her careful concern, I feel as warm as in a great family of our laboratory. To enlighten my research and thought, Professor Yong LU gave me the scientific training with the outstanding guiding ideology and he is always willing to help. His scrupulous and truth-seeking spirit help me acquire a solid foundation for my further research, his diligent and conscientious attitude spur me to keep forging ahead.

I would like to thank my thesis committee: Professor Vitaly ORDOMSKY, Professor Dengsong ZHANG, Professor Yun GUO, Professor Catherine PINEL, and Professor Ye LIU, Professor Chen ZHAO, Professor Xiaohong LI for their insightful comments and encouragements, and also for the instructive questions which can incent me to widen my research from various perspectives.

Besides my supervisors and thesis committee, I would like to express my great appreciations to Madam Yunhua Qian and Professor Mingyuan He. Thanks to their tremendous efforts for the supports of the cooperation program between École Normale Supérieure (ENS) and East China Normal University (ECNU), it is a precious chance for me to accept the training both of scientific and linguistic in this

Sino-French education program. Madam Yunhua Qian and Professor Mingyuan He always cares about the students as their own children, their warm solicitude is a great consolation to me, I was deeply moved and encouraged by their flourishing and invigorated spirit.

My sincere thanks also go to Professor Tom BAKER (University of Ottawa, Canada), who provided me with an opportunity to join his team as a student visitor, and who gave access to the laboratory and research facilities with his warm welcome and many instructions. I am particularly grateful to Mme. Roxanne Clément (University of Ottawa, Canada), who help me a lot for the catalysts test, her neat and efficient work always impressed me. I would like to express many thanks to Mme. Flora Marguerite, Dr. Christian Díaz-Urrutia, Dr. Mehdi Mostajeran, Uttam Das, Kaitie Giffin, Matt Leclerc, Nick Andrella, Thomas McFarland, and all the students in the group of Professor Tom BAKER, without their help it wouldn't have been possible for me to complete the experiments during my visit.

I would like to express my endless thanks to my colleagues in ENS-Lyon: to Dr. Nathalie CALIN for her circumspective help of the XRD characterization and her management of the laboratory, to Mme. Sandrine DENIS-QUANQUIN for her help of the NMR characterization, to M. Lhoussain KHROUZ for his help of the EPR characterization, to Dr. Gilles MONTAGNAC for his help of the Raman characterization, to M. Christian MELKONIAN for his technical support, to Mme. Marie-Francoise GUIOT, Mme. Edwige ROYBOZ, and M. Damien SEON for their administration work, to Mme. Halima HALIMI, Mme. Chuan WANG, Mme. Huajun WANG, Mme. Myriam FRIAT for their kindly help and support. And many thanks for Pro. Chantal ANDRAUD, Pro. Carine MICHEL, Dr. Laure-Lise CHAPELLET, Mme. Delphine PITRAT, Pro. Weï DONG, Pro. Frédéric LEROUGE, Pro. Frédéric CHAPUT, Pro. Christophe BUCHER.

I would also like to express my sincere thanks to my colleagues in ECNU: to Dr. Hao XU, Dr. Lin ZHANG and Mme. Li CHEN for their help of the SEM and TEM characterization, to Pro. Kun Zhang who gave me a lot of suggestion and help, to Mme. Xiaoling LIU and Mme. Xiaoyan LIU who put a lot of efforts into the

cooperation education program, and many thanks to Mme. Ran DU, Mme. Wenjing LONG and Mme. Yinyan ZHANG for their administrative support.

More love and gratitude beyond words to my colleagues and friends in our laboratory both in Lyon and Shanghai: Hanene DOGHRI, Jérémy CHAIGNON, Beltzane GARCIA CIRERA, Luis ESCRICHE-TUR, Guillaume MALCOURONNE, Sonia ZRIBI, Francois-Xavier TURQUET, Delphine DASSONVILLE, Mateusz ODZIOMEK, Isra IRIS, Bruno SECORDEL, Lin FANG, Wenjuan ZHOU, Guofeng ZHAO, Qiaofei ZHANG, Chunzheng WANG, and Junling XING. I would like to express my very special grateful to Yuting ZHENG, who kindly help me as a sister and teach me a lot of things both for the experiments and in life. Also many thanks to all the friends in Lyon. Thanks to all of you for the cheer and joy that you bring to my life with the warm accompany, all the happy moments with you are the treasure memories for me.

I would like to express endless love and gratefulness to my family: my parents and grandparents for their constant support and unconditional love. I love you all dearly.

Last but not least, I would like to thank China Scholarship Council, LIA-FUNCAT, Rhône-Alpes and Caisse Allocation Familliale of France for the financial support, without the scholarship and grant, it is not possible for me to accomplish my research and study, it is a precious experience for me not only with science but also with culture and my life.

On my way to seek the scientific truth, sometimes I feel the path in front of me was shrouded by cloud and mist, once when I was discussing with Professor Laurent BONNEVIOT in the laboratory, I express my misgivings, and he told me: " When you are climbing a mountain, you could not see the top, the higher you climb, the more dangers you will see, but this is a proof that you are climbing. " Then one of my friends translated it into a Chinese verse which is philosophic and aesthetic, here I will use this sentence as the end of this paragraph: "登高莫问顶，途中耳目新".